UNIVERSITY OF CALIFORNIA

SANTA CRUZ

A QUANTITATIVE STUDY OF PECULIARITIES IN GALAXY MORPHOLOGY

A dissertation submitted in partial satisfaction of the

requirements for the degree of

DOCTOR OF PHILOSOPHY

in

ASTRONOMY AND ASTROPHYSICS

by

Katherine Liang-Kai Wu

December 1999

The dissertation of Katherine Liang-Kai Wu is approved:

Sandra M. Faber, Chair

Michael Bolte

David C. Koo

Tod R. Lauer

Dean of Graduate Studies

Contents

List of Figures

List of Tables

Abstract

A Quantitative Study of Peculiarities in Galaxy Morphology

by

Katherine Liang-Kai Wu

I have developed a refined version of the asymmetry parameter first presented by Abraham et al. (1996). Coupled with a simple concentration index, this pair of indices, A_W-C_W, is compared to Abraham et al.'s $\log(A_A)$-$\log(C_A)$ algorithm. These indices are then applied to a large sample of galaxies in the Hubble Deep Field with photometric redshifts from Connolly (1999). This allows investigation of trends at redshifts which have been largely inaccessible until now. The final sample consists of ~350 objects detected by the A_W-C_W algorithms with first-moment radii, $r_1 \geq 0''.2$ (corresponding to F814W$_{AB} \sim 26$).

The distribution of objects in the A_W-C_W plane is found to change with redshift. The region of the A_W-C_W plane populated by objects out to $z \sim 1.2$ is roughly constant. Accounting for bandpass shifting effects, this region resembles that populated by local bright galaxies (Frei et al. 1996) cosmologically simulated at $z = 0.8$.

Beyond $z \sim 1.2$, the distribution of galaxies undergoes a significant change. Highly concentrated objects disappear from the A_W-C_W plane, while high asymmetry objects appear. The high concentration objects below $z \sim 1.2$ all have early-type morphologies. Very low resolution SEDs of these galaxies created using colors from Williams et al. (1996) are used to calculate the expected appearance of these objects at higher redshifts ($z = 1.5$ and 2.3). Assuming their luminosities and SEDs have not changed, one-third of the $z \sim 0.8$

objects would be undetected at $z = 1.5$, and 97% would disappear by $z = 2.3$. Any true drop in the number density of these objects would be completely masked by such strong selection effects.

An increase in the number and degree of asymmetric objects is also seen beyond $z \sim 1.2$. Many of these objects exhibit multiple condensations, consistent with merging. Though the shifting of the ultraviolet galaxy spectrum into the F814W-band may be partially responsible, the majority of the increase in both number and degree of asymmetry appears to reflect a genuinely higher number density of asymmetric objects at earlier epochs.

A_W and C_W are shown to be useful tools for exploring galaxy morphology over a wide range of redshifts. Future refinements combined with better SEDs and evolutionary models will undoubtedly reveal valuable insight into galaxy evolution.

獻給

阿爹 和 好婆

Acknowledgements

I would like to thank my advisor, Sandra Faber, for all of the multi-hour sessions in which I learned so much, for her patience and thoroughness with me as a developing scientist and scientific writer, and for enabling me to discover one of the true passions of my life. I am also indebted to my committee members for their support, both scientific and personal: to Mike Bolte, for introducing me to the joys of observing at the 40" and encouraging me to try "that little project" with Sandy and for all of his wonderful stories about that cute little girl; to David Koo, for all his ideas and the many interesting tidbits that I learn every time we talk and for the wonderful dinner parties that he and Anna and Miranda always host; and to Tod Lauer, who came up with the notions that ultimately became my thesis (sorry I never quite worked out that scruffiness index!), for his input, for enduring my visit at Kitt Peak, and for always being willing to fly all the way out to Santa Cruz just for my defense(s). I would also like to thank John Kolena, and Bruce Carney and Jim Rose and the rest of the Carolina physics/astronomy department for sparking my curiosity about the universe around us.

A special thanks goes out to the postdocs, who have enhanced my life both scientifically and socially: Nicole Vogt, my partner in crime in doing slitmasks the good (?!) ol' fashioned way and in the occasional late night tango! Luc Simard, without whom I'm sure I would never have made it through (zeropoints and all)! I am forever indebted to him for all of his patience with my many questions and his never-ending willingness to help. And, of course, for his wonderful company so very early every morning!... well, almost every morning... And, of course, to the lunch crowd, which varied over the years: Rafael Guzman (I haven't forgotten our deal yet!), James Lowenthal, Chris Mihos, Duncan

Forbes, Drew Phillips, Chip Kobulnicky, and many more whom I just don't have room to name!

And, of course, to my fellow graduate students, with whom I did many late night homeworks, practiced many an hour for the prelim, and played the occasional round of pool! And who could forget all those movies at the Towne. Grad life would not have been the same around here without all of you (in no particular order, since my brain is in no particular order at the moment!): Kathryn, Caryl, Scott, Dan, Neal, Romeel, Charm, Dave, Andrew, Linda, Amy N., Rob A., Amy B., Geoff, Zo, Jon... Most especially, I would like to thank Eric Sandquist and Jennifer Johnson for their constant support and willing ear, even when they'd heard it a million times already! There are no words to express how much I value their friendship.

I would also like to thank all my dance friends for helping to keep me sane! Your support has meant so very much to me over the years! In particular, I would like to mention Steve, Naomi, Darryl, and Mike Y. for some wonderful evenings both in and out of the ballroom; Sandy Foss for her guidance and friendship (and dresses!); and, most specially, I would like to thank Deborah and Rudolph, who have been such wonderful friends through so much more than just dancing, and David W., who may never realize just how much he has given me in these last few months.

Most importantly, I would like to thank my family, who have always been there for me (sometimes even when I didn't think I wanted them to be!). No matter what happens, I know I will always have their love and support. So, here's to all of you: Ah Dieh, Hao Bu, MaMa, 88, GuGu, JeJe, and our most recent addition, Percy!

Thank you all! I couldn't've done it without you!

Chapter 1

Introduction

1. The Hubble Sequence – the Traditional Classification Scheme

The morphological classification of nearby "normal" galaxies is embodied in the Hubble Sequence (Hubble 1936, de Vaucouleurs 1959, Sandage 1961), a system in which galaxies range from ellipticals through spirals to irregulars. This classification scheme works well for large, bright local galaxies for which we can obtain high resolution, detailed images. In these images, ellipticities, bulge-to-disk ratios, and pitch angles of spiral arms can be measured to high accuracy. Even locally, however, the Hubble Sequence is not universally applicable. Low surface brightness (LSB) galaxies, for example, are sometimes difficult to fit into the sequence. Highly distorted objects and merger candidates also have no place in this sequence. Nonetheless, the Hubble Sequence appears to work remarkably well for the majority of bright galaxies that we see locally.

Several groups have, thus, attempted to use the Hubble Sequence classification scheme to describe galaxies seen at high redshift (e.g., Griffiths et al. 1994, Driver et al. 1995, Glazebrook et al. 1995). At high redshift, however, several issues limit the usefulness of this classification scheme. First, the resolution of images of high redshift galaxies is generally lower than it is locally, even with powerful space-based telescopes such as the Hubble Space Telescope (HST). This makes it much more difficult to distinguish the fine details that differentiate one Hubble sub-class from another. In addition to the poorer resolution, the signal-to-noise ratio of images of high redshift galaxies is also lower. Not only does this make it more difficult to detect distinguishing structure, some features will be completely lost in the noise. The Hubble Sequence is also primarily a visual sequence – "classification by the experts," if I may. The result is that the classification is subjective and will vary depending on which "expert" you choose to consult (Odewahn et al. 1996, Naim & Lahav 1997, Brinchmann et al. 1998). One last major drawback of attempting to apply the Hubble Sequence classification scheme to high redshift galaxies is that, as with the local distorted population, there are many galaxies that simply do not fit into the Hubble Sequence at all. These "peculiar" galaxies come in many different shapes and sizes, and consensus on what exactly makes a galaxy "peculiar" has yet to be reached (Naim & Lahav 1997). Nevertheless, to lump these galaxies all into one "catch-all" category, or to merge them with normal irregulars (as discussed in the next section), would be to throw away potentially vital information about galaxy evolution and formation.

2. What *is* a "Peculiar" Galaxy?

Peculiar features in galaxy morphology (e.g., bridges, tails, multiple cores) have long been attributed to galaxy interactions (Zwicky 1953, 1956, 1959; Toomre & Toomre 1972). More recently, these features have been reproduced in numerical simulations of galaxy interactions and mergers (e.g., Mihos 1995). The simulations also indicate that these interactions are capable of inducing bursts of star formation (Mihos & Hernquist 1994, 1996), as suggested earlier by, e.g., Larson & Tinsley (1978). Examples of "peculiar" galaxies can be seen in many forms in the local universe (Vorontsov-Velyaminov 1959, Arp 1966).

An important distinction should be made between "irregular" and "peculiar" galaxies. In many recent works on distant galaxies, these two groups have been lumped into one, when they are, in fact, two very different species. "Irregular" galaxies are the traditional late-type galaxies found at the end of the Hubble Sequence (Sdm, Im classes). They are generally quiescent, gas-rich, isolated systems, similar to the Magellanic Clouds. "Peculiar" galaxies, on the other hand, are found in a variety of different environments, from the field to dense clusters. These galaxies may show a variety of peculiar features such as tidal tails, warped disks, multiple cores, or skewed light distributions.

It is perhaps understandable, though misguided, why these two very different types of galaxies have tended to be grouped together in studies of distant galaxies. Both types of galaxies tend to have blue colors, as both tend to be actively forming stars. The star formation mechanism of the two types of galaxies, however, is completely different. The gas-rich nature of irregular galaxies leads naturally to constant, though quiescent, star formation (e.g., Gallagher, Hunter, & Tutukov 1984). The star formation in peculiars, on the other hand, is often found in strong starbursts induced by interactions with neighbors. Because these two types of galaxies reflect such contrasting star formation mechanisms and activity, it is crucial to study them separately. One should be extremely cautious of trends found when the two types are grouped together.

Peculiar galaxies provide us with unique insight into some of the possible processes of galaxy evolution and formation. The current paradigm for galaxy formation is hierarchical clustering and merging. The frequency of peculiar galaxies at a given epoch likely reflects the merger rate at that epoch. The nature and degree of peculiarities may give us an indication of the types of mergers that have occurred and the relative masses and other properties of the progenitors.

3. Quantifying Morphology at Low and High Redshift

Several groups have developed methods by which to quantify specific peculiar features in otherwise normal-looking local galaxies. Schweizer & Seitzer (1992) introduced the fine structure constant, Σ, which measures ripples, jets, X-structures, and boxy isophotes in elliptical and S0 galaxies. Rix & Zaritsky (1995) used Fourier decomposition to analyze the nonaxisymmetric component of stellar disks. Among other properties, they studied the "lopsidedness" of these stellar disks and quantified the strength of $m = 1$ distortions.

Though developing means to quantify specific morphological features is certainly informative, the need for a more general quantitative, automated galaxy classification scheme is becoming increasingly evident as large surveys of galaxies are designed and carried out. Until recently, morphological classification has generally been done "by eye" by the "experts." With the vast amounts of digital data that are now streaming in, "eyeball" classification is no longer a manageable task. Automated methods of classification need to be developed. Naim et al. (1997a,b) present one such method. They introduce four morphological parameters (blobbiness, isophotal center displacement, isophotal filling factor, and skeleton ratio) by which galaxies are classified using an unsupervised learning method (Kohonen 1989, Mähönen & Hakala 1995) that requires no human training set. The great advantage of this system is that no *a priori* biases from human classifiers are included in the classification scheme. A limitation of this scheme, however, is that it is designed for classification of isolated "normal" galaxies. Application to close pairs and peculiar objects has not been presented, and it is unclear how such galaxies will be handled in this classification scheme.

Detailed images from HST have sparked a surge of interest in morphological peculiarities in both distant and local galaxies. From these images, claims have been made that the frequency of peculiar galaxies at high redshift is much higher than it is locally (Forbes et al. 1994, Driver et al. 1995, Cowie et al. 1995, Driver et al. 1998). Some groups have even pronounced the existence of new types of galaxies, e.g., "chain" galaxies (Cowie et al. 1995).

Quantitative Morphological Classification Techniques

This interest has led to the development of several indices tuned to estimate the asymmetry of galaxies. Schade et al. (1995) developed two indices to measure residual structure in a subset of 32 galaxies in the Canada-France Redshift Survey (CFRS) for which secure redshifts ($0.5 < z < 1.2$) had been obtained. After rotating and subtracting a galaxy image from itself, fluctuations less significant than 2σ are clipped, and the resulting image is subtracted from the original image. This produces an image in which strong asymmetric structure has been removed. A two-dimensional, two-component (disk+bulge) model is fit to this "symmetrized" image and subtracted from the original image, leaving a residual image which contains only the asymmetric components of the galaxy. The total and asymmetric residual fluxes are defined as follows:

$$R_T = \frac{\Sigma \frac{1}{2} |R_{ij} + R_{ij}^{180}|}{\Sigma I_{ij}}, \qquad R_A = \frac{\Sigma \frac{1}{2} |R_{ij} - R_{ij}^{180}|}{\Sigma I_{ij}} \tag{1.1}$$

where I_{ij} is the flux at pixel (i, j) in the original image and R_{ij} and R_{ij}^{180} are the fluxes in the original and rotated residual images, respectively. These two indices are measured for each galaxy within a radius of 5 kpc. Schade et al. found that 10 (30%) of the galaxies in their sample showed some degree of asymmetry (i.e., the sum of the two residual fluxes is greater than 14% of the total galaxy flux), but only 4 (13%) showed clear signs of interaction or merging.

From this work, Schade et al. concluded that the galaxy population at $z \sim 0.75$ is morphologically roughly the same as the local population, and, therefore, exotic evolutionary processes do not dominate the evolution of luminous galaxies. In addition, Schade et al. found that blue nucleated galaxies, which make up 30% of their sample, generally appear to have significant asymmetric structure and are sometimes also associated with apparent interactions and mergers. In other work, e.g., Lilly et al. (1995), significant evolution is claimed for a population of faint blue galaxies in comparison to no-evolution models of galaxy formation. Schade et al. conclude that the blue nucleated galaxies in their sample may contribute significantly to this evolving blue galaxy population.

A comparison of the Schade et al. indices with other asymmetry indices has not been done as there is not a common data set on which all of these indices have been run. Three concerns may, nonetheless, be raised. First, the Schade et al. indices are calculated within a radius of only 5 kpc. For large galaxies, valuable information may be lost from the outer parts of the galaxy, where deviations from the model (e.g., spiral arms or HII regions) are likely to be seen. Second, the total residual flux appears to be better suited to measure either positive- or negative-definite "lumpiness" in a galaxy (but not both simultaneously) rather than asymmetry. One can imagine, for example, a galaxy in which an H II region happens to lie diametrically opposed to a region obscured by dust. The R_T calculated for this galaxy may be quite small, even though the object is, in actuality, asymmetric. The opposite phenomenon may also occur: for a grand-design spiral in which the pitch angle of the arms is almost identical, the calculated R_T may be quite large, when, in reality, the galaxy is quite symmetric. Third, it is unclear why the sum, $R_T + R_A$, is used to define asymmetry. Any asymmetry that exists in the galaxy will be registered in R_A. Since R_T may over- or underestimate true asymmetries, including it in the asymmetry determination seems misleading. An additional advantage to using R_A alone is that a model need not be fit to the galaxy before calculating R_A. The symmetric components of the galaxy will be naturally subtracted out in the process. A comparison of R_T and R_A with other asymmetry indices may be made later (though not as part of this work) to determine whether these concerns are justified.

Abraham et al. (1996b, hereafter A96b) introduced a classification scheme based on an object's asymmetry and central concentration. Their asymmetry parameter, A_A, is a measure of the residual light (relative to the total light) in a galaxy after rotating it by 180° and subtracting it from itself. Their central concentration, C_A, is a ratio of fluxes measured through two elliptical apertures, whose normalized radii are calculated as described in Abraham et al. (1994). These indices were applied to galaxies in the Hubble Deep Field (HDF). A significant over-abundance of "Irregular/Peculiar/Merger" type galaxies was found relative to predictions of no-evolution galaxy models. A96b suggest that this trend may reflect a trend of increasing asymmetry with redshift. In support of this, the asymmetry distribution of the HDF galaxies is compared to that of galaxies from the Medium Deep Survey (MDS, Griffiths et al. 1994, Glazebrook et al. 1995). Since the HDF is a much deeper survey, it is expected that it probes to higher redshifts. The mean asymmetry of the HDF galaxies is, in fact, slightly higher than that of the MDS galaxies.

More conclusive results, however, must await actual redshifts.

One of the shortcomings of the Abraham asymmetry parameter is that it uses the center of the brightest pixel as the center of rotation. This lack of sub-pixel centering sometimes results in artificially high asymmetry values for galaxies that are quite symmetric, e.g., ellipticals. This, and other, limitations of this index are explored in more detail in Chapter 3. In addition, the irregular and peculiar classes have been combined into one category. As mentioned earlier, this is inadvisable, as the two types of galaxies are really quite different.

Conselice et al. (1999) present a variation of the A96b asymmetry parameter and explore correlations of this parameter with various galaxy properties. Their work, thus far, focusses primarily on local objects, their primary sample being the "Catalog of Nearby Galaxies" from Frei et al. (1996). Potential limitations that may arise when this index is applied at high redshift are also discussed. As before, asymmetry is calculated by rotating and subtracting the image of a galaxy from itself. In addition to measuring the absolute value of the residuals (the "ABS" asymmetry), however, Conselice et al. also measure the asymmetry as the sum of the square of the pixels in the residual image normalized by the sum of the square of the pixels in the original image (the "RMS" asymmetry):

$$A_{C,ABS} = \frac{\Sigma|I_0 - I_\phi|}{2\Sigma|I_0|}, \quad A^2_{C,RMS} = \frac{\Sigma(I_0 - I_\phi)^2}{2\Sigma I_0^2}. \tag{1.2}$$

They find that the two methods yield similar results, but the correlation between the ABS asymmetry with color (one of the primary relations they discuss in their paper) is tighter than that between the RMS asymmetry and color. For most of their analysis, therefore, they adopt the ABS asymmetry. The ABS asymmetry is also calculated with a range of rotation angles (not just 180°) through circular apertures spanning a range of galactic radii. A centering algorithm has also been implemented to find the center of rotation that yields the minimum asymmetry for the 180° rotation.

Several interesting results arise from this work: (1) The use of several different rotation angles provides additional morphological information that cannot be found in the 180° rotational asymmetry index alone. For example, comparing the rotational asymmetry for a 90° rotation to that for a 180° rotation, one can gain information about the ellipticity of the galaxy. (2) By studying asymmetry as a function of galactic radius, one can determine an "optimal" radius at which to calculate asymmetries. This study also emphasizes, however, how sensitive the asymmetry index is to the selected radius of the circular aperture used to calculate the asymmetry. This dependence was also found in tests done through circular and elliptical apertures using the algorithms developed in this dissertation. We found that working with isophotal areas proved to be a more consistent method for determining the asymmetry value. (3) A strong correlation is found between color and asymmetry. Such a trend is not surprising. The reddest objects that we see locally are ellipticals, which are generally very symmetric. As we progress along the Hubble Sequence, galaxies gradually become bluer and show more structure, which will register itself as some degree of asymmetry. It is notable, however, that the color-asymmetry relation seems quite effective in isolating particularly asymmetric (possibly interacting or merging) galaxies locally. It will be interesting to see if Conselice et al. find this trend to continue for higher redshift objects. (4) The correlation between asymmetry and concentration index is also revisited, using the new asymmetry and a different concentration index (the logarithm of the ratio of the radii enclosing 20% and 80% of the light). These two parameters show a tighter relation than that of A96b, but the scatter is found to be comparable to that found for the color-asymmetry relation. (5) Simulations were also conducted to determine the effectiveness of these indices for high redshift samples. As expected, the asymmetry is found to decrease with poorer resolution and lower signal-to-noise.

Two concerns arise regarding the Conselice et al. asymmetry parameter: First, as mentioned before, the use of circular apertures may be misleading if the radius is chosen poorly. As Conselice et al. explore a full range of radii, they are able to avoid this potential pitfall. They discuss the need to determine a "standard radius" within which to compute the asymmetry, but this radius has not been specified. Second, the application of the centering algorithm to close pairs of objects, either locally or at high redshift, may result in spurious results. Conselice et al. mention the potential problem of local minima within a given galaxy. In a test of a sub-sample of 21 "representative" galaxies, asymmetries calculated in the central 3×3 arcsec show no significant local minima. One can imagine, however, a bimodal object, for which the Conselice et al. centering algorithm would likely find the minimum asymmetry at a point between the two peaks. If the peaks are of comparable intensity, then the calculated asymmetry could be found to be deceptively small. In summary, Conselice et al. have developed and characterized a useful asymmetry indicator for local galaxies. Its suitability to higher redshift objects is still to be determined.

An alternative approach to quantitative morphology is presented by Takamiya (1999). Takamiya developed a method for measuring the high spatial frequency power ("flocculency") in the disk of galaxies and a metric radius based on the formulation of Petrosian (1976). A high spatial frequency image of each galaxy is created by subtracting a low spatial frequency image of the galaxy from the original image. The flocculency is defined as the ratio of the flux in the high spatial frequency image to that in the original image as measured within elliptical apertures. The nuclear regions of the galaxy are excluded in these computations to avoid high spatial frequency signatures due to the bulge component of the galaxy. The metric radius as originally defined by Petrosian (1976) is the ratio of the average surface brightness within a given radius to the surface brightness at that radius. In Takamiya's work, the metric radius has been re-defined, following the work of Kron (1995), to be the inverse of the original Petrosian definition. These two parameters are applied to a local sample, comprised of the 113 Frei et al. (1996) galaxies and 23 galaxies taken using the 0.9m telescope at Kitt Peak National Observatory, and a high redshift ($z \lesssim 1$) sample of 94 galaxies from the Hubble Deep Field with F450W$_{AB} \leq 25$, as determined by Sawicki et al. (1997). Takamiya finds that, for both the high redshift and local samples, 46% of the galaxies show high flocculency. The metric radii of galaxies in the two samples are also comparable: the HDF galaxies are all larger than the median radius in the HDF of 5 kpc, while the local galaxies with similar flocculency all have radii around 5-10 kpc. No significant evolution in these two parameters is seen out to $z \sim 1$.

Morphological Number Count and Redshift Studies

Several groups have investigated the number counts of galaxies of various morphological types at high redshift. A variety of high redshift samples and classification techniques have been used. A brief description of each study and its results follows.

Glazebrook et al. 1995 studied 301 galaxies down to $I_C = 22$ in the MDS. Classification of galaxies was presumably done visually (no other technique was specified) into three groups: elliptical/S0, spiral galaxies, and irregular/peculiar galaxies. It is unclear, from their definitions, whether traditional irregular galaxies (e.g., the Magellanic Clouds) are included in any of the categories. They find that the elliptical and spiral galaxy counts are consistent, at all magnitudes, with no-evolution models using a high normalization of the Schechter luminosity function. This implies that normal Hubble types have evolved only slowly since $z \sim 0.5$. In addition, they find that the number counts for "irregular/peculiar galaxies, including multiple-peaked, possibly merging objects" are much higher than predictions based on the local population. By $I_C = 22$, these galaxies comprise half of their total counts; they conclude, therefore, that this may be the population responsible for the rapidly evolving component of the luminosity function.

Odewahn et al. (1996) present galaxy number counts down to $B_J \lesssim 27$ using classifications done both visually and using two sets of artificial neural network (ANN) classifiers trained on two different sets of images. The ANN classification was based on galaxy surface brightness and light profile. Galaxies were classified into three groups: E/S0, Sabc, and Sd/Irr+M (where M indicates merging systems). They find that the three different classification methods yield consistent number counts as a function of type. E/S0 number counts are only marginally above no-evolution predictions, while Sabc number counts are at most 0.5 dex above no-evolution predictions for $B_J \gtrsim 24$. Sd/Irr+M galaxies are once again found to dominate the faint galaxy counts. A moderately steep local luminosity function with strong luminosity evolution since $z \lesssim 1$ is invoked to explain this population. Odewahn et al. speculate that these galaxies may be a combination of faint dwarfs at $z \sim 0.5$-1 and compact star-forming galaxies and mergers at $z \sim 1$-3.

Brinchmann et al. (1998) analyzed images of 341 galaxies from the CFRS and the Autofib/Low-Dispersion Survey Spectrograph (LDSS) redshift survey down to $I_{AB} \sim 22.5$ and $b_J \sim 24$, respectively. Classification was done both visually and automatically. Visual classifications used a modified version of the classification scheme of Glazebrook et al. (1995): compact objects and objects with faint extensions ("tadpoles") were separated from the "irregular/peculiar/merger" class. Automatic classification was done using the Abraham asymmetry and concentration indices. Attempts were made to quantify the number of galaxies that would be mis-classified in the Abraham A-C categories when observed at high redshift. After accounting for potential mis-classifications, Brinchmann et al. find that the number-redshift relation for "AC-ellipticals" is consistent with little or no evolution, while "AC-spirals" are best fit by mild evolution models with luminosity evolution of roughly 1 magnitude to $z \sim 1$. The number counts of galaxies with "irregular morphology" again appear to indicate significant evolution since $z \sim 1$ and are once again claimed to be the dominant contributor to the recent evolution of the galaxy population. Brinchmann et al. also suggest that, since there is little decline in the numbers of "regular" galaxies at high redshift, the decrease in the number of "AC-peculiars" at lower redshifts may not simply be a result of these galaxies transforming into the more familiar galaxy types seen today.

Driver et al. (1998) combined the morphological catalog of Odewahn et al. (1996) and an updated version of the photometric redshift catalog of Fernández-Soto et al. (1999) for galaxies with $I < 26.0$ in the HDF. Since Fernández-Soto et al. used the HST AB magnitude system and neither Driver et al. nor Odewahn et al. specify which photometric system was used, we will assume that the I-band used in this work is F814W$_{AB}$. Classification was done both by eye and using Odewahn et al.'s ANNs. Agreement between the two methods was reasonable in most cases; those cases in which the disagreement was greater than 4 T-types were re-examined by eye for the final classification. Driver et al. analyze both the morphological number counts and morphological redshift distribution and come to the following conclusions: (1) E/S0 number counts brighter than $I = 24$ are consistent with zero or minimal passive evolution. At fainter magnitudes, there is a deficit of ellipticals relative to predictions of no-evolution models, leading Driver et al. to conclude that young ellipticals may be masked by dust or may not be morphologically recognizable as ellipticals until their stellar populations have stabilized. They also postulate that the epoch of formation for ellipticals started at $z > 3$. (2) Early-type spiral (Sabc) number counts also appear to be consistent with no evolution for $I < 24$. Some form of luminosity or number evolution is required at fainter magnitudes, however, to explain the excess in numbers relative to no-evolution model predictions. In addition, Driver et al. note the excess of galaxies at $24 < I < 26$ in the redshift distributions at $z = 1.5$ and the subsequent drop in numbers at $z > 1.5$. They conclude that the epoch of formation for present-day disks is at $z \sim 2$. (3) Their "catch-all" class, Sd/Irr/M+Pec, disagrees with the model predictions at all magnitudes and redshifts. They postulate that the more luminous of these objects settle into the regular spirals seen at $z < 1.5$, while the rest of this population gradually fades to become local dwarf and low surface brightness galaxies.

Several important issues arise from a review of these works. The first is a point that was raised early on in this dissertation: the confusion of irregular and peculiar galaxies. In all of the works described above, irregular, peculiar, and merging galaxies are grouped into one category. In some cases, late-type spirals (Sd) are also included in this group. Though peculiars and merging galaxies are likely closely related, irregular galaxies, as mentioned before, are a completely different class of objects. They, and late-type spirals, should be studied separately, though these latter two classes may reasonably be studied together. To add to the confusion, the terms "irregular" and "peculiar" are often used interchangeably and are rarely clearly defined. In this work, the term "irregular" will always refer to galaxies at the tail-end of the Hubble Sequence (e.g., Sm/Im types), while "peculiar" will refer to objects that show such features as tidal tails, multiple cores, and warped or distorted structure.

The value, and even necessity, of redshifts in the interpretation of these data is also quite clear. Without redshifts, it is difficult to determine with any certainty whether, for example, faint objects are nearby and intrinsically faint or distant and very luminous. Glazebrook et al. and Odewahn et al. could draw only preliminary conclusions from their number counts. Brinchmann et al. were limited by their spectroscopic redshifts to study only relatively bright galaxies ($I < 22.5$) out to $z \sim 1$. The addition of photometric redshifts in Driver et al. enabled them to suggest much broader hypotheses for galaxy evolution, such as the formation epochs for various types of galaxies.

Even with redshift information, however, selection effects must be carefully quantified before conclusions may be drawn. For example, as we observe objects through optical filters at higher and higher redshifts, we probe rest wavelengths that extend farther and farther into the ultraviolet regime, where "normal" local galaxies have been shown to appear quite "peculiar" (O'Connell 1997). If not carefully accounted for, such "bandpass shifting" effects may lead to overestimates of the number of peculiar galaxies at high redshift. Though some effort has been made to quantify these effects (e.g., Brinchmann et al. 1998, Conselice et al. 1999), simulations, thus far, have used nothing bluer than B-band images of local galaxies as a starting point. It is risky, moreover, to assume that distant galaxies are identical, or even largely similar, to local galaxies. Much evidence, both observational and theoretical, indicates that the contrary is true. Conclusions made based on such simulations, then, should be viewed with an eye of caution. It would be much more desirable to start with a population of galaxies already at fairly high redshift (say, $z \sim 1$) in order to simulate the appearance of even higher redshift objects. With multi-band photometry, such as that available for the HDF, it is even possible to estimate a crude spectral energy distribution, and, hence, a more realistic K-correction for these galaxies. With this information in hand, we can make more realistic simulations of galaxies at higher redshifts to better understand their appearance, or even detectability, when observed with current instruments and telescopes. One additional note: simulations such as these are of limited value if redshifts for the actual observed population are not available. Without real redshifts, it is difficult to determine the redshifts at which the simulations should be created in order to obtain a meaningful comparison.

4. Goals of this Dissertation

The most important new feature of this work is the addition of photometric redshift estimates for over a thousand galaxies in the HDF. This makes it possible to determine not only the magnitude at which peculiar galaxy morphology becomes significant, but also the epoch at which it begins to dominate. We have made use of these photometric redshifts to study a much deeper redshift sample than has previously been possible in morphological studies. In addition, these redshifts enable us to investigate absolute quantities, such as absolute magnitudes, radii, and surface brightnesses, for a large sample of galaxies to higher redshifts than ever before. The combination of redshifts and colors from the multi-band imaging also enables us to calculate quite accurately the K-correction and cosmological shrinking and dimming terms for galaxies in specific redshift bins. Accurate calculation of these terms is essential for creating realistic simulations.

A second major goal of this dissertation is to improve upon the quantitative methods of measuring peculiarities in galaxy morphology. To this end, refinements have been made to the Abraham asymmetry index to minimize the likelihood of finding artificially high asymmetry measurements. Careful efforts have been made to study the effect of projected pairs of galaxies on the asymmetry index. In addition, several other indices were explored as possible supplements to the rotational asymmetry and concentration indices.

Finally, in order to properly interpret data on peculiar galaxies at high redshift, it is crucial to have a thorough understanding of both the morphological peculiarities of local galaxies and the biases that would appear in the images of local galaxies if they were observed at higher redshifts. It has been shown that galaxies that look perfectly "normal" at optical wavelengths may appear quite "peculiar" at ultraviolet (UV) wavelengths (O'Connell 1997). When observing galaxies beyond $z \sim 1$ through optical filters, one is, in fact, observing in the restframe UV. An increase in the number of apparently peculiar galaxies due purely to these "bandpass shifting" effects is, therefore, to be expected. As one goes to higher redshifts, cosmological surface brightness dimming dramatically decreases the detectability of normal, quiescently star-forming objects. This effect must also be understood in order to avoid attributing trends seen in the data to galaxy evolution when they may merely be a result of observational selection.

In order to gain a more thorough and accurate understanding of the biases caused by cosmological dimming and bandpass shifting, several sets of simulations have been carried out:

- To better understand bandpass shifting effects, I have used local B-band images of galaxies to simulate their appearance at $z = 0.8$ if observed using the Wide Field Planetary Camera - 2 (WFPC-2) through the HST F814W filter. At this redshift, the F814W filter corresponds directly to restframe B; K-corrections are, therefore, unnecessary. Cosmological dimming and shrinking effects are completely accounted for. These simulated images can, thus, be compared directly to observed $z \sim 0.8$ galaxies in the HDF.

- To better understand the effects of resolution and signal-to-noise, the appearance of local images at redshifts ranging from $z = 0.2$ to $z = 5$ was simulated. For these simulations, the local images were treated as flat-spectrum, constant luminosity sources. This assumption is not realistic but rather underestimates the effects of these biases. The simulations show that, even with such conservative estimates, the resulting effects are quite severe. These tests motivated the following two, more realistic, simulations for higher redshifts.
- Since photometric redshifts and multi-band imaging are available for the HDF, it is possible to compute directly the effect of bandpass shifting on the appearance of galaxies at various redshifts observed through the F450W versus the F814W filters. At $z = 0.8$, for example, F450W samples well into the restframe UV (roughly 2500Å), where one might expect to see significantly more asymmetric structure. This comparison, therefore, gives an indication of the bandpass shifting bias that might be expected in moving from $z \sim 0.8$ to $z \sim 2$.
- In order to create fully realistic simulations of how galaxies would appear at high redshifts, galaxies in the HDF with photometric redshift estimates of $z \sim 0.8$ were simulated at redshifts of $z = 1.5$ and $z = 2.3$ using the spectral energy distributions (SEDs) of these galaxies estimated from their W96 F450W and F606W magnitudes. These shifts correspond to observing the galaxies at restframe 3300Å and 2500Å, respectively. By using the galaxies at $z \sim 0.8$ as the starting point, we avoid the assumption that very high redshift objects have morphologies, SEDs, and luminosities similar to those of local galaxies. The extrapolation of these local properties to high

redshift was necessary in previous attempts to characterize morphological biases, since a substantial set of $z \sim 1$ galaxies with reliable redshifts was not available.

The Hubble Deep Field has provided us with a wealth of information with which to study galaxy evolution. The multi-band photometry in the HDF has proven invaluable in many respects. One of the most far-reaching uses of the multi-band photometry has been for photometric redshift estimates. This has, in turn, made the original data all the more rich with information. With the combination of the high resolution imaging of the HDF and photometric redshifts, the time is ripe for studies of galaxy morphology and their implications for galaxy evolution and formation.

Chapter 2

The Data

Three data sets are used in this work:

- 113 galaxies from the Frei et al. (1996) "Catalog of Nearby Galaxies,"
- 4 interacting/merging galaxies from Hibbard & van Gorkom (1996), and
- 1079 galaxies from the Hubble Deep Field (Williams et al. 1996).

A brief description of the catalogs, why they were chosen, and their limitations as related to the study of morphological peculiarities follows. Other data catalogs related to these data will also be discussed.

1. The Local Sample

1.1. The Frei et al. (1996) Catalog

The Frei et al. (1996) catalog (hereafter "the Frei catalog") is a catalog of 113 nearby, bright galaxies. Thirty-one galaxies were observed with the 1.5-meter telescope at Palomar Observatory using the Thuan-Gunn *gri* filters (Thuan & Gunn, 1976). The remaining eighty-two galaxies were observed with the 1.1-meter telescope at Lowell Observatory using the B_J and R bands (Gullixson et al. 1995). For reasons that will be explained later, only the g-band images from Palomar and B_J-band images from Lowell are used in this study. For details on the observations and image processing, please refer to Frei et al. (1996).

A unique feature of the Frei catalog is that foreground stars have already been removed from the images, using a technique developed by Frei (1996). In addition, the authors have made the catalog publicly available on-line. These two features have made this sample a natural choice for many different studies, including Abraham et al. (1996b, hereafter A96b), which used the Lowell sub-sample of the Frei catalog as their local calibration sample. A direct comparison will be made later between the Abraham indices and comparable indices developed in this work.

The primary drawbacks of the Frei catalog are (1) the small number of late-type spirals and irregulars, and (2) the complete lack of peculiar galaxies. The original purpose of this catalog was to provide a suitable data set for testing automatic galaxy classification techniques. For developing quantitative methods for measuring peculiarities in galaxy morphology, however, the ideal local catalog would have a good statistical sample of galaxies of *all* types: the full range of "normal" Hubble types, plus low surface brightness objects and peculiar galaxies. Especially important for comparison with distant galaxies would be a large sample of irregular and peculiar galaxies. As discussed in Chapter 1, the distinction between irregulars and peculiars is crucial. The Frei catalog is poorly equipped to make this distinction. In an attempt to fill this gap, B-band images of late-type spirals, irregulars, and peculiars were taken on the Nickel 40" Telescope at Lick Observatory. Due to poor observing conditions and telescope problems, however, much of the data were of rather poor quality, and these data are not included in this work.

An additional concern regarding use of the Frei catalog as a comparison sample is the fact that this catalog consists primarily of large, bright galaxies. Many of the objects seen at high redshift appear to be small and faint. Is it realistic or meaningful to compare such apparently different objects? A catalog including dwarf galaxies, in addition to the range of galaxies already mentioned above, would perhaps be more suitable. This concern will be addressed in Chapter 6. Though the Frei catalog is not the ideal comparison catalog, the size-magnitude relation of the local and distant samples appears to follow roughly the same track, and supplementing the Frei catalog with a set of simulations created using the Frei catalog appears to be sufficient.

1.2. Interacting and Merger Candidates

In an attempt to quantify, at least partially, the behaviour of local galaxies that would likely be classified as peculiars, images of four interacting and merging systems were kindly provided by John Hibbard (Hibbard & van Gorkom 1996, hereafter HvG) for inclusion in the local sample. These galaxies span a range of merger phases:

- NGC 295: Two galaxies just starting to merge. A tidal corridor connecting the galaxies is clearly visible.
- NGC 2623: A galaxy in the process of merging. Evidence of the two progenitors is still visible, though the cores of both galaxies have begun to be distorted. Long tidal tails extend away from both galaxies. Galaxies in an almost identical state of merging can be found in the HDF.
- NGC 520: A galaxy in the throes of merging. The core has been completely disrupted. On careful inspection, one can also see a faint tidal tail connecting NGC

520 to another small companion nearby.

- NGC 7252: A galaxy in the final stages of merging. Except for several faint tidal features, this galaxy appears quite symmetric and is dominated by a bright, symmetric core.

Foreground Star Removal

Foreground stars and background galaxies in the HvG images were replaced with sky pixels using a pixel-replacement algorithm that was developed independently of the Frei (1996) star-removal algorithm. The procedure is as follows.

- Stars in the image are found using the FIND routine adapted into IDL from the 1986 STSDAS version of DAOPHOT FIND (Landsman 1987).
- A bright isolated star is selected interactively as the reference star. A curve of growth is calculated for this star. The maximum radius within which pixels are replaced is defined as that radius at which the curve of growth of the reference star levels off (i.e., when the flux level in four consecutive apertures agrees to within 10%) .
- The half-width-half-maximum (HWHM) of the curve of growth is also determined and is used to calculate the sigma of the star profile. The fluxes contained within 1.3σ (the radius at which the signal-to-noise is maximized) and the maximum radius (determined in the previous step) are calculated for all detected stars in the image. The size of the aperture within which pixels are replaced is scaled by the square root of the ratio of the 1.3σ flux of each star relative to that of the reference star. If the scaled aperture radius is smaller than three pixels, then an aperture of three pixels is used.

- A five-pixel-wide sky annulus around the object aperture is used to obtain a local sky estimate. A histogram of the sky pixels is created and normalized to unit height. Replacement pixel values fitting the empirically determined local sky distribution are randomly generated using a Monte Carlo-type algorithm. Pixels in the star apertures are replaced with these randomly generated sky values. A precautionary note: large gradients in the local sky (e.g., an object in the wings of a much brighter object) are not properly accounted for. Ideally, if a gradient exists, then the replacement algorithm should reproduce this gradient. However, the number of cases for which this was important was small enough that the program was not refined to this detail.

The local sample of galaxies for this work is comprised of the Frei catalog and the four HvG galaxies. Individual heliocentric velocities, corrected for solar motion with respect to the velocity centroid of the Local Group, are used to estimate the distances of these galaxies in order to create the high redshift simulations discussed in Chapter 4. As a result, three galaxies (NGC 4192, NGC 4406, and NGC 4569) from the Frei catalog were omitted because they have negative velocities. Errors caused by using individual velocities, rather than group or cluster velocities, are expected to be small; nonetheless, in future, we plan to re-create the high redshift simulations using group or cluster velocities.

2. The High Redshift Sample – The Hubble Deep Field

The Hubble Deep Field (HDF, Williams et al. 1996, hereafter W96) is a Director's Discretionary program on the Hubble Space Telescope (HST) "to image an undistinguished field at high Galactic latitude in four passbands as deeply as reasonably possible" (W96). The high resolution of the HST enables the study of galaxy morphology to much fainter magnitudes than previously possible. This makes the HDF an ideal sample for studying the evolution of peculiarity in galaxy morphology.

Numerous objects in the HDF have multiple condensations. Whether or not these condensations are physically associated or merely superpositions of unrelated galaxies along the line of sight is difficult to determine from the images alone. W96 opted to present catalog information on each individual "sub-clump." The geneology of each sub-clump is also preserved, so it is possible to trace each object to whatever degree of splitting is desired.

The issue of multiple sub-clumps highlights one of the most important questions in the study of peculiarities in galaxy morphology, especially at high redshift: what *is* an object? Without redshift information, how does one decide when a pair or group of condensations is one object or several? And if they are several, then are they physically associated or merely superpositions?

One of the powerful new features of this work is the addition of photometric redshift estimates for objects in the HDF. With this information, it is now possible, at least in principle, to determine whether or not multiple sub-clumps are physically related. In practice, current photometric redshifts are not yet perfectly attuned to this need, as complete information and errors for individual sub-clumps are not yet available. Even partial redshift information, however, can be used to tune algorithms to distinguish between true pairs and chance superpositions. The object identification algorithm in this work indirectly takes advantage of this extra piece of information to manually determine the optimal detection level (i.e., several detection levels were tested, at each of which close pairs with known redshifts were checked to see whether they were detected as one or more objects and whether this was in agreement with their known redshifts). A more automated technique for incorporating redshift information in the determination of the detection threshold is still being considered.

Several groups have developed photometric redshift techniques. A comparison of the techniques and resulting redshift estimates from these various groups will be presented in Chapter 5. We have adopted the photometric catalog of Connolly (1999, hereafter C99). For those objects for which spectroscopic redshifts are available, the C99 photometric redshifts provided the best match to the spectroscopic redshifts. Further details on the match between C99 and W96 are presented in Section 2.1 of Chapter 3.

Chapter 3

Introducing the Peculiarity Indices

Several image processing steps are required before the actual calculation of the peculiarity indices for a given galaxy. In addition, the preparatory steps differ slightly for the various data sets, the reasons for which will be discussed in the chapter as appropriate, along with a description of the variations. As an example, let us follow the processing of a typical galaxy in the Hubble Deep Field (HDF) (Williams et al. 1996, hereafter W96). Variations for the local sample will be noted in parentheses.

1. A Roadmap

Before going into the details of each step, the basic processing steps are outlined and a brief introduction to the primary peculiarity indices is given. It is assumed that the image has already gone through the usual image reduction process of bias-subtraction, flat-fielding, and cosmic ray removal.

1.1. Synopsis of the Image Processing Scheme

- Postage stamp creation: In order to avoid having to operate repeatedly on each of the 2048×2048 Wide Field (WF) chips of the HDF, postage stamp images of each galaxy are extracted such that the W96 x, y-pixel coordinates of the galaxy are centered in its postage stamp. (Note that the W96 coordinates give the position of the objects on the individual HST chips, rather than their position on the full HDF mosaic.) The typical size of these postage stamps is 101×101 (see detailed description of postage stamp creation for exceptions).
- Sky subtraction: A local estimate of the sky mode is determined and subtracted from the image.
- Object mask creation: A mask for each object is created. This mask defines which pixels are associated with the object of interest (the "primary" object), which belong to neighboring objects ("extraneous" objects), and which are sky pixels. Peculiarity indices are calculated using only those pixels contained within the primary object. Note: In order to minimize spurious detections, the image is smoothed by a Gaussian with $\sigma = 1$ pixel before the mask is created.
- Pixel replacement: In images where multiple objects are found, the option is available to replace "extraneous" objects with sky values, generated randomly from a representative local sky distribution, in order to avoid contamination by those objects. Pixel replacement is routinely done for all objects in the HDF.

At this point, the images are ready to be operated upon. Before calculating the peculiarity indices, however, one additional useful quantity is calculated – the "half-light" radius, the radius containing 50% of the total light (defined as the total flux contained in the object pixels of the object mask). This radius is used primarily to scale the degree of smoothing of the images at various stages of peculiarity determination.

1.2. Principle Peculiarity Indices

Two principle peculiarity indices are used in this work:

- Rotational Asymmetry: The image of a galaxy is rotated 180° and subtracted from itself. The rotational asymmetry index measures the percentage of the total flux found in the residuals. Low percentages, or asymmetries, are found for smooth symmetric objects such as ellipticals. Higher asymmetries are found for objects with significant amounts of structure. The highest asymmetries are found for objects with multiple cores or skewed light distributions.
- Concentration Index: The ratio of the radii containing 80% versus 20% of the total light in the galaxy is used to measure the sharpness of the light profile of a galaxy. Ellipticals have high concentrations; spirals and irregulars have progressively lower concentrations. Objects with multiple bright regions (H II regions or multiple cores) also tend to register lower concentrations as the profile is flattened out by the multiple, un-centered condensations of light.

Both of these indices are variants of those presented by Abraham et al. (1996a,b, hereafter A96a, A96b), who found that a combination of these two indices can discriminate normal Hubble types from one another and from peculiar galaxies. Details of their calculation, a comparison of their indices to those developed in this work, and brief explorations that were made into other types of peculiarity indices will be presented following a more detailed description of the individual image processing steps.

2. Detailed Image Preparation

2.1. Postage Stamp Creation: A Special Step for HDF Objects

Because of the large (2048x2048) size of each of the WF chips in the HDF, computations on the full image would be very time- and CPU-consuming. It is much more convenient to work on smaller patches, or postage stamps, of the field. Since we are interested in studying the morphological peculiarities of individual galaxies, it makes sense to create postage stamps containing just the galaxy of interest. It is important, however, that the field be large enough to obtain a reliable measure of the local sky, in order to account for any contribution that the sky noise may make to the peculiarity indices. For most objects in the HDF, a postage stamp of size 101×101 pixels ($4''.04 \times 4''.04$) works very well. Larger postage stamps are necessary, however, for galaxies that are either bright or in crowded fields. Forty objects have 201×201 postage stamps, five objects have 301×301 postage stamps, and two objects have 401×401 postage stamps. In all cases, the postage stamp is centered on the W96 x, y-position of the object of interest.

As mentioned in Chapter 1, the identification of objects can be quite confusing in the HDF. For this work, we have created the postage stamp images of all galaxies matched between the W96 catalog and the photometric redshift catalog of Connolly (1999, hereafter, C99). The match between these two catalogs was done using a combined position/magnitude criterion. The matching radius was set at 15 pixels ($0''.6$). Multiple matches in the resulting catalog were disentangled using both the magnitude and position of the objects. The pair of objects with the closest matching magnitude and smallest difference in position was generally chosen as the match. For only a handful of objects did these criteria disagree. These galaxies were inspected by eye to determine the match.

If the matched object from W96 was a "daughter" object (an object that was originally found as part of a larger "parent" object but was later split off from it), the C99 catalog was checked to determine whether it contained any of the other daughters of that parent. If so, then the match remained unchanged. If not, then the object was re-matched to the parent rather than the daughter. In the end, 1079 objects were matched between C99 and W96. Postage stamp images were created for all of these objects.

2.2. Sky Subtraction

There are two steps in determining and subtracting off the sky.

Step 1. An initial estimate of the mode and standard deviation, σ_{sky}, of the sky distribution is obtained using all pixels in the image. Pixels greater than $2\sigma_{sky}$ are removed, and the mode and σ_{sky} are re-calculated. This procedure is iterated upon until the number of pixels kept as sky pixels remains constant. The resulting sky mode is then subtracted from the image.

Step 2. Once this initial sky mode has been subtracted, a "skymask" is created, which masks out all pixels with values greater than $1.5\sigma_{sky}$. The skymode is re-calculated in the same manner as in step 1, but using only the unmasked "sky pixels." This new skymode is then subtracted from the image to produce the final sky-subtracted image.

Several of the Frei et al. (1996) images taken at Lowell Observatory display an unexplained brightening of the background. An attempt was made to correct for this by fitting a second-order polynomial surface to the sky pixels and subtracting off the plane. Ultimately, however, this effect was ignored, as, when the appropriate noise was added for the $z = 0.8$ simulations, in many cases, the effect became negligible.

2.3. Object Mask Creation

One of the key issues in morphological studies of high redshift galaxies is the definition of an object. It is not uncommon to find multiple condensations that share a common envelope. Without redshift information for each of the condensations, however, it is difficult to determine whether they are physically related or merely superpositions. It is critical, nonetheless, to develop a method to clearly define which pixels belong to an object and which belong to neighboring objects or sky. In addition, in order to realistically compare galaxies at various redshifts, the method should ideally consistently sample the same region of a galaxy at all redshifts.

In previous work, a variety of different methods has been used to define the region in which to study morphological peculiarities. Schade et al. (1995) used the central 5 kpc. The advantage here is that a consistent physical region of the galaxy is always used. For larger galaxies, however, choosing such a small radius may result in the loss of pertinent information in the outer parts of the galaxy. A96b appear to use an isophotal $1.5\sigma_{sky}$ cut for both local and high redshift data. For the local sample, this corresponds to a local surface brightness of 24-25 B-magnitudes per square arcsec, depending on the exposure time and observing conditions (e.g., the intrinsic sky level). In the HDF, the same isophotal cut in the HST F814W-band corresponds to a local surface brightness of roughly 26 magnitudes per square arcsec. A comparison of the surface brightness level reached using the local sample versus simulations of the local sample observed at $z = 0.8$ indicates that, at $z = 0.8$, a $1.5\sigma_{sky}$ cut corresponds to an isophote that is roughly 1 mag fainter than locally. The problem, therefore, is that using a σ_{sky}-based isophote results in different regions of a galaxy being measured in different samples and at different redshifts.

In addition, the choice of an isophote based on σ_{sky} is unphysical. The data being compared are taken using different instruments under a variety of observing conditions and using different detectors. A physically meaningful quantity, such as absolute surface brightness, should be chosen instead to define objects. Conselice et al. (1999) studied morphological asymmetries within several radii, based on the η-function (Petrosian 1976). The advantage of these radii is that they are designed to be independent of cosmology. The use of circular apertures, however, while reasonable for normal galaxies, may be less successful for peculiar objects (based on tests that I have run using circular apertures in my algorithms) and in crowded fields.

In previous work, especially at high redshift, no attempt has been made to separate close pairs, in part because redshifts were not available to help differentiate between superpositions and true pairs. The detection level was set to simply enclose as much of the galaxy light as possible, which often resulted in artificial "merging" of close pairs. This will be discussed further in Chapter 6. Since photometric redshifts have been incorporated in this work, the detection level can now be adjusted to separate, with maximum statistical effectiveness, close pairs whose redshift estimates are quite different. It is also important, however, to define a galaxy area that encloses as much of the total galaxy light with as little contamination from nearby objects as possible. In this work, therefore, an object is defined by a combination of two parameters: a detection surface brightness level, μ_{det}, and a growing factor. Because of the relatively high density of objects in the HDF, μ_{det} must be set at a fairly bright level in order to avoid artificial "merging" of close pairs. Setting a high μ_{det}, however, results in a detection area that covers only the brightest part of a galaxy. The detection area of both the object of interest, the "primary" object, and any neighbors, "extraneous" objects, needs to be "grown" in such a way as to enclose as much of the total light of the primary object as possible without including light from extraneous objects. Though this method of defining the area of a galaxy is somewhat unconventional, tests run on local images and simulations of the local images cosmologically shifted to $z = 0.8$ indicate that this method is robust. A more detailed description of the steps in the object mask creation procedure follows.

An object mask is created for each galaxy image. Each pixel in the object mask is marked as either an "object pixel" (a pixel contained within the detection contour of the primary object), an "extraneous pixel" (a pixel contained within the detection contour of extraneous objects), or a "sky pixel" (a pixel that is within neither the primary detection contour nor any of the extraneous detection contours). To minimize detections of spurious noise peaks, the image is smoothed by a 1-pixel Gaussian before the mask is created. Ideally, the smoothing length should be scaled to the physical size of the galaxy, but, herein lies a circular problem: in order to determine, say, the half-light radius, the total light of the galaxy must be known; but, in order to determine the total light of the galaxy, we need to define the pixels that are to be associated with the galaxy, i.e., we need to create the object mask; but in order to create the object mask, it is prudent to smooth the image slightly to avoid detecting spurious noise peaks. The choice of a 1-pixel Gaussian smoothing length was decided upon as a reasonable choice for the smoothing length. It would be instructive, in future, to test the effects of changing this smoothing length in more detail.

As mentioned earlier, two parameters determine whether a galaxy is detected and the final size and shape of the galaxy area:

Detection surface brightness level, μ_{det}: Rather than using a σ_{sky} isophotal detection level, as was done in A96b, a surface brightness level was chosen for object detection. The advantage of computing an absolute rest-frame surface brightness level is that it can be adjusted for cosmological dimming effects and photometric zeropoint differences to reflect the corresponding apparent surface brightness at various redshifts. This would ensure that the same region of a galaxy will be sampled at all redshifts. In this work, we have approximated this treatment by applying the correction from $z = 0$ to $z = 0.8$ (from B-band to F814W-band) to both simulated and observed high redshift objects. This treatment is closely correct for $z \sim 0.8$ galaxies but over-corrects and under-corrects galaxies that are nearer and farther away, respectively. A future improvement would be to customize the detection surface brightness level to the redshift of each individual galaxy.

In addition to accounting for cosmological dimming effects on μ_{det}, K-corrections should also be included. The form of these K-corrections, however, may differ from those used locally. The spectral energy distributions (SEDs) of high redshift objects may be quite different from those of local objects; hence, the applicability of the traditional K-correction is unclear. A K-correction for an individual galaxy could conceivably be determined from its colors. In the present work, however, we take advantage of the fact that, at $z = 0.8$, the F814W band corresponds directly to rest-frame B, and no K-correction is needed.

As described earlier, the addition of photometric redshifts enables the tuning of μ_{det} to separate close pairs whose photometric redshift estimates are distinctly different. Various detection levels were tested and will be discussed in more detail at the end of this chapter. The final μ_{det} is set to $\mu_{F814W,AB} = 24.5$, which at $z = 0.8$ corresponds to a local B-band surface brightness of $\mu_B = 22.75$. The case of multiple detections within a field will be described later in this section.

Growing factor: Because the detection level is at such a high rest-frame surface brightness, only a small part of the galaxy is enclosed by the μ_{det} isophote. In order to gather the rest of the galaxy light, the detection area is grown by 1-pixel contours, tracing the detection contour shape, until the specified growing factor is reached. Several growing factors were tested in combination with various values of μ_{det}. Again, these tests will be described in more detail at the end of this chapter. The final growing factor of 5 was chosen to balance between including as much of the light from lower surface brightness objects as possible while not including too much sky for higher surface brightness objects. For further details, please see the discussion below of the limitations of this algorithm.

For the local sample, a slight modification in the object mask parameters is necessary. Many of the local galaxies are so large that they fill a substantial fraction of the field of view of the image. Using the mask creation parameters described above for the HDF sample often results in the primary object mask filling the whole image as it is being grown. The background correction, therefore, cannot be computed since no sky pixels are available, and the object is deleted from the sample. The local sample is already quite small, so it is preferable not to lose any more of the sample. A surface brightness level of 25.0 B-magnitudes per square arcsecond and a growing factor of 1 (i.e., no growing) are chosen for the local sample. $\mu_B = 25.0$ is the level beyond which noise begins to make a significant contribution to the galaxy light in the local data. Since the goal is to get as much of the galaxy light without including too many sky pixels, no growing factor is needed. It will be shown in Chapter 5 that these two pairs of object mask parameters yield consistent peculiarity values for the local sample; hence, the modification of the parameters for the local sample is acceptable.

Mask creation with multiple objects

It is often the case in the HDF that multiple objects may be found within a given image at the specified detection level. In general, the largest detection contour is assumed to enclose the object of interest, the "primary" object. In the HDF, however, the primary object is sometimes not the largest object in the postage stamp image. For HDF images, therefore, the additional constraint is imposed that the primary object must lie at the center of the image. This constraint is valid since the postage stamps are extracted such that the W96 coordinates of the primary object are centered in the postage stamp. Simply requiring that the central pixel be enclosed within the detection area of the primary object, however, is sometimes not sufficient to find the primary object, as the object shape may be distorted enough that the central pixel ends up *outside* the detection contour. The constraint is modified, therefore, to require only that some part of the detection area lie within the central 5×5 pixels.

As the primary object mask is grown, the masks of the extraneous objects are also grown. With each 1-pixel contour added to the primary object, a 1-pixel contour is added around each extraneous object, following the shape of that object. If the masks of two objects meet, neither mask is grown any further along that boundary, though they continue to extend in other directions. In this way, the edge between the primary object and a close neighboring object is defined. The primary limitation of this method occurs when the primary object has one or more bright neighbors. In these cases, the mask of the primary object often reaches the growing factor before all of the light from the extraneous objects has been masked: the sky mode and σ_{sky} for these images, therefore, may be overestimated. Only a handful of such cases exists, however, so the algorithm was not modified to compensate for them.

An additional note for the HDF object masks: Object masks were created using the F814W images. Peculiarity calculations done on objects in other filters were done using the object masks created in F814W. This was done to ensure that the peculiarity values were calculated on the same region of the galaxy. Consistent comparison between filters is then possible.

Limitations of the detection algorithm

The detection algorithm described above works quite well for the majority of objects in the HDF. There are two groups of galaxies, however, for which the above choice of μ_{det} and the growing factor is not ideal: low surface brightness galaxies (LSBs) and elongated objects.

For LSBs, the selected detection threshold, $\mu_{F814W,AB} = 24.5$ ($\mu_B = 22.75$), is sometimes too bright and one of two things happens: (1) only a very small portion of the galaxy is detected, which, even after being grown by the growing factor, results in an object mask that includes only some portion (often on the order of 50-60%, though sometimes much less) of the true total light of the galaxy; or (2) the galaxy simply is not detected.

For elongated objects (e.g., inclined systems, "hot dog"-shaped objects), the problem that appears is a mis-matched shape. The initially detected region often does not have as high an ellipticity as the outer parts of the object. When the mask is grown, therefore, it remains rather circular, and the ends of the object are truncated.

A sample of 87 low surface brightness, elongated, and/or faint peculiar galaxies were selected and re-analyzed using a fainter detection level of $\mu_{F814W,AB} = 26.0$ ($\mu_B = 24.3$) with a growing factor of 1.5. Tests run on isolated normal galaxies showed that this growing factor is suitable for maintaining roughly the same area as that found using $\mu_{det}(\mathrm{F814W}_{AB}) = 24.5$. Figure 3–1 shows a montage of these 87 galaxies.

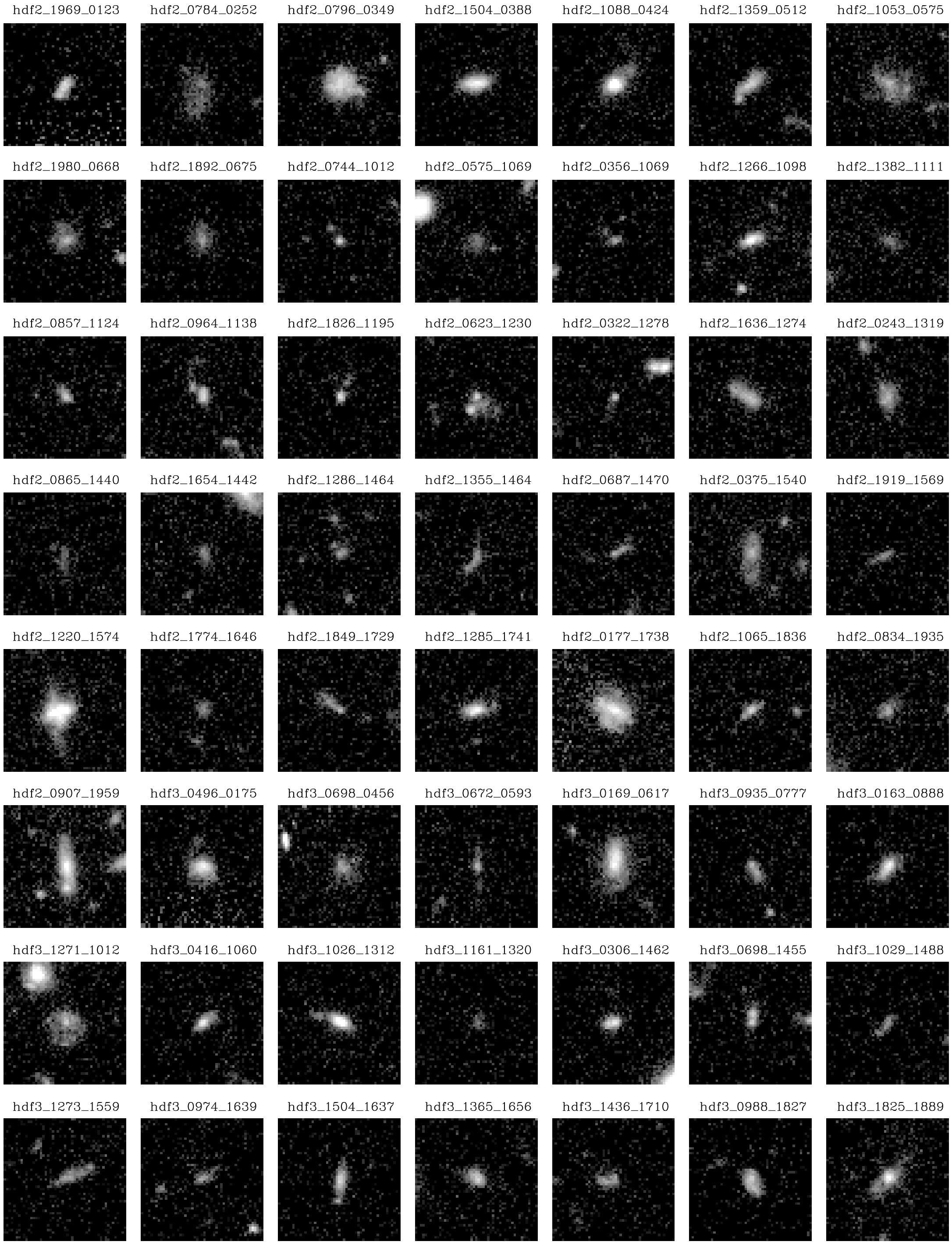

Fig. 3–1.— Montage of 87 low surface brightness, elongated, and/or faint peculiar galaxies selected to be re-analyzed using a fainter surface brightness detection level. Images are 101×101 pixels extracted from the F814W images of the HDF (i.e., not the mosaic).

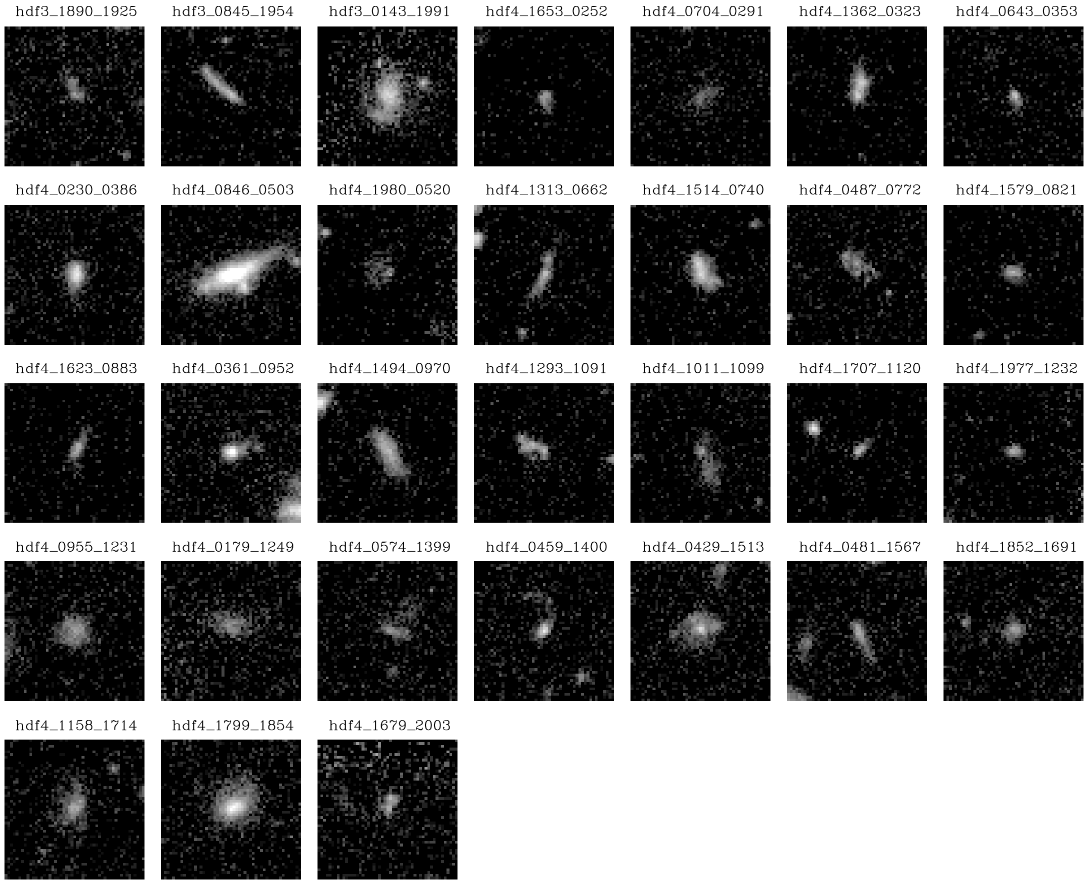

Fig. 3–1. Montage of LSB, elongated, and/or faint peculiar galaxies *(continued)*.

Figure 3–2 shows a direct comparison of A_W and C_W using the canonical detection level used for the HDF and the fainter level described above. Later in this dissertation, A_W-C_W classes will be defined. The relevant concern, therefore, is how many of these low surface brightness, elongated, and/or peculiar galaxies will drift over boundaries and change the statistics of later work. Thirteen out of the 87 objects (15%) are not detected at the brighter μ_{det}. Twenty-two objects ($\sim$25%) are found to cross over the A_W border between low and high A_W, at A_W=0.1, when the fainter μ_{det} is used: these are all cases in which the detected area using the brighter μ_{det} resulted in only a small portion (<50%) of the galaxy being detected, because the galaxy is either low surface brightness or elongated or there are multiple knots in the galaxy that are found as separate objects at the brighter μ_{det}. For C_W, only 5 objects ($\sim$6%) traverse the border at C_W=4. This is not too surprising as most of these objects are, by definition, not highly concentrated. The expected impact on the statistics of the high concentration class should, therefore, be minimal.

The impact on the A_W distribution, however, should be more carefully studied. A cursory "by-eye" look at the data indicates that roughly 225 of the 1079 HDF objects may benefit from a fainter μ_{det}. (This excludes relatively compact symmetric objects and extremely faint objects.) The 87 objects used in these tests were selected to be representative of the original 225 objects. If 25% of the original 225 objects have values of A_W that cross over the A_W boundary, this represents a change for only $\sim$5-6% of the total galaxy population. In addition, it will be shown later that an increase in the number of highly asymmetric objects is found. Lowering μ_{det} will only act to increase this effect, as more objects will be found with high asymmetry. The currently measured increase, then, is a lower limit on the probable true magnitude of this phenomenon. For

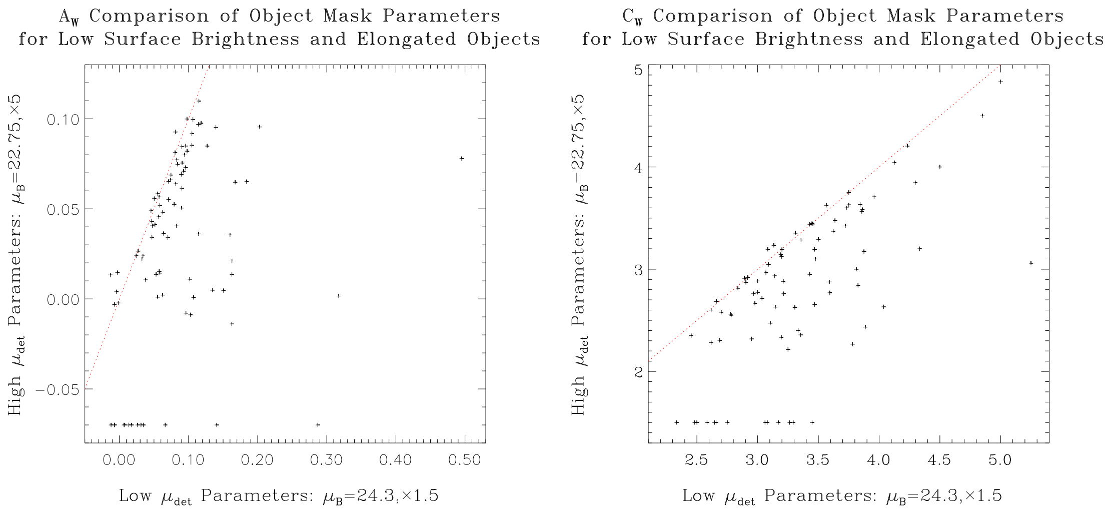

Fig. 3–2.— A comparison of A_W and C_W for 87 low surface brightness, elongated, and/or faint peculiar galaxies using two surface brightness detection levels: $\mu_{det,B}$=22.75 with a growing factor of 5 (the usual pair of parameters used for the HDF sample) and $\mu_{det,B}$=24.3 with a growing factor of 1.5 (a fainter detection level to better detect low surface brightness and elongated objects). Thirteen out of the 87 objects (15%) are not detected at the brighter μ_{det}. 5 galaxies are found to traverse the boundary between high and low concentration classes. 22 objects migrate from the low to high asymmetry class when a fainter μ_{det} is used. Though more detailed study of these effects is needed, the contribution of these galaxies to the A_W-C_W distribution is estimated to be fairly small (∼5%); these low surface brightness, elongated, and faint peculiar galaxies have, therefore, been left in the sample with A_W-C_W values determined using the original (brighter) detection level and growing factor.

now, therefore, these low surface brightness, elongated, and/or faint peculiar galaxies have been left in the sample with A_W-C_W values calculated using the original detection level and growing factor. In future, the detection algorithm will be modified to use the fainter surface brightness detection level, by default, unless close neighbors are present.

2.4. Pixel Replacement

In images where there are multiple detections, it may be desirable to replace extraneous objects with sky values, in order to avoid finding artificially high asymmetries due to contamination by close neighbors. The option to do so is available and works in the following manner.

1. A histogram of all sky pixel values is created and normalized to unit height.
2. Sky values are randomly generated using a Monte Carlo-style technique to reproduce this distribution. The number of values generated is the number of pixels that are to be replaced.
3. Pixels of the extraneous objects are replaced with these randomly generated sky values.

Pixel replacement is routinely done for all objects in the HDF. (Pixel replacement is unnecessary for the local sample, as there is only one object per image.) The object mask of objects for which pixel replacement is done is re-created after the pixel replacement has been completed. Once again, the re-creation of the mask is only done for images taken through the F814W filter. Analysis in the other bands is done using the object mask created in F814W.

2.5. Calculation of the Half-light Radius

At this point, a simplistic half-light radius is calculated through concentric apertures centered on the intensity-weighted centroid of all object pixels in the object mask created in the previous step. The total light of the galaxy is defined as the total counts in the object pixels.

In order to get a finer determination of the half-light radius, the central 10×10 pixels are magnified by a factor of 10. The flux within concentric circular apertures with step size of 1 (i.e., 0.1 times the actual pixel size) is summed. If the half-light flux is not reached within this expanded core, then the core is returned to its original size and the calculation continues using the full image, maintaining a step size of 0.1 pixel. The half-light radius is the radius of the smallest circular aperture containing at least half of the total light.

The original motivation for expanding the core was to try to obtain a finer sampling of the core. Various step sizes both inside and outside the central 10×10 pixels were explored. In practice, it turned out that the expansion was not necessary. Doing the expansion does not affect the final results, however, so the procedure has been left as is.

A corresponding procedure is used to determine the radii containing 20% and 80% of the total light, which are used later for calculation of the concentration index.

A cautionary note: the half-light radii of low surface brightness and elongated objects will be systematically under-estimated as a result of the detection limitations described earlier.

3. The Peculiarity Indices

3.1. Rotational Asymmetry

The rotational asymmetry index developed in this work, A_W, is a refined version of the asymmetry parameter, A, developed by A96b, hereafter referred to as A_A. The image of a galaxy is rotated 180° and subtracted from the original image. The rotational asymmetry index (for both A_W and A_A) is one-half the absolute value of the residuals in the subtracted image divided by the total counts in the galaxy (i.e., the total counts in the object pixels):

$$A_W = \frac{1}{2}\frac{\Sigma|I - I^{180}|}{\Sigma I}. \tag{3.1}$$

The refinements that I have made are designed to avoid finding artificially high asymmetries due to poor determination of the pivot point (the point about which the image is rotated) and of the region of the galaxy to be included in the asymmetry calculation.

Limitations of the Abraham asymmetry parameter

The center of rotation for A_A is chosen to be the brightest pixel in the galaxy, after smoothing the image by a Gaussian with $\sigma = 1$ pixel. There are several weaknesses to this choice and method. First of all, smoothing by a 1-pixel Gaussian results in objects being smoothed by different absolute linear scales at different redshifts and in different samples. Features in the galaxy are, therefore, more severely smoothed as one goes to higher redshift, and a meaningful comparison over a range of redshifts becomes more complicated. Secondly, for spirals, irregulars, and low surface brightness (LSB) galaxies, the brightest point may turn out to be a bright HII region or even a companion far from the center of the galaxy of interest. Using this point as the pivot point can result in a spuriously enhanced asymmetry value. Finally, the rotation is done around the center of the brightest pixel, regardless of whether or not the brightest point is actually centered in that pixel (Abraham 1998). For objects with a sharp central profile, e.g. ellipticals, this can again result in an artificially high asymmetry value. This is well illustrated by the large spread in asymmetry values seen for ellipticals in Figure 1 of A96a and Figure 2 of A96b. The lack of sub-pixel centering becomes progressively more important as one goes to higher redshifts.

The area within which A_A is calculated is the isophotal area enclosed by pixels that are $1.5\sigma_{sky}$ above the sky level. As discussed earlier, however, the same σ_{sky} cut will correspond to different true brightness levels in a galaxy at different redshifts. In addition, A96a and A96b compare data taken with different instruments, detectors, and observing conditions. All of these factors will affect the σ_{sky} level; hence, consistent comparisons between the various data sets is difficult to achieve.

As described above, the limitations of A_A generally act to increase the asymmetry. In addition, the effect of these limitations gets worse as one goes to higher redshifts. As a result, the number of asymmetric objects that one finds at high redshift compared to a local sample may be overestimated. These effects will be explored in more detail in Chapter 6.

Refinements made for A_W

The first refinement is the initial smoothing kernel. The image is convolved with a two-dimensional axisymmetric Gaussian kernel with $\sigma = 0.1r_{1/2}$, where $r_{1/2}$ is the half-light radius. Using a smoothing length that scales with a measured galaxy property ensures that, to first order, the degree of smoothing scales in the same manner for all galaxies. (One should be cautious, however, when the signal-to-noise ratio is small, as simulations, to be presented later, have shown that the extended wings of galaxies may be lost in the noise, resulting in a gross underestimate of the galaxy scale.) This smoothing length is chosen to be large enough to "smooth out" bright regions away from the center of the galaxy in order to prevent them from being chosen as the pivot point, but small enough that close pairs of galaxies can still be distinguished after smoothing. This smoothed image is used only for the calculation of the centroid described below. Calculations of the actual peculiarity indices are done on the original (unsmoothed) image.

The second refinement is the determination of the pivot point. Rather than choosing the center of the brightest pixel, the intensity-weighted centroid of pixels brighter than 50% of the maximum of the smoothed image is calculated. If fewer than 5 contiguous pixels meet this brightness level cut, successive attempts are made to calculate the centroid of pixels brighter than 20%, 10%, and 5% of the maximum. If there are fewer than 5 contiguous pixels brighter than 5% of the maximum of the smoothed image, then no detection is recorded and no further calculations are done on this object. This step acts as an additional detection criterion to that described in Section 2.3 of this chapter, which generally culls out very small and very low signal-to-noise objects.

The centroid is determined to sub-pixel accuracy and is shifted to the center of the central pixel of the image before rotating. This shift is necessary because the W96 x, y-position, on which the postage stamp image is centered, is defined by W96 to be the brightest pixel in a 3×3 pixel grid with the greatest luminosity within their detection area. For objects containing a bright off-center peak, this position may be quite different from the calculated centroid. (In the local sample, the objects are not always centered in the image; therefore, this shift is also required.) Because the shift is done to a fraction of a pixel, bilinear interpolation is used, after which the image is re-normalized to conserve flux. In order to remove residuals at the edges of the image created by the shifting algorithm, the image is cropped to the nearest pixel beyond which the residuals appear. For most objects in the HDF, at most a few pixels are cropped off around the edges. (The amount by which the local images are cropped varies depending on how well centered the galaxy is in the original image.) This is the final image on which A_W is calculated.

One might suggest that the shift (and corresponding interpolation) be avoided by simply rotating the image around the calculated centroid position. Since the centroid is rarely on an integer pixel, however, interpolation would be required regardless. In addition, using the rotation algorithm available in IDL, the correspondence between the pixels in the original and rotated images becomes somewhat complicated, and a shift of one of the two images would still be necessary before they could be subtracted from each other. Since some amount of interpolation is required by either method, the original method described above was adopted.

The final step in the refinement of the centroid is the development of a minimization algorithm designed to find the minimum A_W. A_W is calculated on two grids of pivot points. The first is a coarse 5×5 grid centered on the initial pivot point (i.e., the calculated centroid), with a step size of 0.5 pixels. The pivot point corresponding to the minimum asymmetry found in the coarse grid is then used as the center of the second, finer, grid. The second grid is 7×7, with a step size of 0.1 pixels. The final asymmetry for the galaxy is the minimum asymmetry found in the fine grid.

These refinements provide three improvements: (1) all galaxies are smoothed by roughly the same proportionality factor, (2) localized bright knots or companions are not mistakenly chosen as the pivot point, and most importantly, (3) the minimization process will yield the minimum asymmetry, even if the "best" pivot point is not found initially.

Though this method appears to work quite well for finding the centroid of most objects, two special situations should be considered. (1) For bimodal or multi-modal objects, the centroiding contour level described above (50% of the maximum of the smoothed image) often separates sub-peaks in the object even though the original detection algorithm finds only one object. The pivot point for this object will, therefore, be centered on the centroid of the peak that is centered in the image, as defined in the object mask creation routine. One can see that the resulting asymmetry may be quite high, especially if the peaks are comparably bright. Recall that the rotational asymmetry index is designed to find *peculiarities* in galaxy morphology. Although bimodality is not "asymmetric" in the traditional sense of the word, it is, nonetheless, an indication of peculiarity. Finding a high A_W for a bimodal object is, therefore, preferred. If a fainter contour level were used, the pivot point would likely be found nearly between the two comparably bright peaks. In this case, the two peaks, when rotated and subtracted, would effectively cancel each other out, and a spuriously low A_W would be found. (2) The other interesting case is that of an object within the envelope of a much brighter object. In this case, the minimization routine may pull the pivot point away from the centroid of the primary object because of contamination by the bright envelope. Having a finite-sized grid of pivot points becomes quite useful here in limiting the amount of drift that is allowed. Admittedly, a spuriously high asymmetry may still be found. In practice, however, there are only a handful of these cases in the HDF, and, in most of those cases, the object mask does a good job of isolating the primary object, even within the envelope of the brighter object.

As described in Section 2.3, a final refinement in A_W is the determination of the area within which to calculate the rotational asymmetry. Rather than using a σ_{sky}-cut (as in A96a,b) or a radial cut (as in Conselice et al. 1999), a surface brightness cut with a growing factor is imposed. Recall that this rather unconventional definition is implemented in order to simultaneously satisfy two goals: (1) to statistically separate close pairs of objects determined to be superpositions based on photometric redshift estimates, and (2) to define a region that encloses all of the light of a galaxy with as little contamination from nearby objects as possible. In addition, because the object masks are not symmetric, the area defined by the union of the original and rotated masks is the final area within which A_W is calculated. The union of the two masks is chosen instead of the intersection because using the intersection tends to clip off interesting (i.e., peculiar) features, resulting in a deceptively low A_W. It is unclear whether A96a,b used an intersection or union of their original and rotated images. Conselice et al. used circular apertures, so this is not an issue.

Background correction

Because the rotational asymmetry is calculated as the absolute value of the residuals, noise in the images will always register a positive asymmetry signature. It is important, therefore, to remove the contribution of sky noise to A_W. It is prudent to determine this correction using sky pixels *within* the postage stamp image, rather than simply assuming an average HDF sky distribution, for two reasons: (1) The sky level across the HDF is not completely constant. Using the sky distribution of the full HDF would result in the background correction being overestimated for some objects and underestimated for others. (2) As mentioned earlier, some objects lie near or within the envelopes of bright objects. The background correction for these objects would be significantly underestimated if one were to assume an average HDF sky distribution.

To estimate the background correction, pixels are randomly selected from the sky pixels until an area equal to that of the object is reached. This method is chosen over selecting a contiguous area in the image equal to the area of the galaxy to minimize biases that may result when a gradient in the background exists. In practice, for most objects, both methods work comparably well. The background correction is then the total of the absolute value of the randomly selected pixels in the subtracted image. Because a background correction is calculated for each grid point of the minimization algorithm, the mean of the 74 calculations is taken as the final background correction. The final A_W is then:

$$A_W = \frac{1}{2}\frac{\Sigma|I - I^{180}|}{\Sigma I} - < \frac{1}{2}\frac{\Sigma|B - B^{180}|}{\Sigma I} > \tag{3.2}$$

where $B - B^{180}$ are the randomly selected background pixels in the residual (i.e., rotated and subtracted) image.

For the HDF images, the postage stamp cutout was always made large enough to guarantee that sufficient numbers of sky pixels were available. As was mentioned earlier in this chapter, for a handful of the local galaxies, using the HDF object mask parameters results in the object mask filling the whole image, and no background correction can be made. The object mask parameters for the local sample, therefore, were modified to ensure that a sufficient number of sky pixels is always available.

Errors in A_W

Three primary sources of error in A_W were investigated:

- background error – the error resulting from randomly selecting pixels for calculation of the asymmetry in the background,

- centroiding error – the error introduced by small variations in the choice of pivot point, and
- Poisson error – the error associated with the photon statistics of the image.

Since the background asymmetry is re-calculated at each pivot point using a different set of background pixels, the standard deviation of the 74 realizations of the background asymmetry is taken as the error in the background asymmetry. This term proves to be negligible (generally less than 0.01 in A_W).

The centroiding error on A_W is estimated using the standard deviation of the 74 realizations of the asymmetry index. This is generous estimate of the error as the centroid rarely drifts by more than roughly half a pixel. This is verified in the multiple runs discussed next. This contribution is also quite small, generally on the order of 0.02-0.03 in A_W; for some of the faintest objects at the edge of the detection limit, this error reaches as high as 0.05 in A_W.

As a sanity check, the full sample was run through A_W and C_W six times. The cumulative plot of the A_W-C_W distribution of all six runs is shown in Figure 3–3. This figure shows the combined error due to background sampling and centroiding. Neither contribution is very significant, and our results are robust to these errors.

The final error contribution, the error due to photon statistics, is calculated analytically for each object. A numerical determination has not yet been worked out. Propagating the Poisson errors from each term in A_W, the final average error in A_W, Δ_{Poi}, is found to be:

$$\Delta_{Poi} = \frac{\Sigma \frac{2}{\sqrt{\pi}} \sqrt{I_i}}{2 I_{tot}}, \tag{3.3}$$

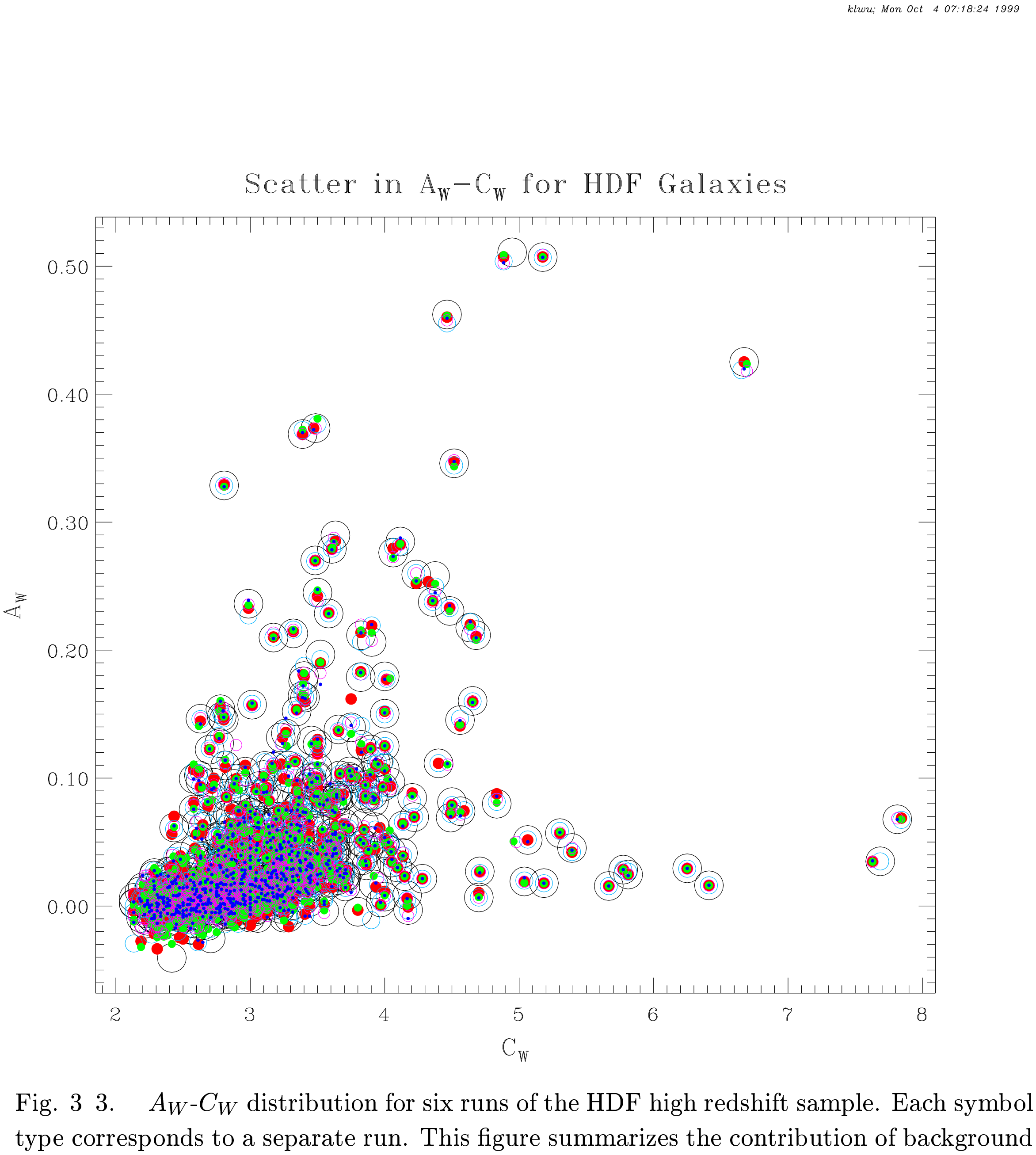

Fig. 3–3.— A_W-C_W distribution for six runs of the HDF high redshift sample. Each symbol type corresponds to a separate run. This figure summarizes the contribution of background and centroiding errors to A_W and C_W. Neither contribution is very significant, and our results are robust to these errors.

where I_i is the total intensity (in photons) in the ith pixel and I_{tot} is the total intensity (in photons) of the object.

Figure 3–4 shows the correlation of the Poisson error in A_W with A_W, F814W$_{AB}$ magnitude, first-moment radius, and redshift. The large errors seen at the lowest asymmetries are likely associated with small, faint objects just barely detectable above sky, while largish errors at high asymmetries are a result of truly large variations in intensity in the object. The correlation with magnitude behaves as anticipated: the smallest errors are found for the brightest objects and increase as the magnitude decreases. Contrary to what one might expect, however, there does not appear to be a significant correlation with the size of the object. It is not clear why this is the case. With redshift, once again, the overall behavior of the errors is as expected: a spread of errors at low redshift and mostly large errors as the redshift increases. There is a handful of objects at $z \sim 4.2$ which appear to have much lower errors than might be expected. The redshifts for these objects may have been mis-estimated as a result of color degeneracies. A few of these objects will also be noticeable in future A_W-C_W diagrams as objects with much brighter magnitudes or larger sizes than the median magnitude or size for that redshift bin.

A limiting error of $\Delta_{Poi} \sim 0.06$ is evident in all of these plots and is likely a consequence of having imposed a radial (and, hence, roughly a magnitude) cut on the sample. In the simple case of all pixels in an object having the same flux, the average error scales as:

$$\Delta_{Poi} = \frac{1}{\sqrt{\pi}} \frac{1}{\sqrt{I_i}}. \tag{3.4}$$

The faintest objects in this sample have ~10-12 counts per pixel. Assuming a gain of 7 electrons per ADU (perhaps an over-estimate for the drizzled HDF images), the average

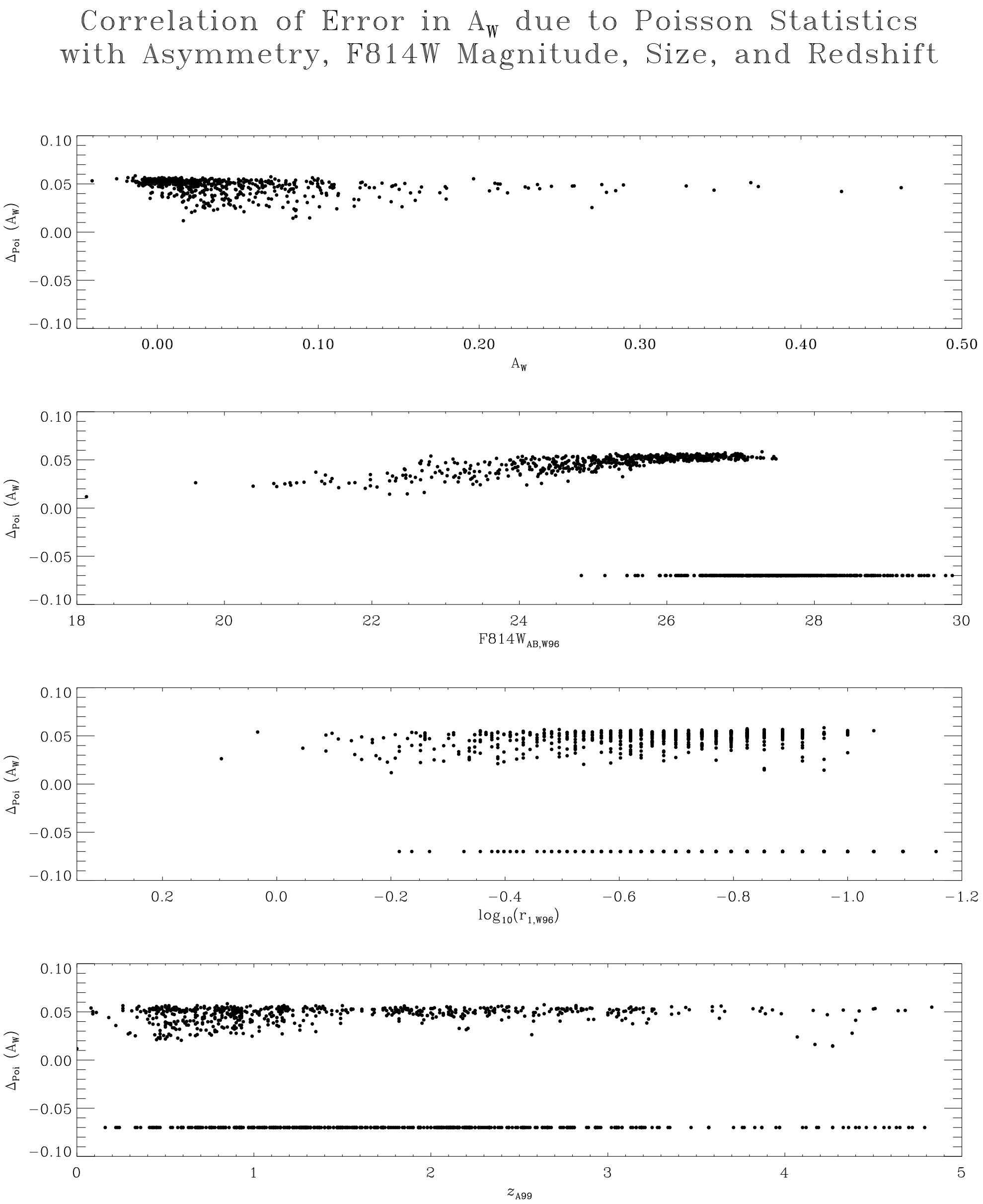

Fig. 3–4.— Correlation of the Poisson error in A_W with A_W(*top panel*), F814W$_{AB}$ magnitude (*second panel*), first-moment radius (*third panel*), and redshift (*bottom panel*). In general, the behaviour of the errors is as expected: largest errors at low and high asymmetries (small, faint objects versus objects with truly large variations in their light distributions); errors that scale inversely with magnitude, and a spread of errors at low redshifts that narrows to large errors at high redshift. Interestingly, no obvious correlation with size is seen. The limiting error of $\Delta_{Poi} \sim 0.06$ is a result of the radial (and, hence, roughly a magnitude) cut imposed on the sample. *(see text for details)* Objects that were not detected by the A_W algorithm are assigned a value of $\Delta_{Poi} = -0.07$.

error in A_W is roughly 0.062-0.067, consistent with what is seen in Figure 3–4. Finally, note that objects that were not detected by the A_W algorithm are assigned a value of $\Delta_{Poi} = -0.07$.

In general, this analytical calculation of the Poisson error in A_W appears to be reasonable. Nonetheless, it will be informative to also develop and carry out a numerical estimate of this error and compare.

3.2. Concentration Index

The concentration index used in this work, C_W, is the ratio of the radii containing 80% versus 20% of the total light of the galaxy. Conselice et al. (1999) use a similar definition of the concentration index, though they consider the logarithm of the ratio, as first defined by Kent (1985). As in the calculation of the half-light radius, the total light is defined as the total counts in the object pixels of the object mask. The radii are computed using concentric circular apertures following the same procedure as that used for the determination of the half-light radius.

The concentration index developed in A96b, C_A, is a ratio of the flux within two elliptical apertures, as described in Abraham et al. (1994). The intensity-weighted second-order moments of the light distribution within their detection isophote are used to estimate an "equivalent elliptical light distribution" with total area equal to the area within the detection isophote. The inner radius is specified as a fraction, generally chosen to be 0.3, of the outer radius.

While a direct translation between the Abraham concentration index, C_A, and C_W is difficult to derive, the general trend for both algorithms is the same: ellipticals have high concentrations while spirals and irregulars have progressively lower concentrations. A more detailed comparison of these two algorithms will be presented in Chapters 5 and 6.

Errors in C_W

The errors in C_W were explored numerically using the images of 11 of the simulated $z = 0.8$ galaxies selected from the Frei Catalog to represent a range of sizes, magnitudes, and morphological types. Noise consistent with that of the HDF images is added to these images and the concentration index is re-calculated. 50 iterations were performed on each galaxy and the mean and standard deviation of the concentration were determined. No obvious trend with size or magnitude emerged. Errors tended to be larger ($\sim$0.2-0.3, rather than $\sim$0.05, in C_W units) for galaxies with significant structure. The random addition of noise in these objects is enough to result in spiral arms or HII regions occasionally being found as a separate object and occasionally not.

As no obvious trend could be established with magnitude or size of the object, a reasonabl approximate error in C_W of ± 0.2 has been adopted for all objects. In future, a more rigorous method of computing the error in C_W will need to be developed.

3.3. Other Peculiarity Indices

Several other peculiarity indices were explored, but, in part due to time constraints and in part because some of these indices were found to correlate well with A_W, they were not studied in as great detail.Nonetheless, they deserve to be mentioned for more detailed study in the future.

Reflection Asymmetry

The reflection asymmetry is a variation of A_W in which the galaxy image is reflected across its minor axis rather than rotated 180°. (The option to reflect across the major axis is also available.) Preparation of the images and asymmetry minimization are done in the same manner as for A_W.

A few additional steps are required in order to compute the reflection asymmetry.

1 - The position angle is determined on the same smoothed image on which the centroid is calculated, but at a lower brightness level. All pixels with count levels greater than 5% of the maximum in the smoothed image are used.

2 - The image is rotated such that the major axis of the galaxy is aligned with the x-axis, and then reflected across the y-axis (the default). The reflected image is subtracted from the original image, and the reflection asymmetry is calculated as one-half the absolute value of the residual image normalized by the total counts in the image.

The primary advantage of this index over A_W is for edge-on galaxies with a dust lane. In many cases, A_W tends to find a high asymmetry value for these objects, as they are rarely viewed exactly edge-on and the dust lane usually lies slightly above or below the major axis. At high redshift, however, it is rare that dust lanes are distinguishable; hence, this algorithm was put aside.

Skewness

The skewness is the intensity-weighted third moment of the light distribution of the object pixels of the object mask. This index was found to correlate reasonably well with both the asymmetry parameter and, to some extent, with centroid drift (described below).

Centroid Drift

The centroid drift is the maximum drift of the intensity-weighted centroid of an object over a range of surface brightness levels. This index is most useful in detecting close pairs of galaxies, as the centroid shifts suddenly when the detection surface brightness at which the galaxies became two distinct objects is reached. An extension of this index would be to look at the slope of the centroid drift versus μ_{det}. An object in which the peak of the light distribution is off-center (i.e., a skewed object) will have a gradually sloping centroid drift, whereas a bi-modal object will show a sharp jump in the centroid at the surface brightness at which the two peaks become separated.

The power of this index has not yet been fully explored. It may, in future, be useful for separating out sub-classes of high asymmetry objects that are, e.g., bi- or multi-modal or skewed to various degrees.

Island Counting

The island counting index counts the number of "islands" that appear at successively brighter surface brightness levels within an initial low surface brightness contour. This index is still at a relatively preliminary stage. The interpretation of the resulting data has not been quantified or compared to the other indices.

Fractal Index

The ratio of the length of a contour to the circumference of a circle enclosing an equal area can be used to measure the distortion of the light profile of a galaxy at various surface brightness levels. Smooth symmetric objects, such as ellipticals, will have a low ratio at all surface brightness levels. Because of their relatively even light distribution, irregulars and amorphous galaxies also tend to maintain a low ratio. Depending on the degree of smoothing imposed, spirals will likely have a slight rise in the ratio at the surface brightness levels at which the spiral arms are prominent. Distorted objects generally maintain a high ratio at all brightness levels.

Because the resolution of high redshift galaxies even with HST is still limited, the discriminatory power of this index was found to be weakened at high redshift. More careful study of the optimal smoothing length before contouring may improve the applicability of this index.

4. Fine-tuning Parameters

4.1. Object Mask Parameters: Changing μ_{det} and the Growing Factor

The creation of the object masks is a crucial step in the determination of the asymmetry and concentration of objects. If the surface brightness detection level, μ_{det}, is too low, then close pairs of objects will be treated as a single object, and spuriously high asymmetries will likely be found for these objects. If too high a surface brightness detection level is chosen, the growing factor must be increased significantly in order to compensate for the small initial detection area. In addition, as μ_{det} brightens, the shape of the resulting detection area is progressively less likely to be representative of the overall shape of the galaxy. The grown mask, therefore, will either miss some light from the galaxy or, if it is grown enough to gather all the light from the galaxy, it will also include a lot more sky pixels than might be desirable. A typical example of this case is that of an edge-on spiral, when the detection level is chosen such that only the bulge is detected. The initial detection area is likely to be almost circular. If the mask is not grown enough, light from the ends of the galaxy will not be included; on the other hand, if the mask is grown enough to enclose the whole galaxy, more than half of the pixels within the mask may be sky pixels. Though the background correction should do a reasonable job of removing the contribution of the sky component, it is preferable to simply start with a mask that more closely fits the galaxy shape.

Several combinations of detection surface brightness level and growing factor were explored. The surface brightness levels that were examined were $\mu_{F814W,AB} = [23.5, 24.5, 25.5]$ with growing factors of 3, 5, and 10. These tests were done using the HDF galaxy sample.

Figures 3–5 and 3–6 show comparisons of A_W and C_W, respectively, for the nominal value of μ_{det}= 24.5 with three different growing factors (3, 5, and 10). In general, A_W is not strongly affected by a change in the growing factor. Several galaxies, however, appear to have significantly higher asymmetries as the growing factor is increased. This results primarily from the fact that these tests were conducted before the pixel-replacement algorithm was implemented. For these galaxies, light from close neighbors may have been inadvertently included in the asymmetry calculation.

The effect of changing the growing factor on C_W is also fairly mild. A slight systematic shift to higher concentrations with larger growing factors can be seen in Figure 3–6;

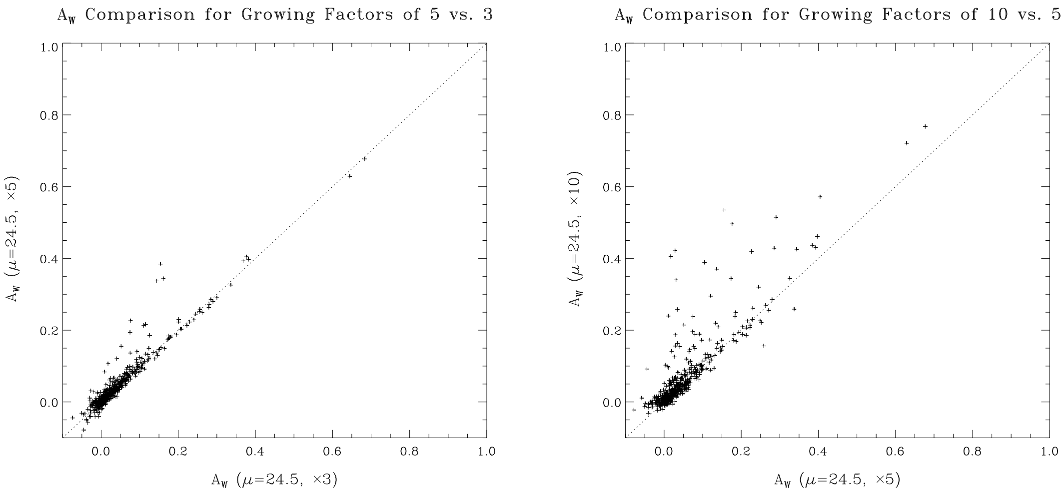

Fig. 3–5.— A comparison of A_W for HDF galaxies at μ_{det}=24.5 for various growing factors. A_W is not strongly affected by the choice of growing factor. There are, however, a number of galaxies whose asymmetries increase with larger growing factors. Unfortunately, this is likely a result of inadvertent inclusion of light from neighbors, as these tests were run before the pixel replacement algorithm was implemented.

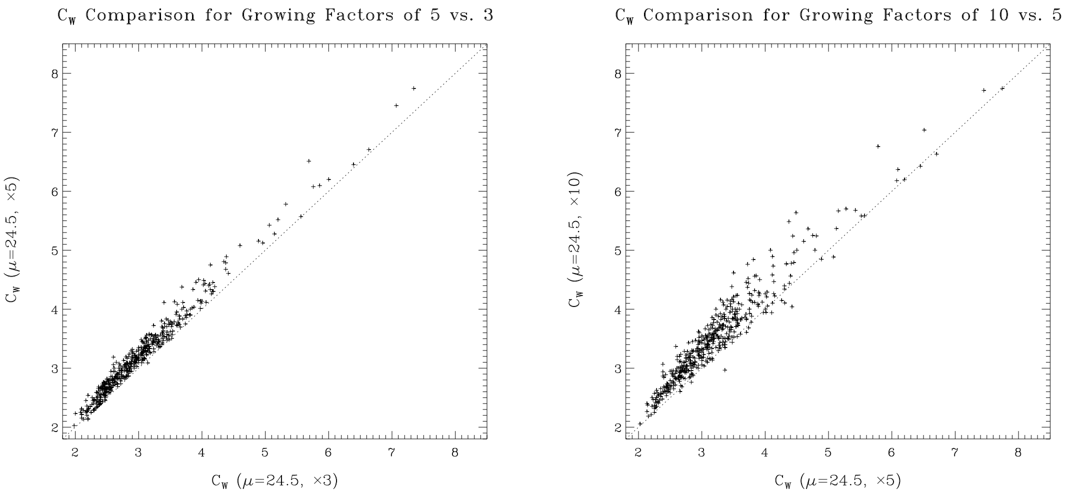

Fig. 3–6.— A comparison of C_W for HDF galaxies at μ_{det}=24.5 for various growing factors. There appears to be a slight dependence of C_W on the growing factor, such that higher concentrations are found for larger growing factors. Increasing the area associated with the galaxy results in a deeper probe of the galaxy profile. As the wings of the galaxy are included, the total light increases slightly. r_{80} tends to grow more than r_{20}, and C_W increases.

this shift, however, is to be expected. Increasing the growing factor at a given surface brightness level increases the area around the galaxy included in the calculation and essentially results in probing deeper into the galaxy profile. As the wings of the profile are included, the inner radius of the concentration index does not change much, but the outer radius will tend to increase, resulting in a higher calculated concentration.

In Figures 3–7 and 3–8, the comparison of A_W and C_W respectively, is shown for three values of μ_{det} (23.5, 24.5, 25.5 F814W$_{AB}$ magnitudes per square arcsec) all with a growing factor of 5. Once again, in general, A_W is not strongly affected, though there is a subset of objects whose asymmetries increase quite dramatically as a fainter μ_{det} is used. This effect is especially noticeable in the comparison between μ_{det}=24.5 and μ_{det}=25.5. In all of these cases, the fainter detection level resulted in close pairs and multiple components being found as single objects. The resulting asymmetry is understandably much higher. Clearly, however, such spurious asymmetries are undesirable. One might also note that fewer objects appear in the comparison of μ_{det}=23.5 vs. 24.5 than in that of μ_{det}=24.5 vs. 25.5. This is simply a result of objects not being detected at the higher surface brightness level. Non-detections are not plotted in these figures.

The choice of μ_{det} has a much stronger effect on C_W than the choice of growing factor (Figure 3–8). The sense, however, is the same. At lower surface brightnesses, objects are found to be more highly concentrated. This can be explained, in part, as a result of probing more deeply into the galaxy profile, as described earlier. In addition, however, the merging of close pairs at lower μ_{det} will also result in lower values of C_W. There also appears to be a lack of objects in both comparisons below roughly C_W=2.8 in the fainter μ_{det}. This is can be understood in the following manner: The limiting value of C_W is 2. Objects in the brighter μ_{det} do, in fact, reach this limiting value. At the fainter μ_{det}, however, by the time

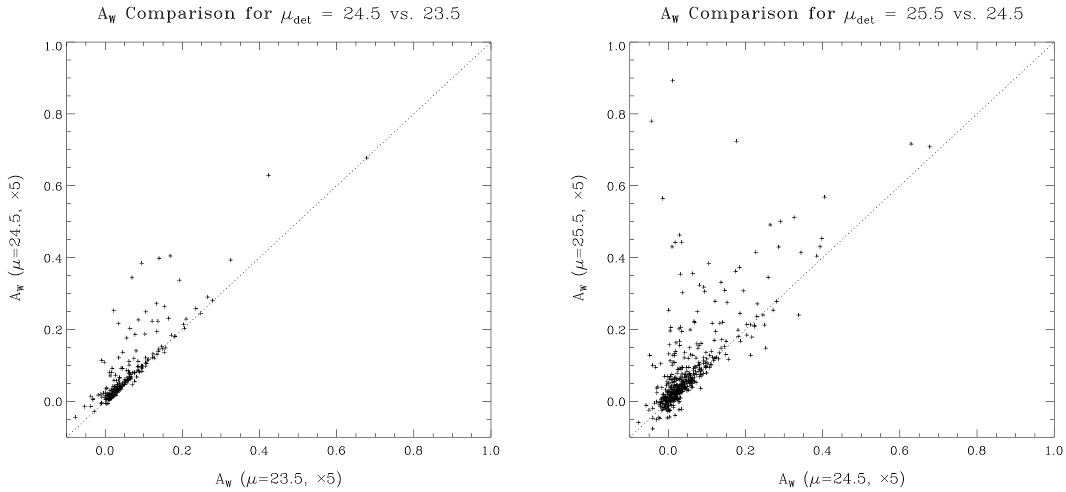

Fig. 3–7.— A comparison of A_W for HDF galaxies using various values of μ_{det} with a growing factor of 5. In general, A_W does not seem to be strongly affected by changing μ_{det}. There is, however, a subset of objects whose asymmetries increase rather dramatically, especially at μ_{det}=25.5. At this faint μ_{det}, close pairs are detected as single objects, and the calculated asymmetry increases significantly.

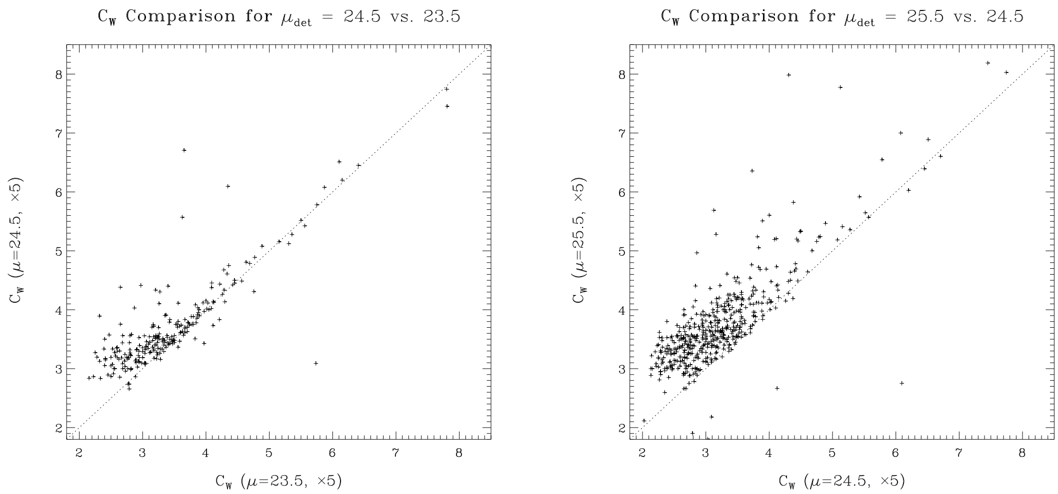

Fig. 3–8.— A comparison of C_W for HDF galaxies using various values of μ_{det} with a growing factor of 5. A significant increase in C_W with fainter μ_{det} is seen. This is likely a result of either probing deeper into the galaxy light profiles or merging of multiple components into one object.

C_W reaches below ~ 2.8, the object is likely no longer being detected at the brighter μ_{det} and, therefore, is no longer plotted. The result is an apparent truncation in C_W for the brighter μ_{det} at higher C_W than the usual limiting value of 2. Note that, if one investigates the range of C_W for all objects, including those that are not detected at the brighter μ_{det}, the limiting value is still C_W=2.

It is interesting to explore whether the shift of the concentration index is more strongly affected by the shape of the detection area (i.e., μ_{det}) or the total area within which the concentration index is calculated (i.e., the growing factor). Two pairs of μ_{det}-growing factor combinations, thus, are compared (Figure 3–9):

1. μ_{det}=25.5 with a growing factor of 5 ("25.5×5") versus μ_{det}=24.5 with a growing factor of 10 ("24.5×10"): In this case the total areas of the objects are designed to be roughly comparable on average, but the initial detection area of the object is different (the "initial area" comparison).

2. μ_{det}=24.5 with a growing factor of 10 ("24.5×10") versus μ_{det}=24.5 with a growing factor of 5 ("24.5×5"): This is a pure test of whether the change in area is the culprit. The starting masks are exactly the same – only the growing factor is changed (the "total area" comparison).

Figure 3–9 shows the ratio of C_W for the two pairs of μ_{det}-growing factor combinations (enumerated above) relative to the ratio of their corresponding areas: the "initial area" comparison on the left and the "total area" comparison on the right. Color and symbol size scale with the area of the object found using μ_{det}=24.5 with a growing factor of 10. As expected, the bulk of the objects in the "initial area" comparison cluster around an area ratio of 1 and a corresponding C_W ratio of 1. Extreme ratios of C_W (C_W-ratio $\gtrsim 1.2$ with area-ratio $\lesssim 2$ or $C_W \lesssim 0.8$) are cases where larger (and, presumably, brighter) objects are merged with neighbors (red, orange, and green symbols). Ratios larger than 1 are found when the merged companion is fainter than the primary object; ratios less than 1 are found for merging of a brighter companion or multiple companions. Note that, except in the special cases just noted, C_W only starts to drift to higher values when the ratio of areas begins to increase as well. In these cases, one of two things is happening: (1) small (and, presumably, faint) primary objects are merged with nearby objects at the fainter μ_{det} (the more comparable the objects are in magnitude, the higher the area ratio tends to be) (purple points), or (2) the object is a low surface brightness object for which the brighter μ_{det} captured only a small part of the galaxy (blue and green points). In both of these cases, the C_W calculated at the fainter μ_{det} is expected to be larger. The overall effect, however, is no more than 15%-20% for the majority of the objects, and, as will be shown in Chapter 6, errors of this magnitude do not strongly influence our results.

The "total area" comparison (Figure 3–9,*right panel*) indicates that the increase in C_W seen in Figures 3–6 and 3–8 may be fully accounted for simply by increasing the total area in which the concentration index is calculated. As has been described before, this effect can be understood as a result of probing more deeply into the light profile of the galaxy. Errors in sky subtraction, however, may also affect the calculated concentration index; it is preferable, therefore, to minimize the amount of sky included in the object mask. As is the case for the "initial area" comparison, however, the overall effect is small and can be disregarded for now.

Ideally, μ_{det} and the growing factor should be chosen to balance between three factors: (1) μ_{det} must be bright enough to separate close pairs that, based on photometric

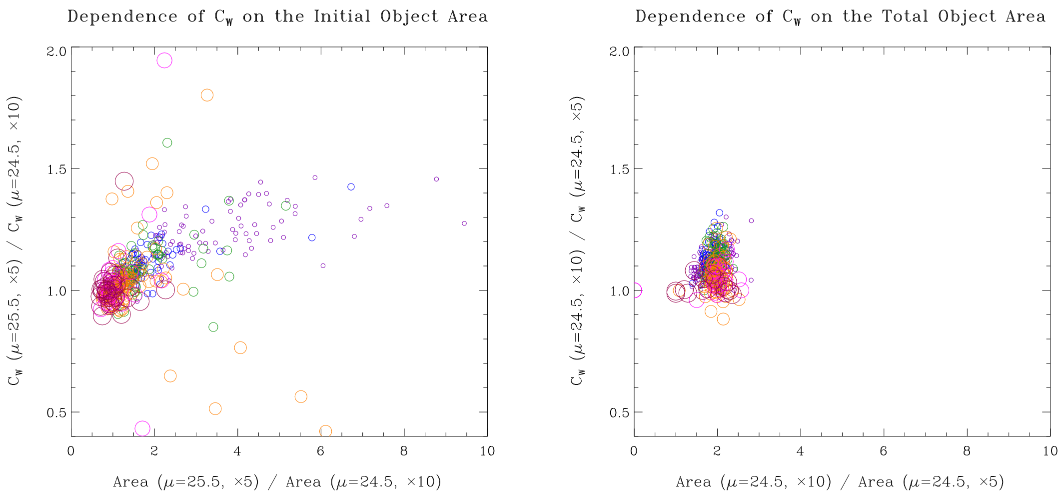

Fig. 3–9.— An exploration of the source of the dependence of C_W on the choice of μ_{det} or the growing factor, as seen in Figures 3–6 and 3–8. The color and size of the circles scales with the magnitude (big red circles correspond to bright objects; symbol size decreases as the color traverses through the optical spectrum to small purple circles, which correspond to faint objects). The left-hand panel compares C_W for two pairs of μ_{det}+growing factor that are designed to result in comparable average areas for most galaxies. As expected, the bulk of the objects cluster around an area ratio of 1 and a corresponding C_W ratio of 1. Drifts to higher and lower C_W ratios generally result from the fainter μ_{det} merging close pairs or encompassing a more complete area of LSB objects *(see text for details)*. The right-hand panel compares C_W for a single μ_{det} with two growing factors. Clearly the apparent dependence of C_W on the choice of μ_{det} and/or the growing factor can be understood as a dependence on the total area in which C_W is calculated. The overall magnitude of this effect, however, is quite small and is not likely to strongly influence the results.

redshift information, are not likely to be physical pairs; (2) μ_{det} should be faint enough to encompass a large enough initial area for low surface brightness and elongated objects that, when grown, all of the light from these objects is detected; and (3) the growing factor should be chosen to maximize the final object mask area of elongated and low surface brightness objects while minimizing the number of sky pixels that are included in the masks of higher surface brightness objects. Based on the tests presented in this section, a surface brightness of $\mu_{F814W,AB} = 24.5$ with a growing factor of 5 was found to be the best compromise between these three criteria.

4.2. Mis-estimating the Sky Level

Another concern is the sensitivity of the peculiarity indices to mis-estimates of the mean sky level. If too much or too little sky is subtracted, will A_W or C_W change significantly? To test this, the mean sky level in the HDF images was increased and decreased by $1\sigma_{sky}$. The new sky level was subtracted from the images, and the indices were re-calculated. As is clearly shown in Figure 3–10 and 3–11, the indices are unchanged. The background correction is successfully compensating for the error in the mean sky value for A_W.

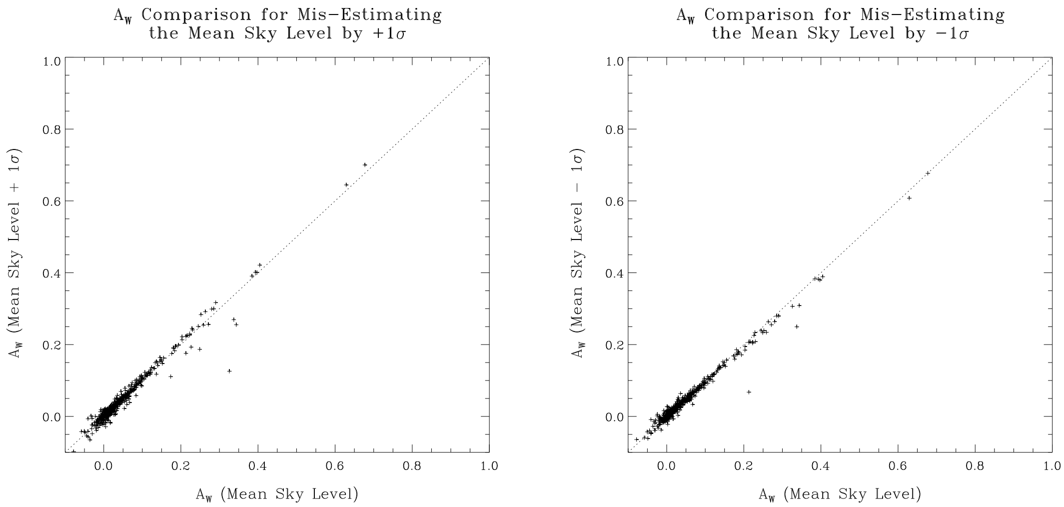

Fig. 3–10.— The effect of mis-estimating the sky level by $\pm 1\sigma$ on A_W for HDF galaxies. Mis-estimating the mean sky level by $\pm 1\sigma$ essentially does not affect the calculated value of A_W in the HDF. The background correction successfully compensates for the error in the mean sky level for A_W.

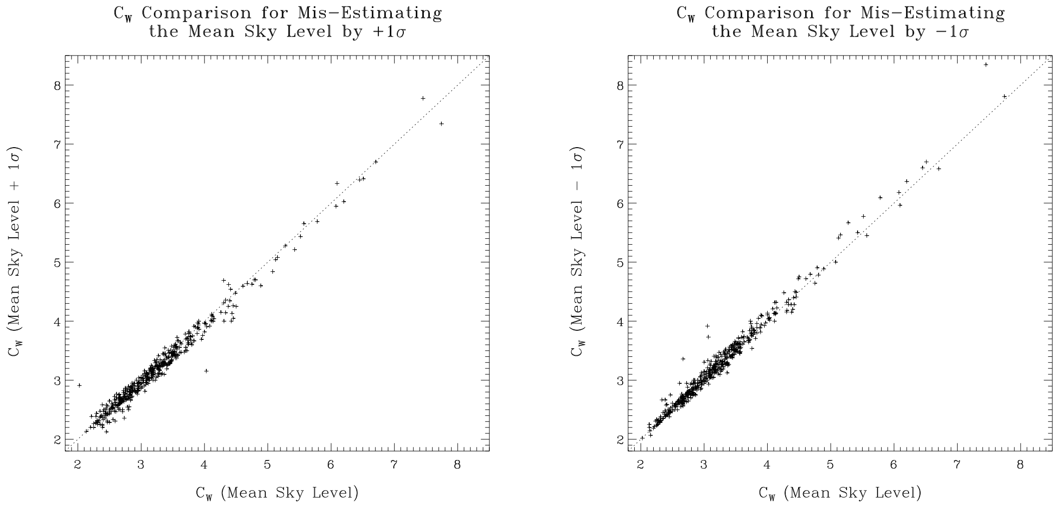

Fig. 3–11.— The effect of mis-estimating the sky level by $\pm 1\sigma$ on C_W for HDF galaxies. Mis-estimating the mean sky level by $\pm 1\sigma$ essentially does not affect the calculated value of C_W in the HDF.

Chapter 4

A Comparison of Photometric Redshifts

With the onset of the Hubble Space Telescope and the new generation of large ground-based telescopes, the volume of imaging data for distant galaxies has increased by orders of magnitude. In order to properly interpret all of the observed properties of these galaxies, accurate distances are crucial. Ideally, spectroscopic redshifts would be gathered for all of these objects. Even with today's multi-slit and fiber-optic spectrographs, however, spectroscopic redshifts are still quite time-consuming to obtain, and the limiting magnitudes that can be reached with spectroscopy are still 2-3 magnitudes brighter than what can be achieved with photometry.

The use of photometric properties to estimate distances to galaxies is not a new idea, although, in recent years, it has gained a new popularity. Baum (1962) used photoelectric photometry of galaxies through nine medium-wide filters to estimate the distance to the cluster 3C395. His photometric estimate, $z \sim 0.44$, turned out to be very close to the spectroscopic value, $z \sim 0.46$, obtained later. Koo (1985) used the average color and curvature of the galaxy spectrum (represented by combinations of two and three colors) to estimate distances to 100 faint galaxies to illustrate the feasibility of using optical colors to estimate redshifts. The agreement with spectroscopic redshifts was within ± 0.06 in redshift. Another photometric distance estimator that has recently received a lot of attention is the "Lyman-break" technique, e.g., Steidel & Hamilton (1993) and Lowenthal et al. (1997). This technique has been used recently primarily to find high redshift galaxy candidates based on a significant drop in flux, or even disappearance, of a galaxy in the bluest of several passbands, as the Lyman break enters that band. In the U-band, for example, this occurs at a redshift of $z \sim 3$. As this break enters redder passbands, even higher redshift candidates may be found. Once again, however, this technique is not as innovative as it might seem; it has been in use since, e.g., Partridge (1974) and Koo (1986).

A variety of photometric parameters can be used, in addition to and in combination with pure photometry, to estimate distances to galaxies. These include spatial correlations, surface brightnesses, one or more colors either alone or in combination with light profiles or structural parameters. For a nice summary of these various techniques, see Koo (1999). In this work, I will be referring to "photometric redshifts" as those derived from multi-band colors of galaxies.

The multi-band imaging of the Hubble Deep Field has enabled several groups to determine photometric redshifts to deep limits for galaxies in this field. The combination of accurate photometric redshifts with the detailed imaging data of the HDF provides a unique opportunity to study morphological peculiarities to much greater depths than previously possible. With this motivation, I undertook a comparison of the photometric redshifts from four groups whose data were available to me: Connolly and collaborators (Connolly 1998 (hereafter, C98), 7-band; Connolly 1999a (hereafter, C99), 6-band);

Lanzetta, Fernández-Soto, & Yahil and collaborators (Lanzetta, Yahil, & Fernández-Soto 1996 (hereafter, LYF96), 4-band; Fernández-Soto, Lanzetta, & Yahil 1999 (hereafter, FLY99), 7-band; Lanzetta & Yahata 1999 (hereafter, LY99), 7-band); Sawicki, Lin, & Yee (Sawicki, Lin, & Yee 1997 (hereafter, SLY97), 4-band); and Gwyn & Hartwick (Gwyn & Hartwick 1996 (hereafter, GH96, 4-band). Much appreciation goes to Connolly and Lanzetta & Yahata for kindly sharing pre-publication data for this comparison. All four groups used the optical data taken in the four HST WFPC-2 passbands (F300W, F450W, F606W, F814W). The additional data used in C98, FLY99, and LY99 are from ground-based near-infrared JHK imaging from the Kitt Peak National Observatory (KPNO). The additional passbands used in C99 are the NICMOS F110W and F160W passbands from HST. A summary of the methods and passbands used by each group is given in Table 4–1. This comparison evolved through several stages as more recent data became available.

1. Multi-band Photometric Redshift Techniques

Two primary techniques have emerged in the multi-color photometric redshift game. *Empirical-fitting methods* (e.g., Connolly et al. 1995, Brunner et al. 1997) use observed magnitudes and colors of galaxies for which spectroscopic redshifts are known to calibrate photometric redshift estimates. *Template-fitting techniques* (e.g., GH96, SLY97, FLY99) derive redshifts from comparisons with template spectral energy distributions (SEDs). A brief description of the two techniques and their primary advantages and disadvantages are given below. Details of the individual techniques can be found in the cited references.

Empirical-fitting methods, such as those of Connolly et al. (1995) and Brunner et

Table 4–1: Summary of Photometric Redshift Methods Used by Various Groups

Catalog[a]	Bands	Photo-z Method[b]	Object Detection Package[c]	Object Detection Band(s)	Completeness[d]	W96 ID provided?[e]
C98	F300W, F450W, F606W, F814W, KPNO J,H,K	empirical	used FLY99 catalog & photometry			yes
C99	F300W, F450W, F606W, F814W, F110W, F160W	eigen-templates	SExtractor	F110W+F160W	F160W $\sim$ 27	no
LYF96	F300W, F450W, F606W, F814W	template-fitting (CWW80)	SExtractor	F814W	F814W$_{AB}$ $<$ 28	no
FLY99	F300W, F450W, F606W, F814W, KPNO J,H,K	template-fitting (CWW80)	SExtractor	F814W	F814W$_{AB}$ $<$ 28[g]	yes
LY99	F300W, F450W, F606W, F814W, KPNO J,H,K	template-fitting (CWW80 + 2 starbursts)	used FLY99 catalog & photometry			yes
SLY97	F300W, F450W, F606W, F814W	template-fitting (CWW80 + 2 very blue GISSEL SEDs)	PPP	F814W, F606W[h]	F814W$_{AB}$ $<$ 27[i]	no
GH96[f]	F300W, F450W, F606W, F814W	template-fitting (BC93)	SExtractor	F300W, F450W, F606W, F814W	F814W$_{ST}$ $<$ 28	no

[a] Abbreviations for catalogs are as follows: C98 = Connolly 1998; C99 = Connolly 1999a; LYF96 = Lanzetta, Yahil, & Fernandez-Soto 1996; FLY99 = Fernandez-Soto, Lanzetta, & Yahil 1999; LY99 = Lanzetta & Yahata 1999; SLY97 = Sawicki, Lin, & Yee 1997; GH96 = Gwyn & Hartwick 1996.

[b] BC93 = Bruzual & Charlot 1993; CWW80 = Coleman, Wu, & Weedman 1980; GISSEL SEDs = galaxy models of Pozzetti et al. (1996).

[c] SExtractor: Bertin & Arnouts 1996; PPP: Yee 1991.

[d] For reference, F814W$_{AB}-$F814W$_{ST}$ $= -0.819$.

[e] Object matches to the W96 catalog were done by the Lanzetta group.

[f] Gwyn & Hartwick (1996) used galaxy positions determined by Couch (1996); objects were detected in all four passbands and merged to form three "master" catalogs, one per WF chip.

[g] 121 objects in the shallower outer parts of the HDF mosaic (including the external borders of the WF chips and the PC chip) have a brighter limiting magnitude, F814W$_{AB}$ = 26.

[h] Object-finding in SLY97 was done in both F814W and F606W; results were edited by eye and combined into a single catalog.

[i] SLY98's F814W$_{AB}$ completeness limit is 28.0, but since faint objects were often not detected in all four passbands, analysis was confined to objects with F814W$_{AB}$ $\leq$ 27.0.

al. (1997), require a large sample of "calibration" galaxies for which multi-band photometry and spectroscopic redshifts both exist. The data from these galaxies are used to determine the best combination of magnitudes and colors to reproduce the known spectroscopic redshifts. Once this dependence of redshift on magnitudes and colors is established, multi-band photometry of target galaxies measured through the same set of filters can be used to estimate the redshifts of those galaxies.

The primary advantage of this technique is that it is based entirely on actual data. This is, however, also its primary limitation: the technique is only truly reliable for galaxies having SEDs of the same form as those of the calibrators and for redshifts at which spectroscopic redshifts are available. Beyond these limits, extrapolations must be made. It is crucial, therefore, to have a calibration sample that is fully representative of the galaxies and redshifts for which photometric redshifts are desired.

Template-fitting techniques have been implemented by several groups: e.g., GH96, SLY97, FLY99. Template SEDs are derived either from galaxy evolution models, such as those of Bruzual & Charlot (1993), or from actual galaxy spectra, such as those of Coleman, Wu, & Weedman (1980), for all galaxy types over the redshift range of interest. In some cases, e.g., SLY97, empirical SEDs are supplemented with model SEDs where empirical SEDs are limited or unavailable (e.g., for starbursts or in the far UV). Multi-band photometry of the target galaxies is converted into a coarse SED, which is then compared to the template SEDs. The best-fitting template SED (e.g., from χ-squared minimization) then yields the redshift of each target galaxy.

The primary advantage of this technique is that it is simple and requires no spectroscopic redshifts (except for comparison purposes). In addition, the use of model galaxy templates allows extension of photometric redshift estimates beyond the limits of spectroscopic redshifts, since the models can be carried out to whatever redshift is desired. The obvious drawback, of course, is that the models may not accurately represent the real world: The template SEDs are usually based on *local* galaxies; high redshift galaxy SEDs may be quite different. The choice of templates is also crucial. Even if high redshift galaxies have SEDs similar to those of local galaxies, using the SEDs for only a limited number of galaxy spectral types, e.g., four as in FLY99, may result in misleading trends when those SEDs do not cover a wide enough range of galaxy types. For example, FLY99 consistently underestimates the photometric redshifts of galaxies between $z \sim 1.5$ - 4 when compared to GH96, SLY97, and Connolly (1998, hereafter, C98). As can be seen in Figure 4–1, the addition of two starburst SEDs dramatically improves agreement with other photometric redshift estimates.

Ideally, one would like to find a method that combines the best of both techniques. A few groups have begun to explore such "hybrid" methods (Connolly 1999b, Mobasher & Mazzei 1999 [photo-z workshop]). In particular, Connolly 1999b has developed a method in which the photometric data of objects with spectroscopic redshift determinations are used to create a set of "eigen-template" SEDs directly from the galaxies themselves. These templates are found using principal component analysis and essentially represent different stellar populations. Real galaxy SEDs are then assumed to be linear combinations of the eigen-templates. The SEDs of target galaxies are compared to these eigen-templates to determine the best-matching combination of eigen-templates and redshift.

The advantage of this method is that it uses real data to develop the set of eigen-templates to which the high redshift galaxy SEDs are compared. The use of eigen-templates avoids the assumption that high redshift objects have the same SEDs as local galaxies. Any linear combination of the eigen-templates is allowed, not just those combinations that are reproduced locally. It will be exciting to follow the development of these hybrid photometric redshift techniques as they mature. As this is still a new technique, however, the rest of this chapter will focus on the former two techniques.

2. Limitations and Potential Pitfalls of Photometric Redshifts

Before beginning the comparison between various photometric redshift catalogs, it is important to understand the limitations and potential pitfalls of photometric redshifts. A few of these issues have already been addressed in the previous section.

One of the primary limitations of photometric redshifts is their dependence on some sort of calibration sample: either spectroscopic calibrators, as is needed by empirical methods, or template SEDs for template-fitting methods. Empirical-fitting methods rely on the assumption that the color-magnitude-redshift relation derived for the spectroscopic calibrators is valid for all galaxies. Template-fitting methods work on the basis that the template SEDs, created from some set of (usually local) calibration galaxies, are representative of the SEDs of target galaxies or that galaxy evolution models, also created primarily based on local galaxies, are valid for all galaxies at all redshifts. Unfortunately, it is unclear whether either of these assumptions is necessarily valid. The alternative, however, is to have no constraints whatsoever on the appearance of high redshift galaxies, an even less appealing option to consider. We will continue, therefore, as others have, on the assumption (and hope?) that the spectroscopic calibrators and template SEDs being used in photometric redshift estimates are fully representative of the galaxy population at all redshifts. The overall agreement between photometric and spectroscopic redshifts (to be shown later) seems to indicate that this assumption is probably not unreasonable.

Another limitation shared by both methods of photometric redshift determination is the dearth of comparison spectroscopic redshifts between $1.2 < z < 2.2$. In this redshift range, a lack of strong spectral features at optical wavelengths makes it difficult to determine spectroscopic redshifts: at $z \sim 1$, the 4000 Å break shifts out of the optical passbands; the 912 Å break, however, does not shift into the U-band until $z \sim 2.2$. Inclusion of near-infrared observations, however, can ease this difficulty by following the 4000 Å break beyond optical wavelengths.

Because photometric redshifts are often based on just two or three colors, situations will arise when two very different redshifts may be consistent with the colors of an object. For example, a red object may be nearby and intrinsically red or at high redshift and apparently red due to the shift of the Lyman break into the bluer band. An example of such degeneracies can be seen in Figure 4–2 which shows a comparison of photometric redshifts from SLY97, which use only the four optical HST bands, to those of C98, which include near-infrared data and should, therefore, be better able to break the color degeneracies. The colors of the symbols are coded to the observed (F606W-F814W) (i.e., $(v - i)$) color. Redshifts at which degeneracies occur are evident: the bluest objects may be objects at $z \sim 0 - 0.5$ or $z \sim 1.5 - 4$; degeneracies for redder objects may occur between $z \sim 0.5 - 1$ and $z \sim 3.5 - 4.5$.

Two techniques may be used to help break these color degeneracies. The first method, the Bayesian technique (e.g., Benítez 1998), uses additional information, such as luminosity or size, to estimate the probability that the chosen photometric redshift is valid. The symbol sizes in Figure 4–2 scale with the total apparent magnitude of the objects in the

F814W band (larger symbols indicate brighter magnitudes). In cases where there is a disagreement between SLY97 and C98, the magnitude of the objects can sometimes be used to indicate which of the two redshift estimates is more probable.

This leads us to the second means of breaking color degeneracies: the inclusion of near-infrared (IR) photometry. As mentioned earlier, SLY97 use only the four HST optical passbands (F300W, F450W, F606W, F814W) to determine photometric redshifts, while C98 uses the same four optical passbands in combination with three ground-based near-infrared passbands (KPNO JHK). This allows C98 follow the 4000 Å break beyond the optical wavelengths and, therefore, avoid mistaking apparently red high redshift objects from intrinsically red low redshift objects. This improvement is shown in Figure 4–3, which compares two methods that both include near-infrared data in their photometric redshift estimates. Since 7-band (optical + near-infrared) photometric redshifts from the SLY97 group were not available at the time for comparison, this figure shows a comparison of the 7-band FLY99 versus C98 photometric redshifts. Note that this is a reproduction of Figure 4–1a with color and magnitude information added. The decrease in the number of "confused" redshifts, especially between $1.5 \lesssim z \lesssim 2.5$, using 7 bands is evident even with the underestimated redshifts of FLY99 at $1.5 \lesssim z \lesssim 4$ (to be discussed later).

Another major concern with photometric redshifts is the determination of errors. Errors in comparison to spectroscopic redshifts have certainly been calculated. The shape of the redshift error distribution function, however, still needs to be derived. Sources of errors (e.g., random measurement errors, systematic errors due to intrinsic dispersions in the SEDs of galaxies or other unknown sources) need to be determined and quantified. In addition, the dependence of errors on galaxy parameters, such as color, luminosity, redshift, or morphology, should be characterized. Ideally, these errors and their distributions and dependencies should be incorporated in the actual determination of the redshift of objects, rather than finding simply the "best-fitting" redshift.

All of these limitations need to be investigated in order to more thoroughly understand the behaviour of photometric redshifts and the conditions under which they are most effective. Such a detailed investigation, however, is beyond the scope of this dissertation and will be left to the photometric redshift experts for further study.

3. Catalog Matching and Redshift Comparisons

The task of matching the various photometric redshift catalogs for the HDF proved to be more complicated than originally anticipated. Each group used a different object identification procedure and different object deblending criteria (i.e., the criteria used to determine whether a given multiple condensation should be treated as one or more objects). Not only are slightly different positions found for each object by the various object identification procedures, but the deblending criteria occasionally found different divisions of multiple-condensation objects. In addition, object detection was performed using images from different combinations of passbands by each group. These last two effects sometimes resulted in drastically different positions being determined for the same "object" by different groups. Lanzetta et al. are the only group to identify their objects with those in the Williams et al. (1996, hereafter, W96) HDF catalog. This match was later checked and 65 objects which were mis-identified were corrected (see Section 3.2). All other groups were matched to W96 primarily on the basis of object positions and apparent magnitudes, though an occasional "by eye" judgment was necessary.

3.1. 4-band Photometric Redshifts versus C98 (7-band)

The initial match was made between C98, GH96, LYF96, and SLY97. The match between the latter three catalogs was done by Sawicki et al. and is available on Sawicki's website (Sawicki 1997). All four catalogs were matched to the W96 HDF catalog as described below.

GH96, LYF96, and SLY97 are all based on 4-band photometry using the four HST filters, F300W, F450W, F606W, and F814W. C98 used the photometry presented in FLY99, which used the four HST filters supplemented with ground-based JHK photometry from KPNO (Dickinson 1999). (FLY99 photometric redshifts were included in the comparison at a later stage.) Since the FLY99 catalog included identification with objects in W96 using the W96 IDs, the match between C98 and W96 was simply by W96 ID. Once objects were matched between C98 and W96, the GH96, SLY97, and LYF96 catalogs were matched to the previous two catalogs using the object's (x, y)-position on the individual chips with a matching radius of 5 pixels. Figure 4–4 shows the comparison of each of these catalogs to spectroscopic redshifts obtained by Cohen et al. (1996), Steidel et al. (1996), and Lowenthal et al. (1997).

The overall agreement of the photometric and spectroscopic redshifts is remarkably good, especially at $z \lesssim 1$, where the scatter relative to spectroscopic redshifts is less than 0.2 for all four catalogs. C98 clearly agrees most closely with spectroscopic redshifts with an overall scatter of $\sigma_{rms} = 0.19$, though SLY97 runs a close second with $\sigma_{rms} = 0.20$). The overall scatter and the number of mis-identified redshifts in LYF96 and GH96 are both larger ($\sigma_{rms} = 0.28$ and $\sigma_{rms} = 0.23$, respectively). In addition, LYF96 appears to underestimate redshifts between $2 \lesssim z \lesssim 4$. This discrepancy will be discussed in more detail later in this section. Though the overall scatter in SLY97 is comparable to that seen in C98, SLY97 appears to have difficulty estimating redshifts around $z \sim 1$. It is not too surprising that C98 agrees most closely with spectroscopic redshifts. As mentioned earlier, inclusion of the near-IR bands lessens the chances of confusing high redshift, Lyman-break objects with low redshift, intrinsically red objects. In addition, C98 uses empirical-fitting methods, which are directly calibrated on spectroscopic redshifts; better agreement is, therefore, expected. One might note, however, that C98 appears to slightly underestimate redshifts around $0.5 \lesssim z \lesssim 1$. Connolly (personal communication) believes that this underestimate may be due to a poor match of the template galaxy colors to real galaxy colors at ultraviolet wavelengths. Nonetheless, the C98 redshifts still appear to be the best match to spectroscopic redshifts; this catalog is, therefore, chosen as the reference catalog for a comparison of the four photometric redshift techniques as applied to HDF galaxies.

Figure 4–5 shows the comparison of photometric redshifts from LYF96, SLY97, and GH96 to C98. Once again, the overall agreement is quite reasonable. As might be expected from the previous figure, SLY97 and C98 agree quite well *(upper right)*. LYF96 and C98 correlate well with each other, but a large systematic offset is again obvious between $1.5 \lesssim z \lesssim 4$ (see below). GH96 and C98 agree below $z \sim 0.8$ and beyond $z \sim 2$, but a large scatter exists in between. Between $1 \lesssim z \lesssim 2.2$, the advantage of 7-band photometric redshifts is quite evident: a large scatter is seen in all of the 4-band catalogs. In the end, because of the limitations of four-band photometric redshifts, none of the four-band photometric redshift catalogs was used.

As mentioned earlier, LYF96 appear to systematically underestimate redshifts between $1.5 \lesssim z \lesssim 4$ by as much as 1. This effect persists in FLY99 redshifts, which used the same templates as LYF96. Benítez (1998) showed, however, that augmenting the template set of FLY99 with two starburst SEDs was sufficient to remove this discrepancy. Lanzetta and his collaborators have since re-fit their photometric redshifts including two starburst models. Their agreement with spectroscopic redshifts as well as with other photometric redshift catalogs has improved significantly in this most recent iteration (LY99).

3.2. Photometric Redshifts with Near-Infrared Photometry

The next stage of catalog matching was between two 7-band catalogs: C98 and FLY99. Both of these catalogs use the photometry of FLY99, which included photometry using the four HST filters plus near infrared photometry through the JHK filters taken at KPNO. As was shown in Figure 4–3, not only is the scatter tighter, the number of objects for which the two catalogs strongly disagree has declined significantly in comparison to the 4-band catalogs. The underestimated redshifts between $1.5 \lesssim z \lesssim 4$ in FLY99 are still present, as their set of template SEDs had not yet been augmented. As mentioned earlier, C98 redshifts between $0.5 < z < 1$ also appear to be slightly too small (up to 0.5 in redshift) due to a poor match of the template galaxy colors to real galaxy colors at ultraviolet wavelengths (Connolly, personal communication).

Two updated, but as yet unpublished, catalogs were later kindly provided by N. Yahata (collaborator of the Lanzetta et al. group) and Connolly. The final comparison was between these two catalogs.

The new catalog from Lanzetta, Yahata, and collaborators (hereafter, LY99) adds two starburst templates to the original set of four, in order to improve their redshift estimates at $1.5 \lesssim z \lesssim 4$. The object catalog and photometry were not changed (i.e., they are the same as in FLY99). As mentioned earlier, the match between the Lanzetta et al. object catalog and the W96 catalog was checked, and 65 objects were found to be questionable matches. These objects were independently checked by me and by Alberto Fernández-Soto with the following conclusions. 54 objects were cases in which one redshift was given for a multi-component system (i.e., a "parent" in W96), but the system was then identified as one of the sub-components (i.e., a "daughter" in W96). In all of these cases, the W96 ID is re-assigned to that of the parent object. Deblending differences explain seven of the remaining mis-matches. Two objects are located in the overlap region between chips 3 and 4; in both cases, the object lay more fully on chip 3 but was identified by FLY99 with its appearance on chip 4. One object in FLY99 is unidentified in W96. One object's positions in the two catalogs do not agree very well, but no alternative match was obvious. One object was noted by Fernández-Soto (private communication) as a "particular case" in which two deblending alternatives are possible, and both are reasonably consistent with later spectroscopic observations. In the process of re-matching, the agreement between the F814W$_{AB}$ magnitudes calculated by FLY99 and W96 for these objects also improves (Figure 4–6). The remaining mismatches (in the magnitude comparison) are mostly sub-components of multiple component objects for which the deblending of the objects may account for the differences in magnitude. Without the actual object masks from the various groups, however, it is difficult to verify this hypothesis.

The new Connolly catalog (hereafter, C99) differed from the original catalog in several ways: (1) 6 passbands were used: the four WFPC-2 passbands (F300W, F450W, F606W, F814W) + two NICMOS passbands (F110W, F160W). (2) Object detection was done in the combined F110W+F160W image using SExtractor (Bertin & Arnouts 1996). (3) The photometry was re-done in all 6 passbands using object masks created by SExtractor based on the F110W+F160W image. No requirement was made that an object actually be detected in any of the optical passbands. C99 uses fluxes instead of magnitudes and, therefore, can handle negative fluxes. (4) Photometric redshifts were calculated using their new hybrid eigen-template method (Connolly 1999b). This catalog contained 1291 objects with redshifts.

Connolly did not match his latest catalog to W96, so the match was done in the following manner. A large initial tolerance of $0''.6$ (15 pixels) was used, resulting in a total of 1707 matches (the "preliminary" matched catalog). The following criteria were used to resolve multiple matches:

1. If a "parent" and a "daughter" from W96 were both matched to one object in C99, the catalog was checked to see if any of the other "daughters" had been matched to another object. If so, then the C99 object was given the W96 ID of the "daughter;" if not, then the W96 ID of the "parent" was assigned to the C99 object. There were a few exceptions in which a comparison of the C99 and W96 magnitudes indicated that a daughter was a better match than the parent even though the other daughter(s) may not have been detected by C99.

2. If two "parent" objects in W96 were matched to one object in C99, the W96 ID of the object closest in magnitude and separation was assigned. For the handful of objects for which these criteria disagreed, the galaxies were inspected by eye to determine the best match.

3. Near the edges of the WFPC-2 chips, the images become quite noisy. Objects lying in these regions (roughly 30-50 pixels from the edge of the images) were thrown out.

4. No objects in the PC1 chip were included in the catalog.

An initial "blind" pass through the preliminary catalog using the first two criteria resulted in 190 matches being deleted. These were mis-matches of two types: (1) the daughters of a W96 parent object are all present in the preliminary catalog, so the mis-match to the parent is deleted; or (2) two parent W96 objects are matched to one C99 object, but, based on its position and magnitude, one of the two W96 objects is obviously a mis-match. Any ambiguous cases were left to the second pass, in which the images were individually examined to determine the best match. In this pass, the following objects were deleted: 79 PC1 objects (criterion 4), 44 matches in the noisy edges of the images (criterion 3), and 187 parent-daughter and parent-parent matches (criteria 1 & 2). 81 objects in C99 had no match in W96. After these two passes, a matched catalog of 1126 objects remained. Five pairs of C99 objects were matched to single objects in W96. In all five cases, one object was clearly a mis-match (by both position and magnitude) and was deleted. 43 objects in C99 are daughters without siblings. These are the cases mentioned in criterion 1, in which the daughter position and magnitude matched more closely than that of the parent. In all but six cases, the match held; three of the remaining cases turned out to be better matched to a "grand-daughter," while the other three were ambiguous and were deleted. Postage stamps of these 1118 objects were created and gone through by eye for one final pass. Obvious stars, diffraction spikes, and objects near stars, diffraction spikes, or the noisy edges of the images (39 objects) were deleted, leaving a final catalog of 1079 objects.

As shown in Figures 4–7 and 4–8, both new catalogs are improvements over their respective older versions when compared to spectroscopic redshifts. The comparison *between* the two new catalogs, however, shows a poorer agreement (Figure 4–9). Although LY99 no longer underestimates redshifts in the interval $1.5 \lesssim z \lesssim 4$, the scatter and the number of disagreements between the two catalogs is quite large. Much of both of these effects, however, appear to be dominated by faint (F814W$_{AB} \lesssim 26$) objects, denoted by the smallest (red and orange) circles. Most of our results (Chapter 6) will be based on a pruned sample of objects cut at roughly this magnitude, so these discrepancies for the faintest objects are not important. Connolly (private communication) believes that the disagreement is rooted in the differences in the photometry of the two groups. At this writing, this issue has not yet been resolved, but it has been left in the capable hands of the photometric redshift experts. For the purposes of this thesis, the photometric redshifts from C99 will be used as the primary photometric redshift catalog, as its agreement with spectroscopic reshifts is marginally the best.

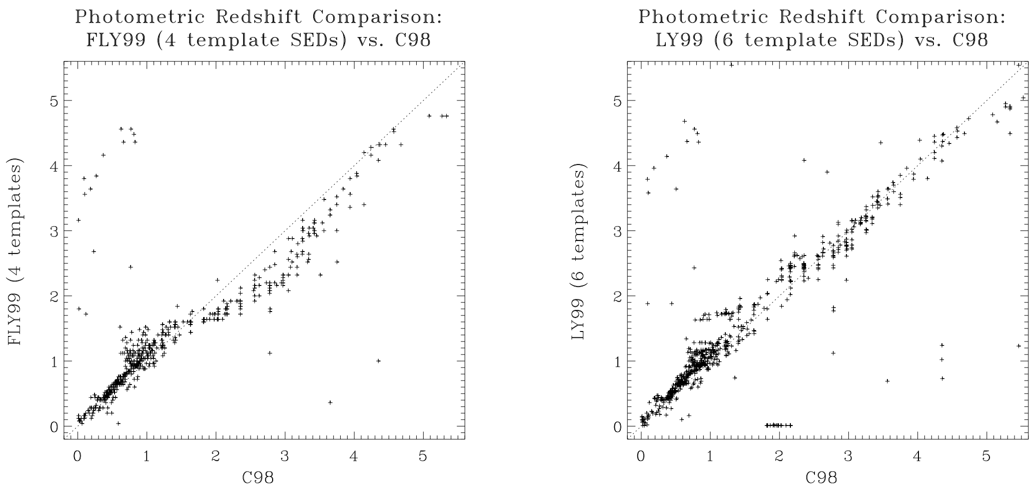

Fig. 4–1.— The influence of the template SED selection on photometric redshift estimates. This figure illustrates the importance of having a complete, i.e., fully representative, set of template SEDs when determining photometric redshifts. FLY99 *(left)* use only 4 template SEDs for their photometric redshifts estimates. A systematic underestimate of redshifts in the range $1.5 \lesssim z \lesssim 4$ is evident. With the inclusion of 2 starburst SEDs in LY99 *(right)*, the agreement with C98 improves dramatically.

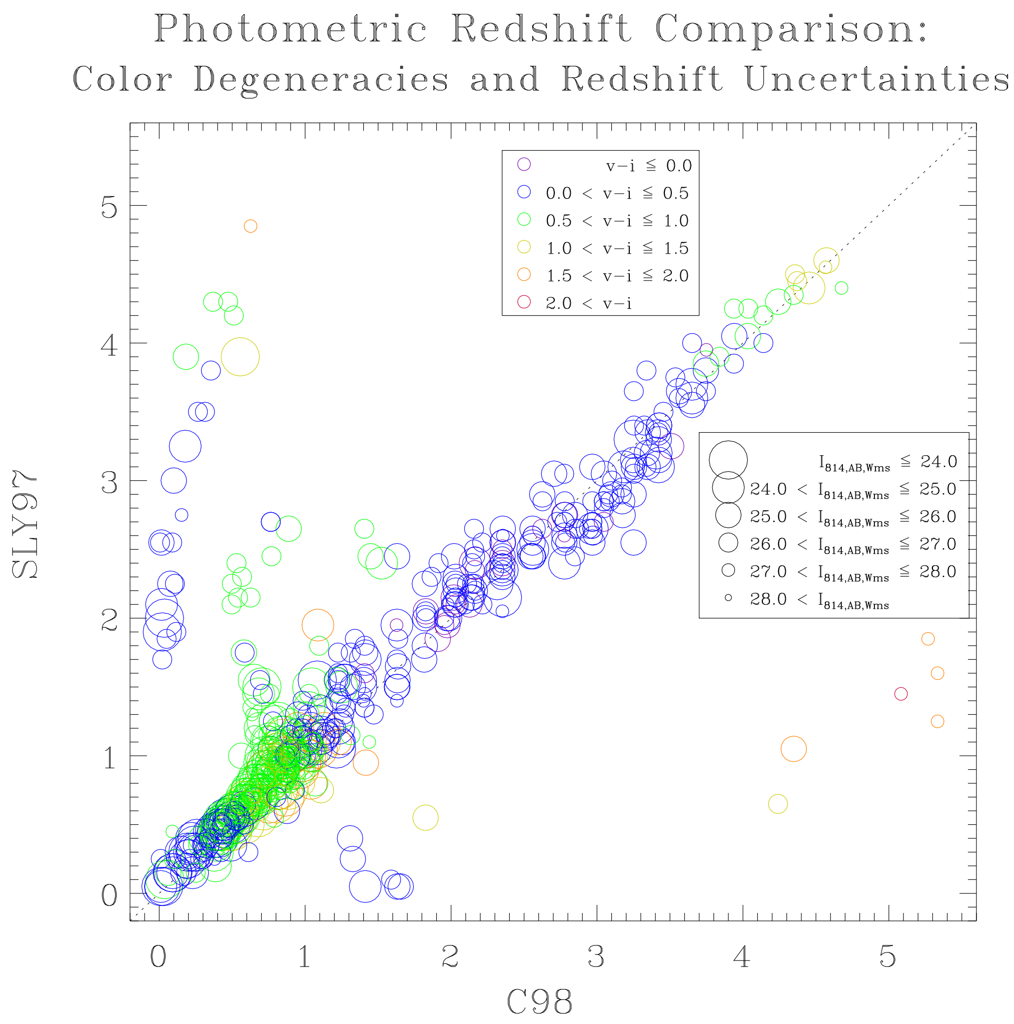

Fig. 4–2.— Color degeneracies and redshift uncertainties. With multi-band photometric redshift estimates, the colors of an object may found to be consistent with more than one redshift. For example, a red object may be nearby and intrinsically red or at high redshift but apparently red due to the shift of the Lyman break into the bluer band. In such cases of "color degeneracy," the redshift assigned to an object may be incorrect. Presented here is a comparison of photometric redshifts from SLY97, which use only the four optical HST bands, to those of C98, which include near-infrared data from KPNO and should, therefore, be better able to break the color degeneracies. Some of the redshift ranges for which color degeneracies are important are illustrated in this figure: the bluest objects (purple and blue circles) may be objects at $z \sim 0 - 0.5$ or $z \sim 1.5 - 4$; degeneracies for redder objects may occur between $z \sim 0.5 - 1$ and $z \sim 3.5 - 4.5$.

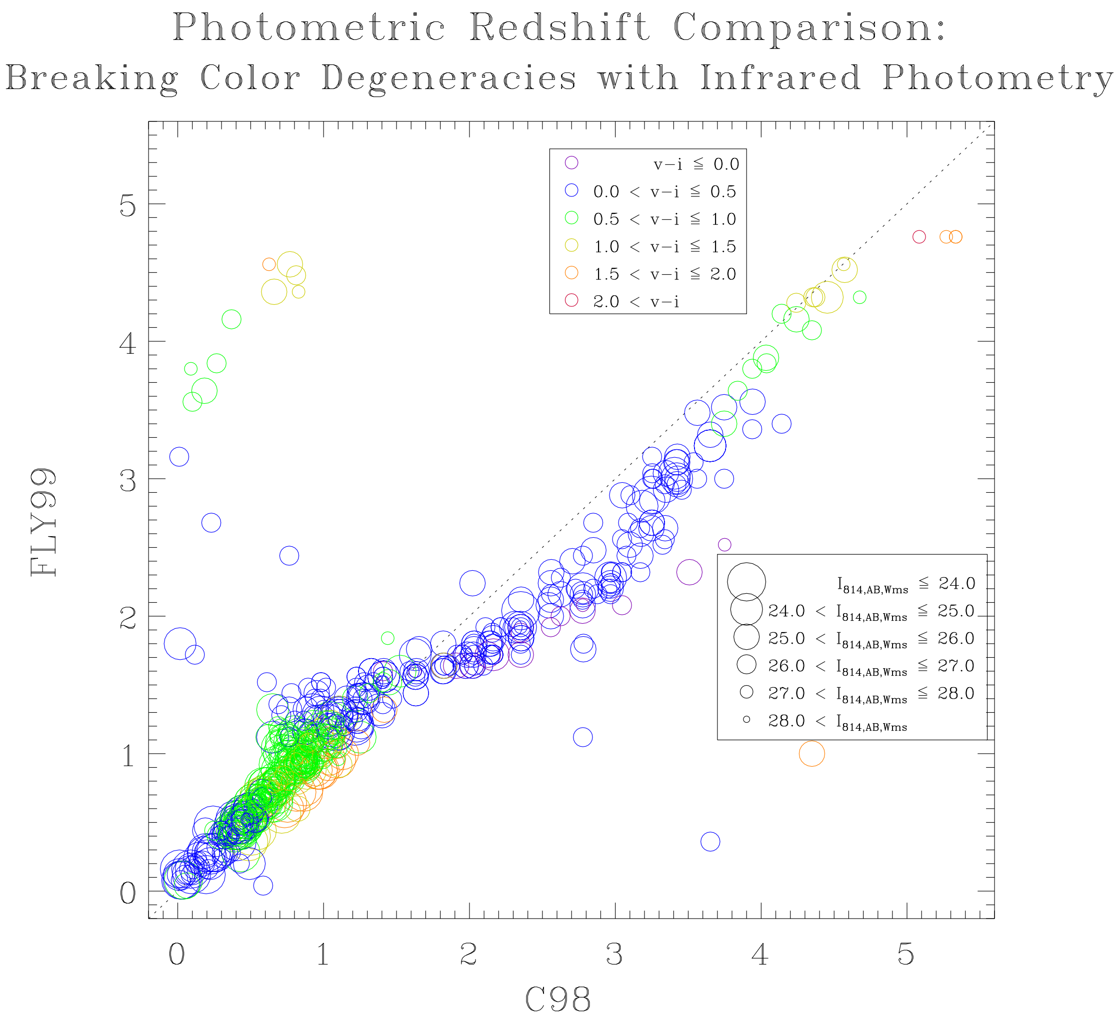

Fig. 4–3.— Breaking color degeneracies with infrared photometry. With the inclusion of near-infrared photometry in FLY99, the number of mis-identified redshifts, especially between $1.5 \lesssim z \lesssim 4$, has decreased significantly. A 7-band (optical + near-infrared) photometric redshift catalog from the SLY97 group was, unfortunately, not available at the time of comparison, so a direct comparison between this figure and Figure 4–2 is not possible.

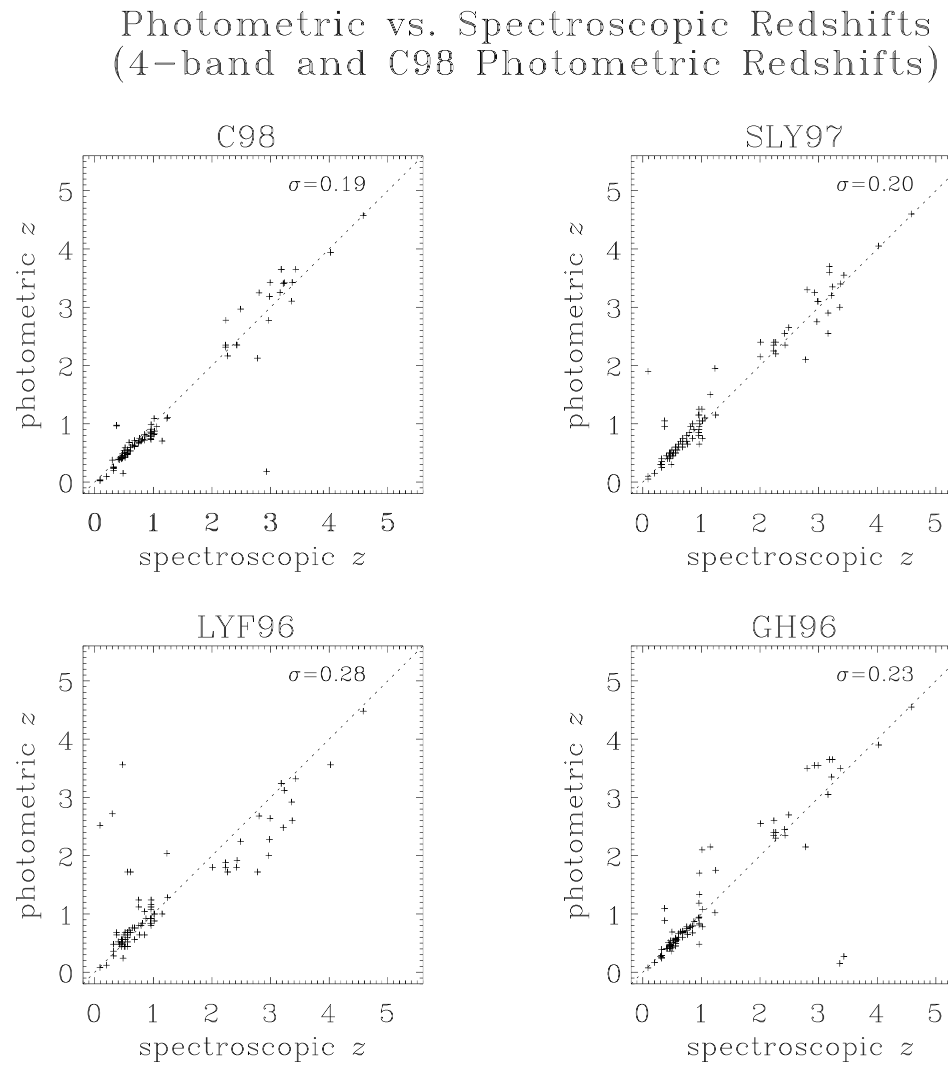

Fig. 4–4.— A comparison of photometric redshift estimates from C98, LFY96, SLY97, and GH96 to spectroscopic redshift determinations. The overall agreement of all four photometric catalogs with spectroscopic redshifts is quite reasonable. C98 and SLY97 agree most closely with spectroscopic redshifts, though SLY97 appears to have some difficulty estimating redshifts around $z \sim 1$. LYF96 and GH96 both show significantly more scatter and a larger number of mis-identified redshifts.

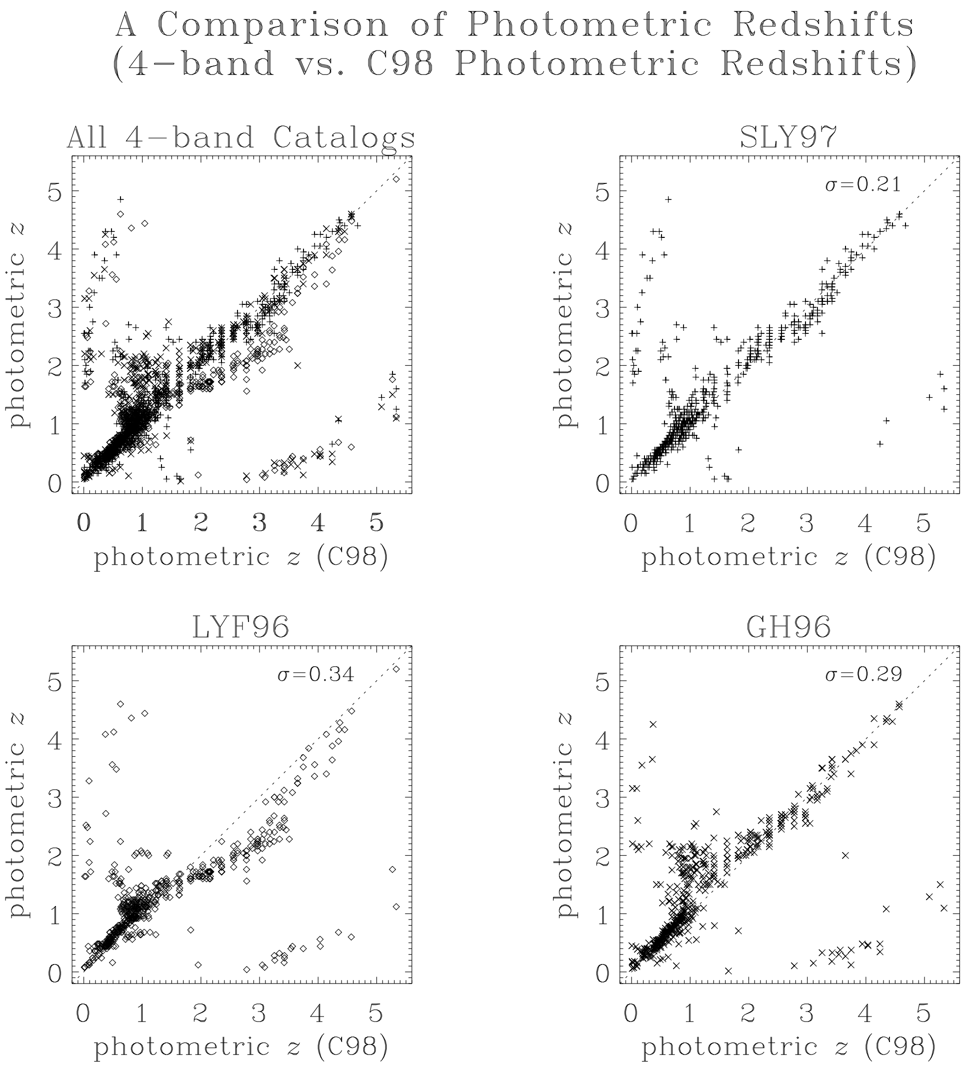

Fig. 4–5.— A comparison of 4-band photometric redshift estimates from FLY99, SLY97, and GH96 to C98. The agreement between SLY97 and C98 is quite good, as might be expected from the close agreement of both of these catalogs to spectroscopic redshifts, as shown in Figure 4–5. A strong correlation exists between LYF96 and C98; however, a systematic offset between the two catalogs is also evident. As discussed in the text, this offset is primarily due to an insufficient template set in LYF96. GH96 agrees reasonably well with C98 below $z \sim 0.8$ and beyond $z \sim 2$; a large scatter exists in between.

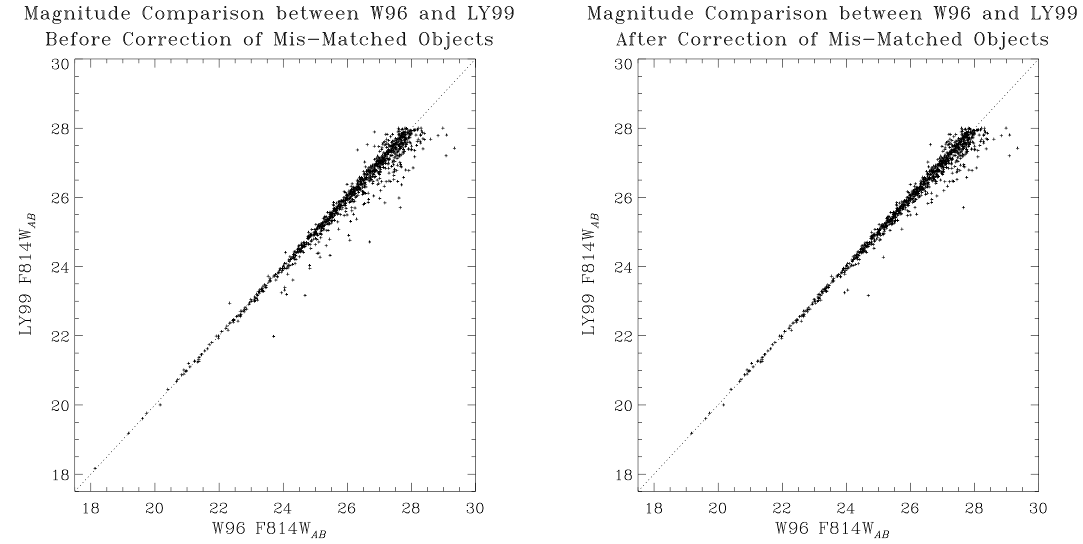

Fig. 4–6.— Magnitude comparison between FLY99 and W96 before and after correcting mis-matches. The number of discrepant magnitudes between FLY99 and W96 decreases after the mis-matches have been corrected. The remaining outliers in this magnitude comparison are mostly sub-components of multiple component objects for which the deblending of the objects may account for the differences in magnitude. Without the actual object masks from the various groups, however, it is difficult to verify this hypothesis.

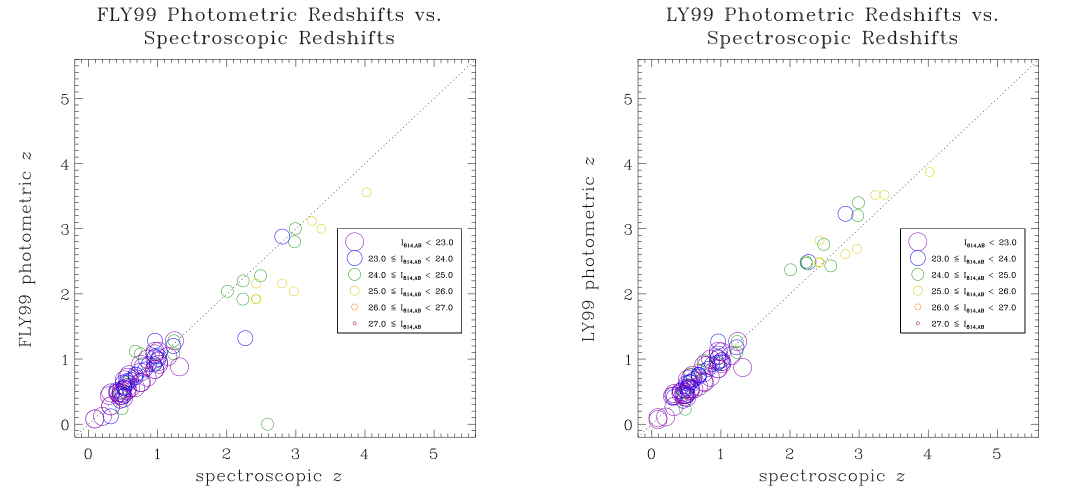

Fig. 4–7.— A comparison of FLY99 and LY99 photometric redshifts with spectroscopic redshift. Clearly the addition of the two starburst templates in LY99 improves agreement with spectroscopic redshift, especially between $2 \lesssim z \lesssim 4$.

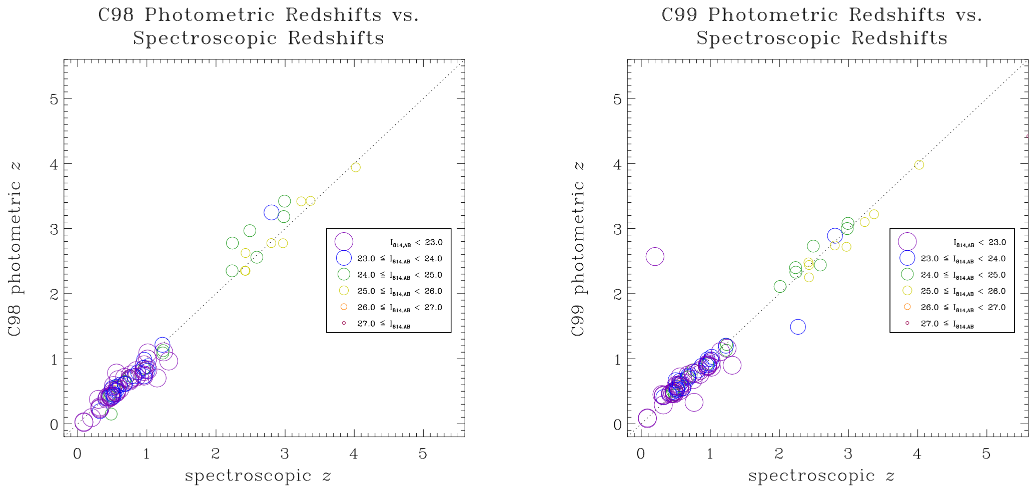

Fig. 4–8.— A comparison of C98 and C99 photometric redshifts with spectroscopic redshift. Inclusion of the HDF-NICMOS data in combination with implementation of the new hybrid eigen-template method of photometric redshifts improves agreement with spectroscopic redshifts.

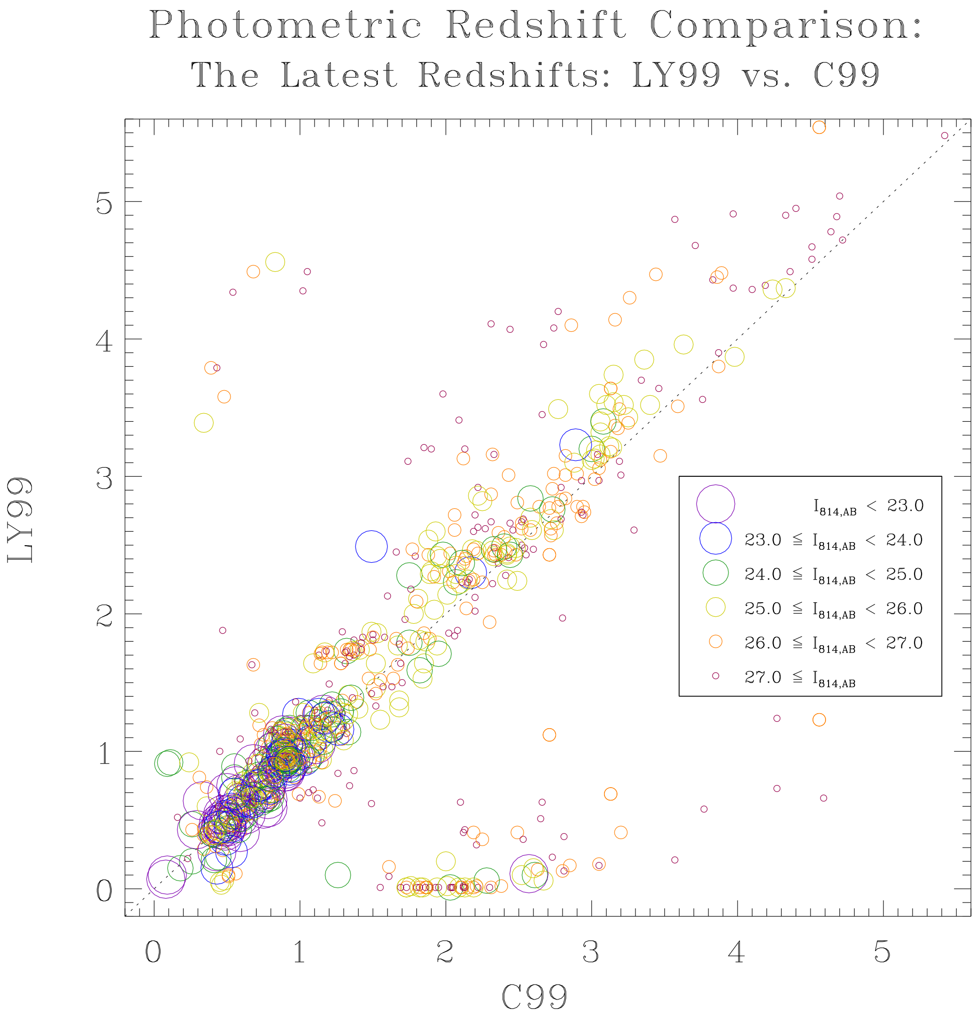

Fig. 4–9.— A comparison of the "best" photometric redshifts currently available from LY99 and C99. Figures 4–7 and 4–8 indicate that both of these latest catalogs agree very well with spectroscopic redshifts. The agreement *between* the two catalogs, however, is less convincing, possibly due to differences in the photometry of the two groups (Connolly, private communication). The largest scatter is seen below F814W$_{AB}$ $\sim$ 26, denoted by the smallest (red and orange) circles. As most of our results are based on a sample of objects pruned at roughly this magnitude, these discrepancies should have little effect on our conclusions.

Chapter 5

Calibration of the Peculiarity Indices Using Local Galaxies

The local sample (the Frei et al. 1996 catalog [hereafter, the Frei catalog] and the four interacting galaxies from Hibbard and van Gorkom 1996 [hereafter, HvG]) is used to characterize the behaviour of the peculiarity indices. For the rest of this work, we will focus on the rotational asymmetry, A_W, and the concentration index, C_W.

1. Local vs. High Redshift Object Mask Parameters

As described in the object mask creation section of Chapter 3, the object mask parameters for the local sample are different from those for the high redshift sample: the "high-redshift" object mask parameters are μ_{det}=22.75 B-magnitudes per square arcsecond with a growing factor of 5, while the "local" object mask parameters are μ_{det}=25.0 B-magnitudes per square arcsecond with a growing factor of 1 (i.e., no growing). Figure 5–1 shows a comparison of A_W and C_W for local objects using the two pairs of object mask parameters. Overall the agreement is reasonable, but several sources of discrepancy appear in this comparison.

One of the primary reasons for modifying the object mask parameters for the local sample is the inability to calculate a background correction when the object mask grows to fill the entire image of the galaxy. In the local sample, we do not have the luxury that is available with the HDF images to simply increase the size of the image to ensure a sufficient number of sky pixels. If no background pixels are available, no background correction can be made, and the asymmetry value for these objects is over-estimated. Four of the six cases, shown in the left-hand panel of Figure 5–1, in which A_W is significantly larger using the high redshift object mask parameters than using the local object mask parameters are cases in which no background correction could be made. C_W is less seriously affected by the filling of the object mask. Only one of the discrepant points in the right-hand panel of Figure 5–1 is explained by this phenomenon.

A second cause of discrepancy is the presence of the peculiar brightening of the sky background found in several of the Lowell images, as mentioned in Chapter 3. The local μ_{det} is low enough that a significant portion of the brightened sky is sometimes included in the galaxy contour. Use of the high redshift mask parameters avoids this problem because the brighter μ_{det} finds a surface brightness contour that is unaffected by the brightened sky. When this region is grown, only a small portion of the "bad" sky background ends up being included within the galaxy contour. Using the "local" object mask parameters, therefore, results in a higher asymmetry and lower concentration for these objects than using the high redshift mask parameters. Five of the 6 strongly discrepant points below the 1:1 line in the A_W comparison are a result of bizarre background characteristics. As expected, a much higher asymmetry is calculated when using the local object mask parameters where the brightened background is inadvertently included in the object detection area. Once again, C_W appears to be less affected by this phenomenon: only the two objects above the 1:1 line in the C_W comparison are severely affected. As expected, the concentration calculated using the local object parameters (where the sky in included) is lower than that calculated using the high redshift object parameters. These are two cases in which the brightened sky is particularly severe. C_W appears to be less sensitive to milder sky eccentricities.

The high redshift object mask parameters are less satisfactory, however, when dealing with low surface brightness objects. Because of the high μ_{det}, only a portion of these galaxies is detected. Even when the mask is grown, the full galaxy is often still not encompassed. Interesting structure in the outer parts of the galaxy may be missed, and a slightly lower asymmetry is found. The least discrepant point of the 6 outliers below the 1:1 line in the A_W comparison is an example of an LSB galaxy for which the high redshift μ_{det} resulted in an object mask that was not large enough to enclose all of that galaxy's light. This loss of light also results in a lower calculated concentration for these objects. Half of the most discrepant points below the 1:1 line in the C_W comparison are LSB galaxies.

The final few highly discrepant objects are cases in which the high redshift mask parameters detect spiral arms and HII regions of galaxies as separate objects. These pieces of the galaxies are then masked out and excluded from further calculations. Higher asymmetries, therefore, tend to be found in comparison with using the local mask parameters, where the spiral arms and HII regions are all found within the galaxy contour. Parts of the galaxy that would have balanced out comparable regions on the opposite side of the galaxy are now excluded from the calculation. Though there may have been some contrast in brightness between two opposite regions of the galaxy, this contrast, and therefore the asymmetry, is now even greater than it originally would have been. As with the low surface brightness objects, the concentration index is again found to be slightly low, since some of the outer light of the galaxy is no longer included in the concentration calculation.

Though it is important to understand these discrepancies, the peculiarity indices calculated for the majority of the local galaxies through both the local and high redshift object masks agree rather well. Since more difficulties appear for the local sample using the high redshift object masks, the local object masks were used to calculate the asymmetry and concentration index of the local sample. In Chapter 6, simulations of the local sample to a redshift of $z = 0.8$ will be presented, and, again, it will be shown that peculiarity indices calculated using the two pairs of object mask parameters agree well, and only a few outliers are found. The subsequent comparisons to observed high redshift objects whose peculiarity indices are calculated using the high redshift object mask parameters are, therefore, valid.

2. The A_W-C_W Relation for the Local Sample and a Comparison to A96b

Figure 5–2 shows the A_W-C_W relation for the local sample using the local object mask parameters. The plot is made in logarithmic coordinates for easier comparison with comparable figures in A96b to be presented later. Galaxy positions in the A_W-C_W plane are marked by the revised morphological type, T, from the *Handbuch der Physik* system used in the *Third Reference Catalogue of Bright Galaxies* (RC3) (de Vaucouleurs 1959, 1963; de Vaucouleurs et al. 1991). The color of the number groups these galaxies into three general morphological classes: E/S0 (T $\leq$ 0; red), Sabc (0 $<$ T $<$ 9; green), and

Sdm/Sm/Im/Peculiar/Merger (T $\geq$ 9; blue). The classes correspond to those used in A96b in order to enable a direct comparison of algorithms; as a result, late-types and peculiars are grouped together, something against which we generally recommend. However, truly peculiar objects (i.e., the HvG galaxies) are distinguished from late-types by plotting their NGC number rather than their morphological T-type.

The trend followed by the Hubble types in the A_W-C_W plane is clearly illustrated. Ellipticals are high concentration, very low asymmetry objects. For progressively later-type galaxies, C_W decreases, while A_W increases slightly. Peculiar galaxies appear to have a range of concentrations but distinctly higher asymmetries relative to the "normal" objects at those concentrations. In contrast, irregular galaxies (symbols "9"-"11") appear closer in the A_W-C_W plane to intermediate- to late-type spirals, with lower values of A_W than peculiars. We will see that, in simulations at high redshift, irregulars move even closer to normal spirals and further away from peculiars. Unfortunately, there are very few late-type objects in the Frei catalog, and a larger sample of local irregulars is badly needed. Nevertheless, the trends we see, even with these small numbers, appear plausible.

As noted earlier, the interacting galaxies from HvG, labelled by their NGC number in Figure 5–2, all have distinctly larger asymmetries than most of the Frei catalog galaxies. NGC 295 does not appear in this plot because the centroid found for the concentration index was found to lie between the two objects, while the pivot point for the asymmetry index was found to be on the brighter of the two galaxies. This is a problem that still needs to be investigated. Similar pairs of objects in the HDF were checked, however, and their centroids matched. NGC 7252 is the only HvG galaxy whose asymmetry is relatively low. This is expected, however, since this late-stage merger is dominated by a very bright symmetric core. The faint tidal features provide only a small contribution to the total flux. When compared to other objects of comparable concentrations (i.e., true ellipticals), NGC 7252 is notably more asymmetric. NGC 520 and NGC 2623 are two of the most asymmetric objects in this sample, while their concentrations are roughly comparable to those of typical spirals. Both of these results are consistent with their highly disrupted cores. Several spiral galaxies are also found to have asymmetries approaching those of the interacting galaxies. All of these objects show some form of peculiar morphology: structure indicating a possible recent interaction (e.g., NGC 5792), a warped disk (e.g., NGC 3079), or asymmetric spiral arms (e.g., NGC 4088). It is reassuring that the algorithm finds these objects to be moderately asymmetric as well.

A96b present the results of applying their A_A and C_A to the Lowell sub-sample of the Frei catalog. In Figure 5–3, the A-C values of the two pairs of algorithms are compared. The morphological T-types in the A_W-C_W plot have been replaced by symbols, though the color coding is still the same: E/S0 (T $\leq$ 0; red ellipses), Sabc (0 $<$ T $<$ 9; green spirals), Sdm/Sm/Im (9 $\leq$ T $\leq$ 11; blue asterisks). Peculiar/merger galaxies (T $\geq$ 90; blue "P"s, for future reference) do not appear in these plots, as A96b did not include the HvG galaxies in their local sample. The A_A-C_A plot is reproduced using the numbers given in Table 2 of A96b. Note that in their paper, A96b plot only galaxies with asymmetries larger than $\log_{10}(A_A)$ = -2.2, whereas we show all galaxies. This lower boundary is marked by the dotted line in the right-hand panel of Figure 5–3. Galaxies with negative asymmetries (due to a background correction that is larger than the actual galaxy asymmetry) are assigned an asymmetry of 0.001 ($\log_{10}(A_A)$ = -3.0).

From this comparison, one can see that A_W-C_W and A_A-C_A are qualitatively equivalent. The centers of the galaxies are generally well defined, with centroids that lie very close to the brightest point in the galaxy; hence, the difference in the pivot points determined by the two algorithms should be minimal. Measures of both concentration and asymmetry would be expected to be similar, since the basic principles behind the algorithms are the same. The separation between ellipticals and spirals in A_W-C_W is perhaps slightly clearer than in A_A-C_A, particularly in the asymmetry dimension. The minimization algorithm in A_W, which finds the centroid to sub-pixel accuracy, avoids finding high asymmetries for ellipticals due to poor centering of the pivot point within a pixel. A few spiral galaxies in A_A-C_A have unusually low asymmetry values. The images of all of these galaxies show the peculiar brightening background, discussed earlier in this chapter and in Chapter 3. For these objects, choosing a contiguous region in which to calculate the background correction to the asymmetry (as is done by A96b) may result in an over-correction of the asymmetry parameter. Using the average of several background corrections, each determined from randomly selected background pixels, minimizes the effect that global sky features may have on the final asymmetry value determined for an object. These two refinements in A_W result in a better separation of ellipticals and spirals in the asymmetry dimension. These differences notwithstanding, it is important to note that, in both algorithms, irregular galaxies share essentiall the same region of A-C space as spirals. This bolsters the argument that irregulars and peculiars should not be grouped into one category for evolutionary studies.

Because the primary focus of this work is on peculiar galaxies, plotting A and C on a linear scale more clearly differentiates peculiar from "normal" galaxies. Figure 5–4 shows the linear version of A_W-C_W shown in Figure 5–2. Except for occasional comparisons to A96b, all future plots of A_W-C_W will be in linear coordinates.

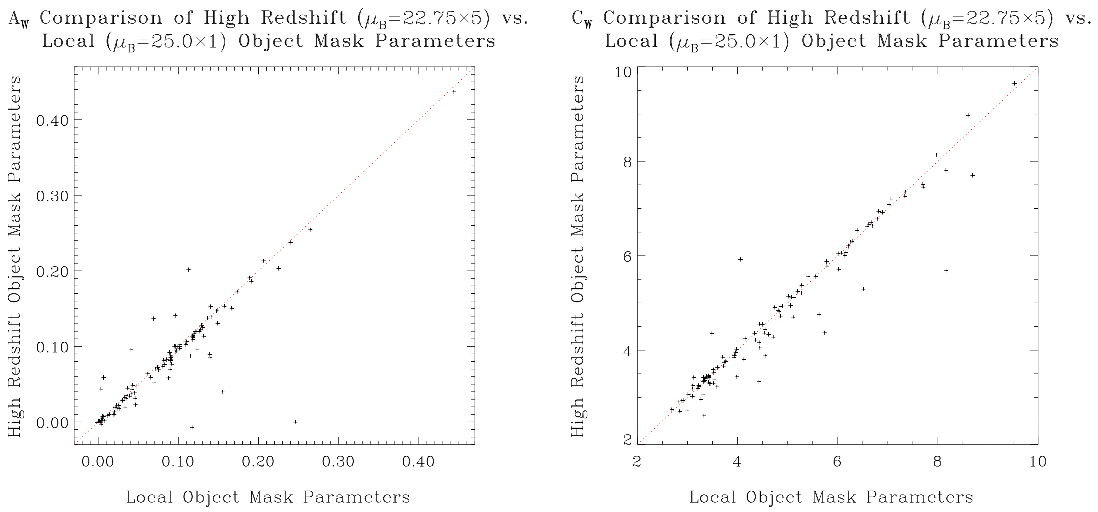

Fig. 5–1.— A comparison of A_W and C_W for the local sample calculated using the local vs. high redshift object mask parameters. The overall agreement is reasonably good. The causes of disagreements are discussed in the text.

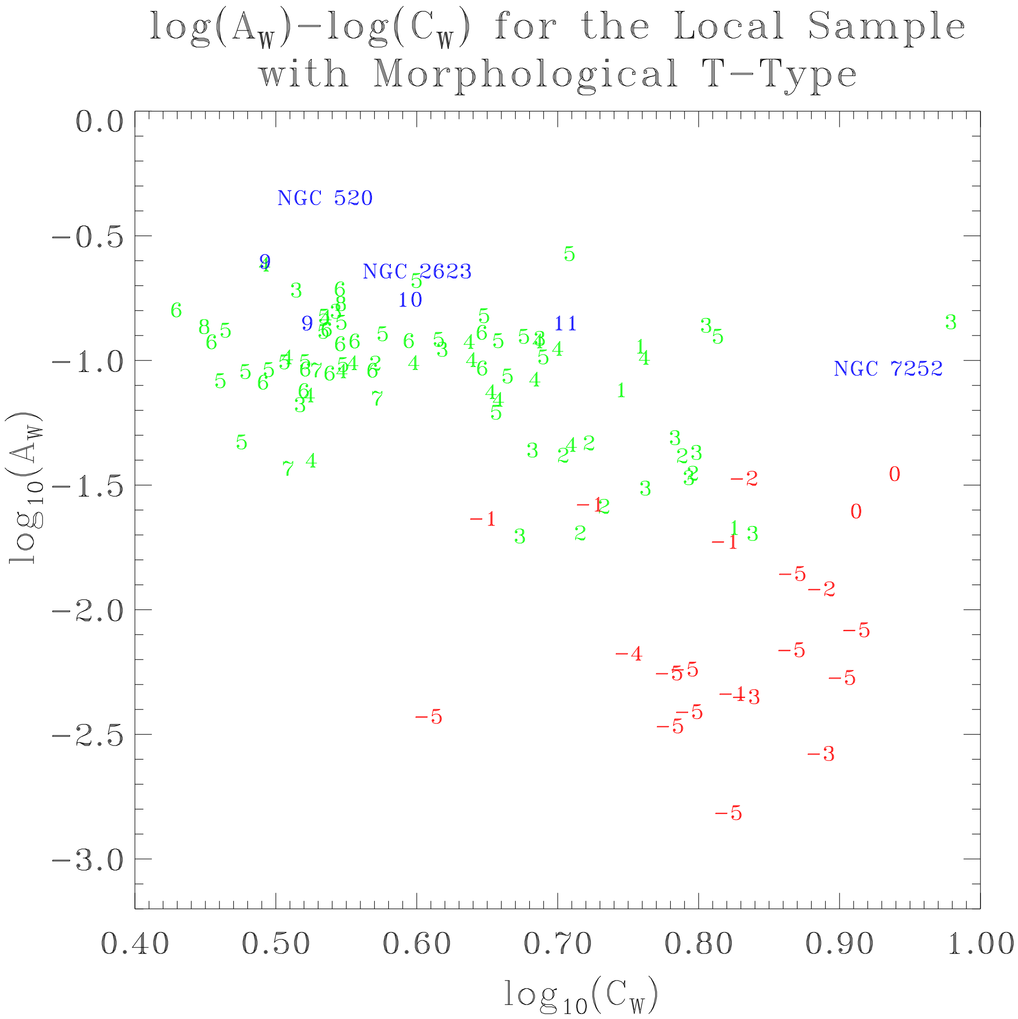

Fig. 5–2.— log(A_W)-log(C_W) for the local sample. Galaxy positions are marked by the revised morphological T-type of the galaxy. The color of the T-type divides the galaxy into three general classes for comparison with A96b: red denotes galaxies with T $\leq$ 0, green denotes 0 $<$ T $<$ 9, and blue denotes T $\geq$ 9. The HvG peculiar galaxies are blue and marked by their NGC number. These galaxies generally lie at the upper envelope of the distribution with higher than average values of A_W. The T $= -5$ galaxy with a surprisingly low C_W is NGC 4125, which suffers severely from the peculiar brightening of the sky background. A large portion of the "bad" sky is included in the galaxy detection isophote, resulting in the low calculated value of C_W. The T $= 3$ galaxy with an inordinately high C_W is NGC 4216, a highly inclined spiral galaxy with strong dust lanes and a bright bulge, the combination of which likely results in a calculated value of C_W that is higher than that expected for most spirals. Given the structure, however, it is not surprising that C_W is high.

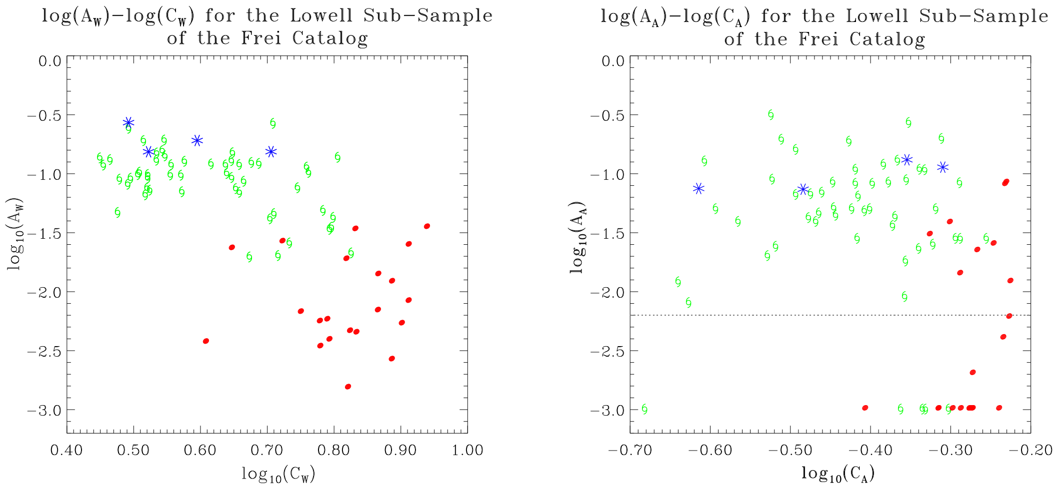

Fig. 5–3.— A comparison of log(A_W)-log(C_W) and log(A_A)-log(C_A) for the Lowell sub-sample of the Frei catalog. The color-coding of the symbols is the same as the color code in Figure 5–2. E/S0 galaxies are denoted by red ellipses; Sabc galaxies by green spirals, late-type galaxies by blue asterisks. There are no peculiar galaxies in the Lowell sub-sample. The dotted line shows the lower boundary of plots presented in A96a,b. From this comparison, A_W-C_W and A_A-C_A are qualitatively equivalent, though the separation between ellipticals and spirals is perhaps slightly better using A_W-C_W *(see text for details)*. Note that irregular galaxies are found by both algorithms to occupy roughly the same region of the A-C diagrams as spirals. This supports the argument that irregulars and peculiars should not be grouped together into one category for evolutionary studies.

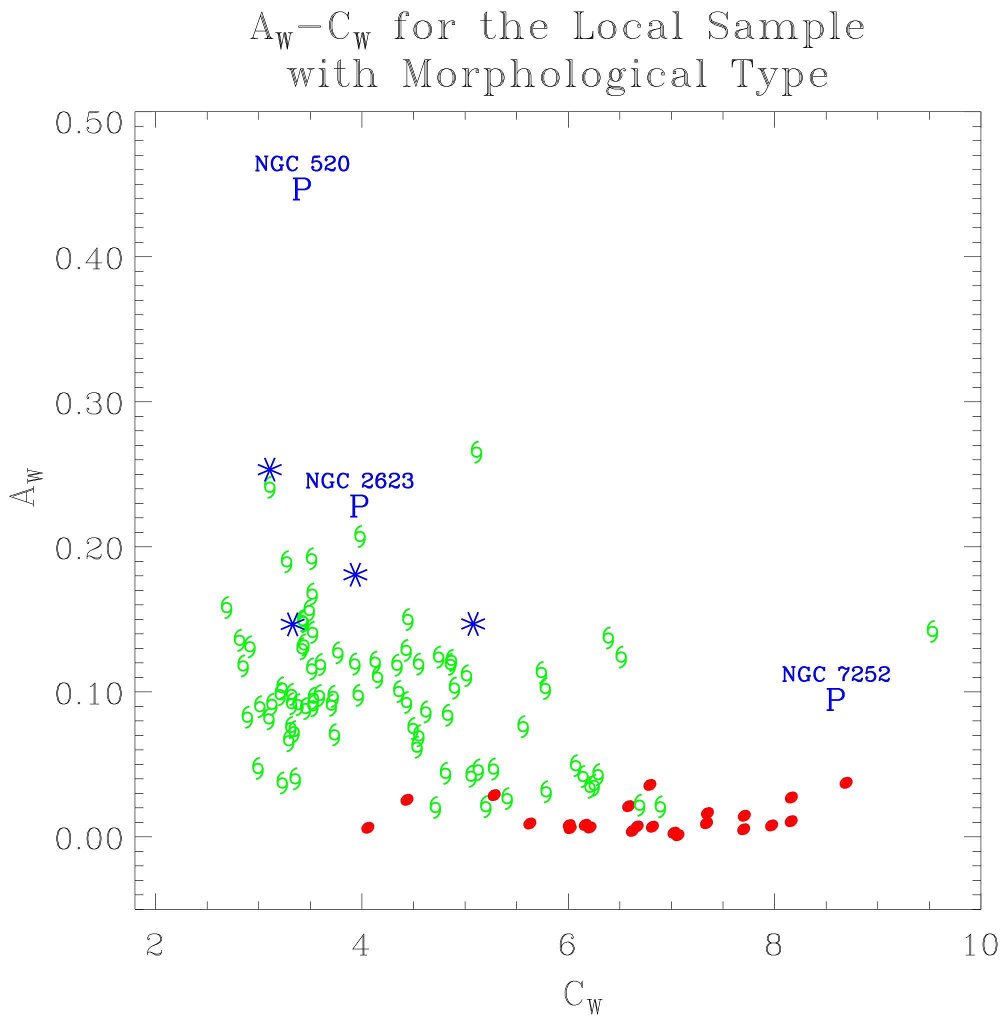

Fig. 5–4.— A_W-C_W for the local sample plotted on a linear scale to emphasize asymmetric objects. Symbols are the same as those in Figure 5–3. Peculiar galaxies (denoted by blue "P"s and labelled with their NGC number) now stand out even more distinctly from the rest of the galaxies.

Chapter 6

Morphological Peculiarities in the HDF

Figures 6–1 show the montage of all HDF galaxies with photometric redshifts from Connolly 1999 (C99). Objects are ordered by W96 ID (roughly y-position on each of the individual chips) to allow for reasonably easy identification of pairs of galaxies. Most postage stamps are 101×101 images centered on the x, y-position of the object as given by W96. 47 images are larger and have been shrunk to fit in this montage. Data presented in the montage are: chip_x_y position in the header, photometric redshift from C99 in the top left corner, F814W$_{AB}$ and $(v-i)$ color from W96 in the top right corner (magnitude is above color), W96 ID in the bottom right corner, and A_W and C_W in the bottom left corner (C_W above A_W). The check mark to the left of the name label indicates that the object is in the final pruned sample. In addition, the A_W-C_W class is denoted by a small dot to the right of the name label: red = High-C_W; grey = Low-$A_W C_W$; and blue = High-A_W. If no dot is present, then the object was not detected in the A_W-C_W algorithm.

Fig. 6–1.— Montage of 1079 galaxies in the Hubble Deep Field with photometric redshifts from Andrew Connolly (1999). Objects are ordered by W96 ID (roughly y-position on each of the individual chips) to allow for reasonably easy identification of pairs of galaxies. Note that, in cases where there are multiple objects within the field, the object of interest is centered in the field (as described earlier in the 'Postage stamp creation' section in Chapter 3). The size of the postage stamp is indicated by the color of the stamp label: black is $101\times$ 101 pixels, red is $201\times$ 201, green is $301\times$ 301, and blue is $401\times$ 401. Postage stamp sizes for 47 objects are increased from the usual $101\times$ 101 pixel size in order to ensure that sufficient numbers of sky pixels are available to calculate the background asymmetry correction. These larger postage stamps have been shrunk to fit in this montage. Data presented in the montage are as follows: chip_x_y position in the name label above the postage stamp, photometric redshift from C99 in the top left corner, F814W$_{AB}$ from W96 in the top right corner, $(v-i)$ color underneath the magnitude (also in top right corner), W96 ID in the bottom right corner, A_W in the bottom left corner, and C_W above A_W in the bottom left corner. Objects with a check mark to the left of the header label are those which remain in the sample after a radial cut at $r_{1,W96} \geq 0\farcs2$ has been imposed. Colored dots to the right of the header label indicate the A_W-C_W class of the object: red = High-C_W; grey = Low-$A_W C_W$; and blue = High-A_W. Objects without a dot were not detected by the A_W-C_W algorithms.

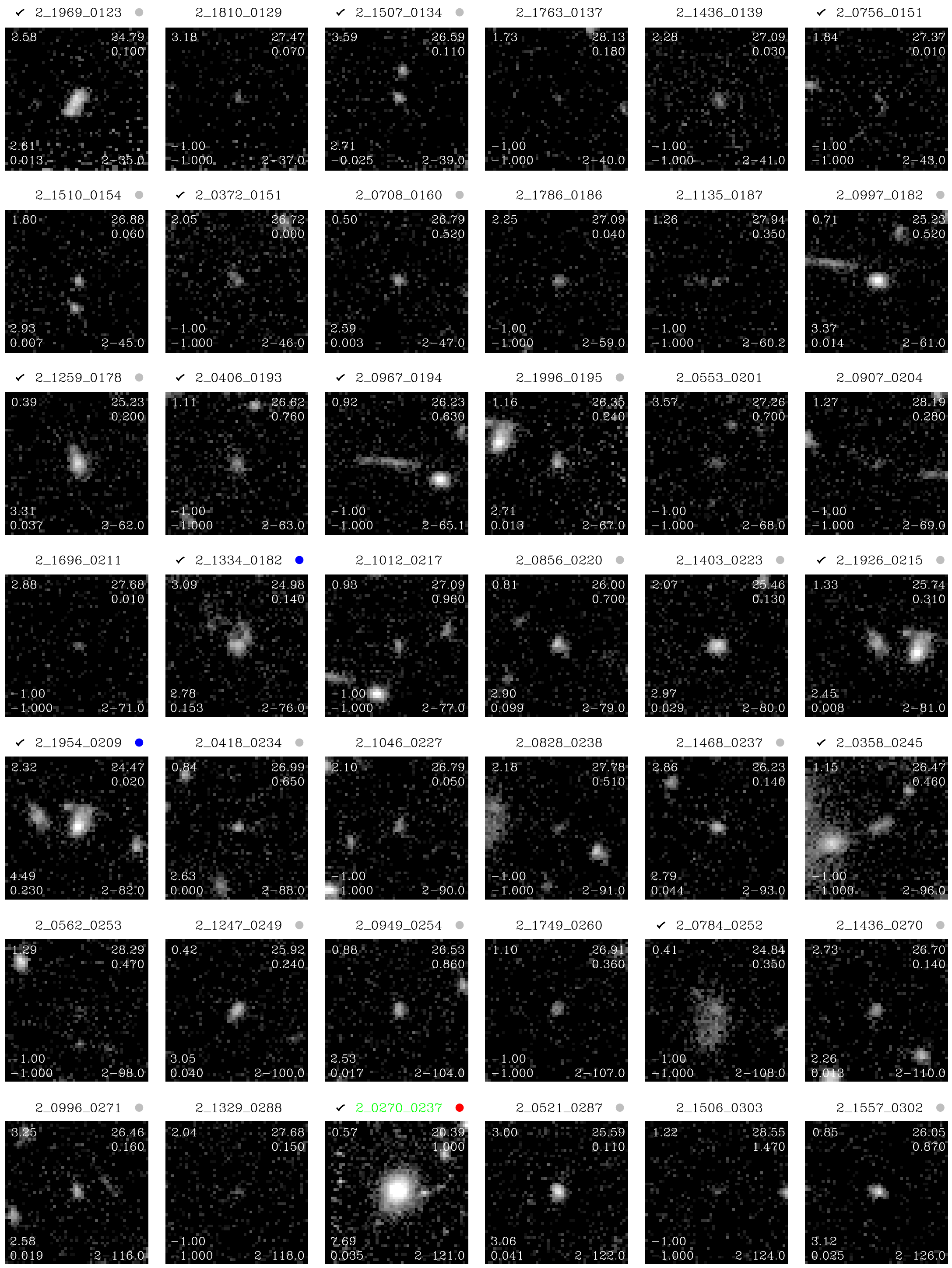

Fig. 6–1a. HDF montage.

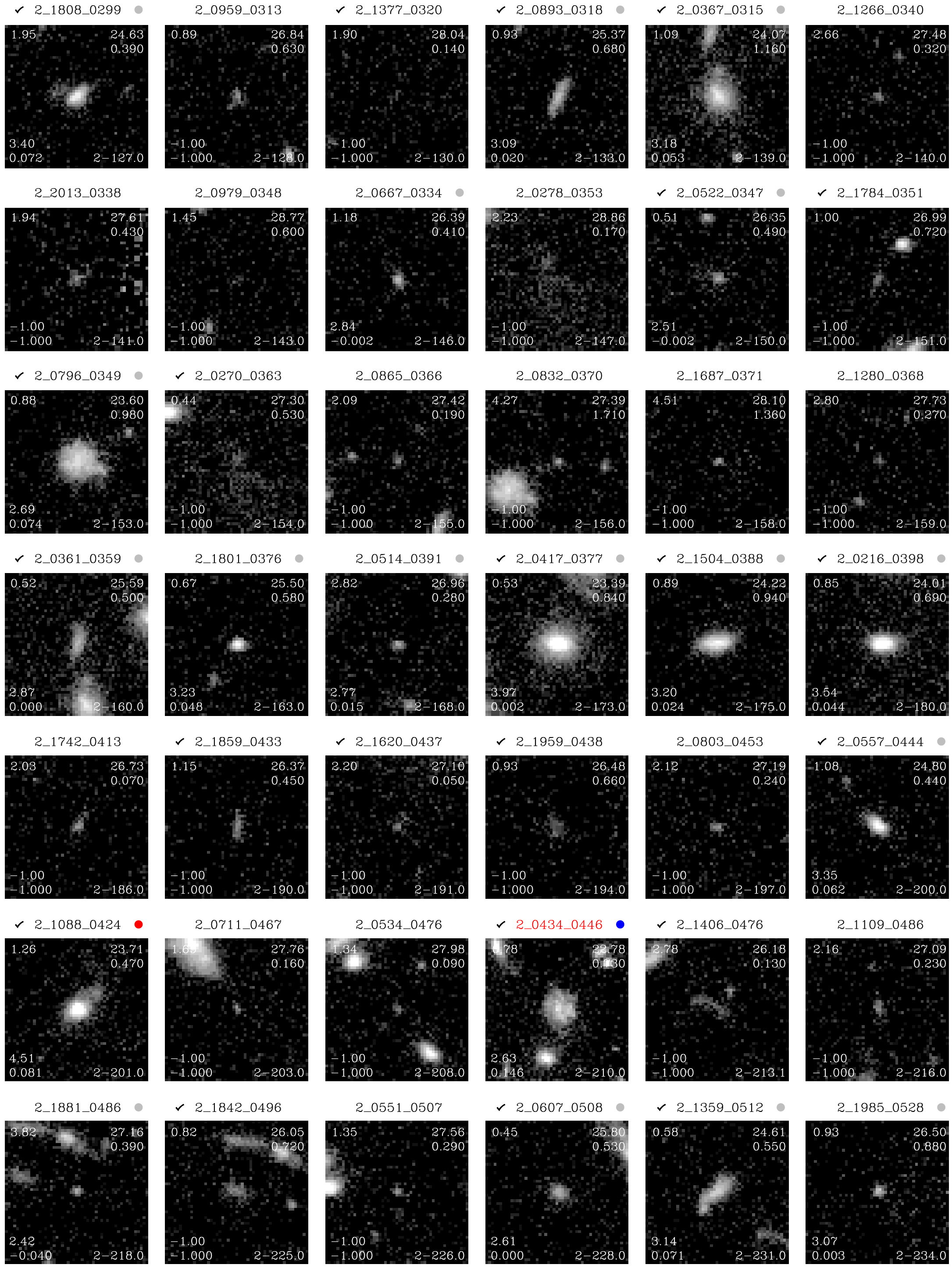

Fig. 6–1b. HDF montage *(continued)*.

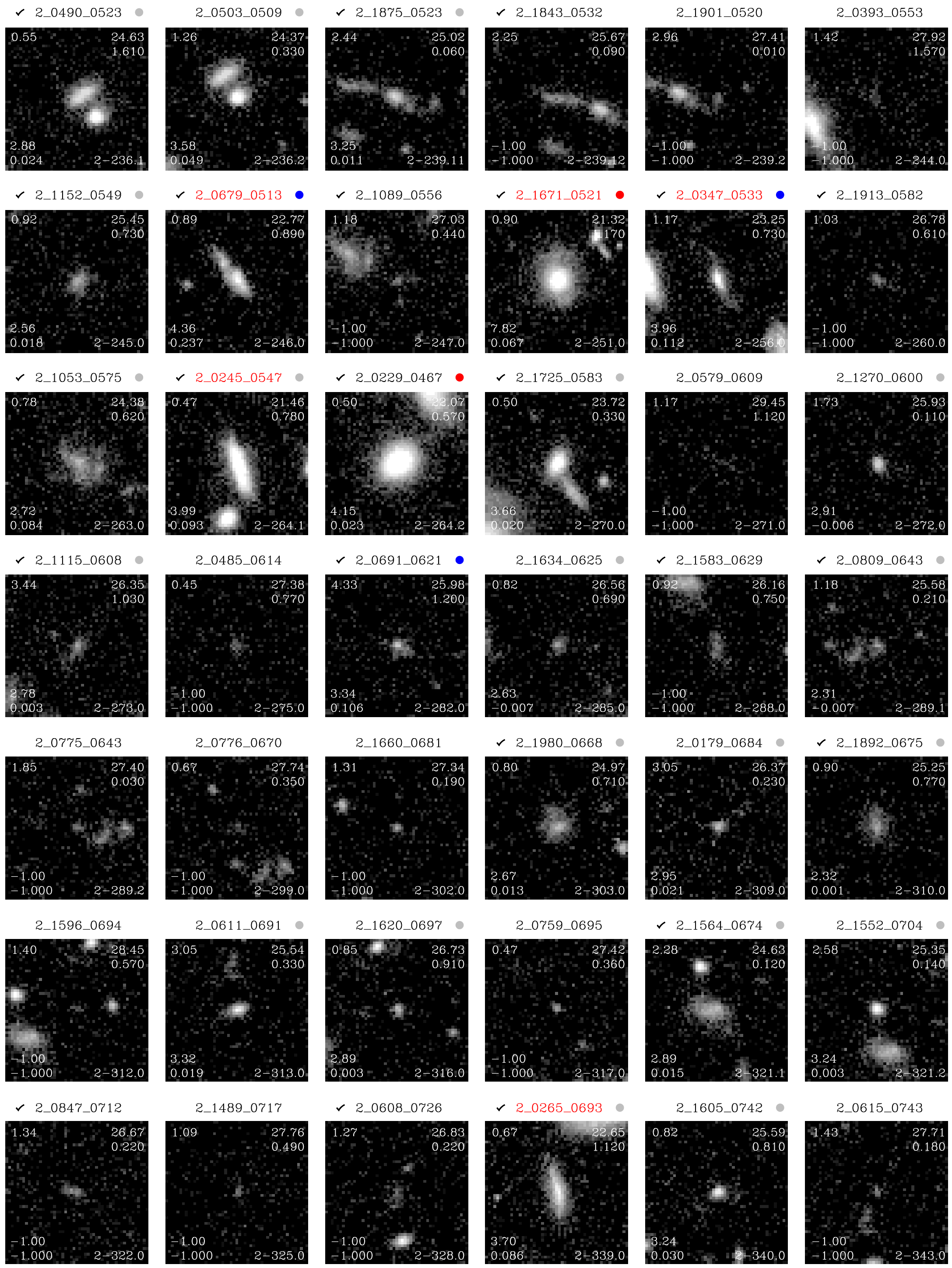

Fig. 6–1c. HDF montage *(continued).*

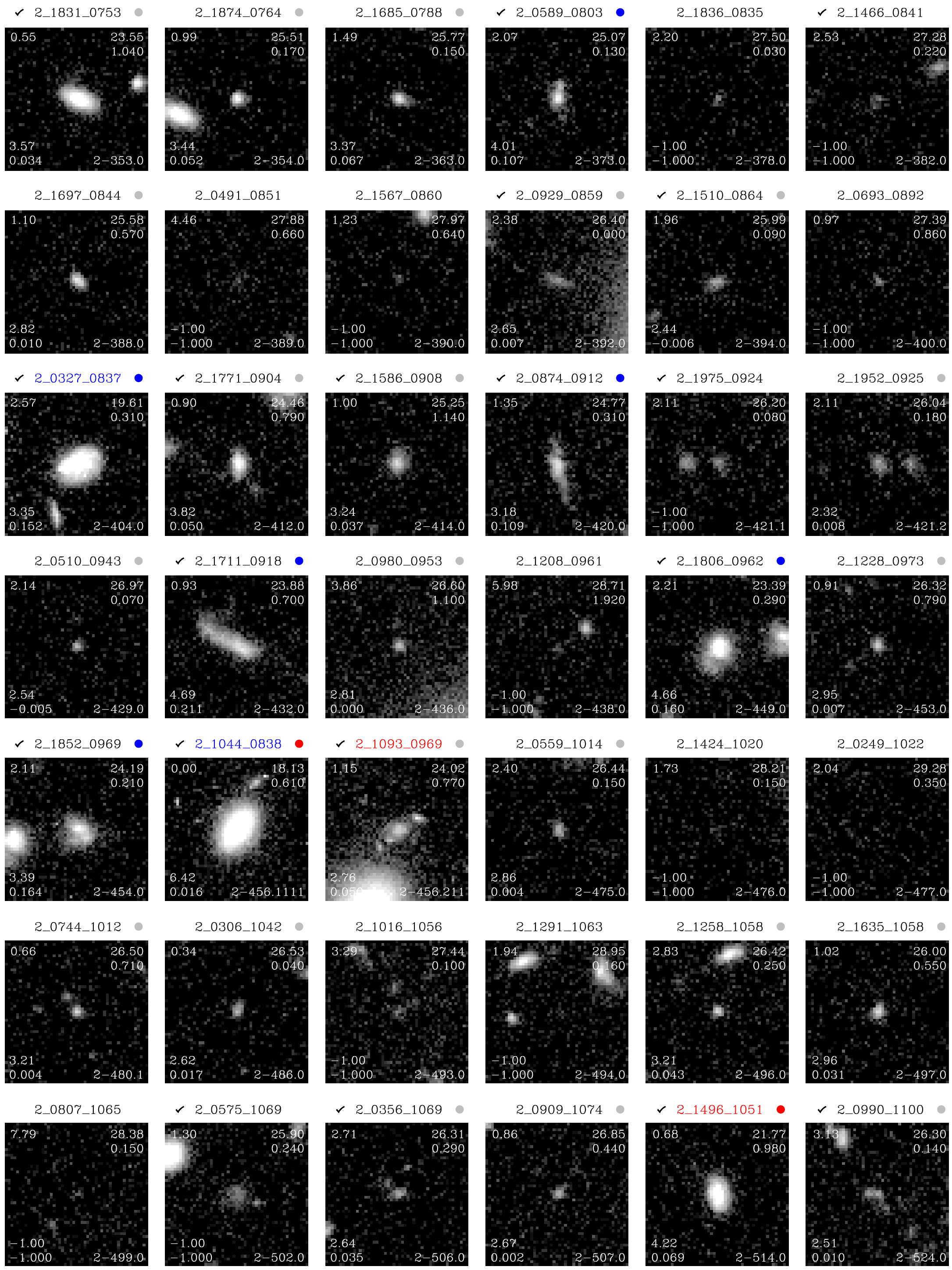

Fig. 6–1d. HDF montage *(continued)*.

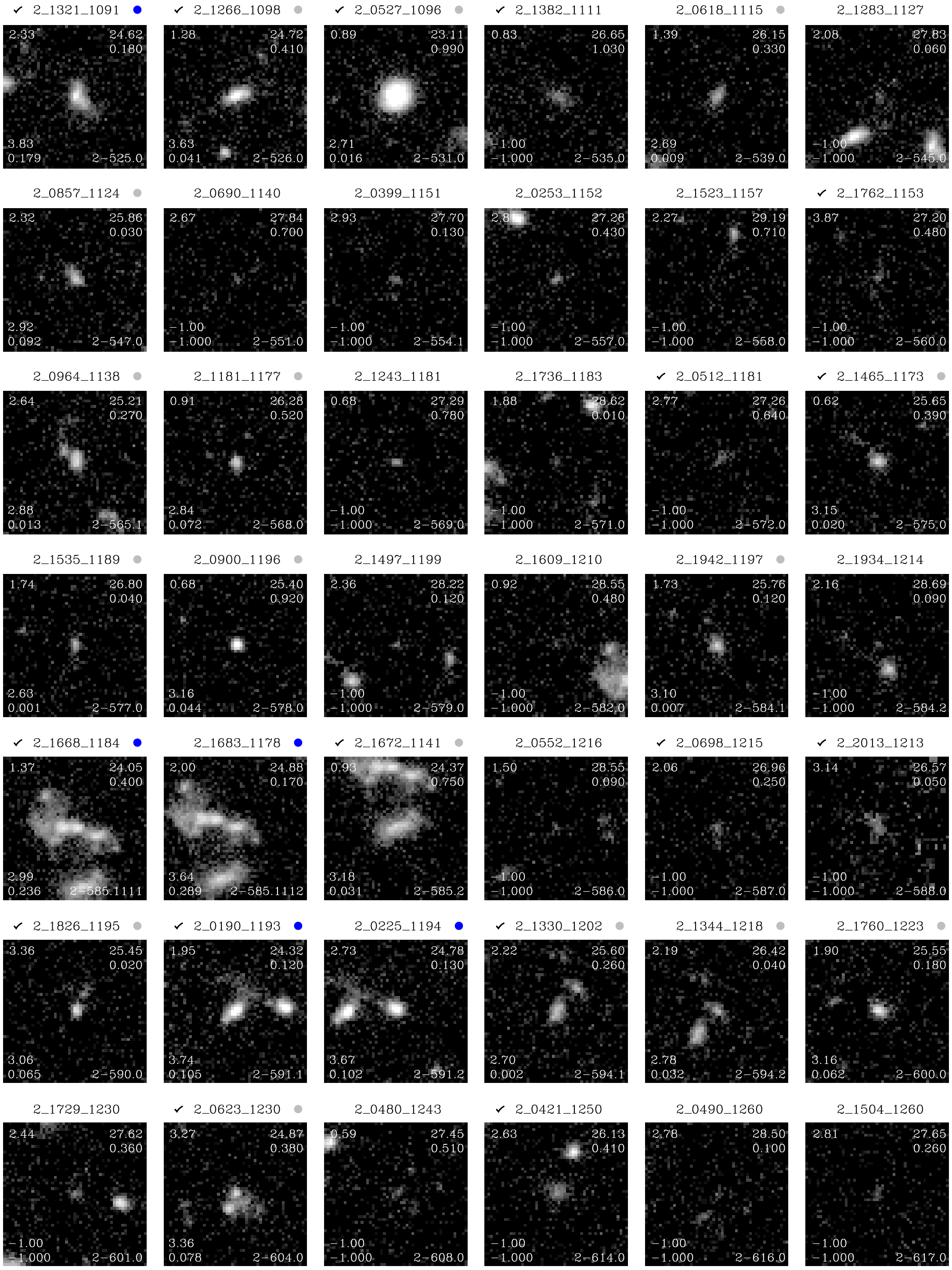

Fig. 6–1e. HDF montage *(continued)*.

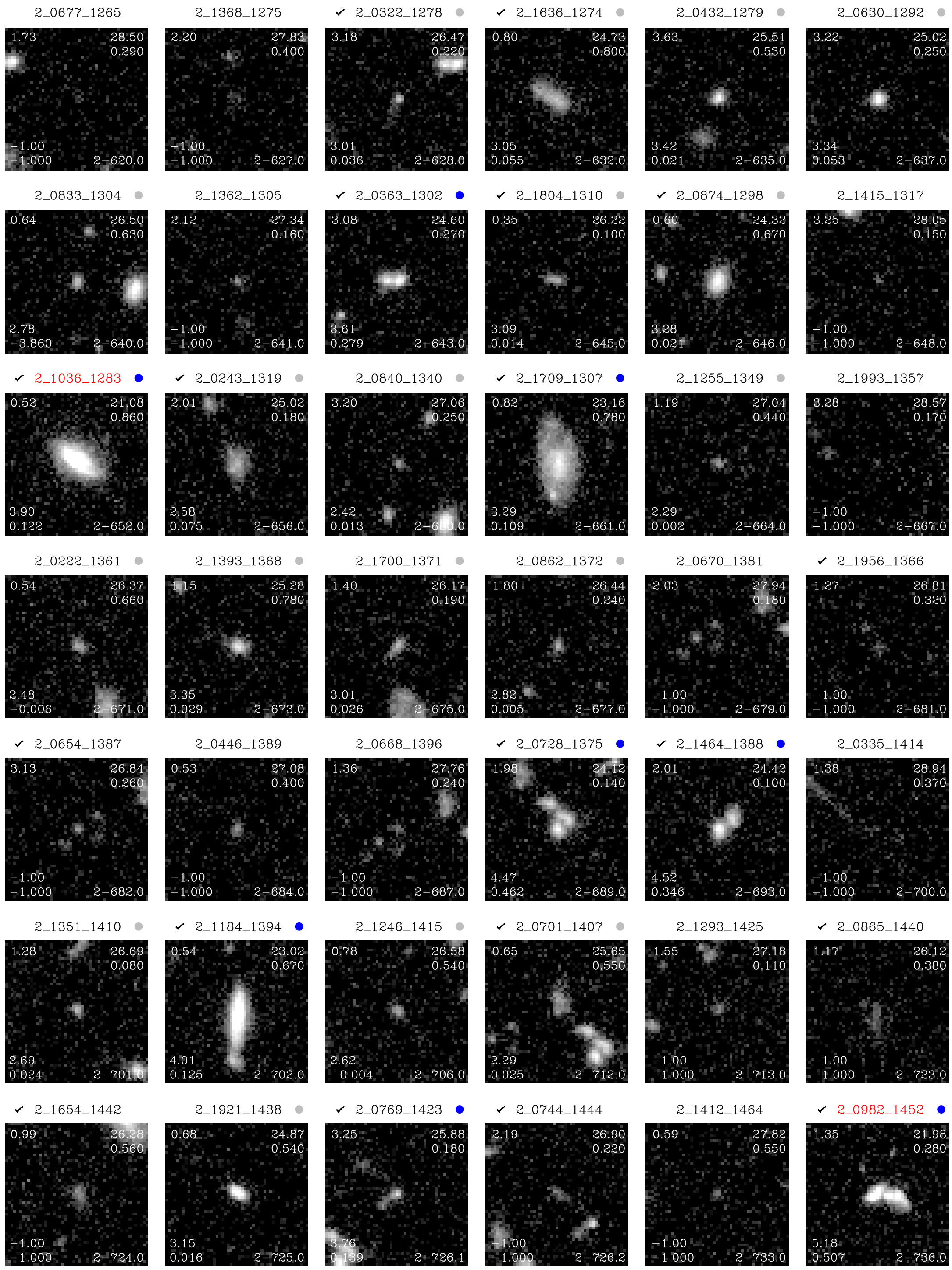

Fig. 6–1f. HDF montage *(continued)*.

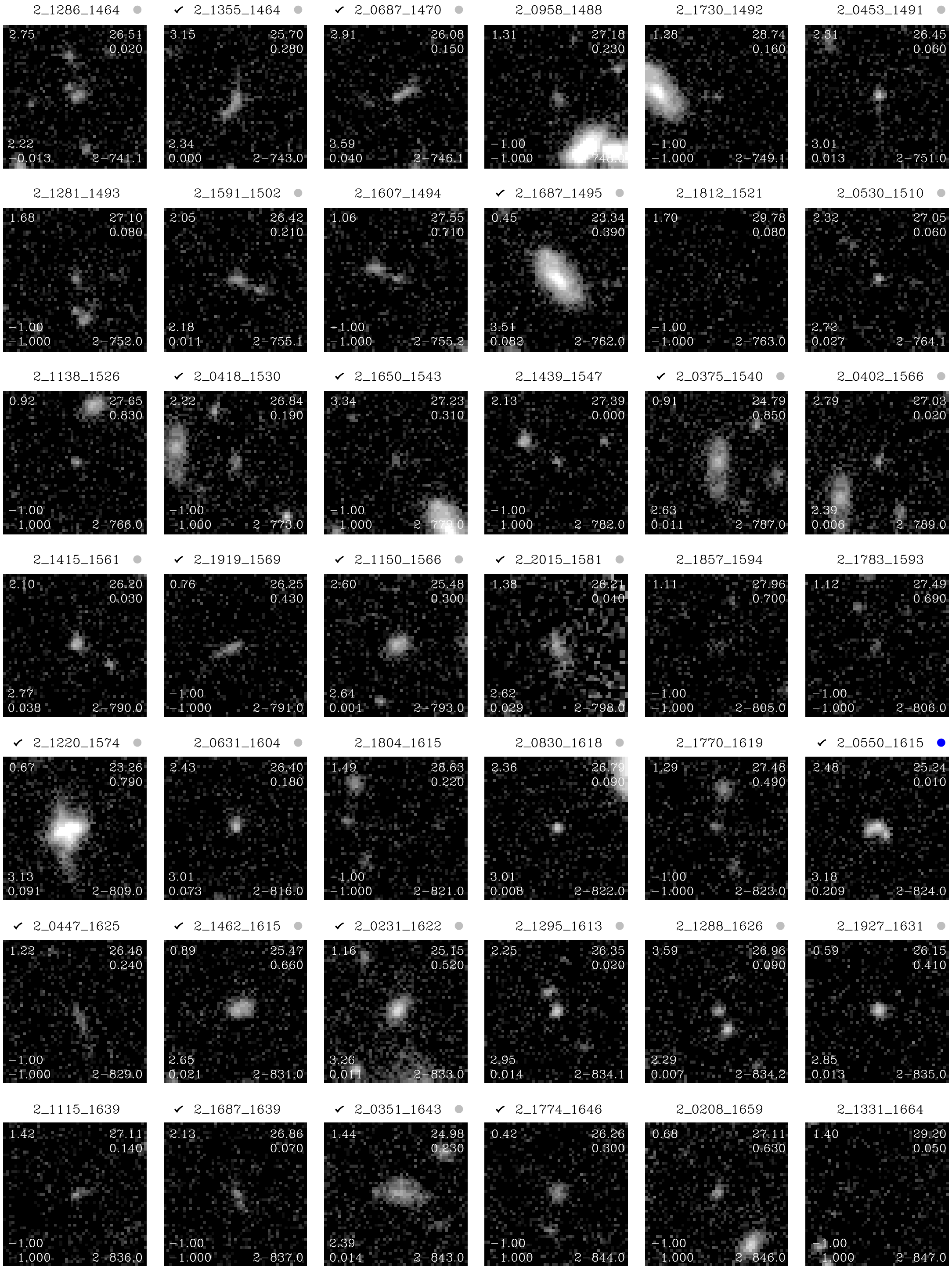

Fig. 6–1g. HDF montage *(continued).*

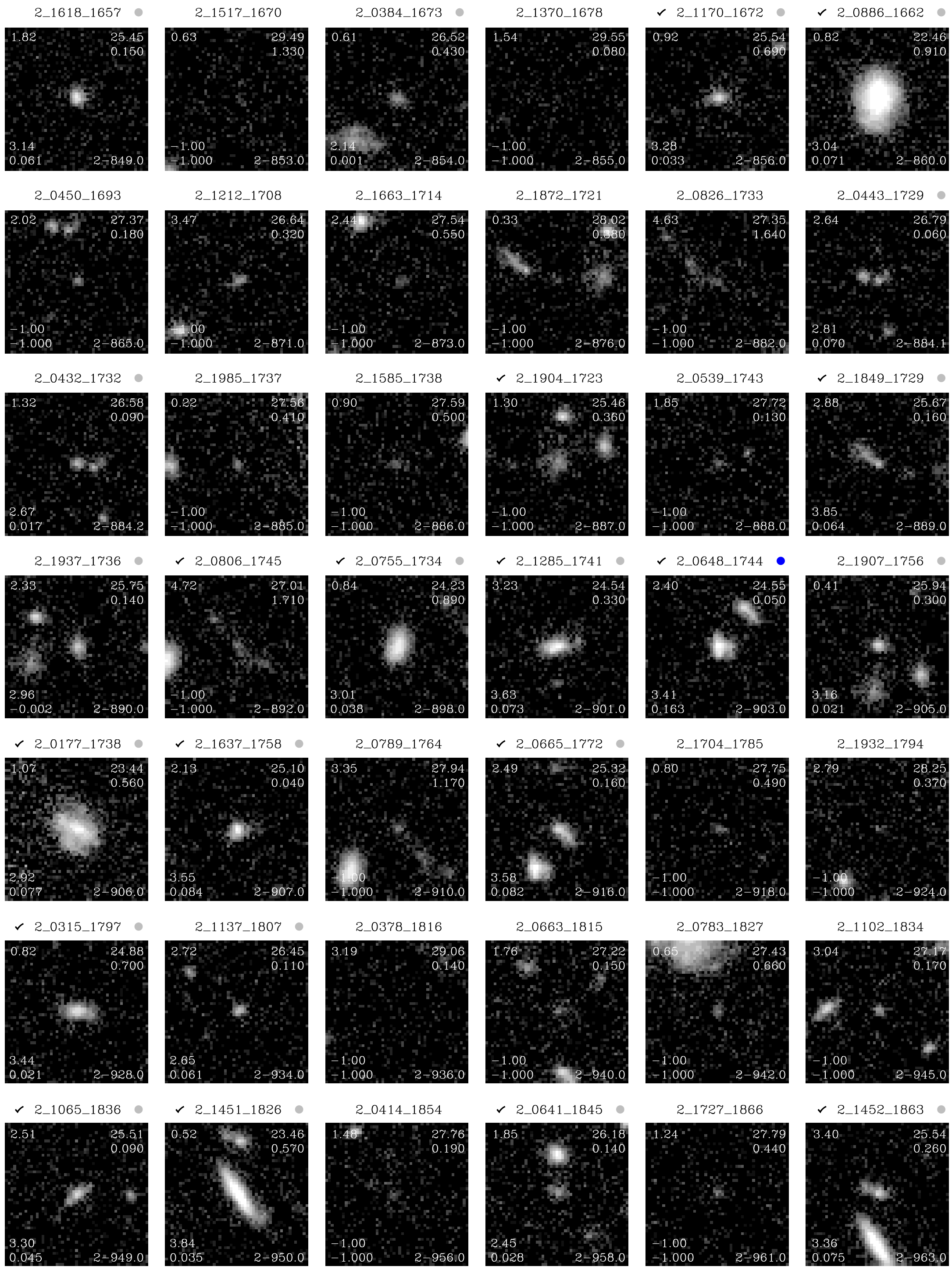

Fig. 6–1h. HDF montage *(continued).*

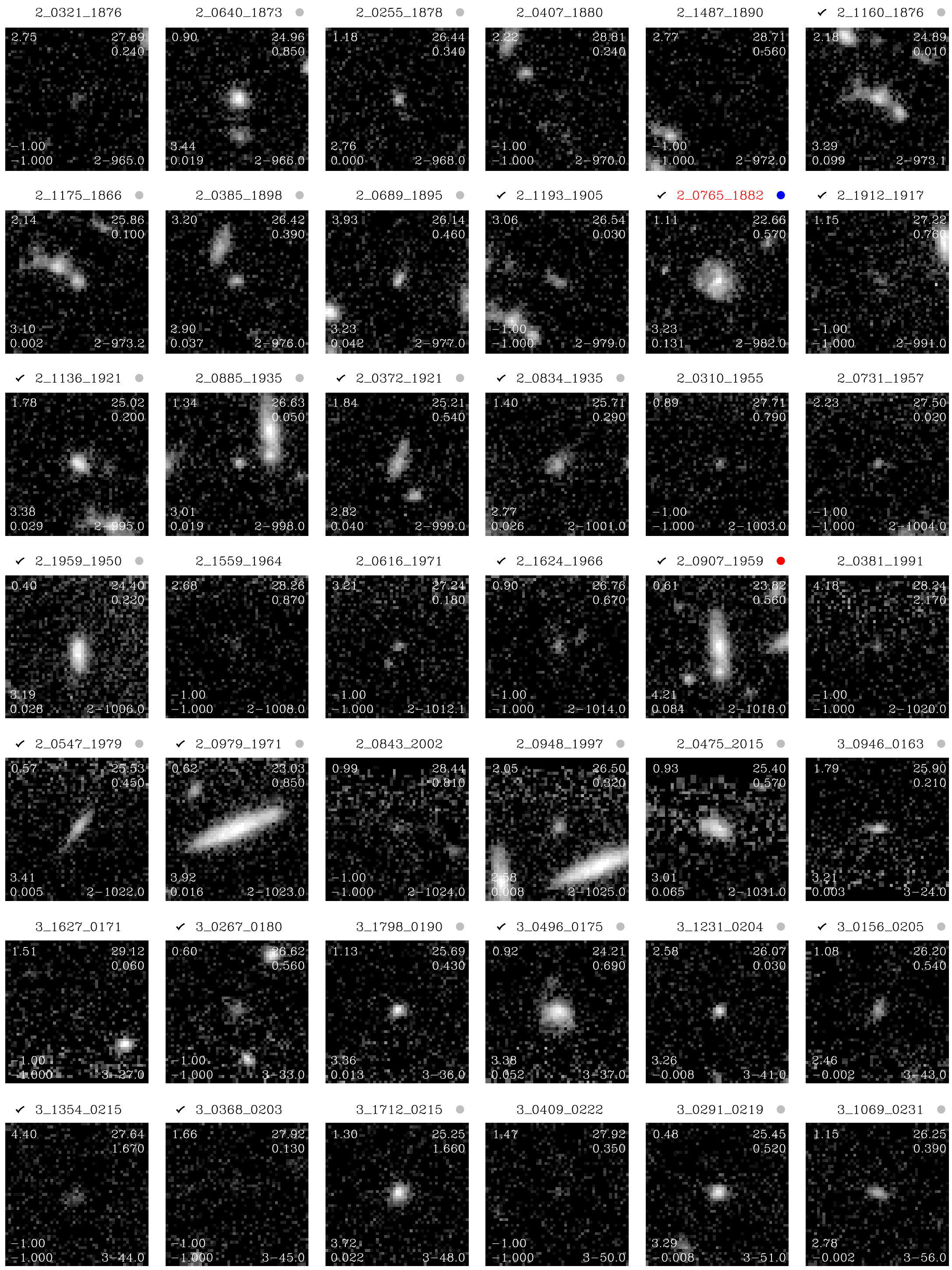

Fig. 6–1i. HDF montage *(continued)*.

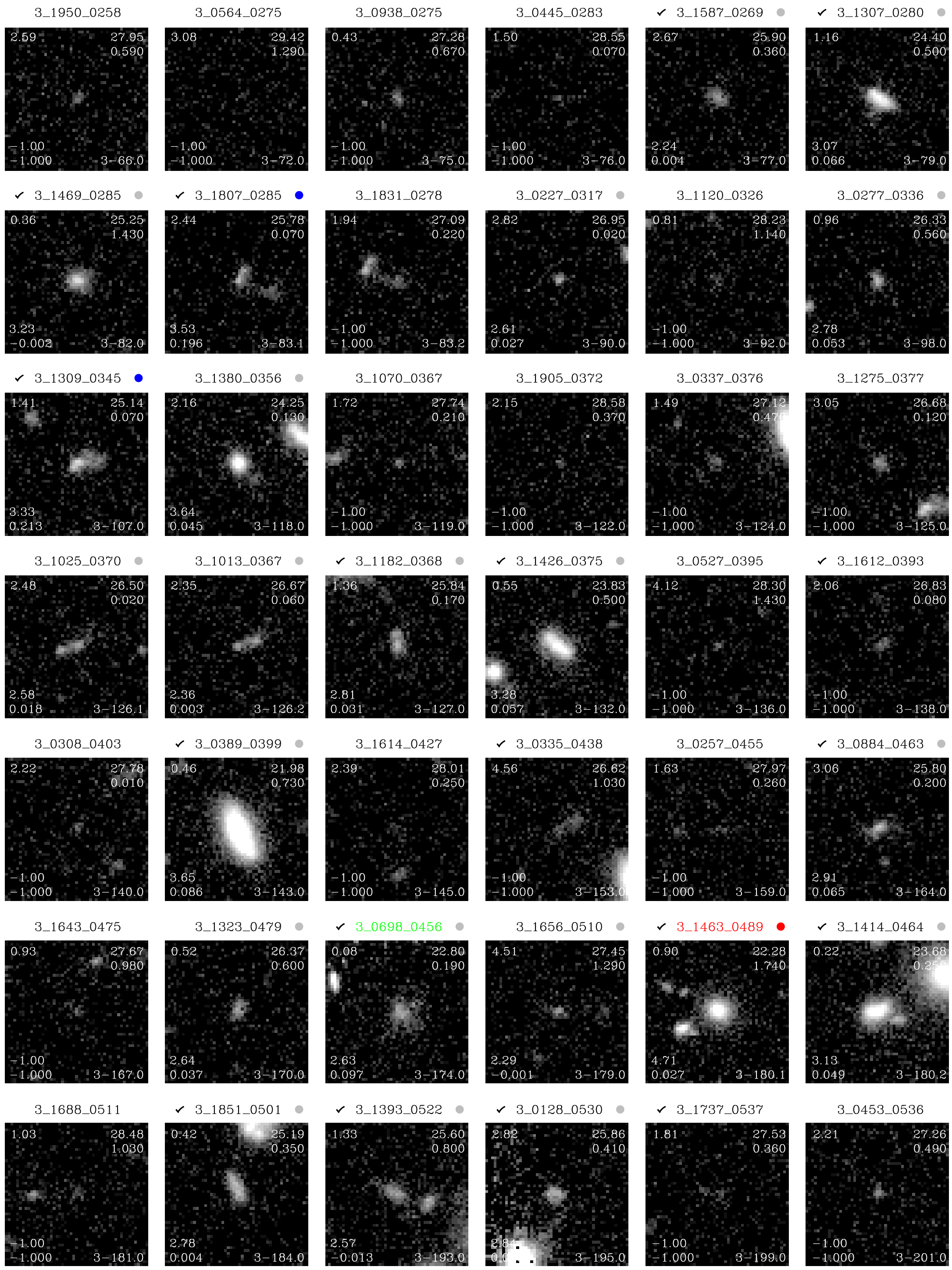

Fig. 6–1j. HDF montage *(continued)*.

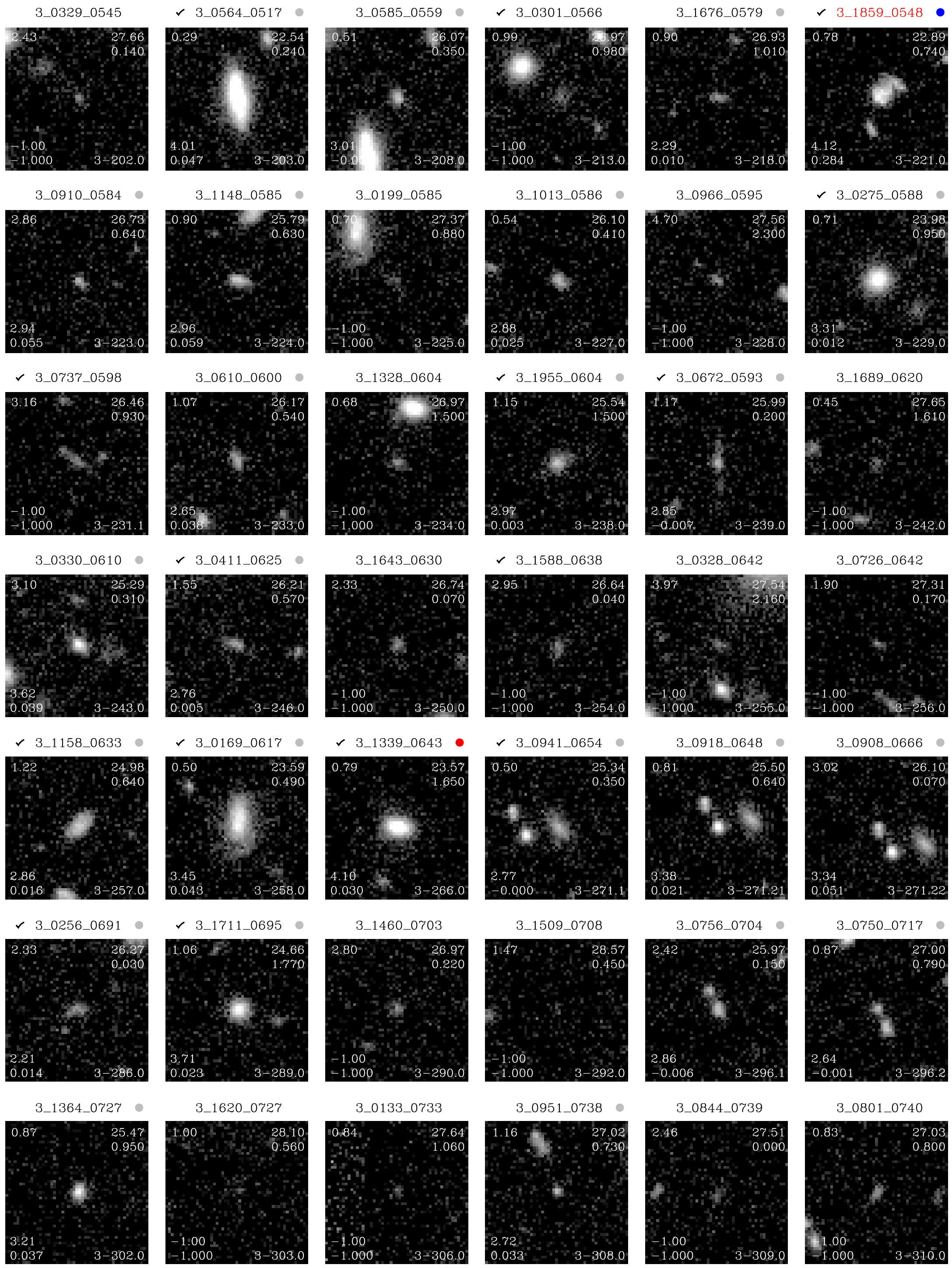

Fig. 6–1k. HDF montage *(continued)*.

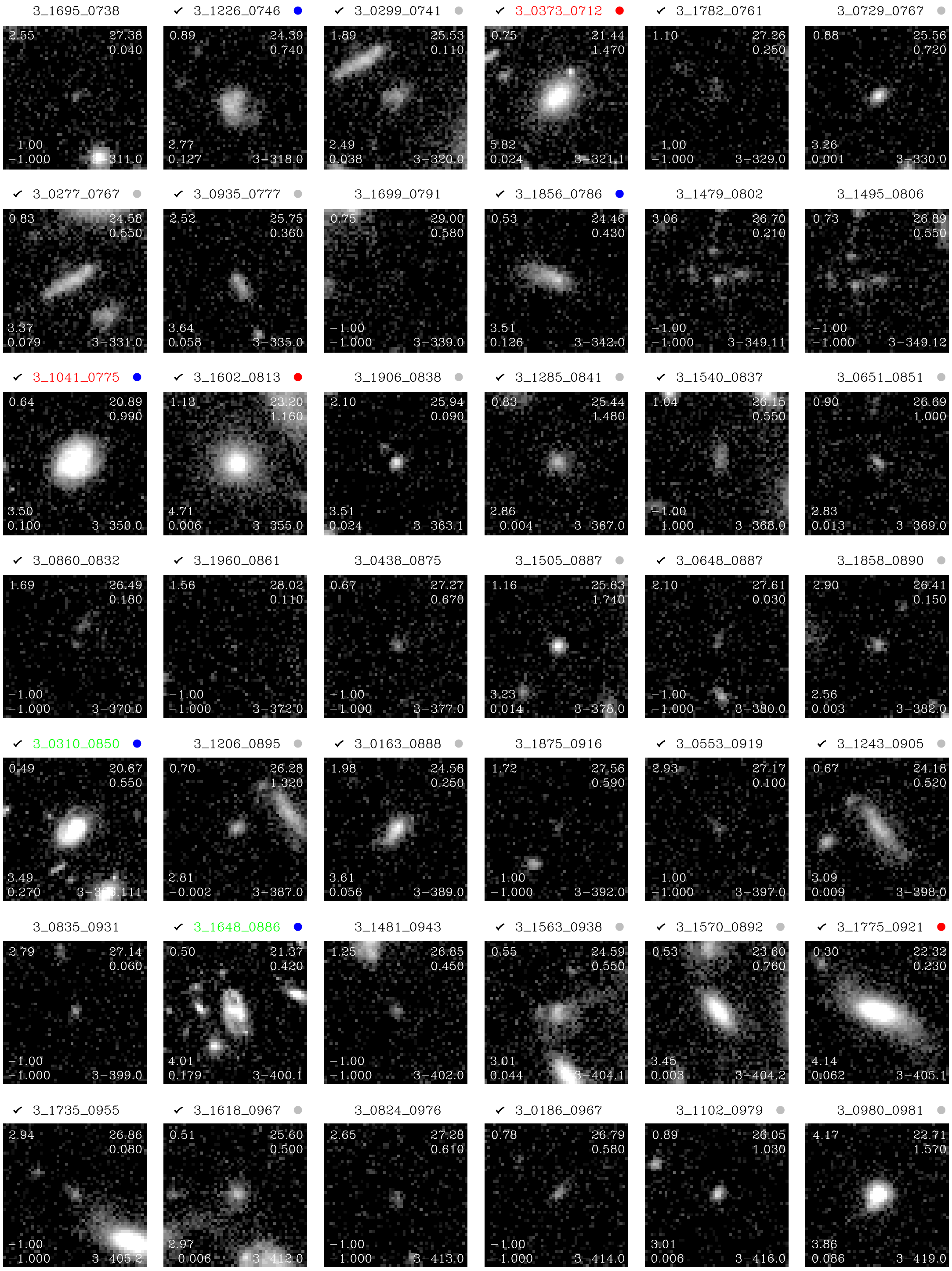

Fig. 6–11. HDF montage *(continued)*.

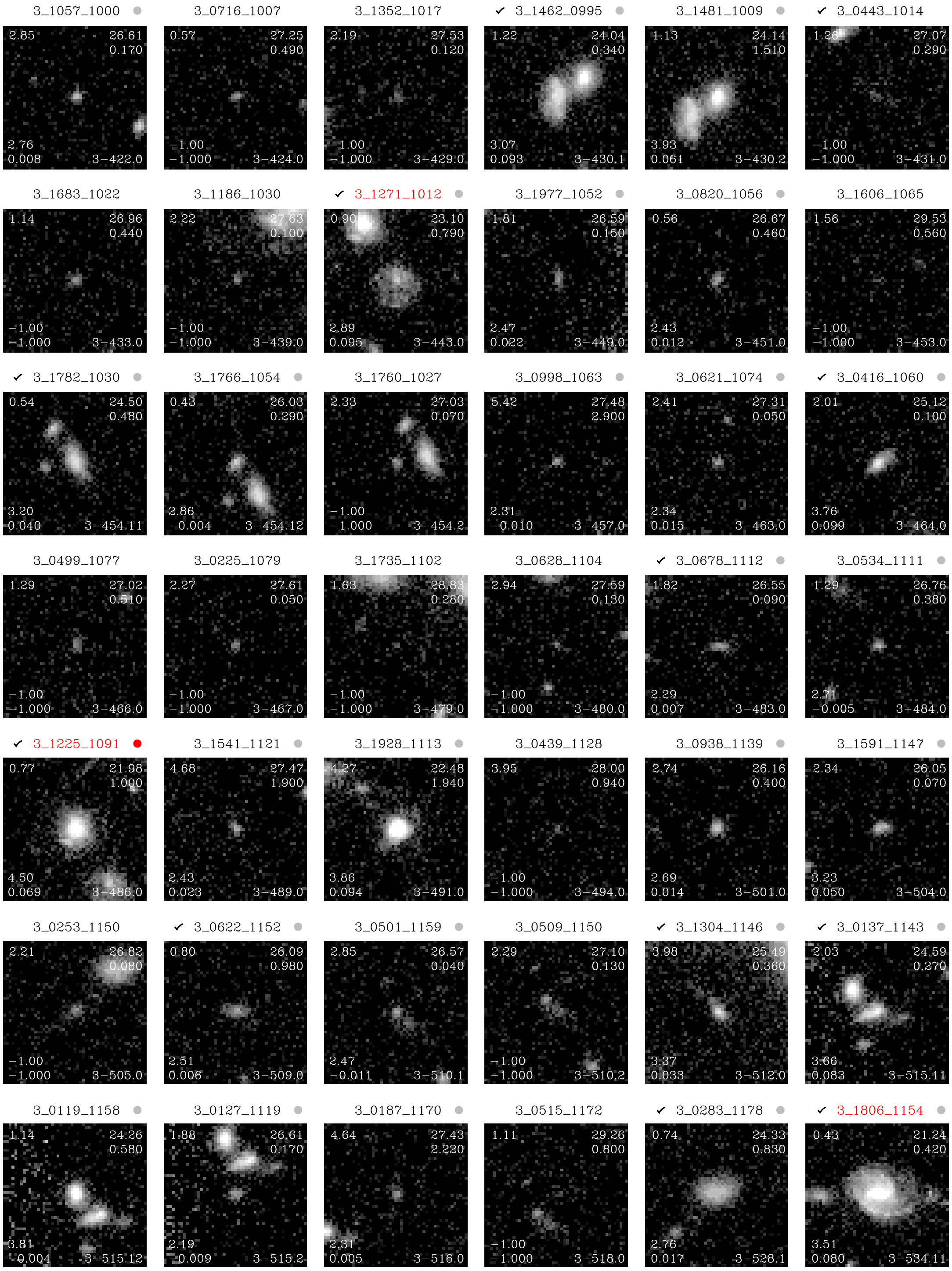

Fig. 6–1m. HDF montage *(continued)*.

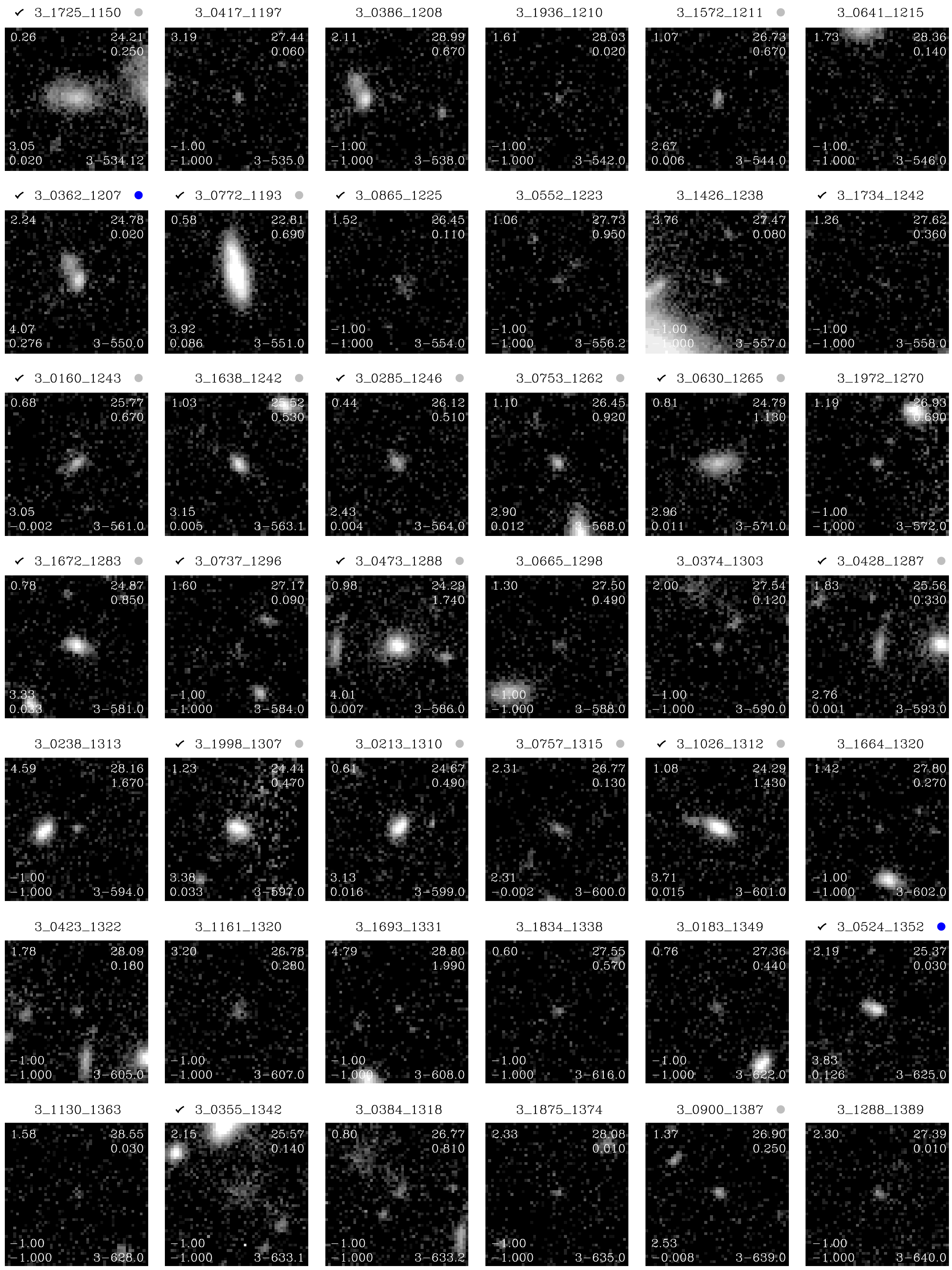

Fig. 6–1n. HDF montage *(continued).*

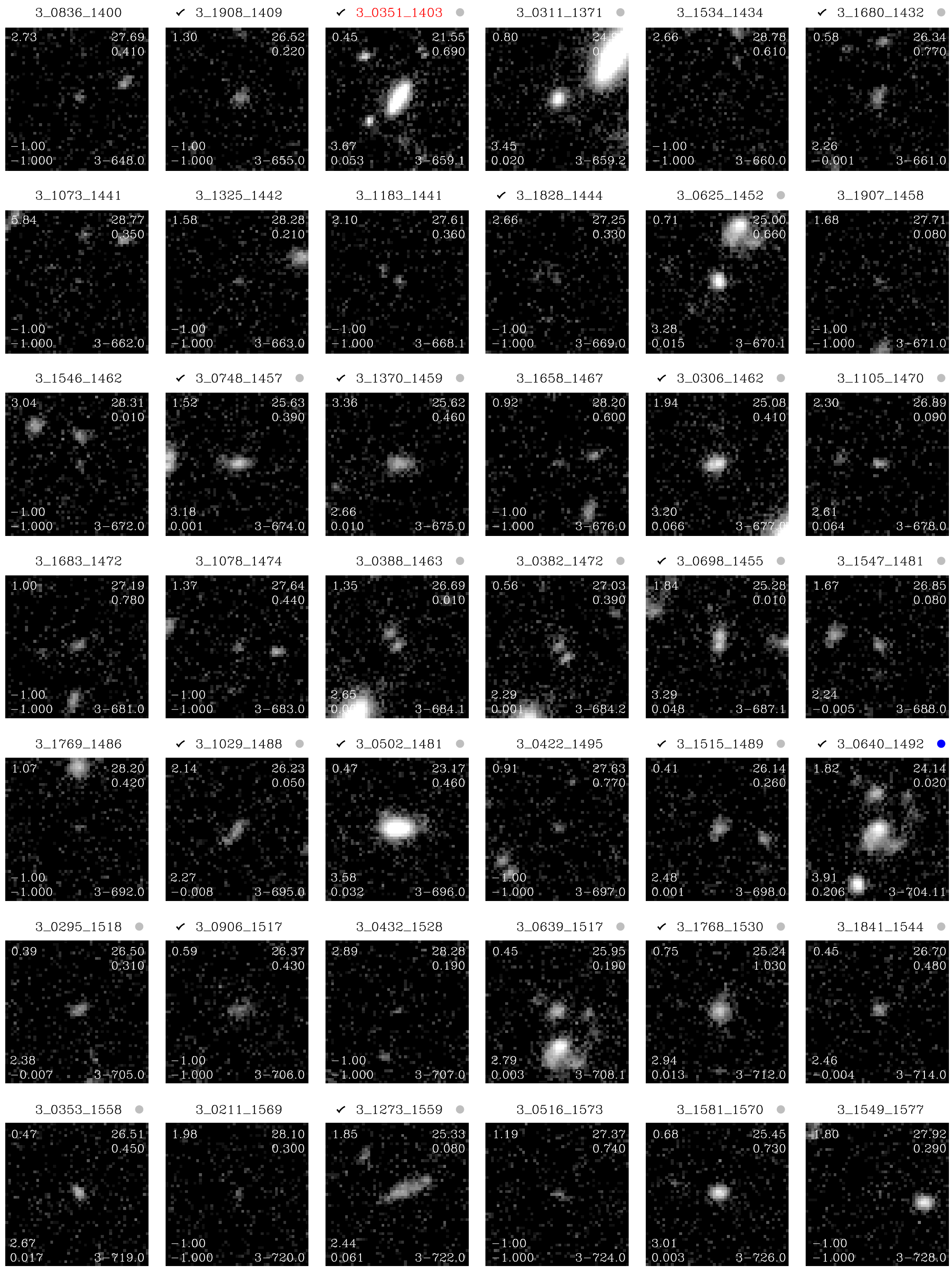

Fig. 6–1o. HDF montage *(continued)*.

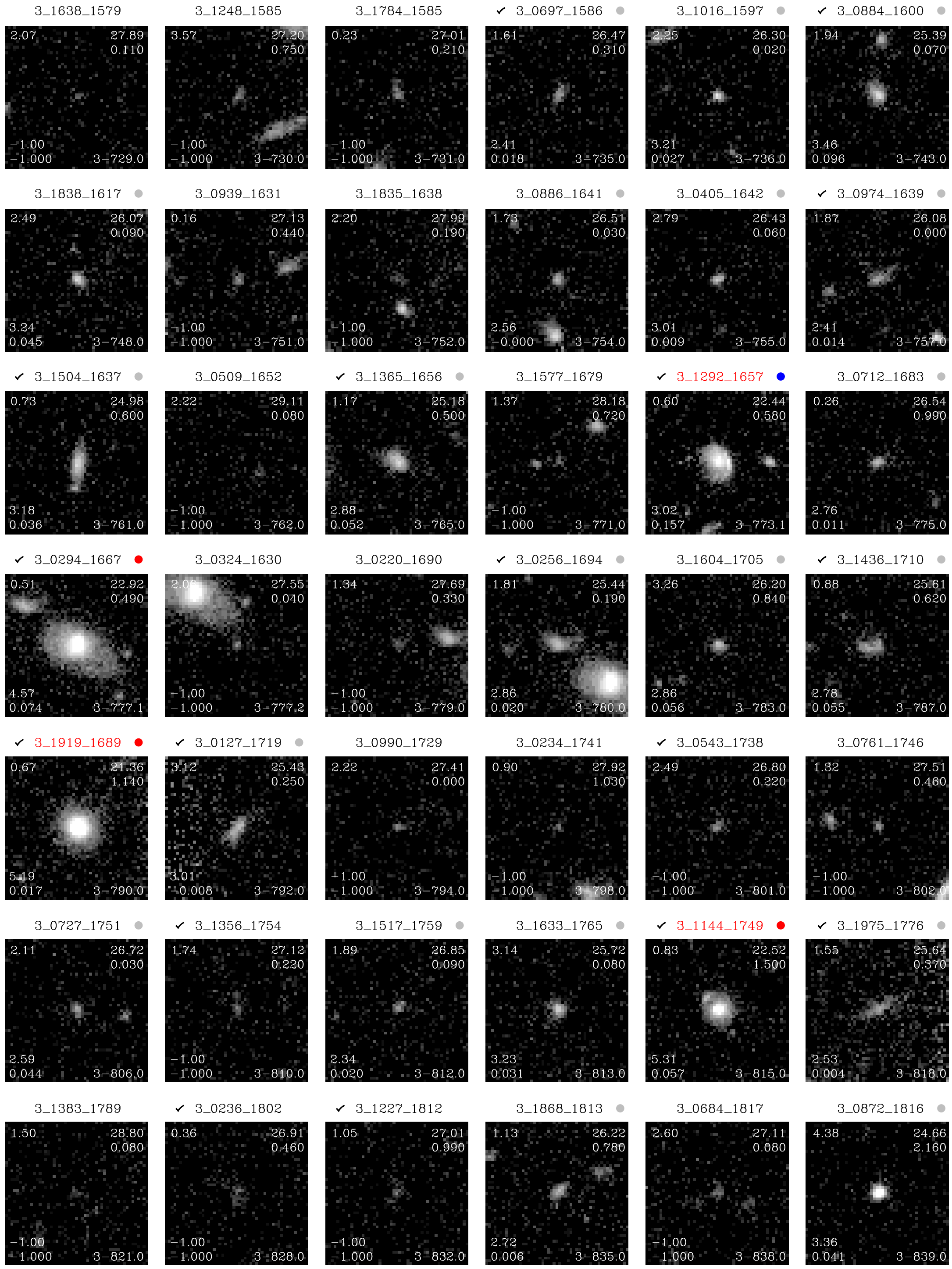

Fig. 6–1p. HDF montage *(continued)*.

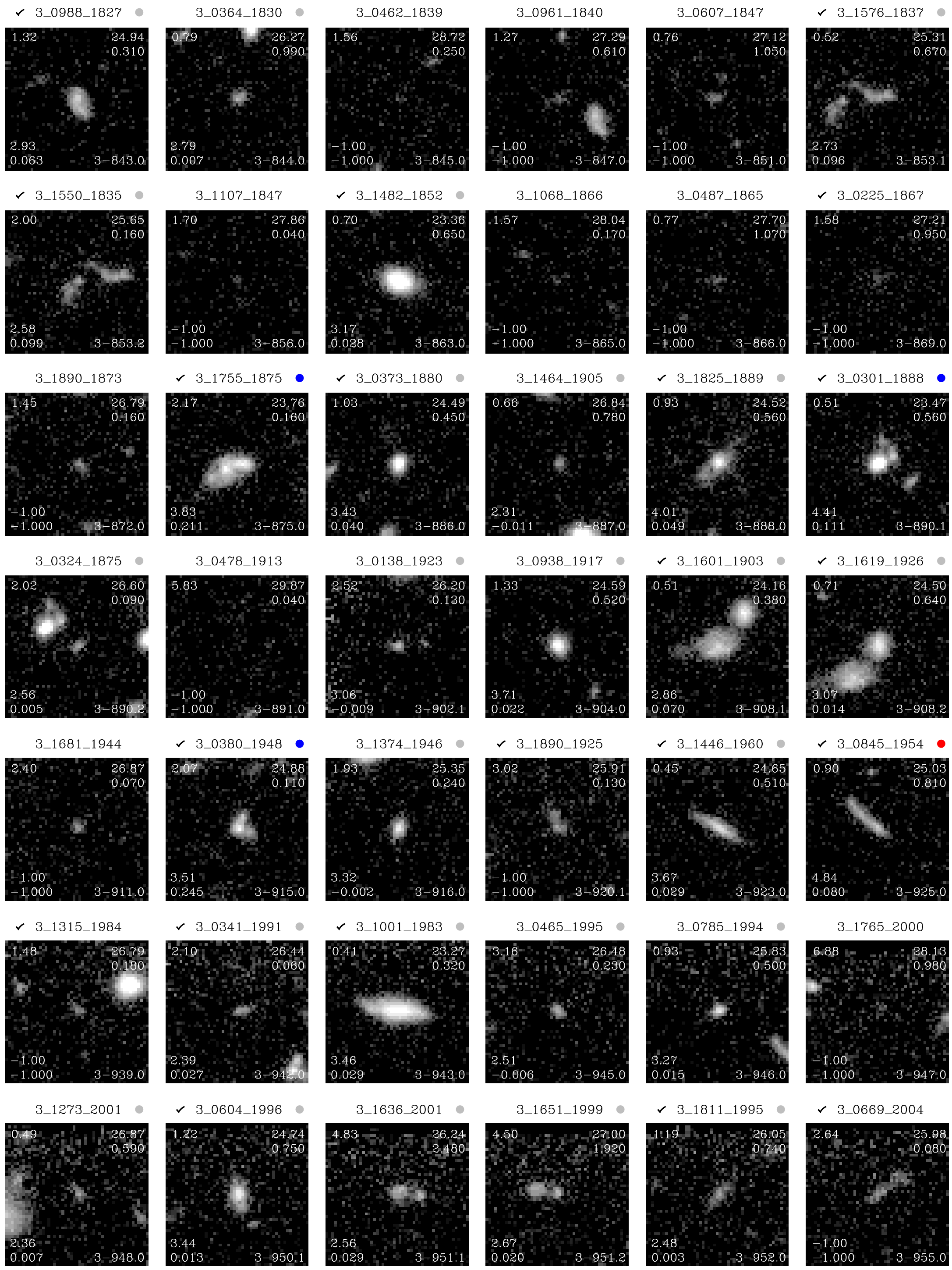

Fig. 6–1q. HDF montage *(continued)*.

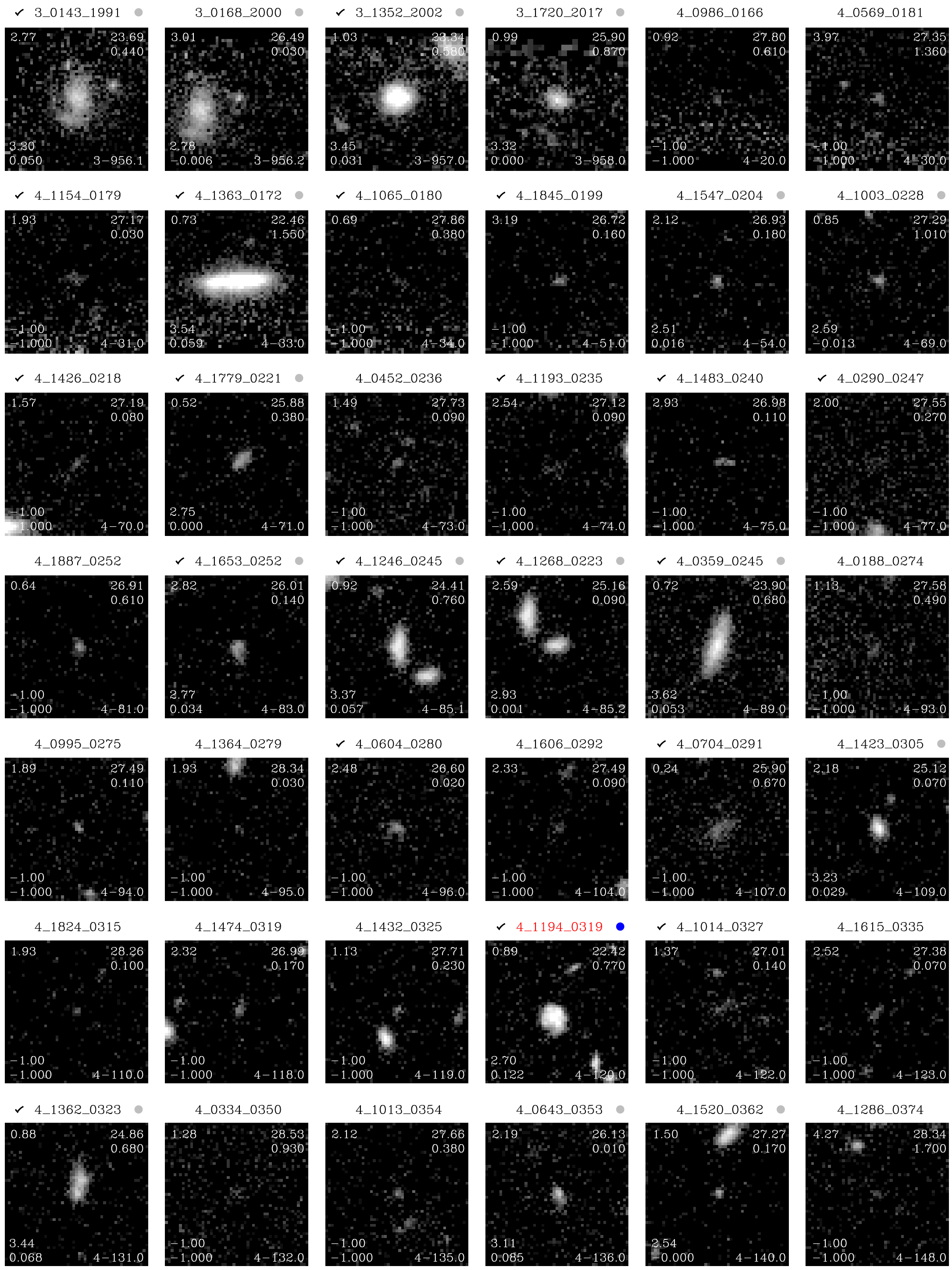

Fig. 6–1r. HDF montage *(continued).*

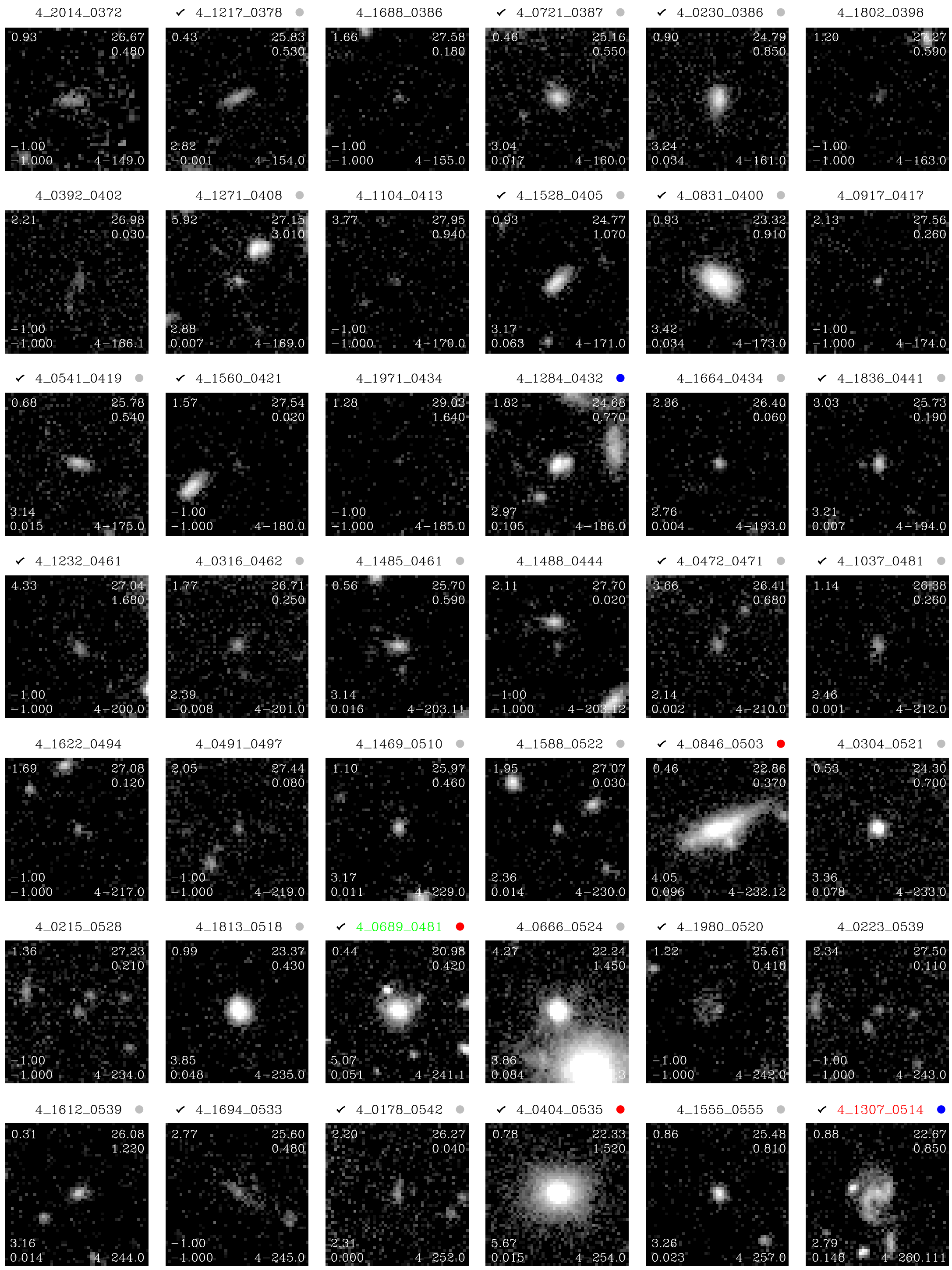

Fig. 6–1s. HDF montage *(continued)*.

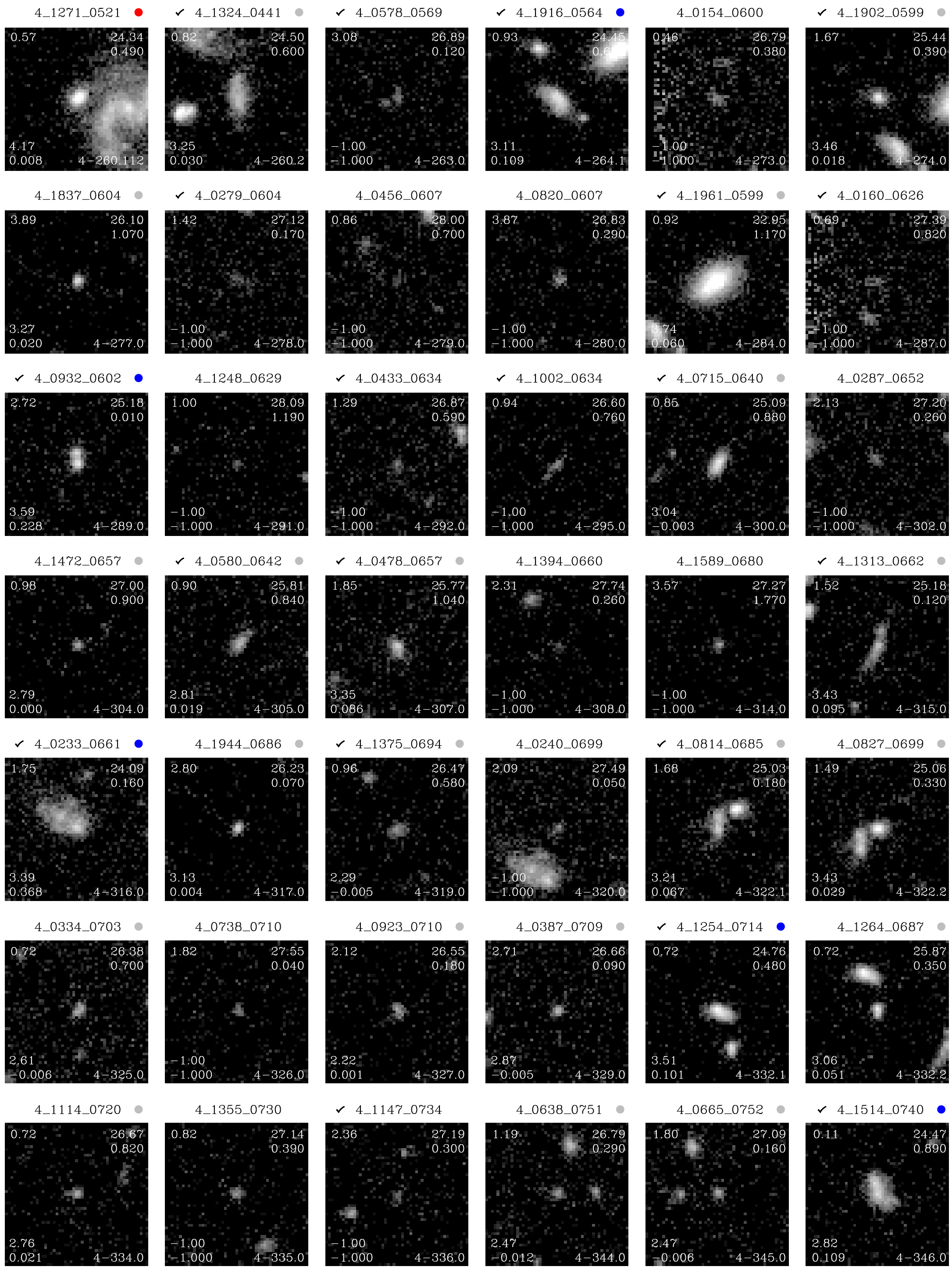

Fig. 6–1t. HDF montage *(continued)*.

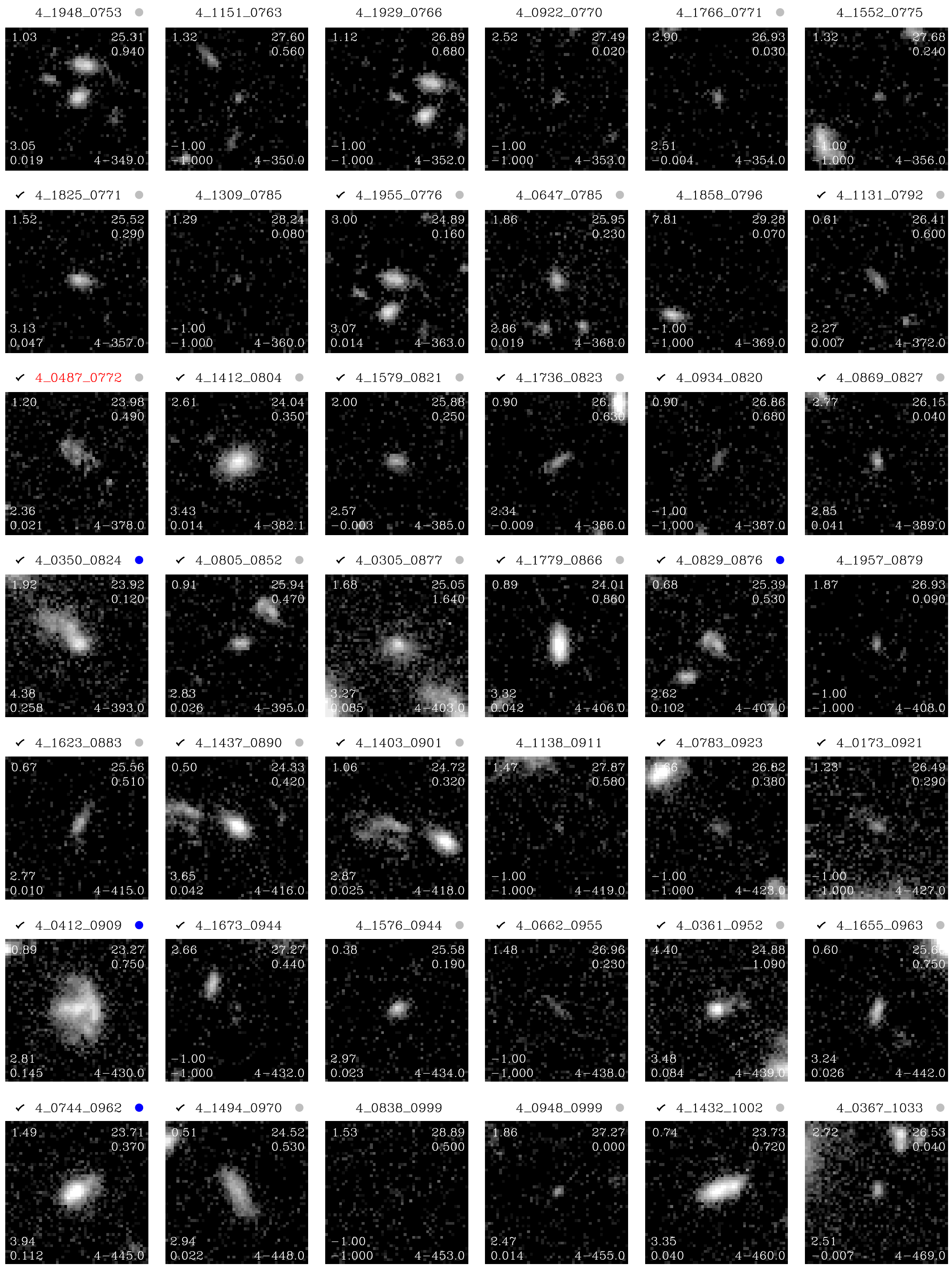

Fig. 6–1u. HDF montage *(continued)*.

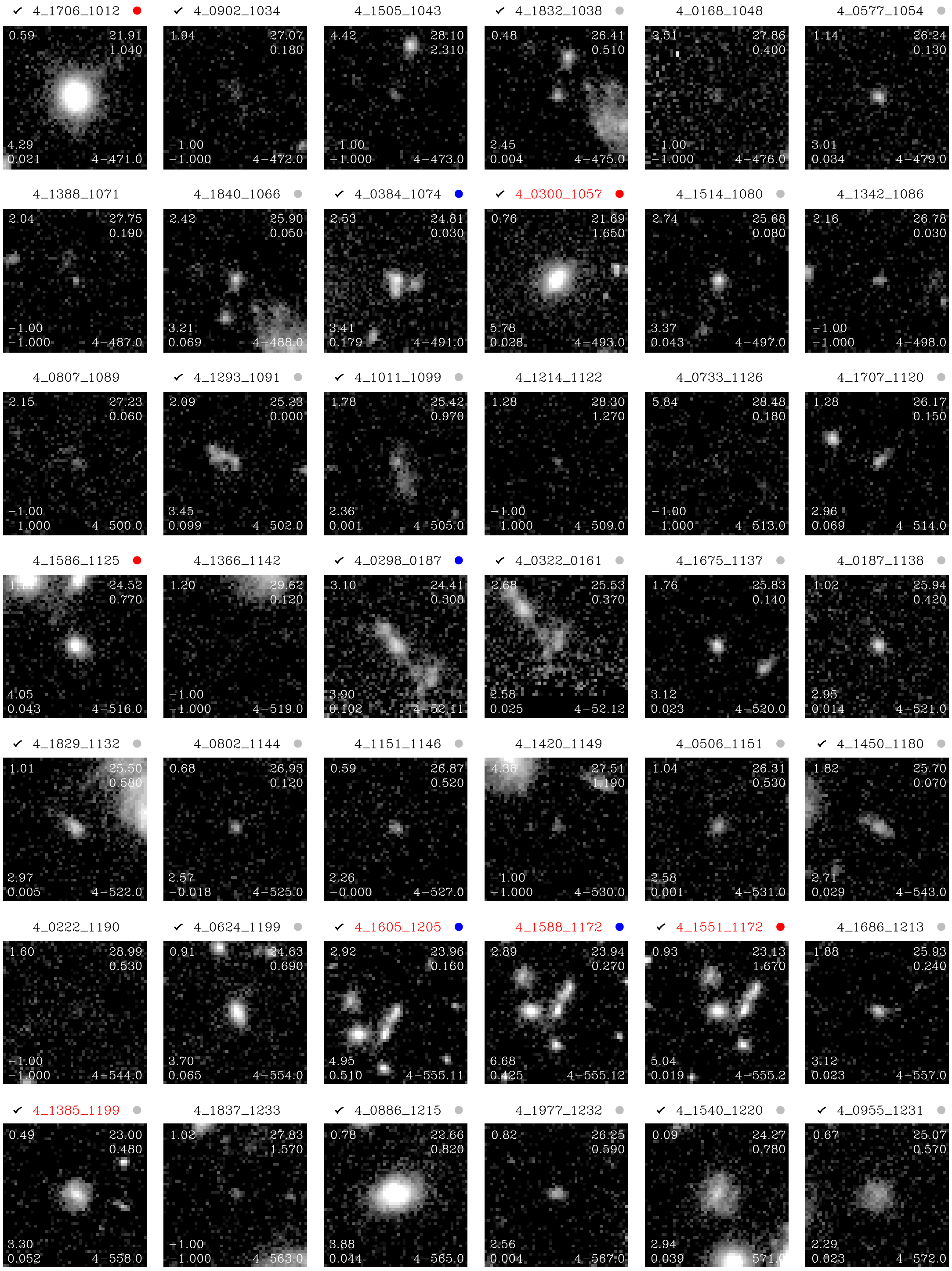

Fig. 6–1v. HDF montage *(continued)*.

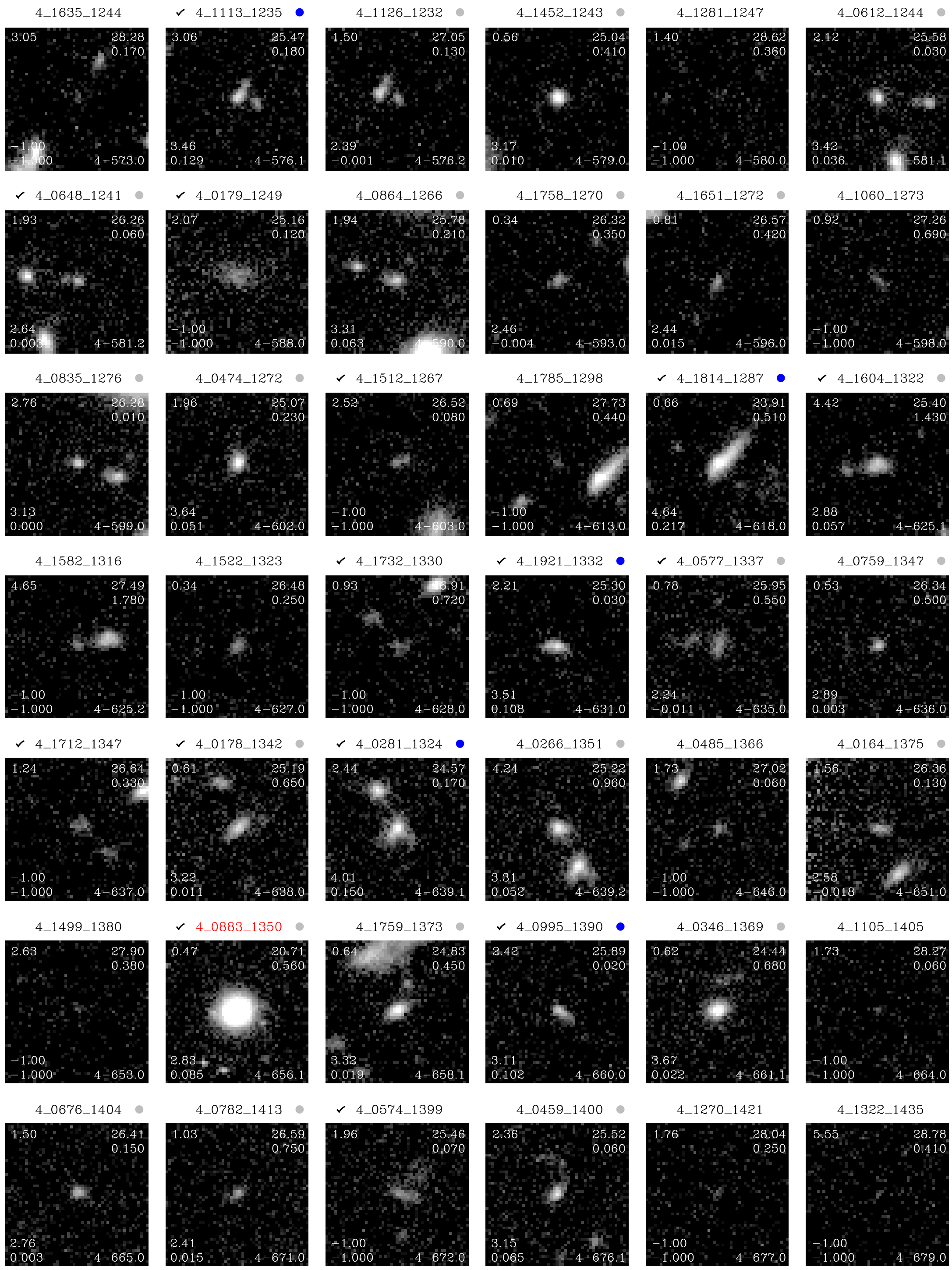

Fig. 6–1w. HDF montage *(continued)*.

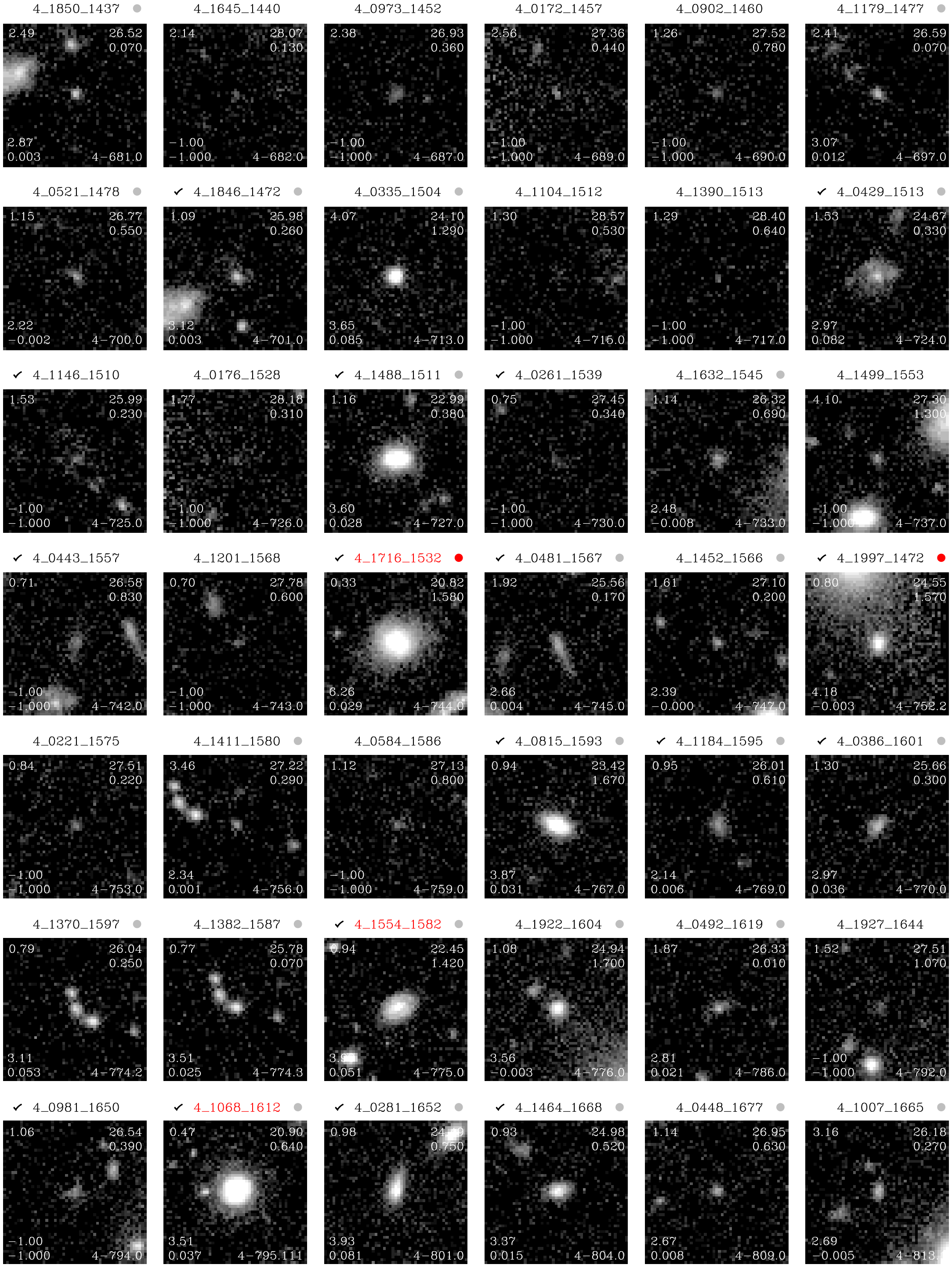

Fig. 6–1x. HDF montage *(continued)*.

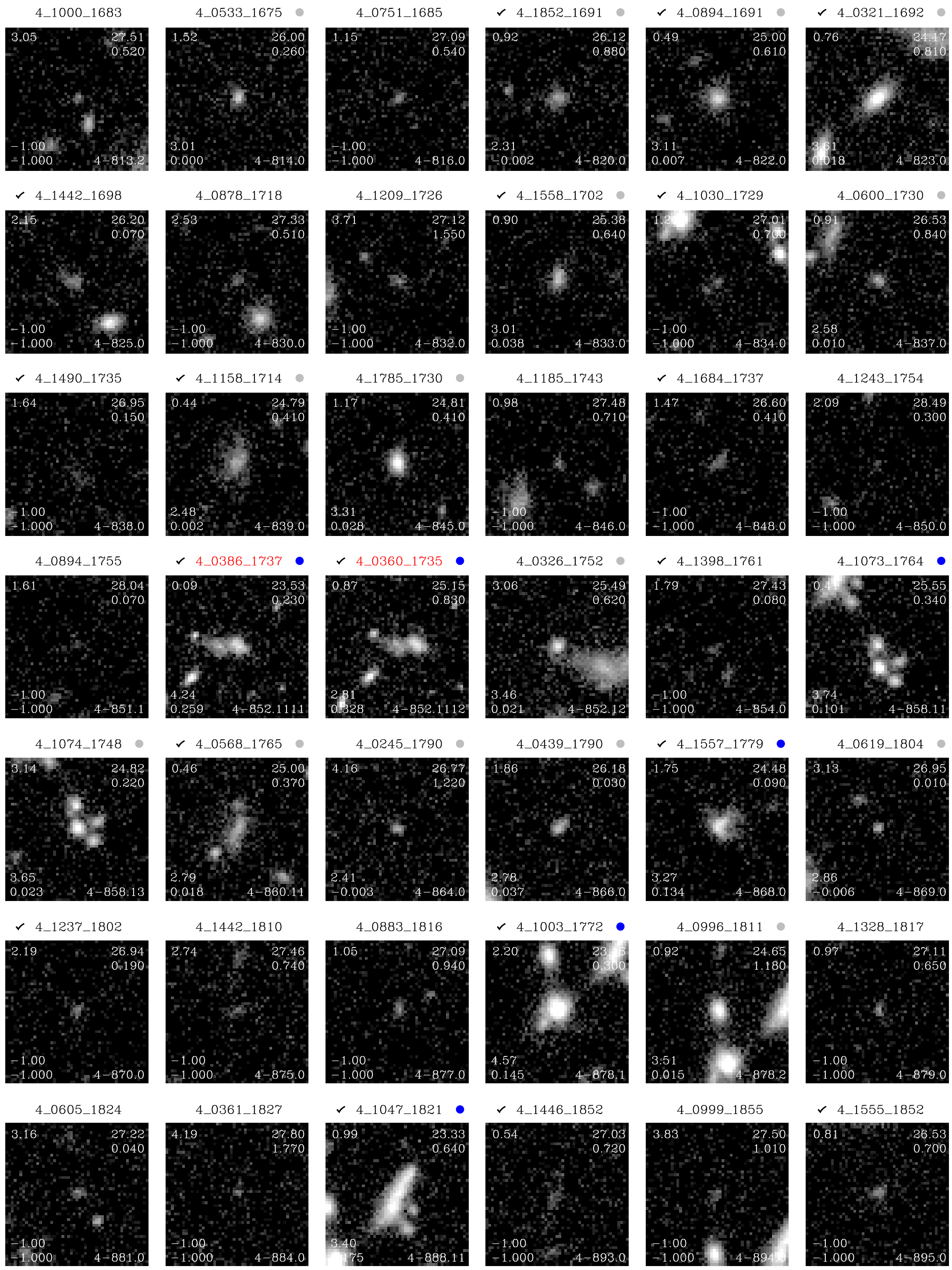

Fig. 6–1y. HDF montage *(continued).*

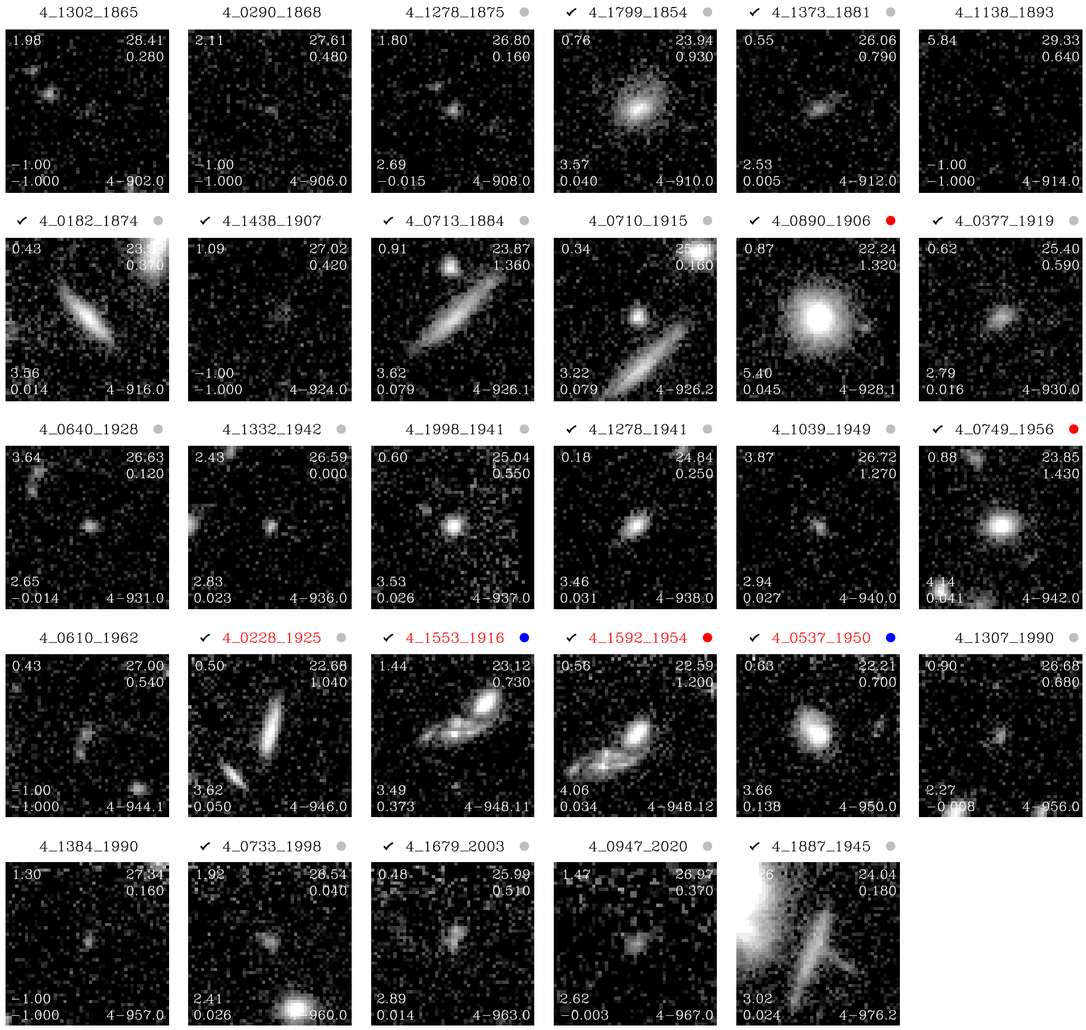

Fig. 6–1z. HDF montage *(continued)*.

1. The Raw A_W-C_W Relation for HDF Galaxies

Now that we have seen the distribution of local galaxies in the A_W-C_W plane, the application of A_W and C_W to the full HDF sample can now be studied. Figure 6–2 shows the A_W-C_W relation for all galaxies that we have measured in the W96 HDF catalog with photometric redshifts from C99. Objects are divided into five redshift bins: $z \leq 0.6$ (blue), $0.6 < z \leq 1.2$ (green), $1.2 < z \leq 2.0$ (yellow), $2.0 < z \leq 3.0$ (orange), and $z > 3.0$ (red). The symbol size is scaled to the apparent total magnitude of the objects as given in W96. One immediately sees the large number of objects with low concentration and low asymmetry. This result is also clearly seen in Figure 6–3, which presents histograms of A_W in the same five redshift bins. As will be demonstrated later through application of A_W and C_W to simulations of galaxies shrunk and dimmed by various amounts, the degradation of resolution and signal-to-noise (or, equivalently, the shrinking and dimming of a galaxy) causes both A_W and C_W to tend towards smaller values. (Recall that the limiting value of A_W is zero, although slightly negative values may occasionally appear if the background correction is larger than the raw asymmetry. C_W reaches a limiting value of 2, when the surface brightness profile is completely flat, or, alternatively, if all of the light is in a single pixel. The areas containing 80% and 20% of the light are then simply 80% and 20% of the total area; hence, r_{80}/r_{20} is 2.) Because of these selection effects, caution must be taken in interpreting the large number of low-A_W low-C_W objects.

In order to facilitate future discussion, we have divided the A_W-C_W plane into three classes:

- High-C_W consists of high concentration ($C_W > 4.0$), low asymmetry objects ($A_W < 0.10$). From Figure 5–2, one can see that, for the local sample, objects in

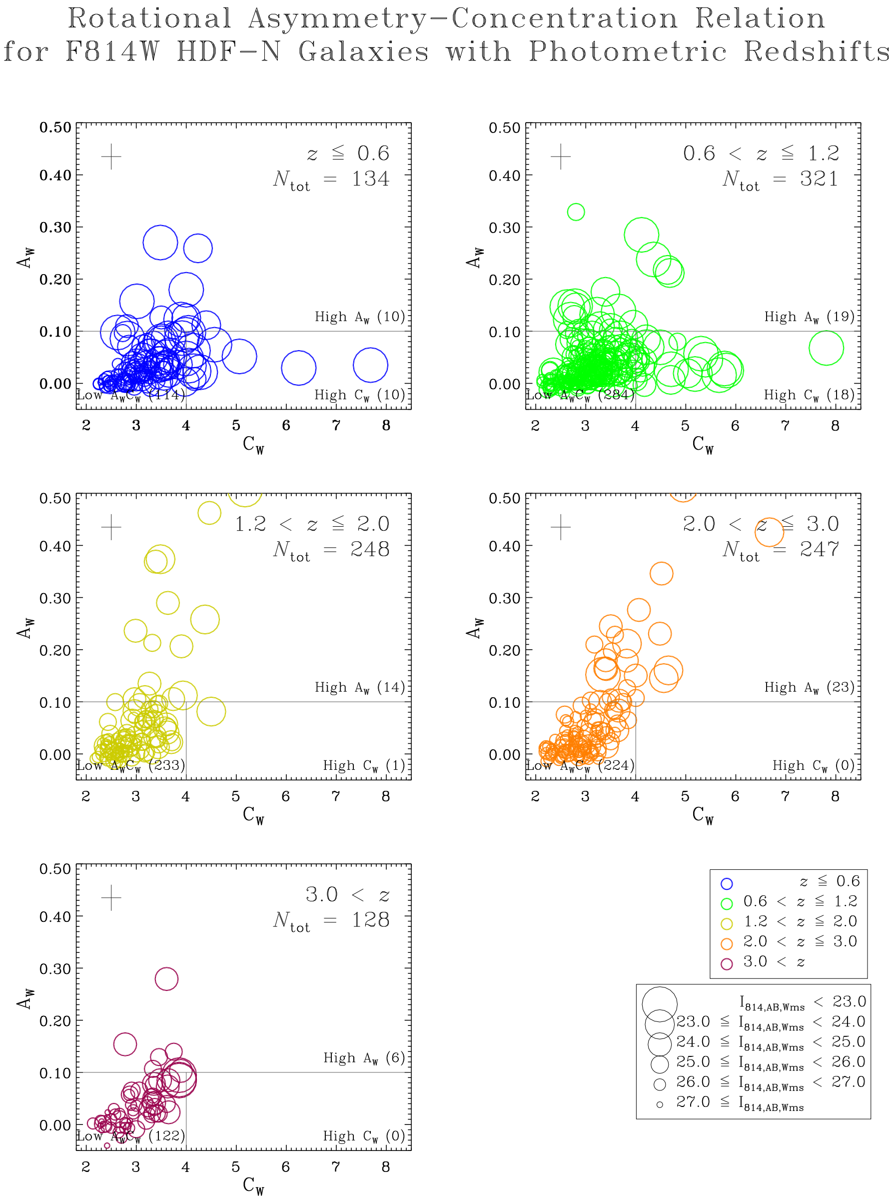

Fig. 6–2.— The A_W-C_W relation for the full HDF sample with photometric redshifts from C99. Objects are divided into five redshift bins: $z \leq 0.6$ (blue), $0.6 < z \leq 1.2$ (green), $1.2 < z \leq 2.0$ (yellow), $2.0 < z \leq 3.0$ (orange), and $z > 3.0$ (red). The symbol size is scaled to the apparent total magnitudes of the objects as given in W96: large symbols are bright objects, smaller symbols correspond to progressively fainter objects. Thin lines separate the three A_W-C_W classes, which are labeled with the class name and the number of objects within that class. Representative estimated errors in A_W and C_W are indicated by the error bars in the top left corner. The redshift bins and the total number of objects in each redshift bin are indicated in the top right corner.

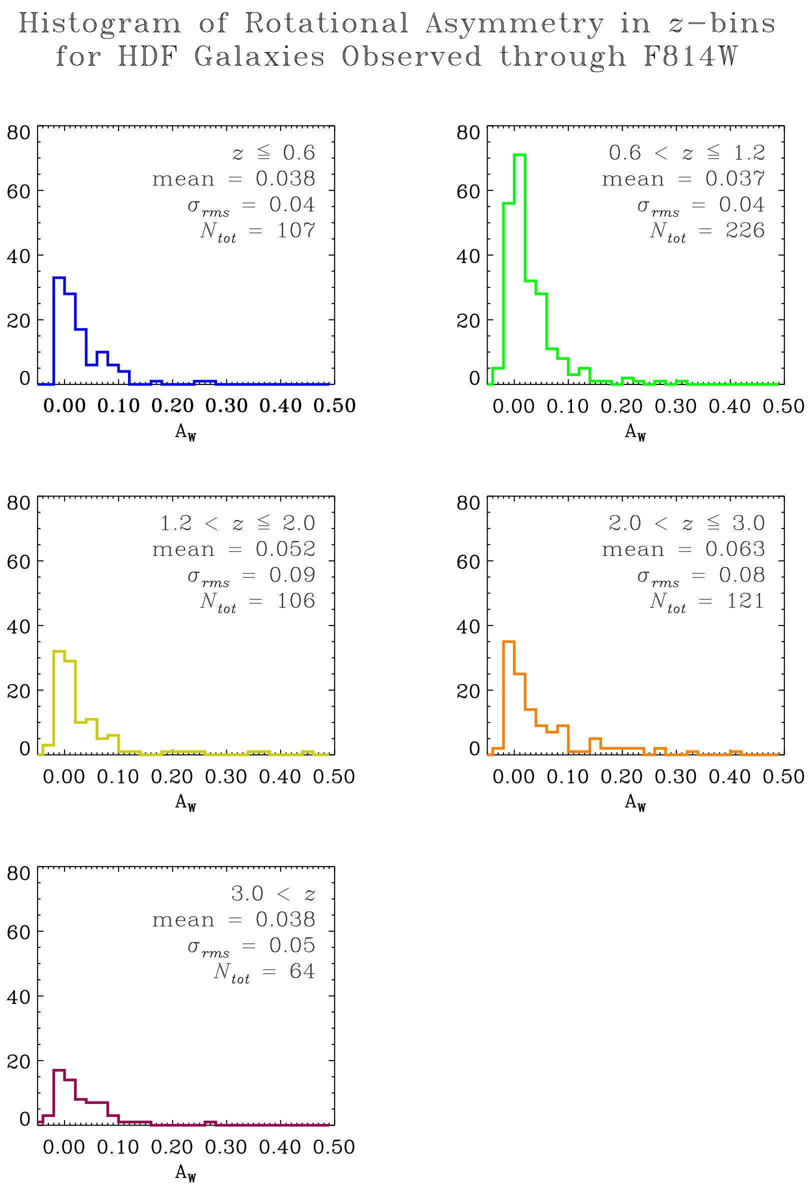

Fig. 6–3.— Histograms of A_W for the full HDF sample with photometric redshifts from C99 divided into five redshift bins. The mean and standard deviation of the distribution of asymmetries are noted in the top right corner.

this class are typically bright ellipticals with a few regular early-type spirals. The peculiar galaxy, NGC 7252, also falls in this class, but, as mentioned earlier, this galaxy is dominated by a bright symmetric core. Relative to other galaxies in this class, NGC 7252 still shows a significantly higher A_W. In the high redshift sample, this class is also dominated by early-type objects. (See Figure 6–4.)

- Low-$A_W C_W$ consists of low concentration ($C_W < 4.0$), low asymmetry objects ($A_W < 0.10$). In the local sample, these are typically mid- to late-type spirals and irregulars. At high redshift, however, the situation is a bit more complicated. Late-type spirals and irregulars do indeed continue to populate this part of the A_W-C_W diagram. As will be shown in later simulations, however, many other galaxies are driven into the Low-$A_W C_W$ regime simply because they are too small and faint to be able to resolve their structure. The wide range of objects in this class can be seen in Figure 6–5.

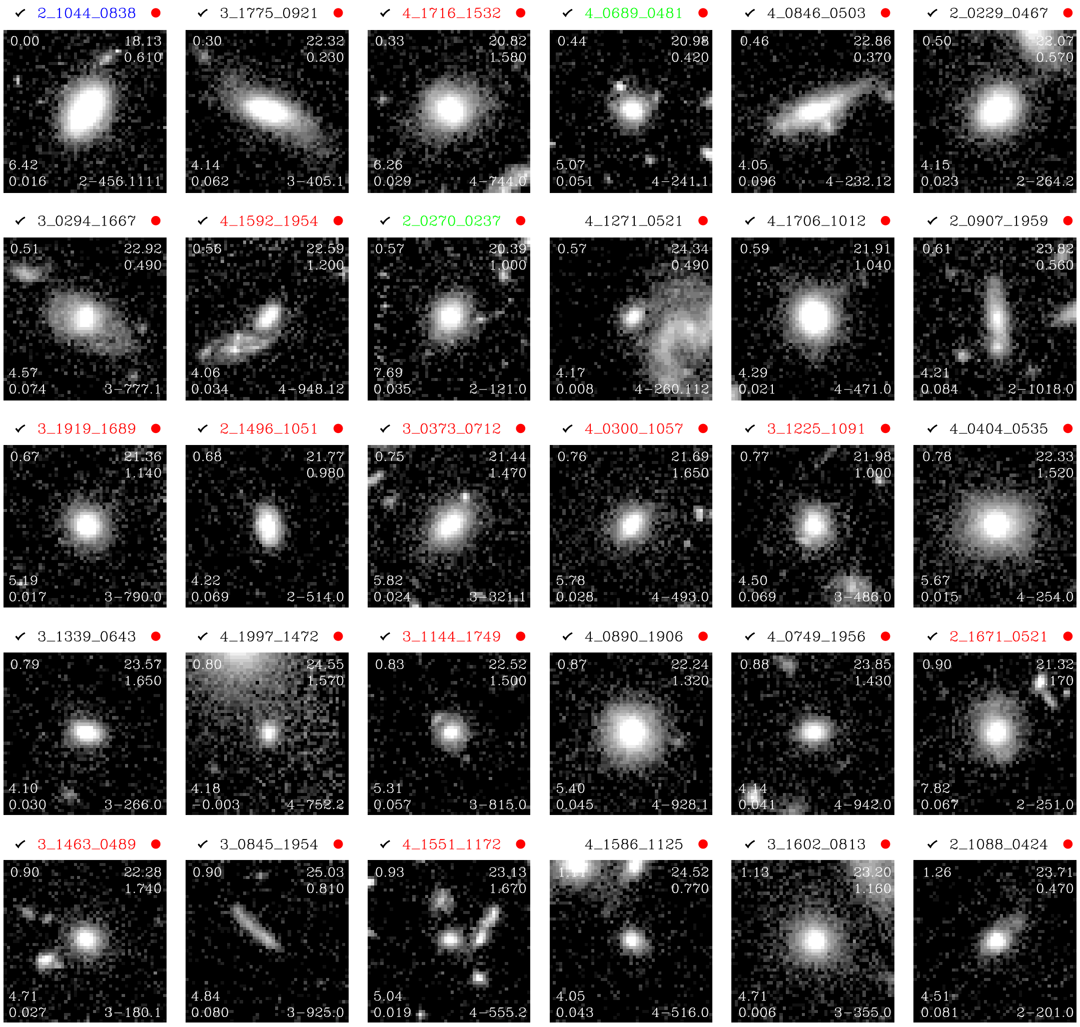

Fig. 6–4.— Montage of High-C_W objects in the HDF, in order of increasing redshift. Annotation and symbols are the same as was described for the full montage (Figure 6–1). As expected, most have early-type morphologies. Two objects appear, however, that may not normally be expected to have high concentrations: hdf2_0907_1959 and hdf3_0845_1954. In both of these case, the galaxy contains a fairly bright, compact core (not so obvious for hdf3_0845_1954 on the hardcopy) with a diffuse envelope. This combination is the likely cause of the high value of C_W for these two objects.

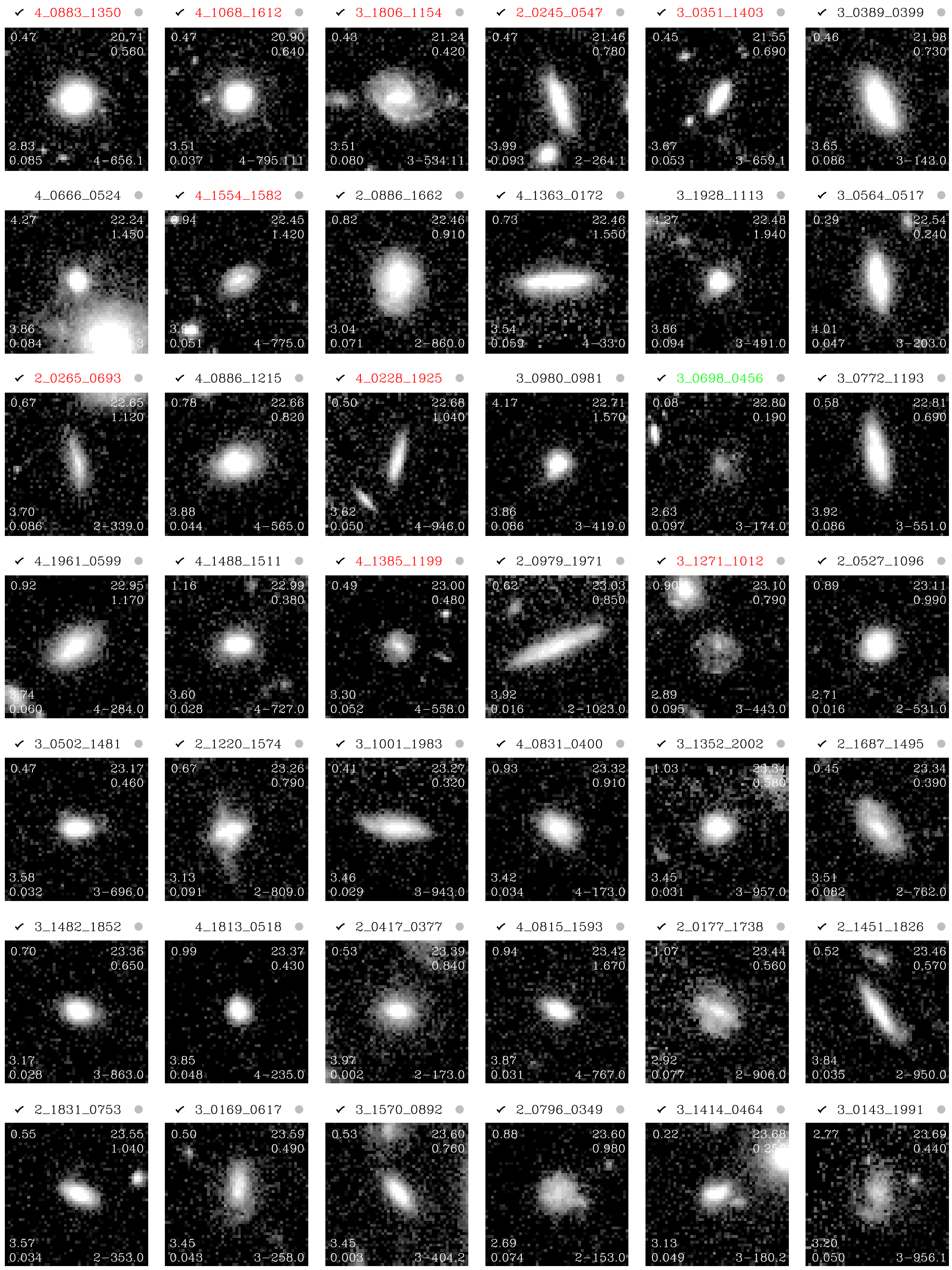

Fig. 6–5.— Montage of Low-$A_W C_W$ objects in the HDF, in order of increasing magnitude. Annotation and symbols are the same as was described for the full montage (Figure 6–1). This class contains a wide variety of objects ranging from typical spirals, similar to the local sample, to small, faint objects for which meaningful morphological information is difficult to obtain.

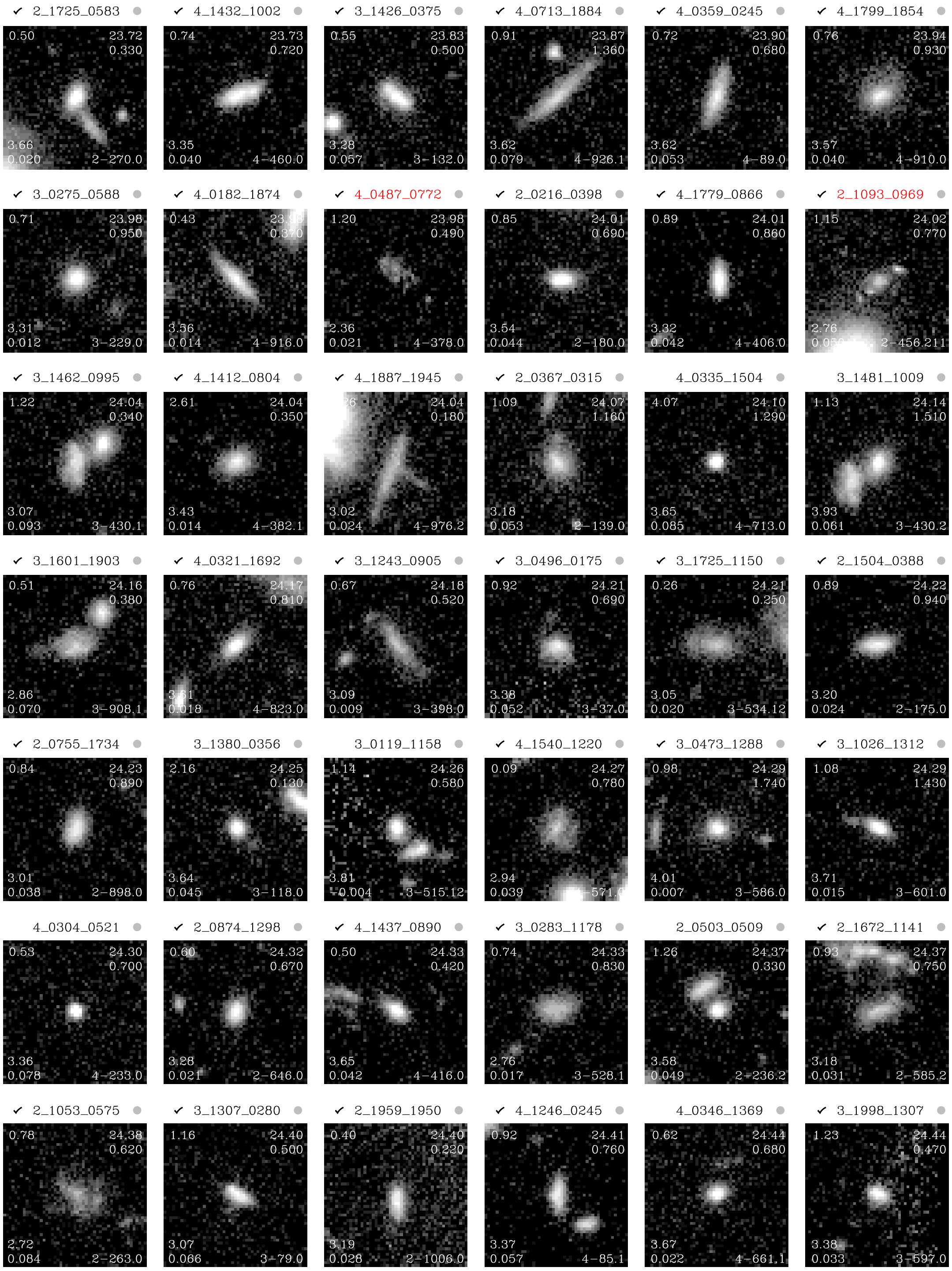

Fig. 6–5b. Low-$A_W C_W$ montage *(continued).*

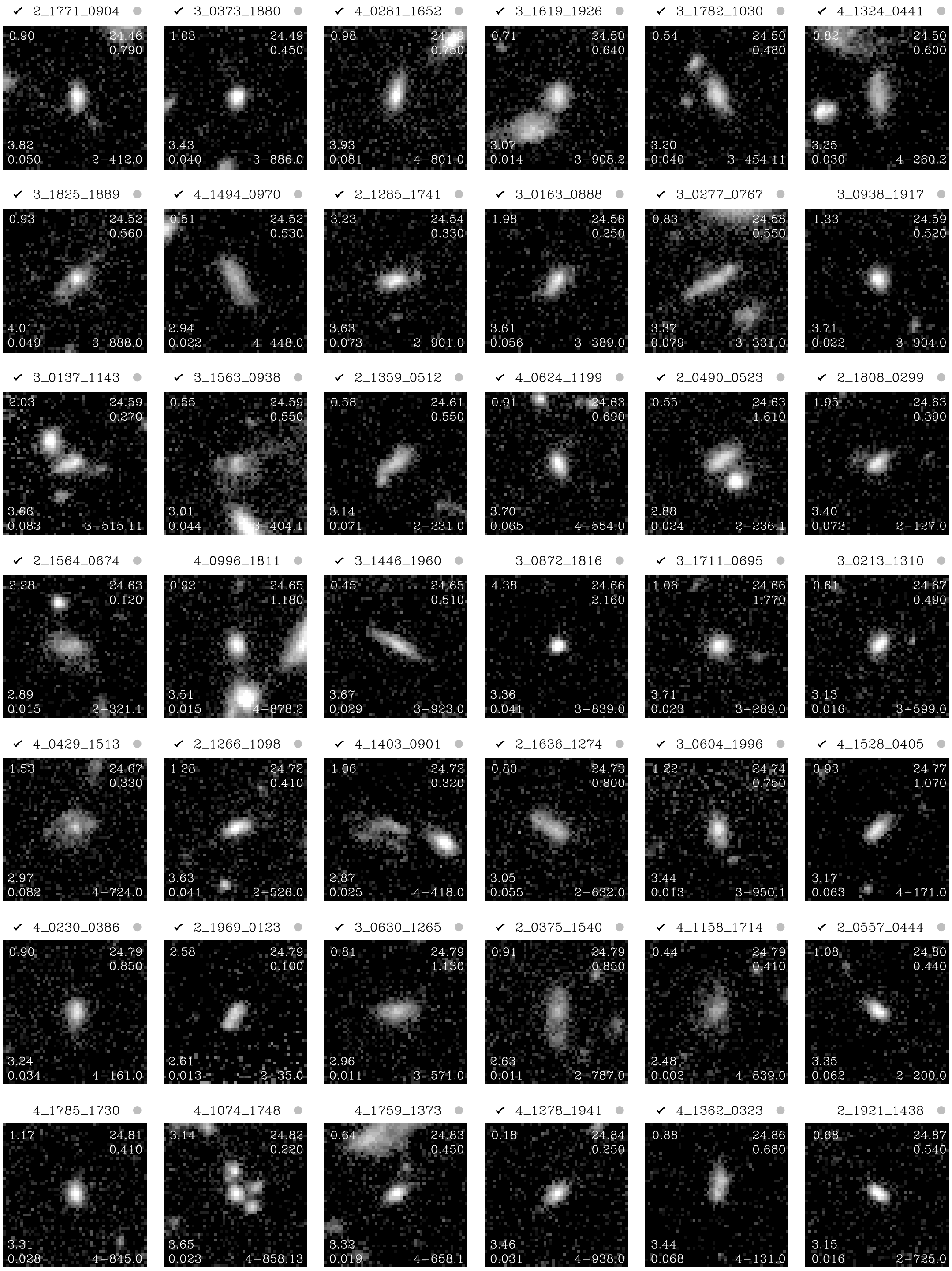

Fig. 6–5c. Low-$A_W C_W$ montage *(continued)*.

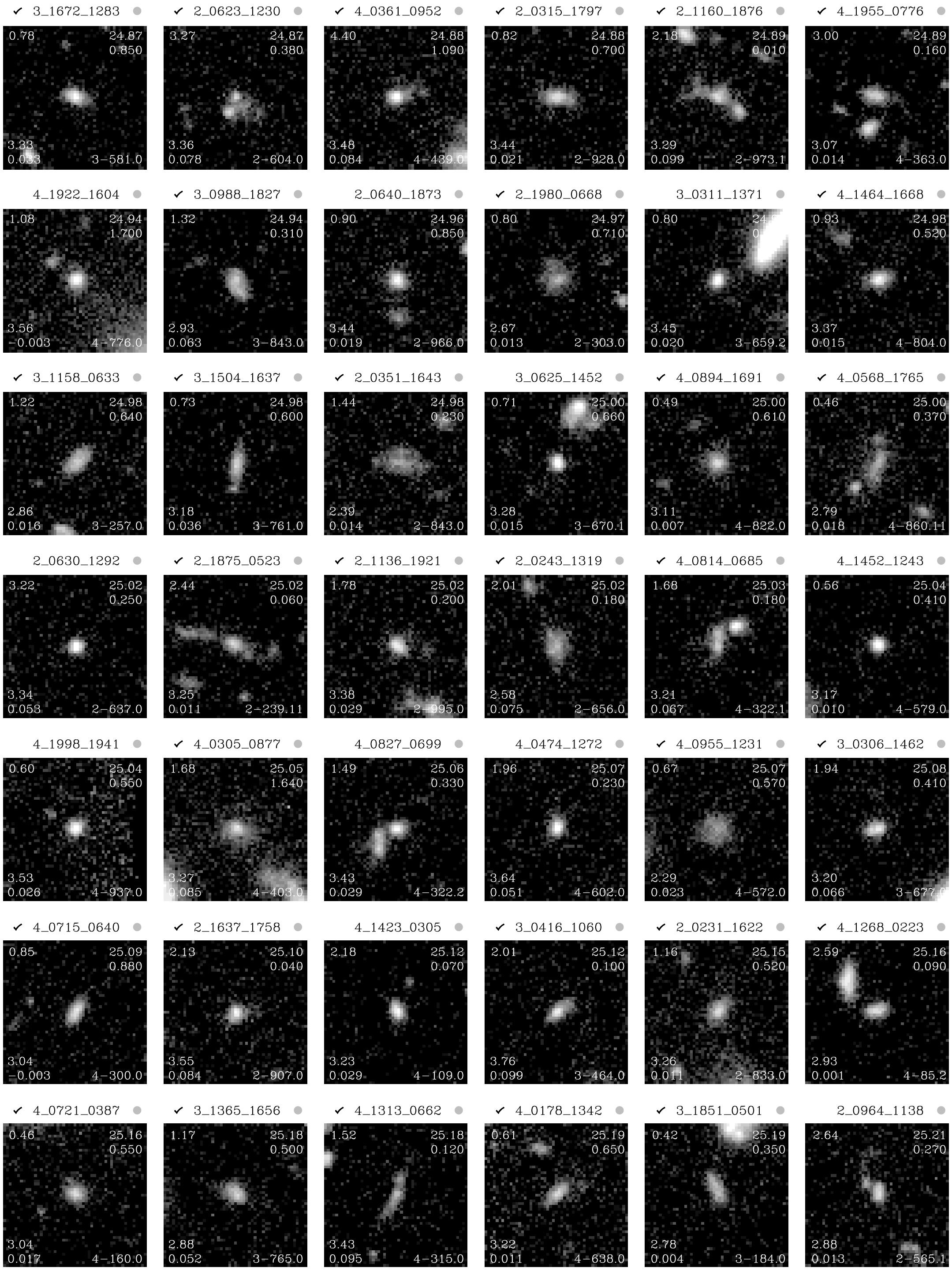

Fig. 6–5d. Low-$A_W C_W$ montage *(continued).*

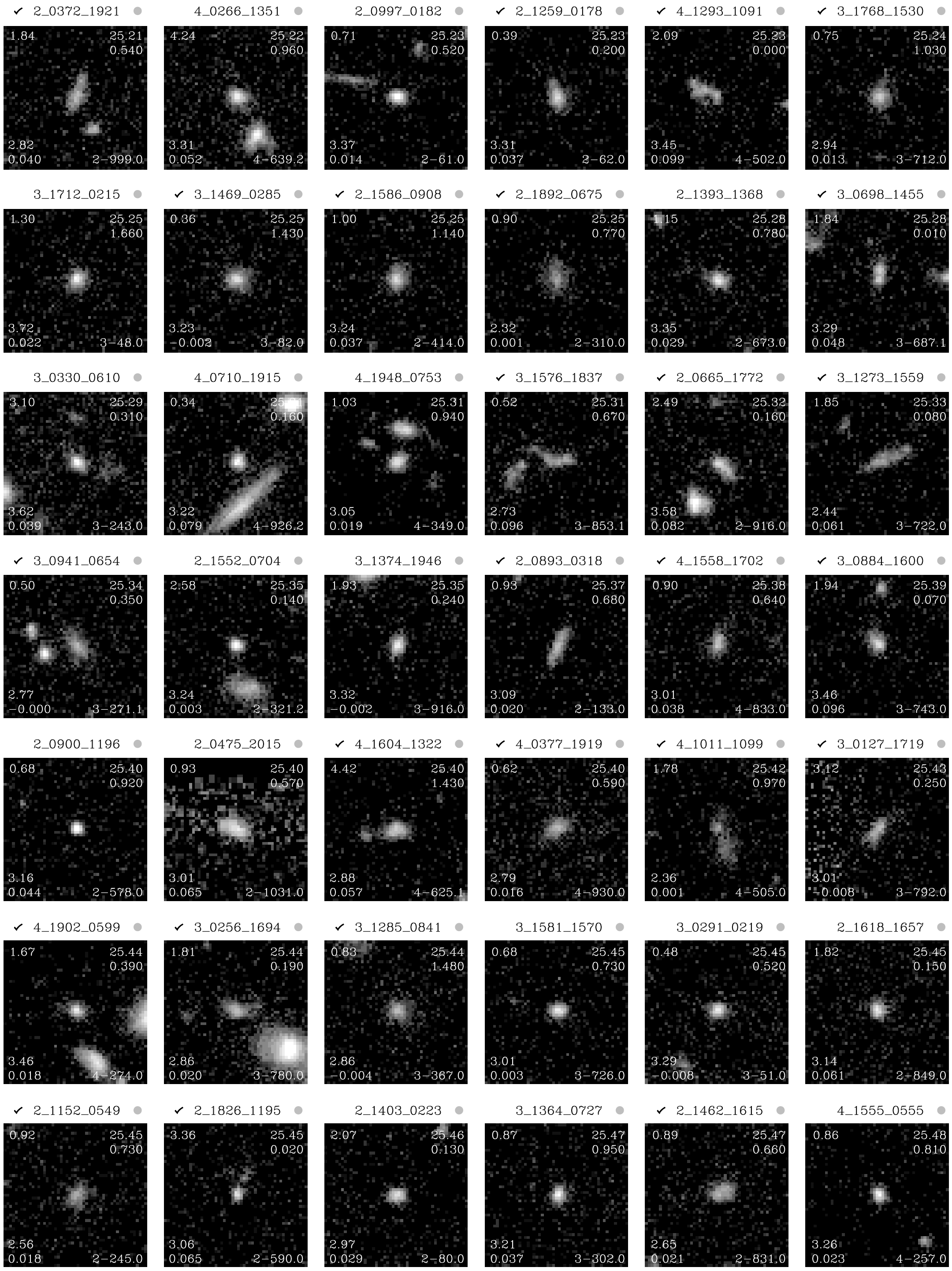

Fig. 6–5e. Low-$A_W C_W$ montage *(continued).*

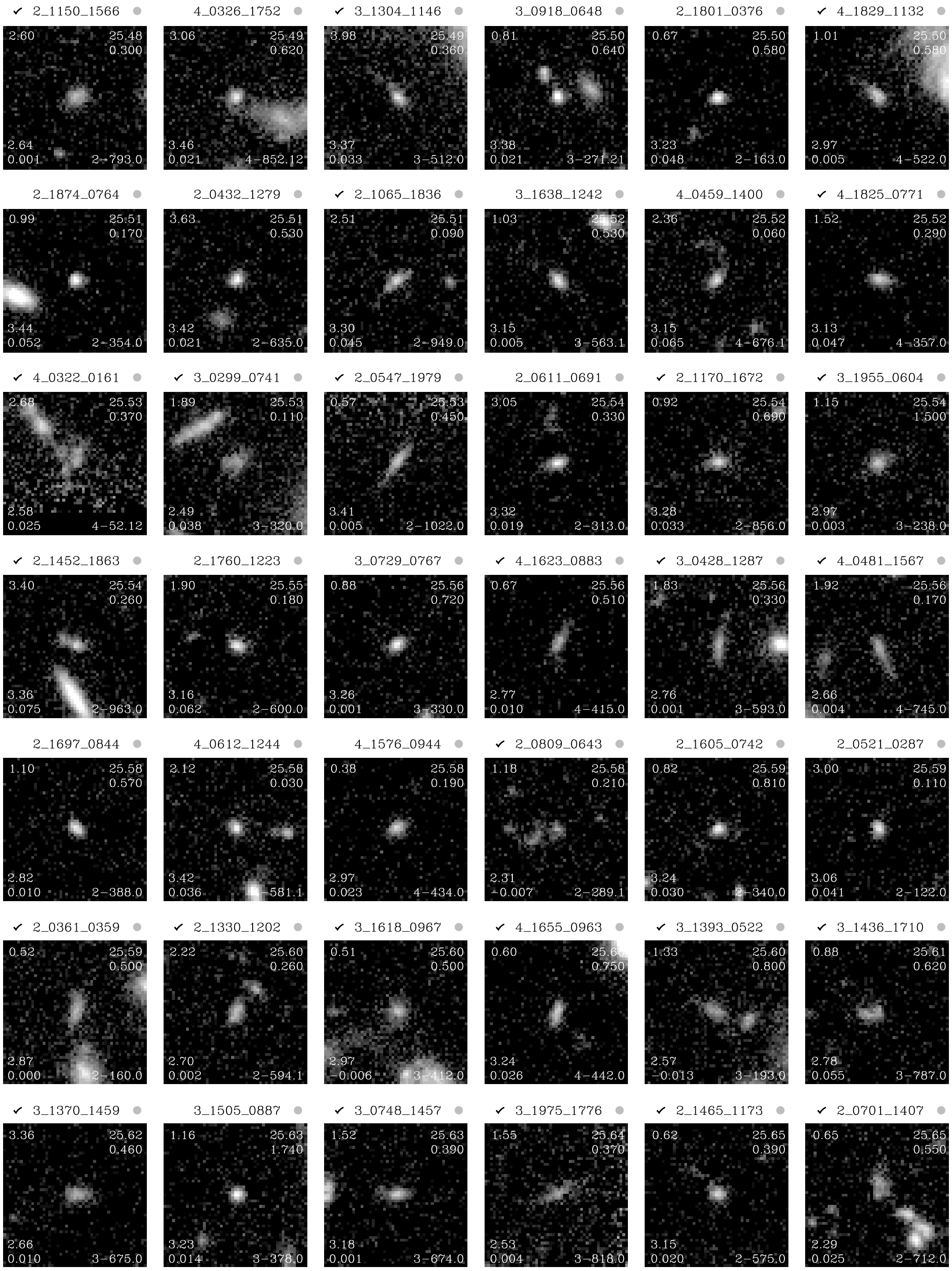

Fig. 6–5f. Low-$A_W C_W$ montage *(continued)*.

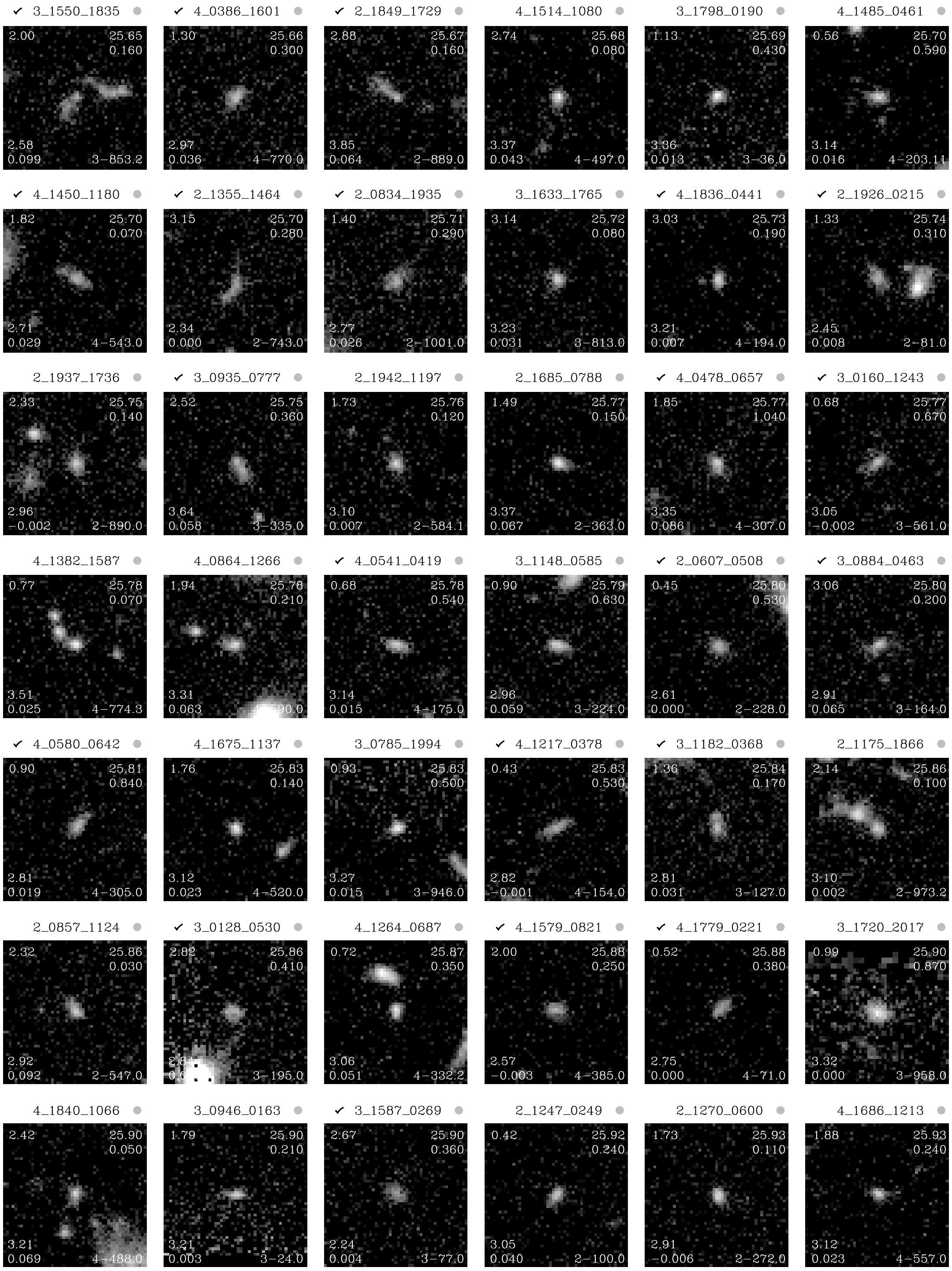

Fig. 6–5g. Low-$A_W C_W$ montage *(continued).*

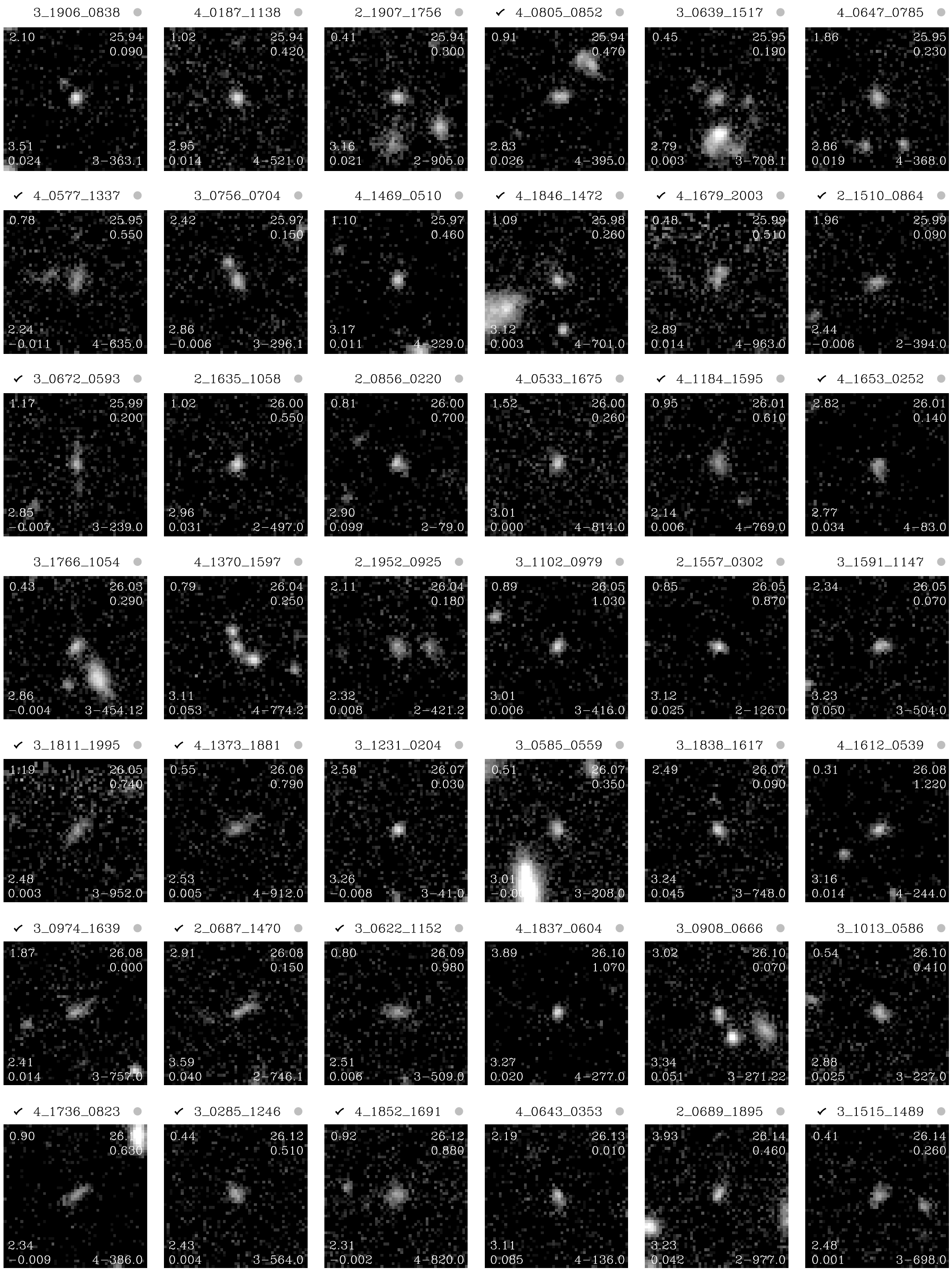

Fig. 6–5h. Low-$A_W C_W$ montage *(continued).*

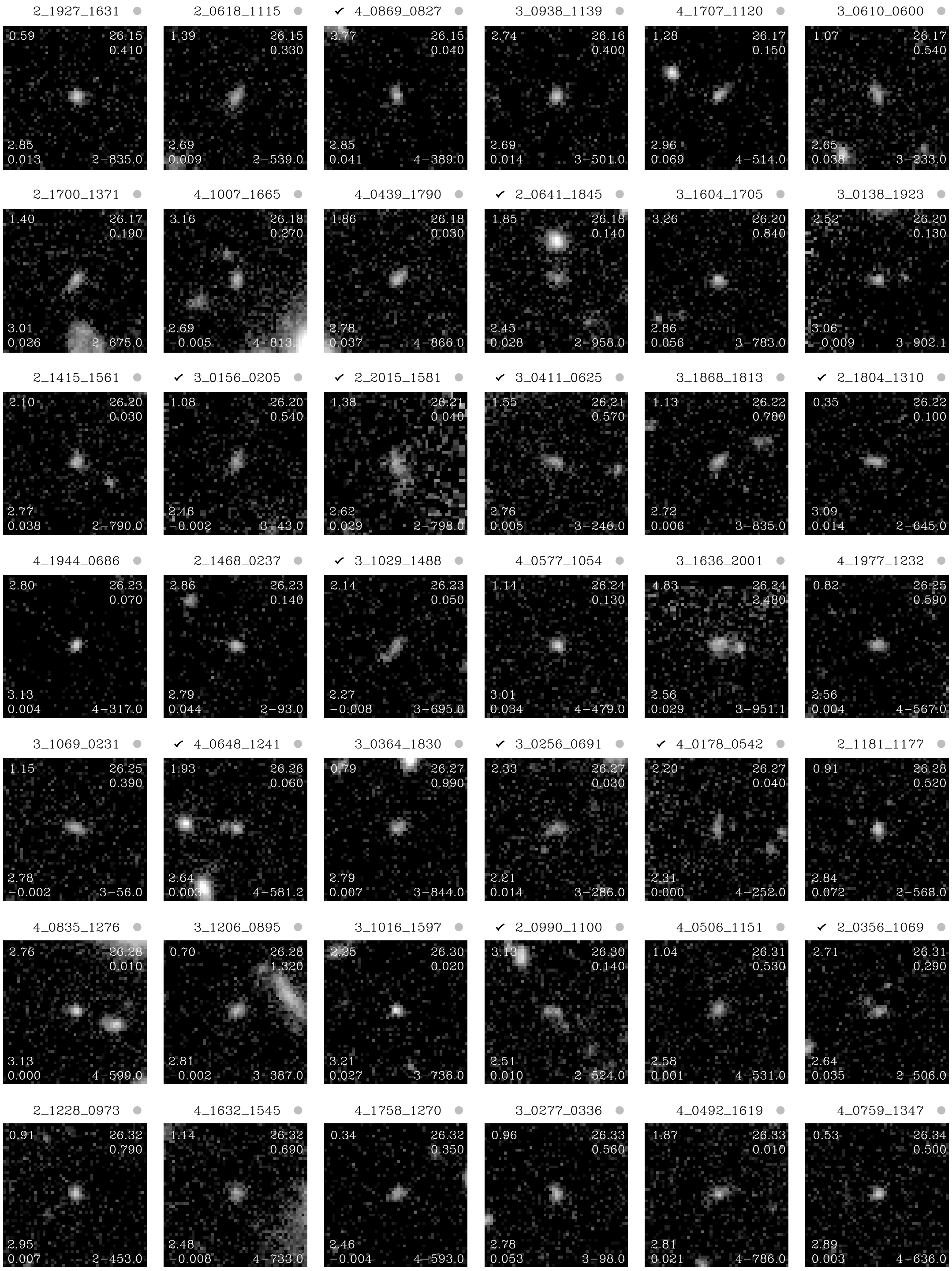

Fig. 6–5i. Low-$A_W C_W$ montage *(continued).*

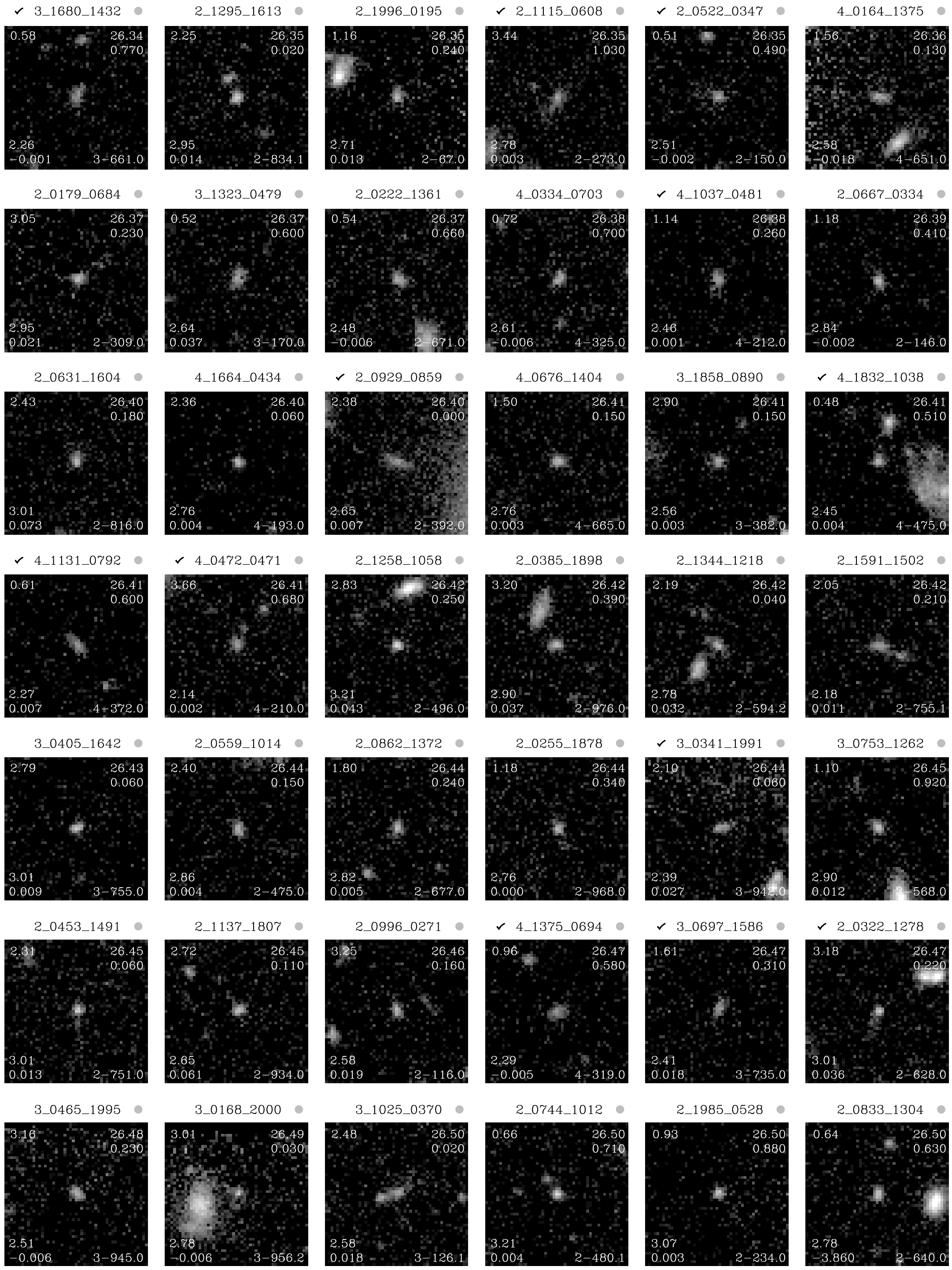

Fig. 6–5j. Low-$A_W C_W$ montage *(continued)*.

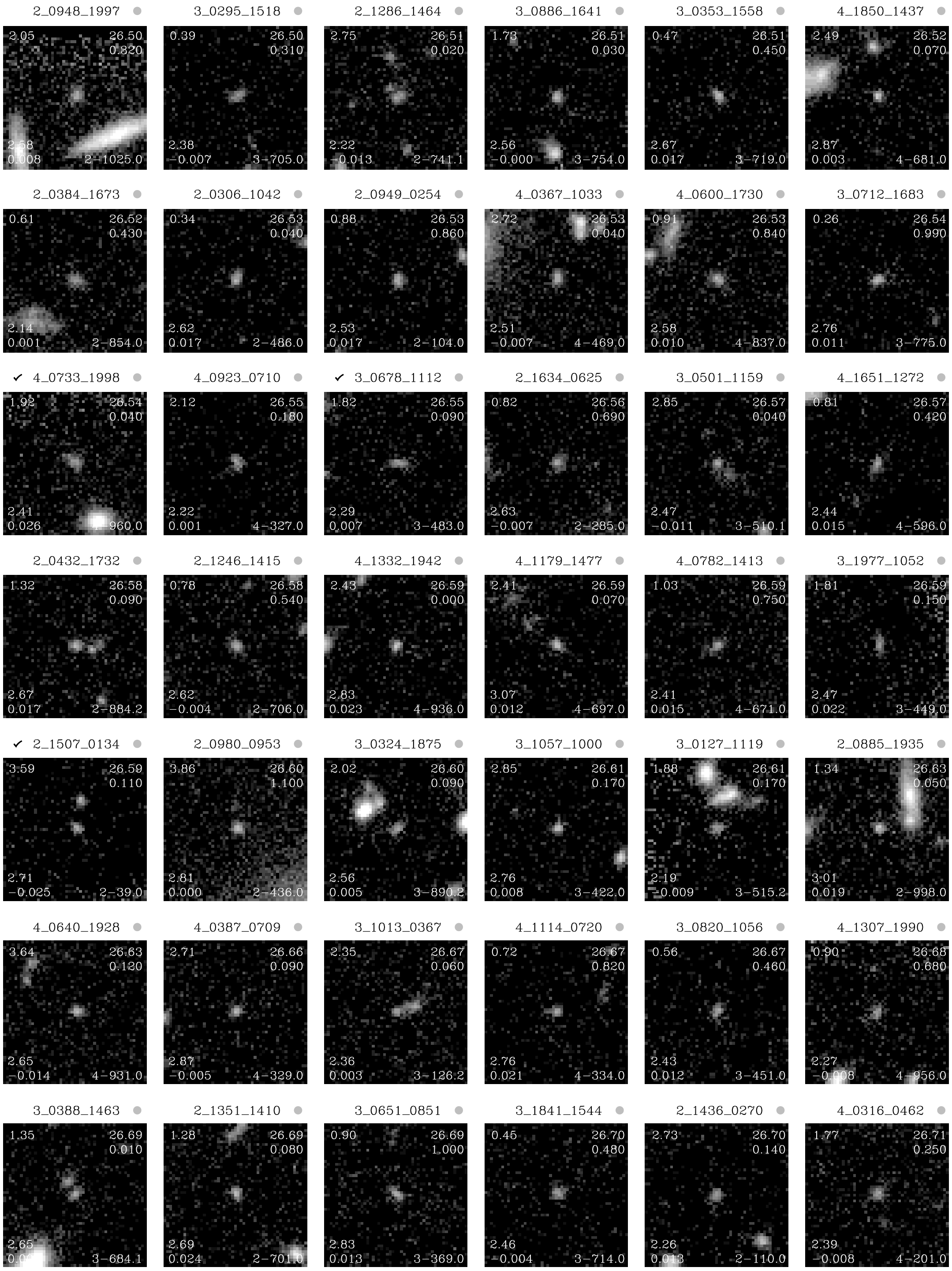

Fig. 6–5k. Low-$A_W C_W$ montage *(continued)*.

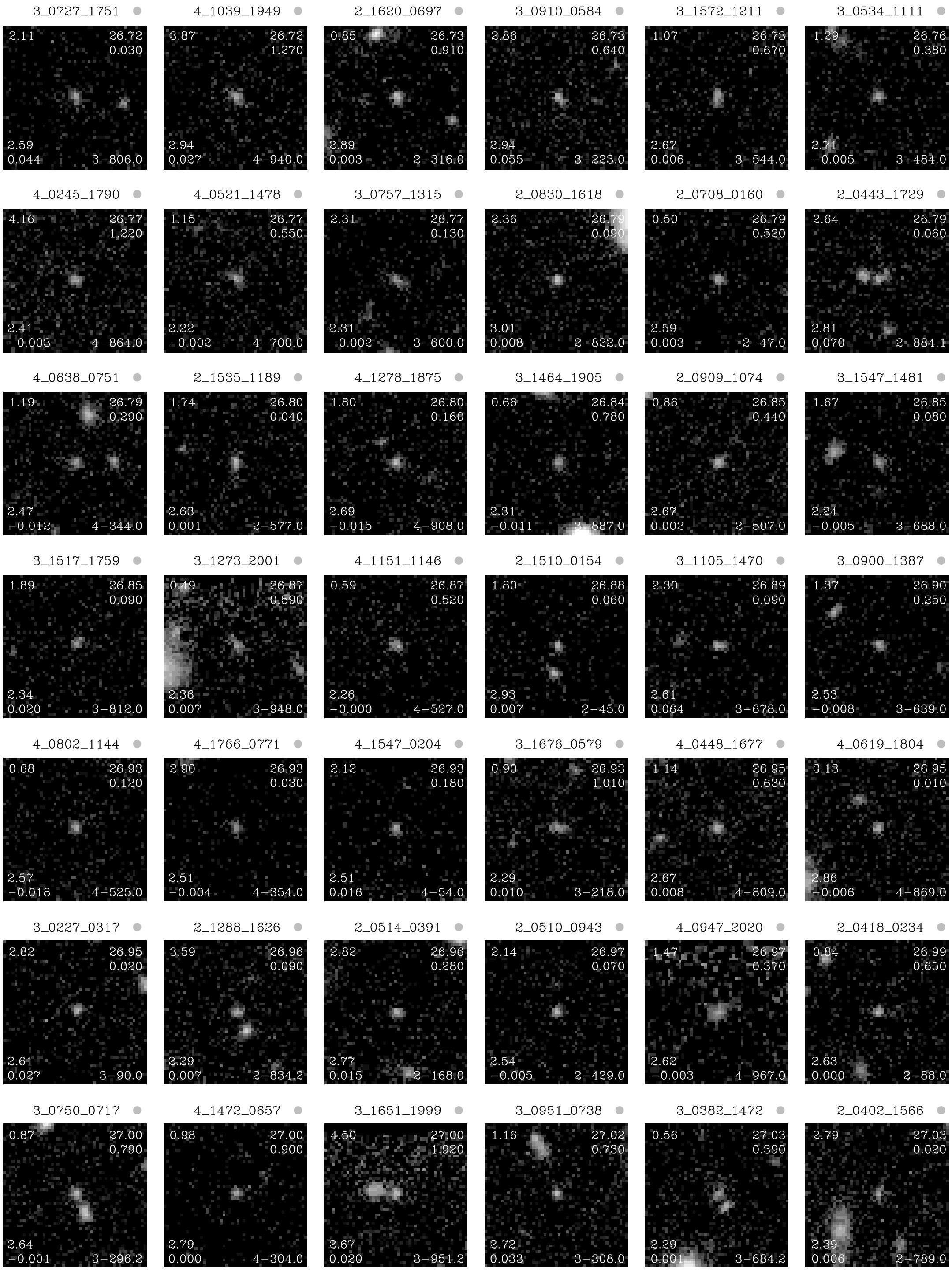

Fig. 6–5l. Low-$A_W C_W$ montage *(continued)*.

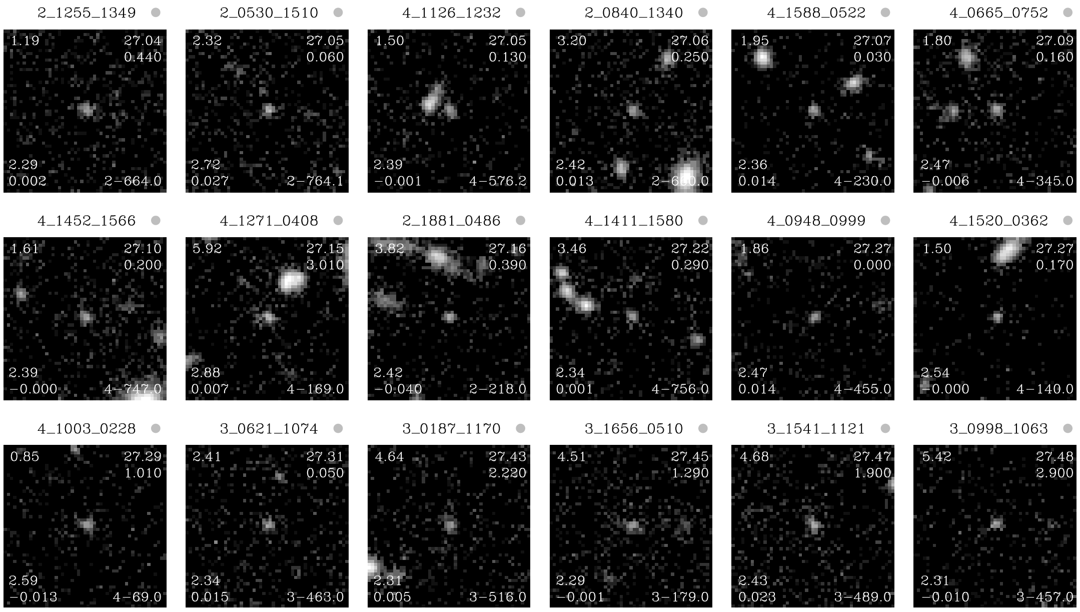

Fig. 6–5m. Low-$A_W C_W$ montage *(continued)*.

- High-A_W includes all high asymmetry objects ($A_W > 0.10$). For the local sample, this includes the two peculiar galaxies, NGC 520 and NGC 2623, as well as several of the "normal" spirals that show interesting structure indicative of possible interactions in the recent history of the galaxy. At high redshift, a wide range of interesting objects populate this part of the A_W-C_W diagram. (See Figure 6–6.)

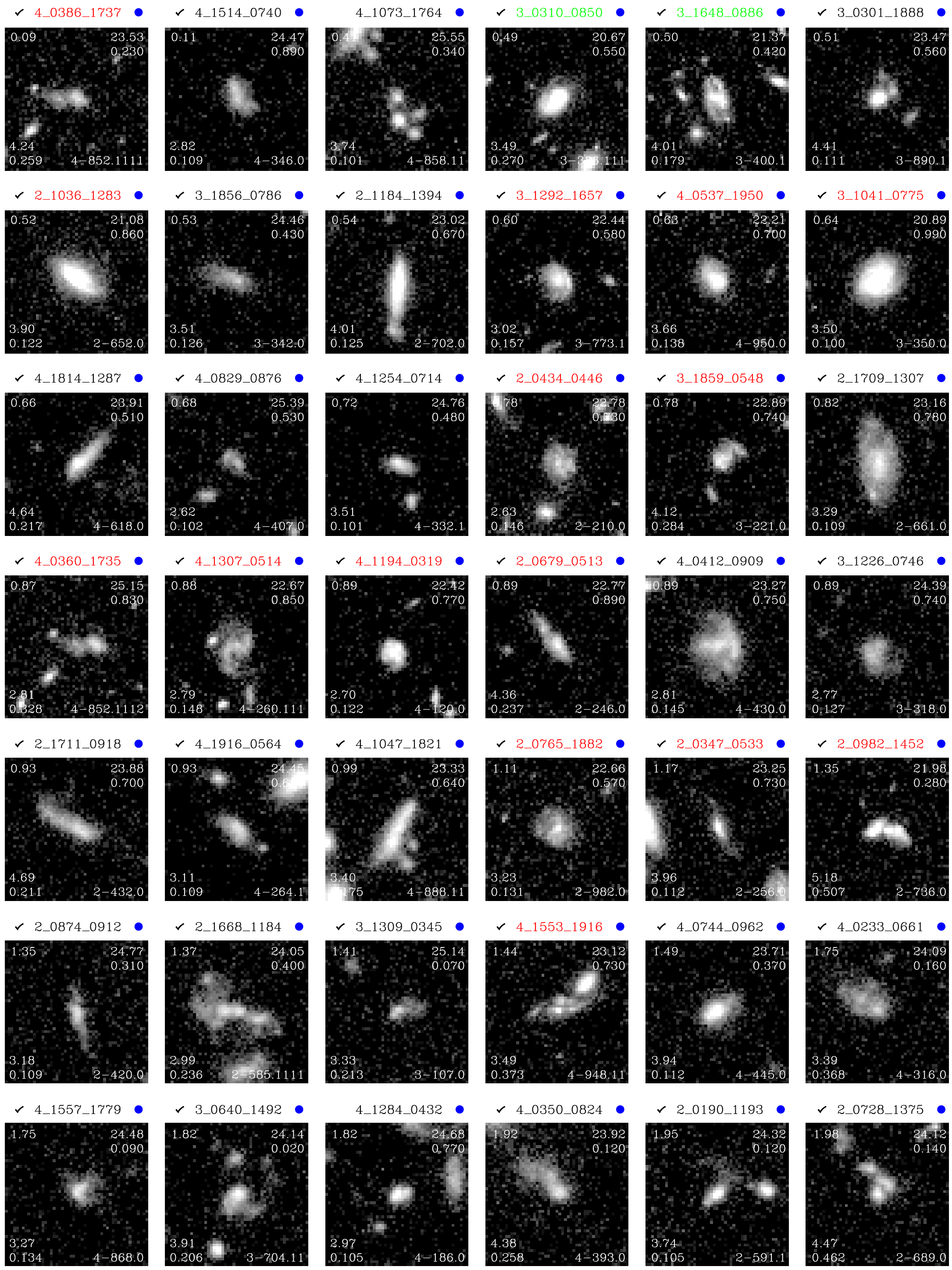

Fig. 6–6.— Montage of High-A_W objects in the HDF, in order of increasing redshift. Annotation and symbols are the same as was described for the full montage (Figure 6–1). A quick glance at these galaxies illustrates the wide variety of peculiar morphologies that exist.

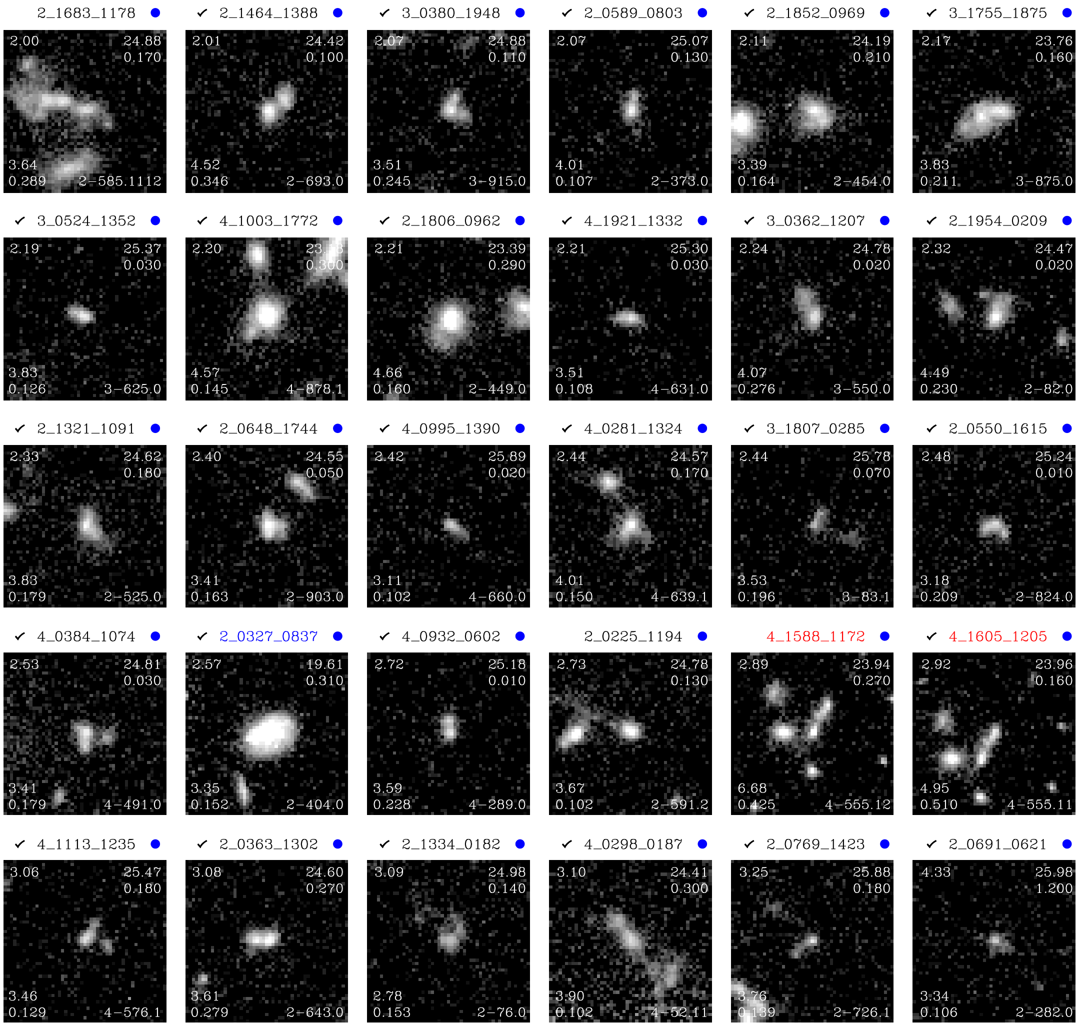

Fig. 6–6b. High-A_W montage *(continued).*

The boundaries between these three classes, especially the selected asymmetric-symmetric boundary, will impact conclusions drawn later. The choice of these boundaries will be discussed in light of simulations to be presented later.

For the moment, however, another issue needs to be resolved. The statistics of the distribution of objects in the A_W-C_W plane is dominated by the large number of objects in Low-$A_W C_W$(Figure 6–3). Most of these objects are small, faint objects for which small values of A_W and C_W are obtained simply because their structure is poorly resolved. It is useful, therefore, to "prune" the sample to only those objects for which meaningful values of A_W and C_W can be measured.

One means of determining which objects to prune is to consider the magnitudes and sizes of objects for which we can clearly measure asymmetries. In Figure 6–7, the magnitudes and sizes of High-A_W objects are compared to those of the full HDF sample. One can see that no High-A_W objects are found fainter than F814W$_{AB} \sim 26$, and very few are found to be smaller than $r_{1,W96} \sim 0\farcs2$, i.e., $\log(r_{1,W96}) \sim -0.7$. Ultimately, the sample was pruned using only a radial cut of $r_{1,W96} = 0\farcs2$, as this seemed to be more physically motivated. High-A_W objects are likely active star-bursting objects. Using a magnitude cut may result in losing objects that are physically similar to High-A_W objects, simply without such strong star formation. Using a radial cut, on the other hand, works to some degree in the opposite sense. The radius of a star-bursting object is more likely to be underestimated, simply because the bright burst may dominate the light profile. Since it is preferable to include as many objects to which our High-A_W objects may be comparable, the radial cut was chosen, keeping in mind that some of the smallest objects in this "pruned" sample may be, in reality, physically smaller than High-A_W objects.

2. The Pruned A_W-C_W Relation for HDF Galaxies

Figure 6–8 presents the A_W-C_W distribution of the "pruned" HDF sample divided, as in Figure 6–2 above, into five redshift bins. Without the huge pile-up of small, dim objects

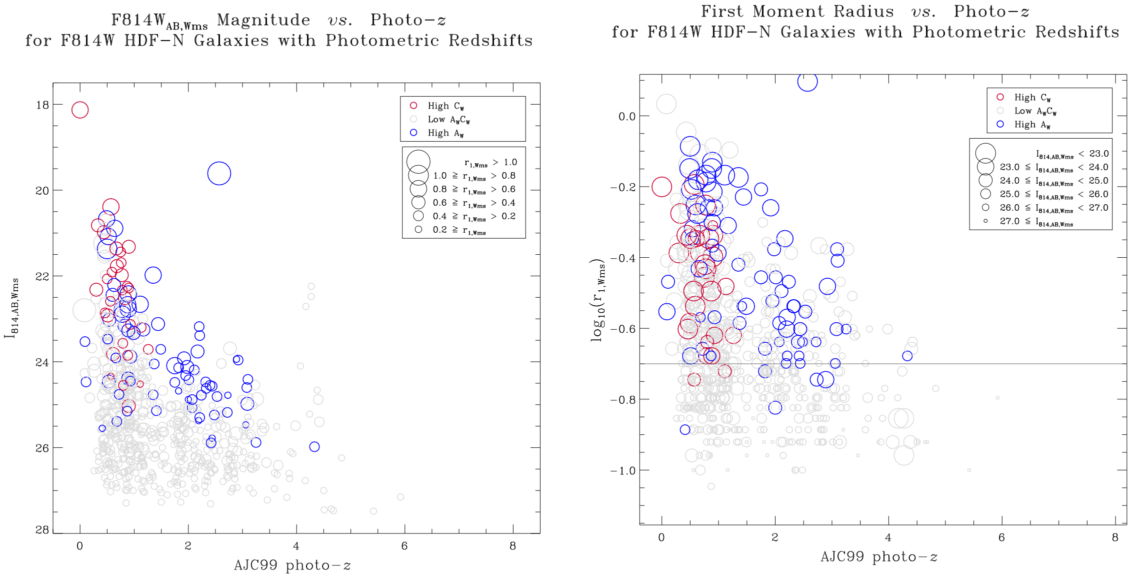

Fig. 6–7.— Comparison of magnitudes and sizes of High-A_W objects relative to the full HDF sample. All High-A_W objects are brighter than F814W$_{AB} \sim 26$, and most are larger than $r_{1,W96} \sim 0.''2$. This latter value is used to create the pruned sample (denoted by a check mark in the full HDF montage).

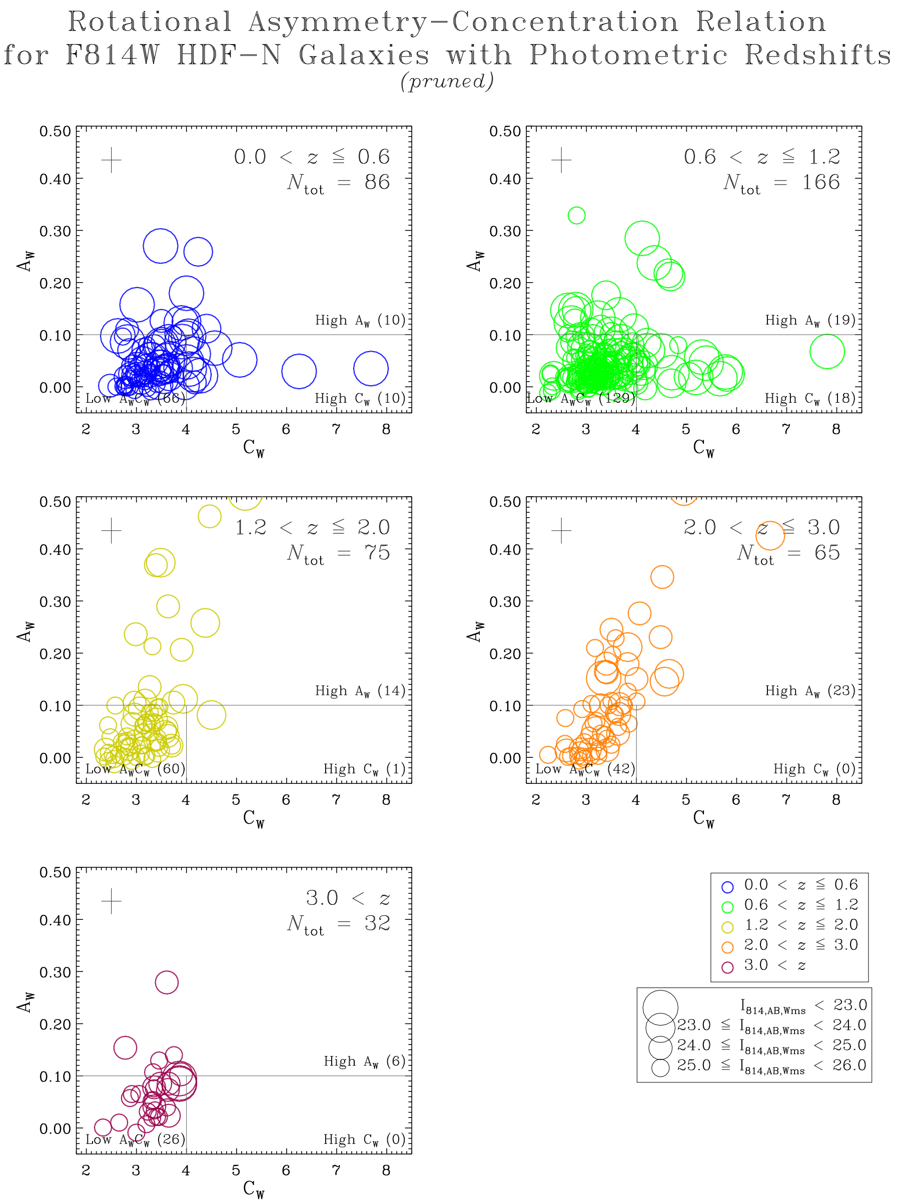

Fig. 6–8.— The A_W-C_W relation for the pruned HDF sample with symbols scaled to total apparent F814W$_{AB}$ magnitude. Symbols, lines, and annotation are the same as that of Figure 6–2. Without the large numbers of small, faint objects in the Low-$A_W C_W$ corner, the drift of the mean asymmetry to higher values at higher redshifts is much more evident. In fact, the mean value of A_W for the pruned sample doubles beyond $z \sim 1.2$.

in the Low-$A_W C_W$ corner, the drift of the mean asymmetry to higher values at higher redshifts is much more evident. In fact, the mean value of A_W for the pruned sample doubles beyond $z \sim 1.2$. The histograms of A_W for the pruned sample clearly show this trend (Figure 6–9). It is also interesting to note that, below $z \sim 1.2$, the distribution of galaxies in the A_W-C_W plane appears to be unchanged. The overall distribution of galaxies in C_W also does not change much before versus after pruning, though the large number of low-C_W objects has also thinned out in the pruned sample.

The choice of boundaries between redshift bins clearly will influence the prominence of any trends that are seen with redshift. In particular, the choice of $z = 1.2$ was chosen primarily to emphasize most strongly the differences seen below and above this redshift. From Figure 6–7, one can see that any boundary between $1.1 \lesssim z \lesssim 1.5$ would work well. Once this boundary was chosen, the remaining boundaries were selected primarily to yield roughly comparable numbers of objects in each redshift bin. The last redshift bin was isolated to show, once again, that, as objects become more distant and, hence, fainter and smaller, meaningful values of A_W and C_W are no longer measurable, and all of these objects end up in the Low-$A_W C_W$ corner.

Several features may be noted in these figures. Each of these will be discussed separately along with possible sources for these trends, such as selection effects, which are not due to true evolution.

2.1. The A_W-C_W Distribution out to $z \sim 1.2$ and beyond

Comparison of the first two panels in Figure 6–8 ($z \lesssim 1.2$) with the local calibrating sample (shown in Figure 5–4) indicates that the distribution of galaxies in the A_W-C_W

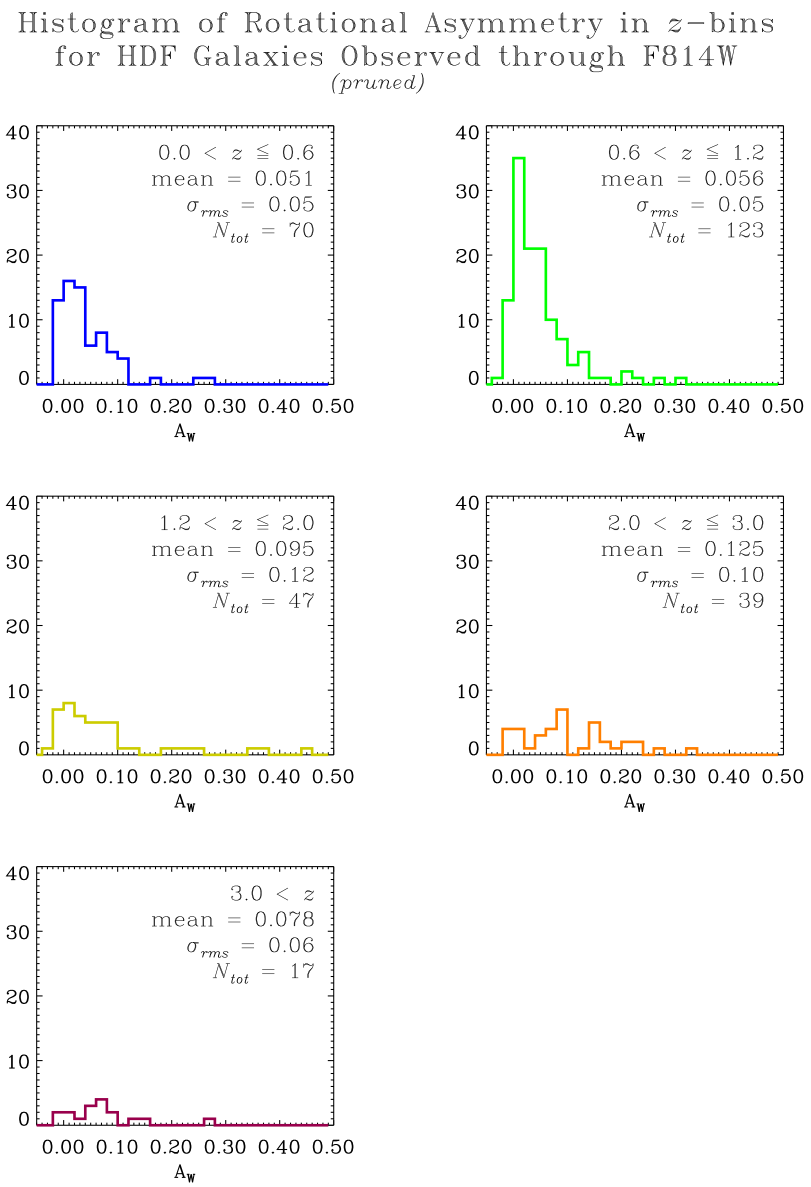

Fig. 6–9.— Histograms of A_W for the pruned HDF sample divided into the same five redshift bins as before. The drift of the mean asymmetry is clearly seen. At $z \sim 1.2$, the mean asymmetry essentially doubles, while the overall distribution flattens out.

plane out to $z \sim 1.2$ resembles that of the local galaxies. A large number of objects populate the lower left corner, which corresponds to the locus of local spirals. The population tails off to high concentrations, where local early-type galaxies lie. The overall locus of HDF galaxies in A_W-C_W appears to be shifted slightly to both lower A_W and lower C_W relative to the local sample. As will be shown in simulations, this is likely due to the reduced resolution and brightness of the objects in the HDF. The number of objects with very low A_W and C_W is also distinctly larger in the high redshift sample; in fact, there are almost none in the local sample. Recall, however, that the local sample consists almost exclusively of large bright galaxies. Local dwarfs and LSB galaxies would almost certainly fill in this low A_W - low C_W corner. Even with these caveats, however, the overall impression is one of strong similarity between the local A_W-C_W distribution and that of objects out to $z \sim 1.2$.

The distribution of galaxies in the A_W-C_W plane appears to undergo a distinct change around $z \sim 1.2$: (1) high concentration-low asymmetry objects no longer appear and (2) distinctly higher asymmetry objects begin to appear in the A_W-C_W plane. This change can also be seen in Figure 6–7, where the A_W-C_W classes are indicated by the color of the symbol (High-C_W in red, Low-$A_W C_W$ in grey, and High-A_W in blue). The sharp drop in high-C_W objects and increase in the percentage of high-A_W objects is quite evident. For now, our use of the words "appearance" and "disappearance" of objects in the A_W-C_W plane is simply a phenomenological statement of whether objects are detected by the object mask parameters and make it into the final pruned sample. For example, very small and/or low surface brightness objects with high concentrations may exist in the real universe beyond $z \sim 1.2$, but they may not make it past the detection or pruning cuts defined in this study; they would, therefore, not appear in these A_W-C_W distributions.

Before we can draw any conclusions about the evolution of galaxy morphology, we must understand the cause of these apparent changes in the A_W-C_W distribution. Are these trends real or simply a result of observational selection effects?

2.2. The Influence of Selection Effects on the A_W-C_W Distribution

The disappearance of high concentration-low asymmetry objects above $z \sim 1.2$

Beyond $z \sim 1.2$, almost no High-C_W objects are visible. In fact, there are almost no objects of any A_W with $C_W > 5$. Do these objects simply not exist beyond $z \sim 1.2$, or have they faded so much that they have disappeared in the noise? In the latter case, these objects may still exist at these redshifts; however, we are unable to detect them with the currently available instruments and telescopes with reasonable exposure times. Simulations are required to test this possibility.

Previous simulations (e.g., A96b and Brinchmann et al. 1998) have generally used local galaxies (e.g., the Frei catalog) as the basis for studying the expected morphologies of galaxies at high redshift. K-corrections are also done using the spectral energy distributions (SEDs) of local galaxies, e.g., Coleman, Wu, & Weedman (1980). The problem, however, is that high redshift galaxies may well have SEDs that are quite different from those of local galaxies. The expected appearance of high redshift galaxies would, therefore, be mis-estimated based on these simulations.

In order to create more realistic simulations of the expected A_W-C_W distribution of high redshift galaxies, SEDs of galaxies around $z \sim 0.8$ were used to estimate the expected K-correction for these galaxies simulated at $z = 1.5$ and $z = 2.3$. A brief investigation of the colors of High-C_W objects at $z \sim 0.8$, for example, revealed that many of them are quite blue and, therefore, not well-matched to the local ellipticals that would likely have been used in previous work to estimate their K-correction. The effect at higher redshifts would be even more extreme. By using the actual (though somewhat crude) SEDs of $z \sim 0.8$ objects, the hope is that a more realistic view may be attained of the behaviour of high redshift objects. Although this is an improvement over what has been done previously, it may still be an underestimate as galaxies may have been even bluer and brighter beyond $z \sim 1$.

The procedure, then, is as follows: individual SEDs were created for each galaxy within the redshift range, $0.75 < z < 1.2$, using their integrated colors as determined by W96. Simulations of these galaxies shifted to $z = 1.5$ and $z = 2.3$ were then created, starting with the F814W images and using K-corrections estimated from the integrated SEDs. In other words, the F606W-F814W color (roughly $v - i$) was used to fade the galaxies the appropriate amount to shift to $z = 1.5$, while the F450W-F814W color (roughly $b - i$) was used to estimate the K-correction for shifting to $z = 2.3$. Poisson noise was then added to the image. As a result of fading, the overall noise level was reduced. As a final step, therefore, the noise level in each image was adjusted to reproduce the original noise level before cosmological dimming. Because the change in the size of the objects between $z \sim 0.8$ and $z \sim 2.3$ is no more than 5-10% (galaxies are actually getting bigger in this redshift range), the image size was not changed for these simulations.

Figure 6–10 shows the results of these simulations. Each row contains two sets of three galaxies, which, together, make up one simulation: the original $z \sim 0.8$ image on the left, the simulated $z = 1.5$ image in the middle, and the simulated $z = 2.3$ image on the right. One is immediately faced with the rapid disappearance of most galaxies into the noise.

Fig. 6–10.— Montage of galaxies at $z \sim 0.8$ simulated at $z = 1.5$ and $z = 2.3$. Each row contains two sets of three galaxies, which, together, make up one simulation: the original $z \sim 0.8$ image on the left, the simulated $z = 1.5$ image in the middle, and the simulated $z = 2.3$ image on the right. One is immediately faced with the rapid disappearance of most galaxies into the noise. At $z = 1.5$, only 50 out of the original 151 objects are still detected. By $z = 2.3$, only 5 galaxies still survive the detection limits of A_W-C_W. If galaxies at redshifts beyond $z \sim 1.5$ have the same luminosities and SEDs as objects at $z \sim 0.8$, the large majority of them would be completely undetectable using today's telescopes and detectors! Any evolutionary effects must be carefully extracted from such a strong selection effect.

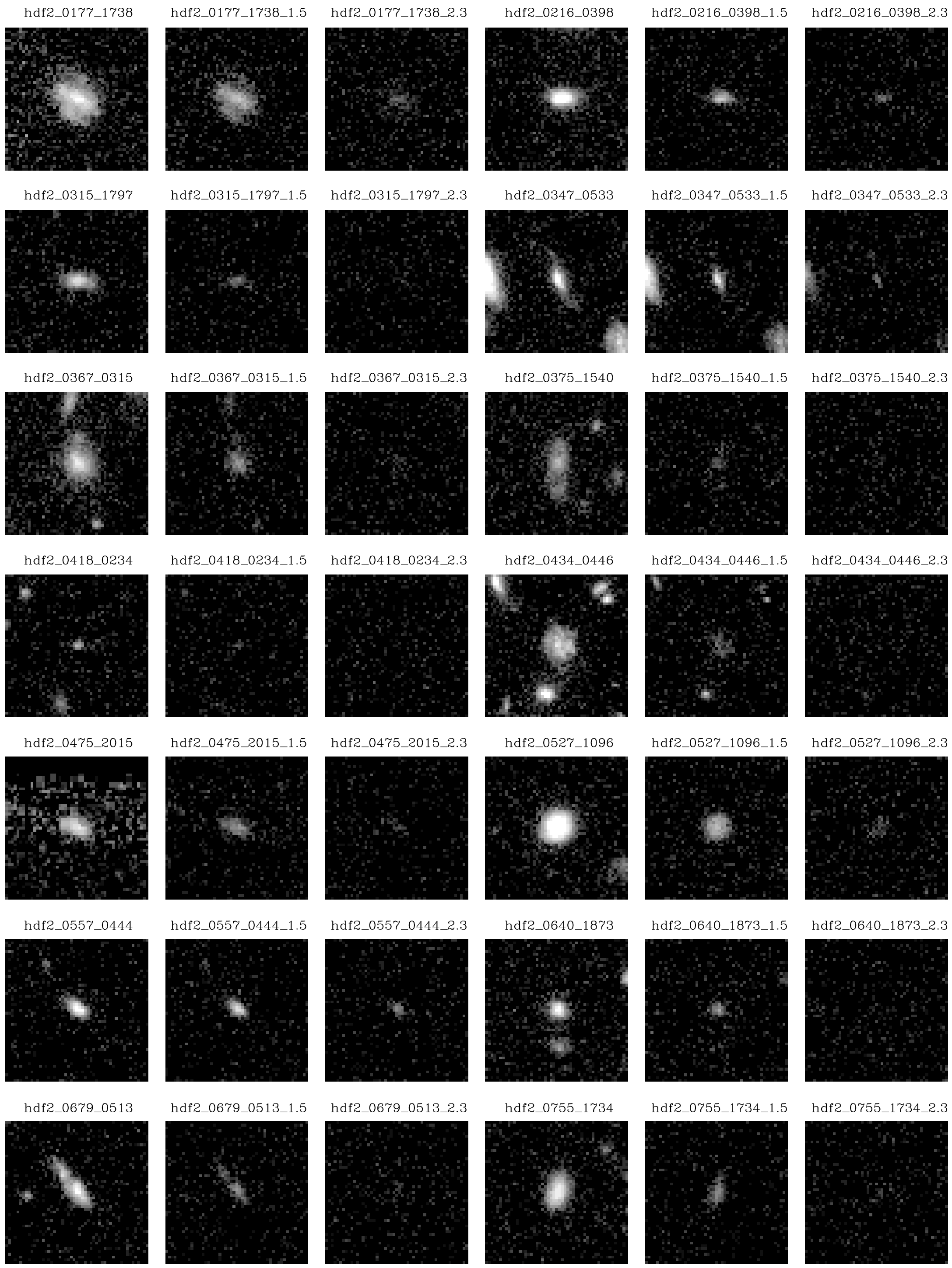

Fig. 6–10a. Montage of $z \sim 0.8$ galaxies simulated at $z = 1.5$ and $z = 2.3$.

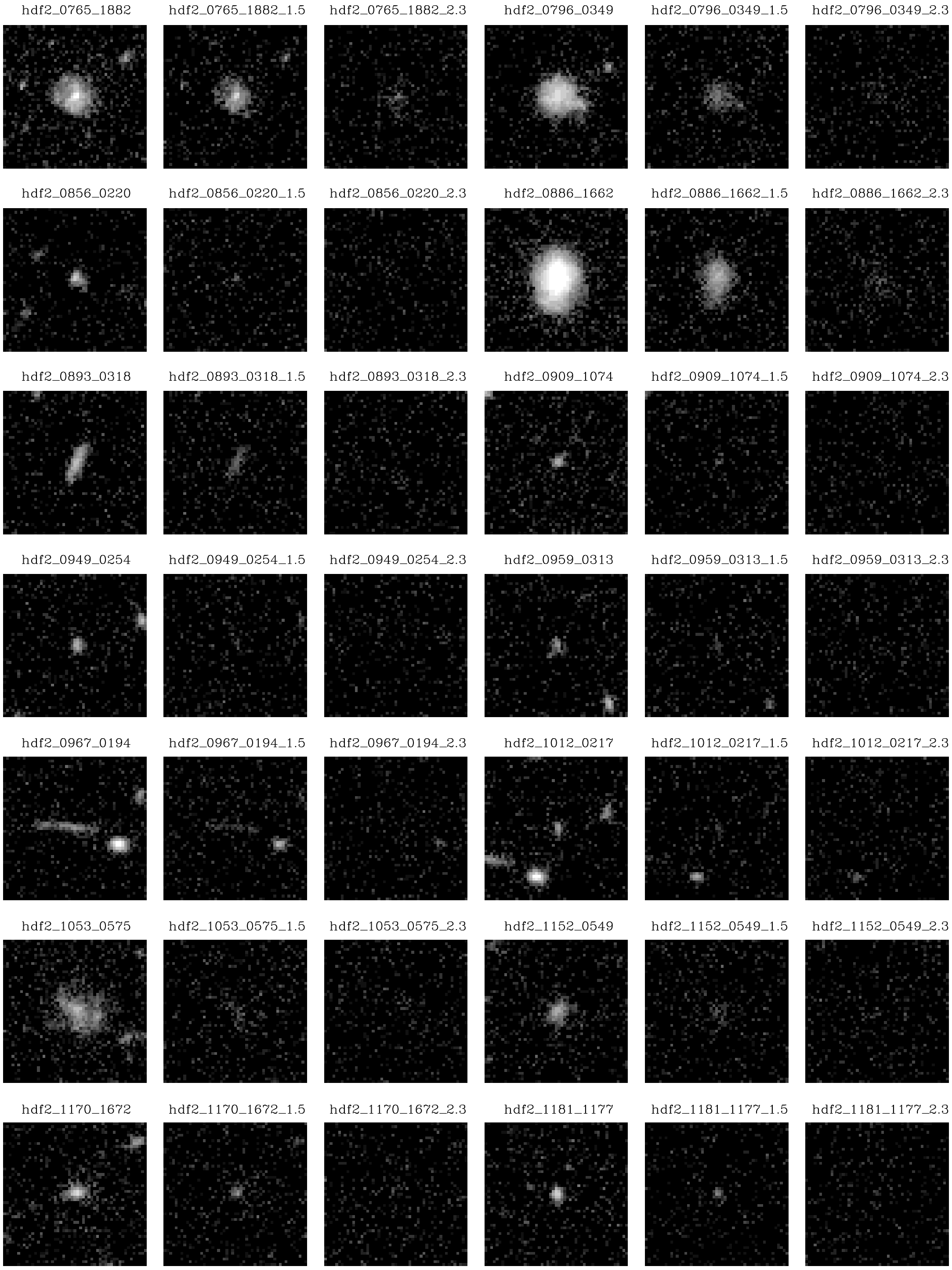

Fig. 6–10b. Montage of $z \sim 0.8$ galaxies simulated at $z = 1.5$ and $z = 2.3$ *(continued).*

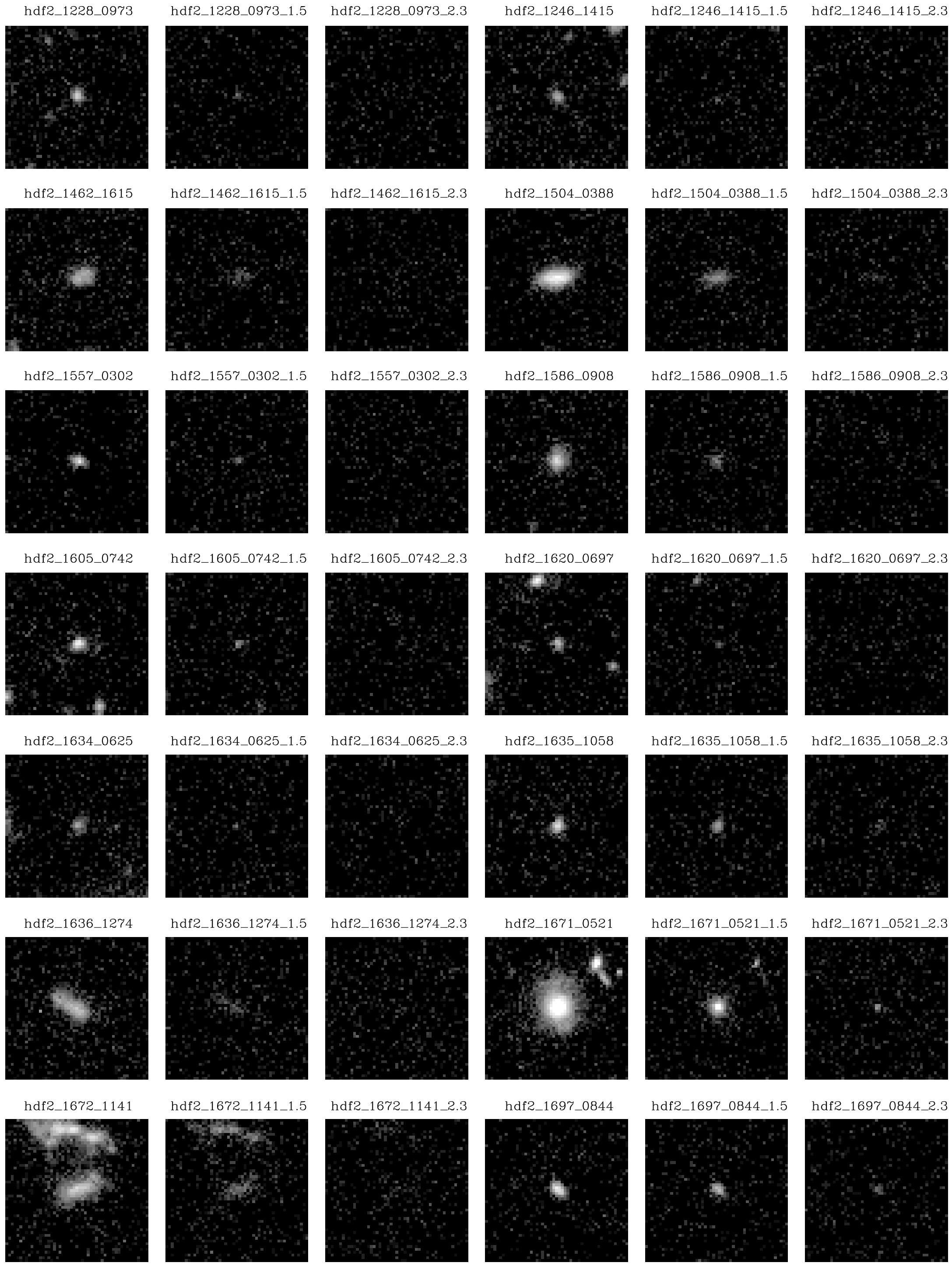

Fig. 6–10c. Montage of $z \sim 0.8$ galaxies simulated at $z = 1.5$ and $z = 2.3$ *(continued).*

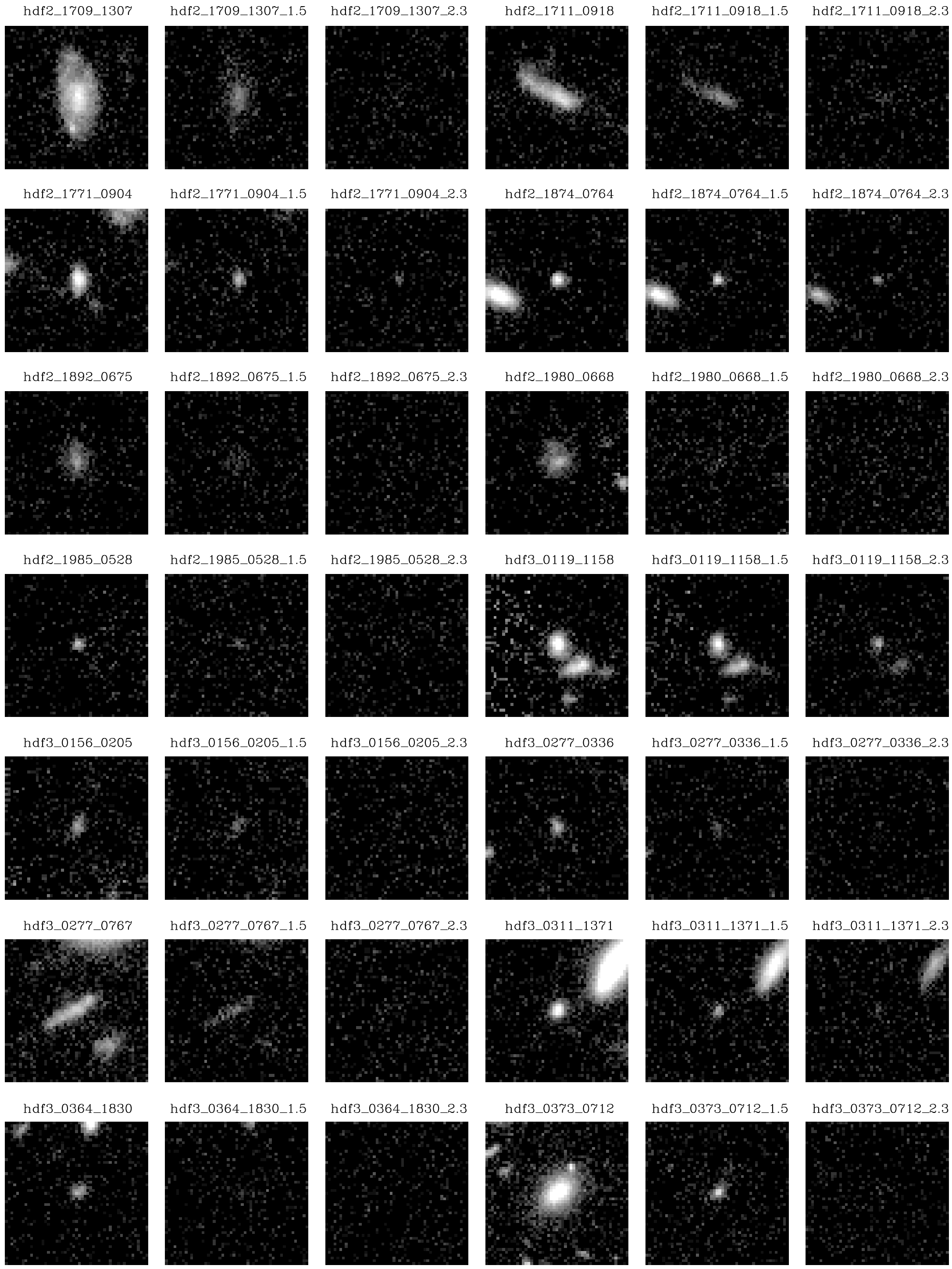

Fig. 6–10d. Montage of $z \sim 0.8$ galaxies simulated at $z = 1.5$ and $z = 2.3$ *(continued).*

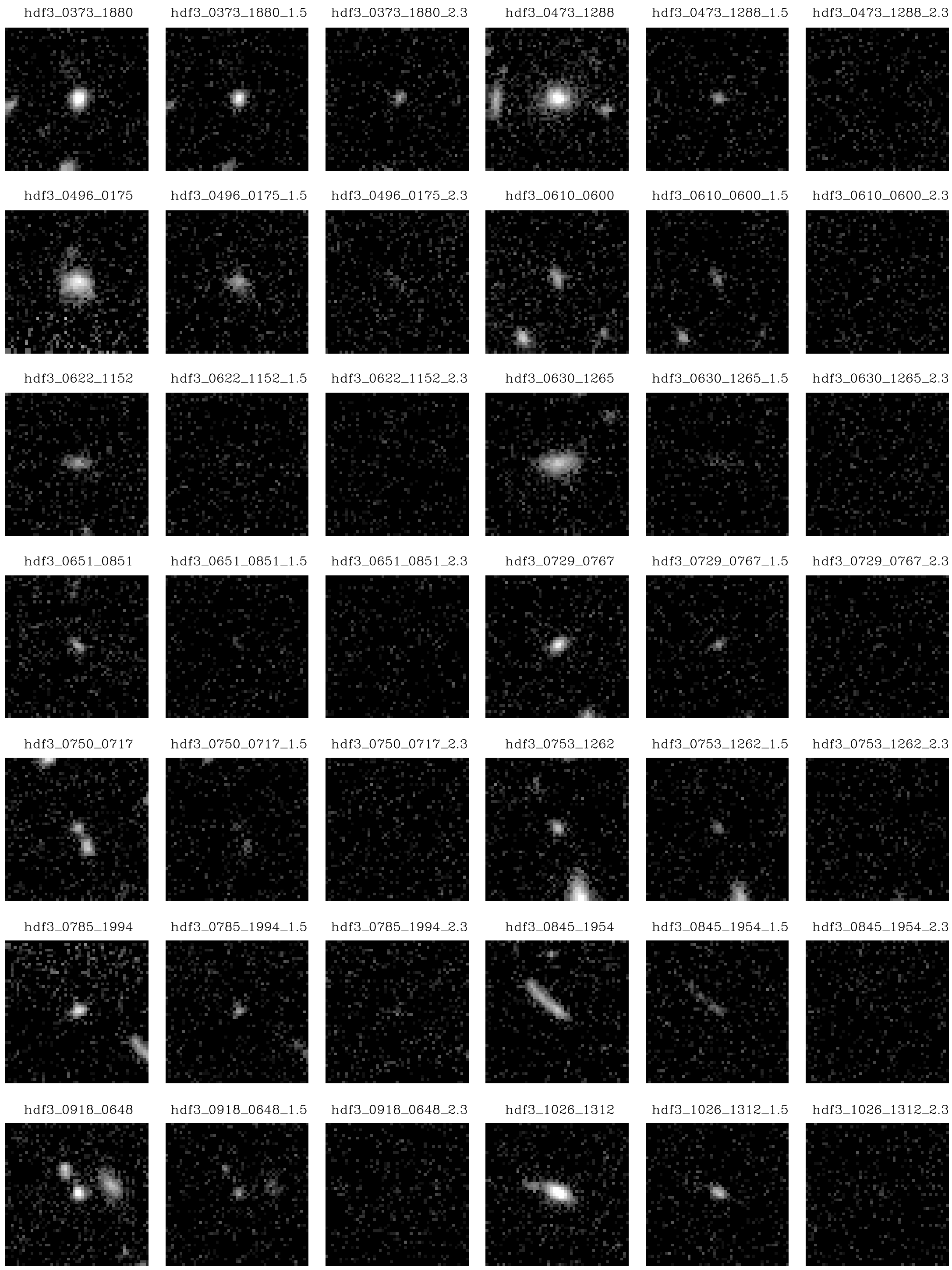

Fig. 6–10e. Montage of $z \sim 0.8$ galaxies simulated at $z = 1.5$ and $z = 2.3$ *(continued).*

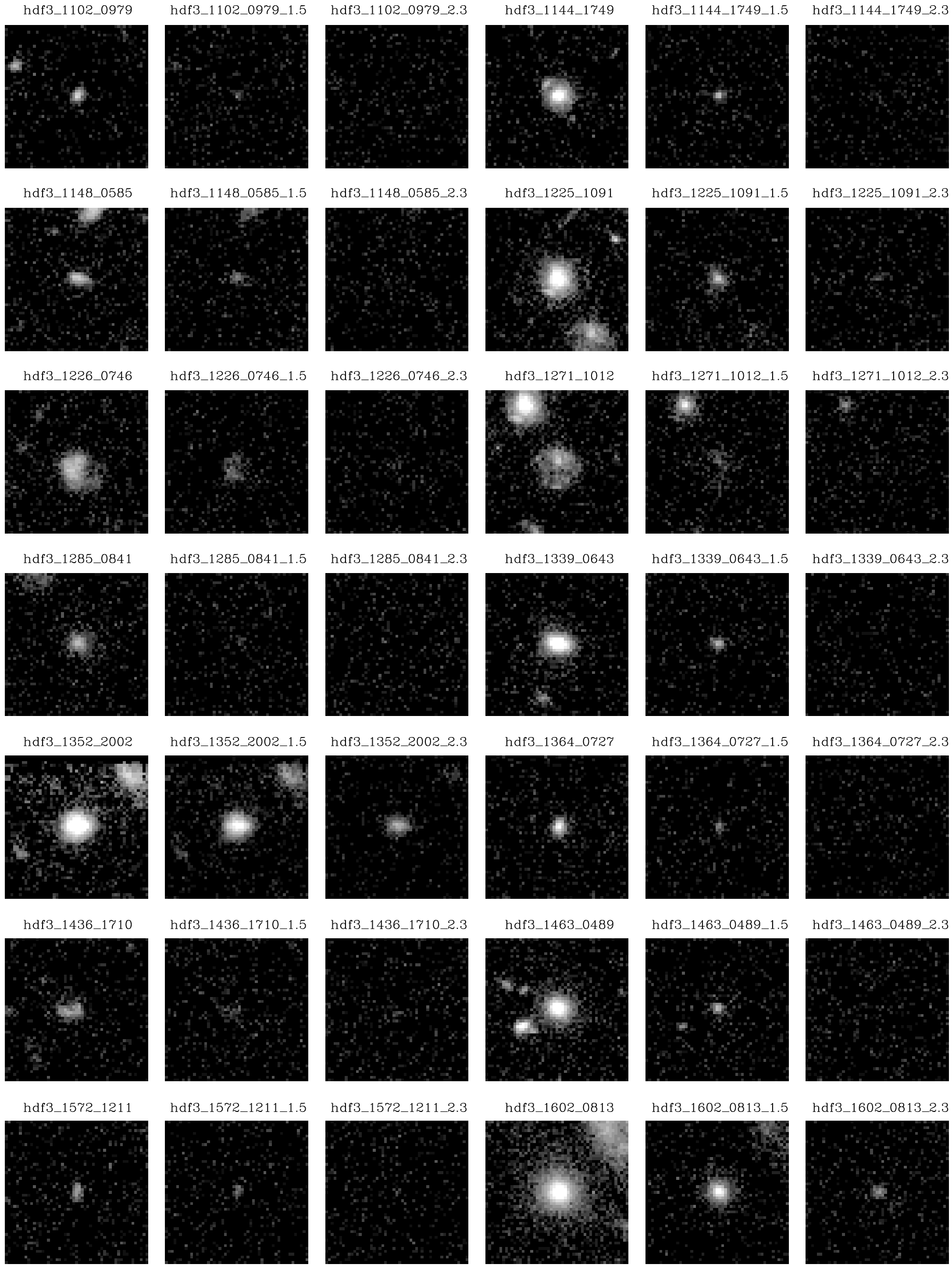

Fig. 6–10f. Montage of $z \sim 0.8$ galaxies simulated at $z = 1.5$ and $z = 2.3$ *(continued).*

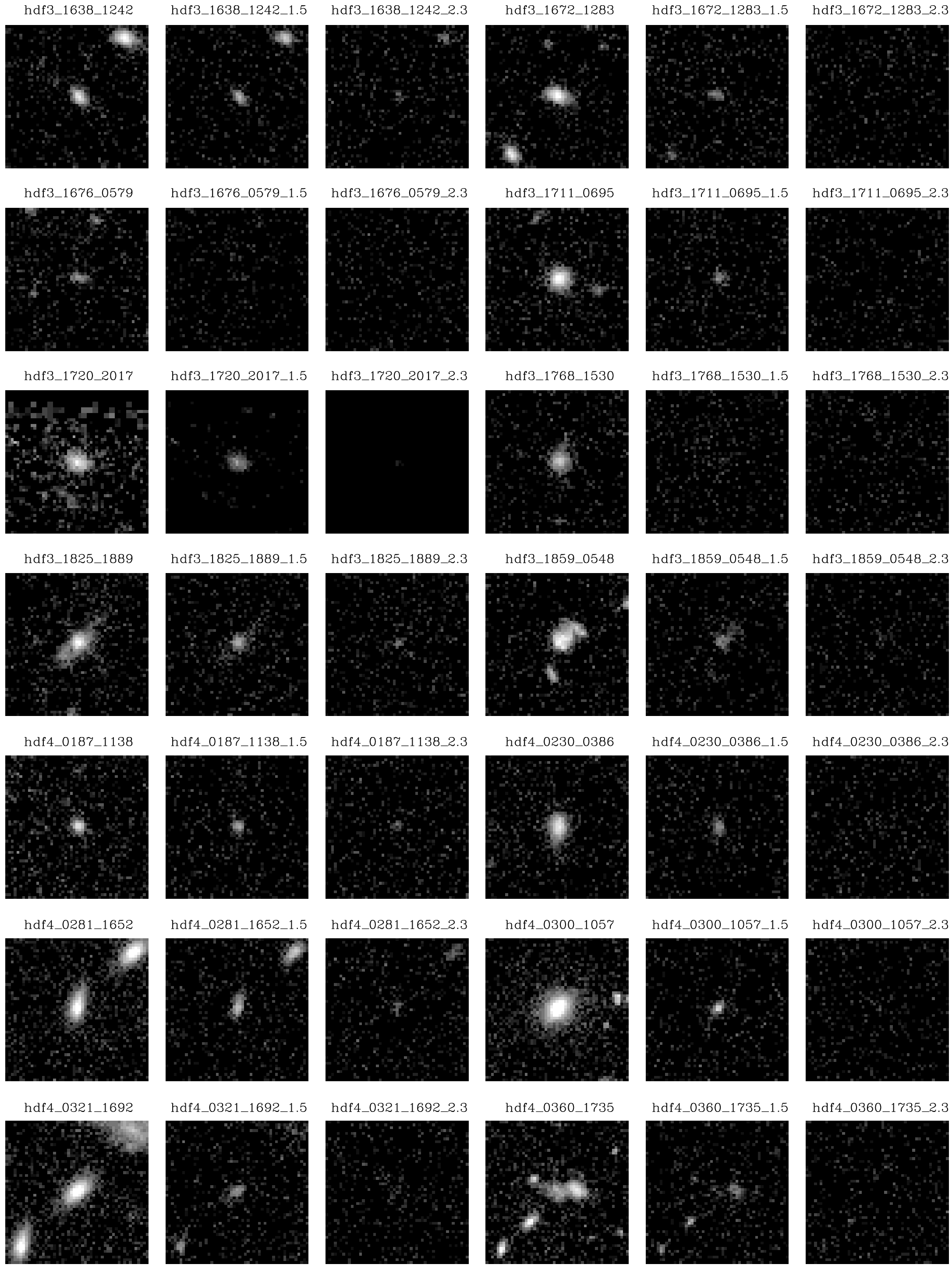

Fig. 6–10g. Montage of $z \sim 0.8$ galaxies simulated at $z = 1.5$ and $z = 2.3$ *(continued).*

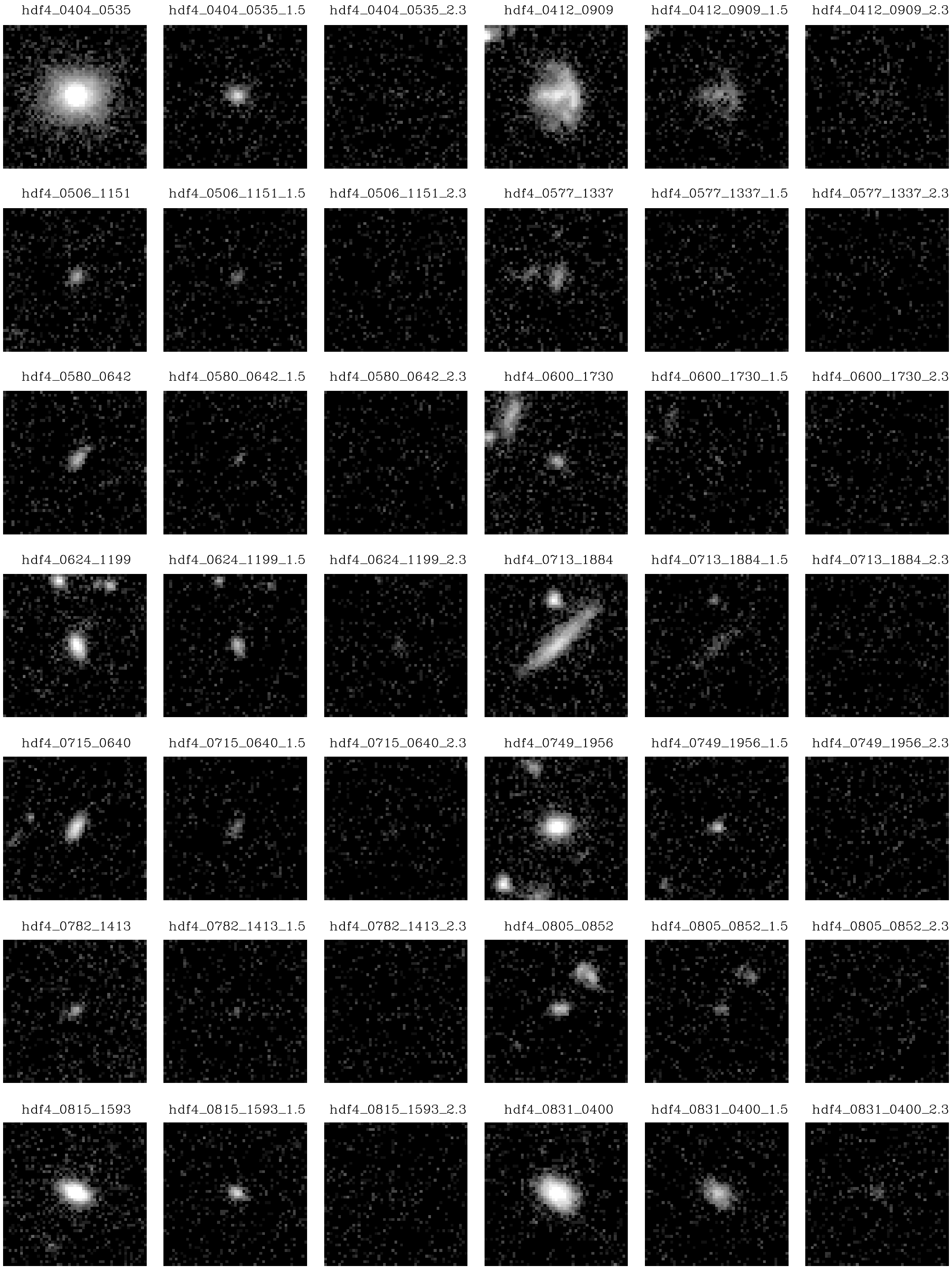

Fig. 6–10h. Montage of $z \sim 0.8$ galaxies simulated at $z = 1.5$ and $z = 2.3$ *(continued).*

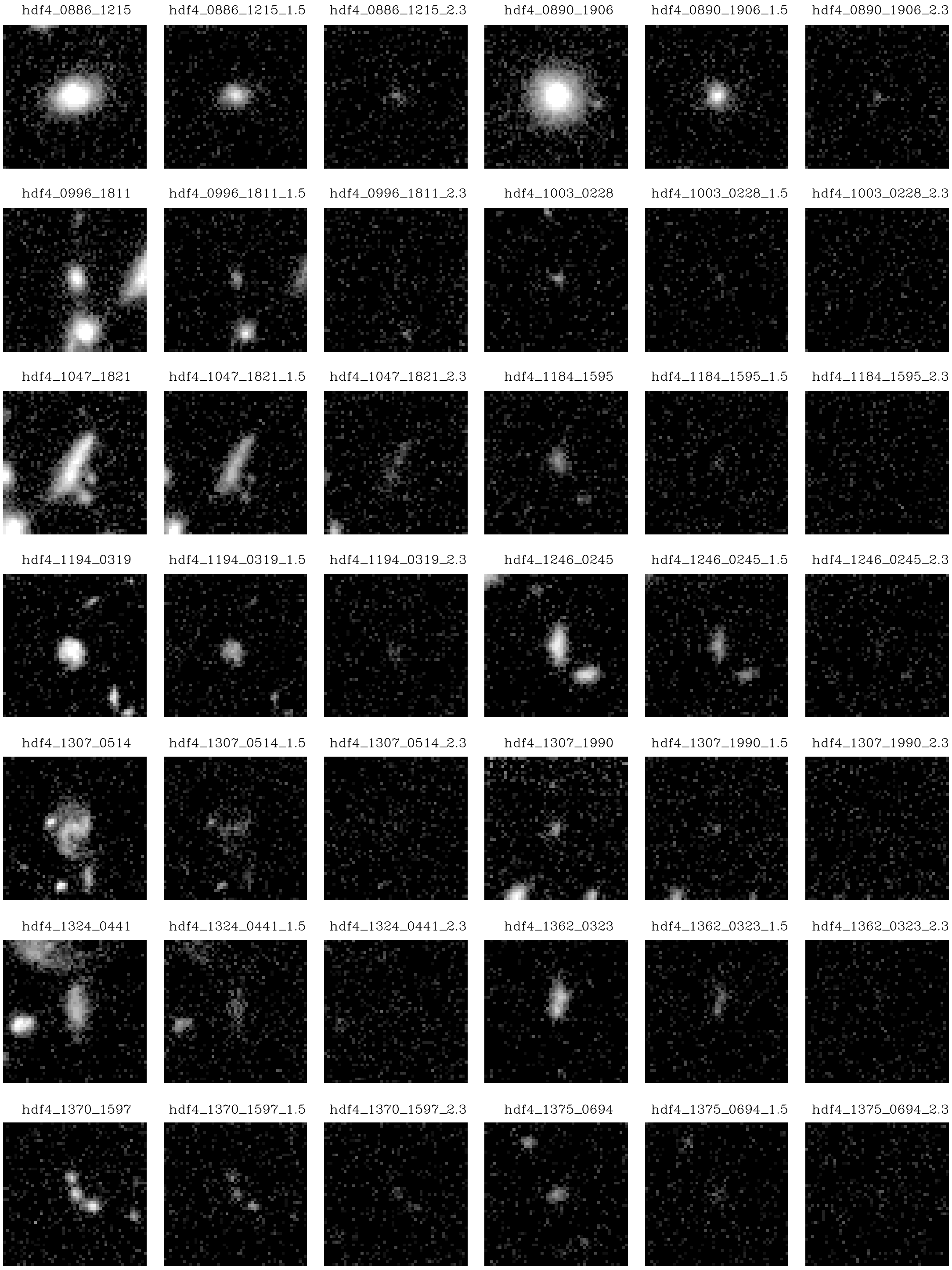

Fig. 6–10i. Montage of $z \sim 0.8$ galaxies simulated at $z = 1.5$ and $z = 2.3$ *(continued).*

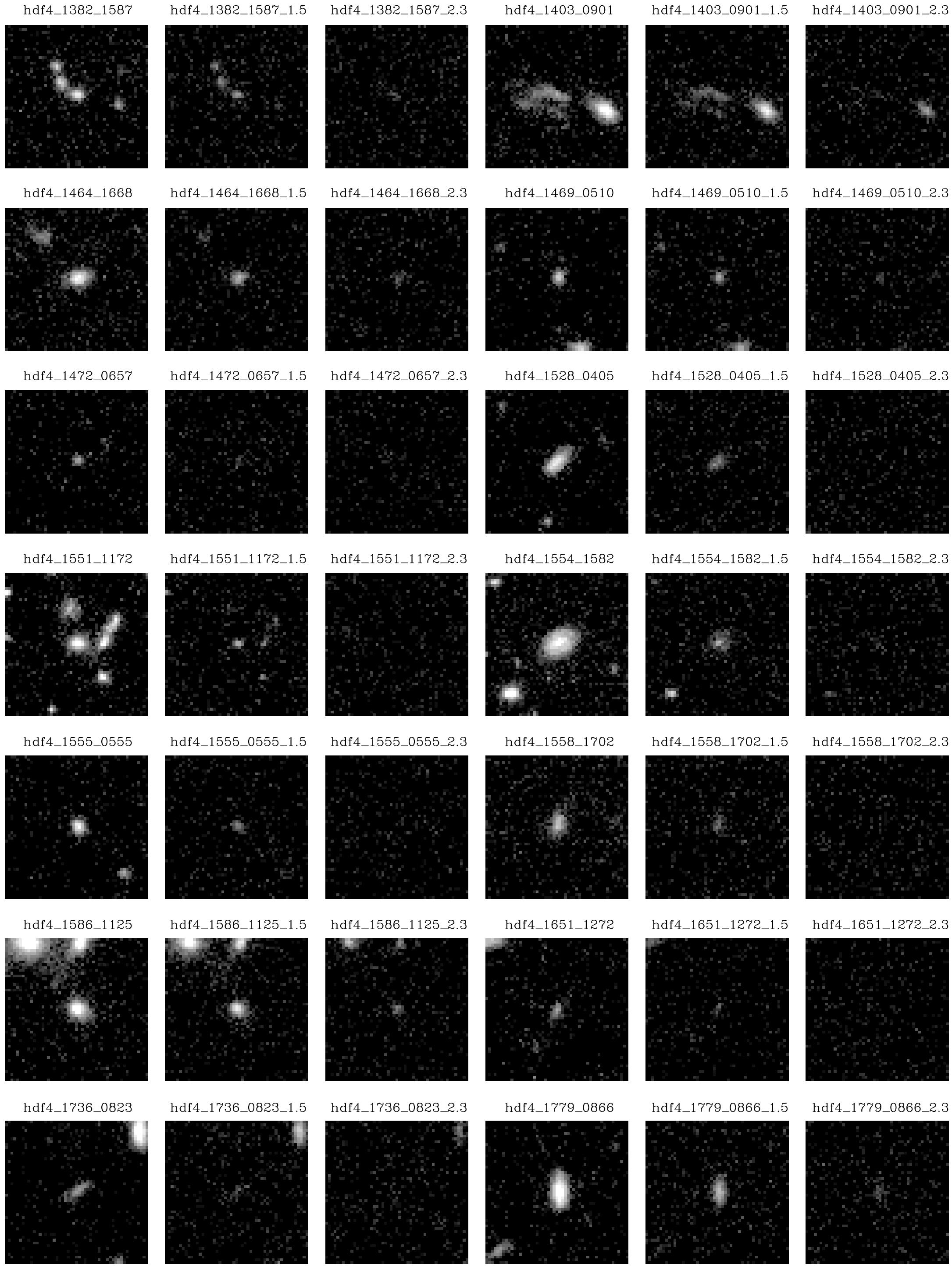

Fig. 6–10j. Montage of $z \sim 0.8$ galaxies simulated at $z = 1.5$ and $z = 2.3$ *(continued)*.

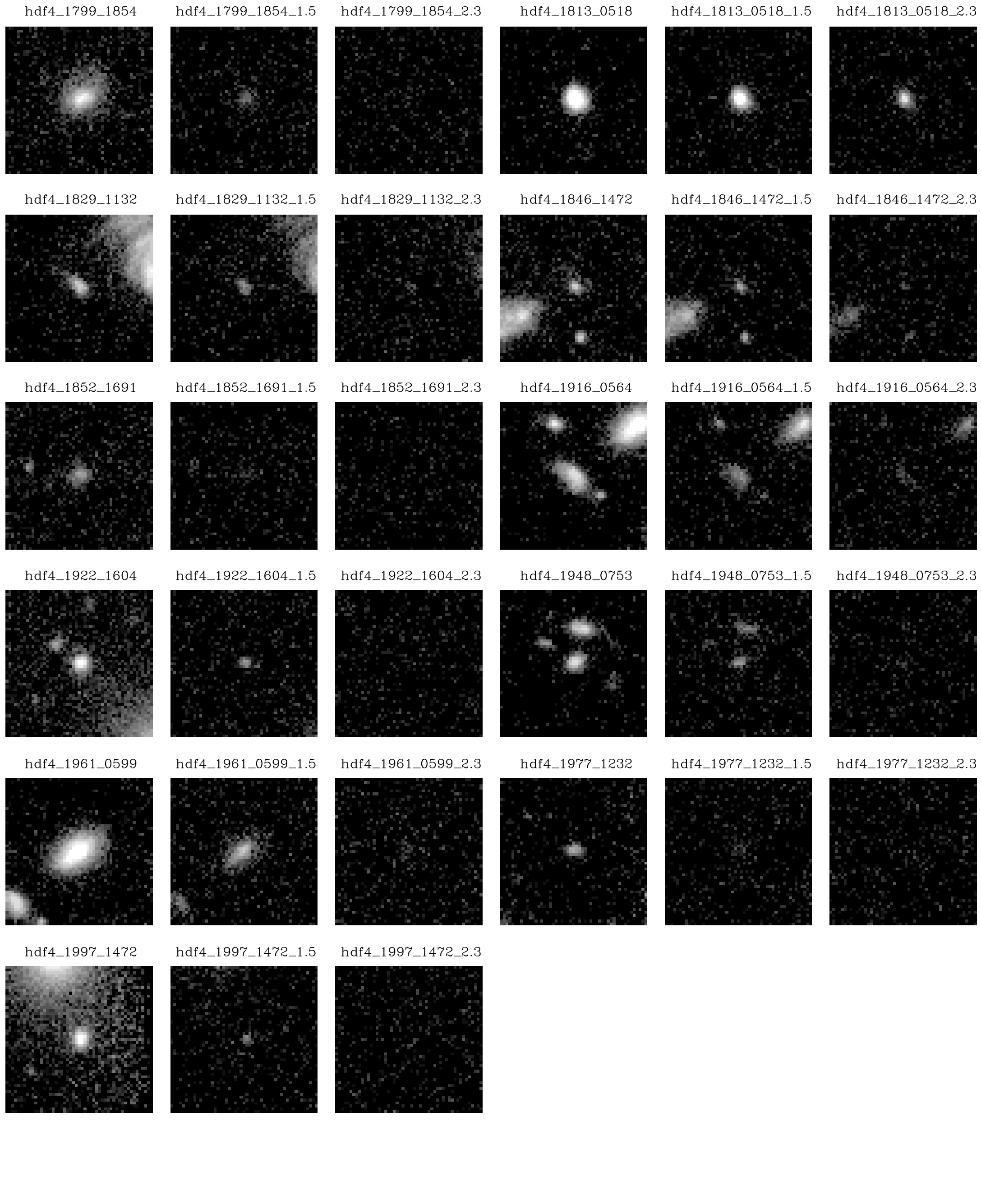

Fig. 6–10k. Montage of $z \sim 0.8$ galaxies simulated at $z = 1.5$ and $z = 2.3$ *(continued).*

Figure 6–11 shows the distribution in the A_W-C_W diagram of the $z \sim 0.8$ objects *(open circles, left panel)* simulated at $z = 1.5$ *(blue dots, right panel)* and $z = 2.3$ *(red dots, right panel).* At $z = 1.5$, two-thirds of the objects are no longer detectable above the noise, and all have diminished A_W and C_W; by $z = 2.3$, only five objects out of the original 150 still survive the detection limits. In other words, if high redshift objects have SEDs and luminosities similar to those of objects at $z \sim 0.8$, 97% of them would not be detected in a HDF-type observation by $z \sim 2.3$. The disappearance of High-C_W objects beyond $z \sim 1.2$ is, therefore, almost certainly heavily modulated by selection effects. That said, however, many objects are clearly still visible beyond $z \sim 1.2$, indicating that either they are more luminous or their SEDs are not as blue as those of objects at $z \sim 0.8$. The steady-SED assumption, therefore, is too conservative, and these objects must have evolved. More detailed understanding of the lack of High-C_W objects, however, will require realistic evolutionary models.

The appearance of high asymmetry objects above $z \sim 1.2$

The simulations presented above show that, as a galaxy is cosmologically dimmed (i.e., the signal-to-noise is decreased), the measured asymmetry decreases. Simulations in the next section will show that as the size of a galaxy is shrunk, the measured asymmetry also decreases. As galaxies move to redshifts below $z \sim 1.2$ from higher redshifts, they tend to become brighter and remain roughly the same size. Neither of the two primary selection effects, therefore, is active, and there is no reason to expect that highly asymmetric galaxies beyond $z \sim 1.2$ should disappear at lower redshifts.

A third selection effect should now be considered. O'Connell (1997) showed that

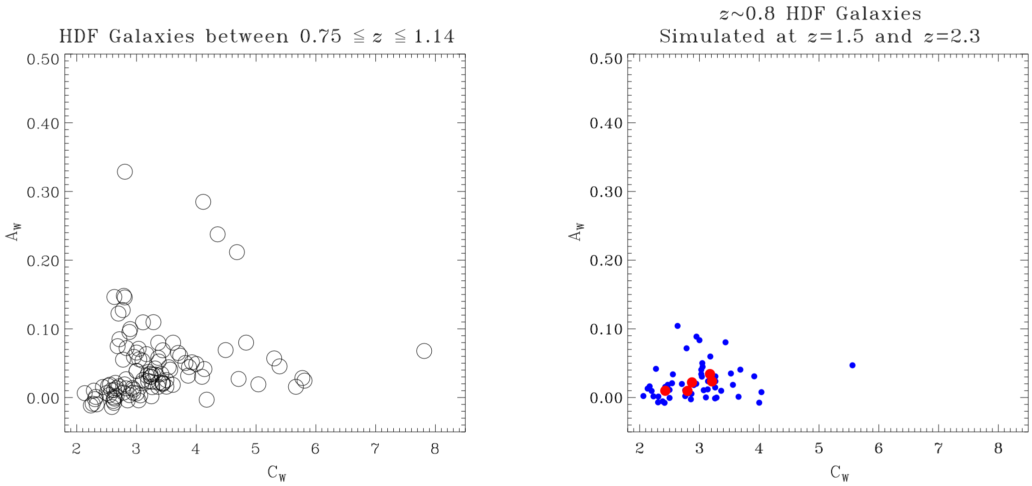

Fig. 6–11.— The distribution of the $z \sim 0.8$ objects in the A_W-C_W plane is shown in the left panel. Simulations of these galaxies at $z = 1.5$ and $z = 2.3$ were created using coarse SEDs derived from colors given in W96. The distribution of these simulated galaxies in the A_W-C_W plane is shown in the right-hand panel: $z = 1.5$ (small blue dots) and $z = 2.3$ (larger red dots). At $z = 1.5$, two-thirds of the original sample are no longer detected by the A_W-C_W algorithm. At $z = 2.3$, only 5 objects out of the original 150 still survive the detection limit. When interpreting observations at these redshifts, therefore, one must be cautious not to attribute to evolution what may be reasonably explained by simple selection effects.

galaxies that appear perfectly "normal" at optical wavelengths may appear quite "peculiar" when observed in the UV. Is the appearance of asymmetric galaxies beyond $z \sim 1.2$, therefore, simply a "bandpass shifting" effect?

The general question of bandpass shifting is explored for the entire data set in Figure 6–12, which repeats the redshift-binned A_W-C_W panels of Figure 6–8, but now with images taken in the F450W filter rather than the F814W filter. Comparison of each of the F450W panels with its corresponding F814W filter shows that, in general, the agreement is good, i.e., the shift to bluer wavelengths does not significantly affect the A_W-C_W distribution. The disappearance of High-C_W objects and the increase in High-A_W objects at $z \sim 1.2$ is still present, and the distribution of objects in the two bins below $z \sim 1.2$ is still roughly similar. In detail, points at $z > 3.0$ appear to scatter more in F450W than in F814W, probably due in part to larger errors for these faint galaxies in the F450W band. The number of High-A_W objects in the second redshift bin ($0.6 < z < 1.2$) also roughly doubles in the F450W band. Relative to the number of galaxies in Low-$A_W C_W$, however, the numbers are still quite small. The comparison of A_W-C_W in this redshift bin is a rather severe test. At $z \sim 0.8$, the F814W band corresponds roughly to rest-frame 4400 Å, while the F450W band corresponds to rest-frame 2500 Å, well below the Balmer break and much more sensitive to any hot stellar population. While not absolutely zero, bandpass shifting effects from 2500 Å to 4400 Å do not appear to have a large effect on the A_W-C_W distribution, at least not at $z \sim 0.8$.

One might be concerned, however, that the depth to which the galaxies are probed in the F450W band is not as deep as that probed in the F814W band. If this is the case, then this comparison may be a bit misleading. In order to address this concern, the signal-to-noise ratio (SNR) of the two sets of galaxies are calculated and compared.

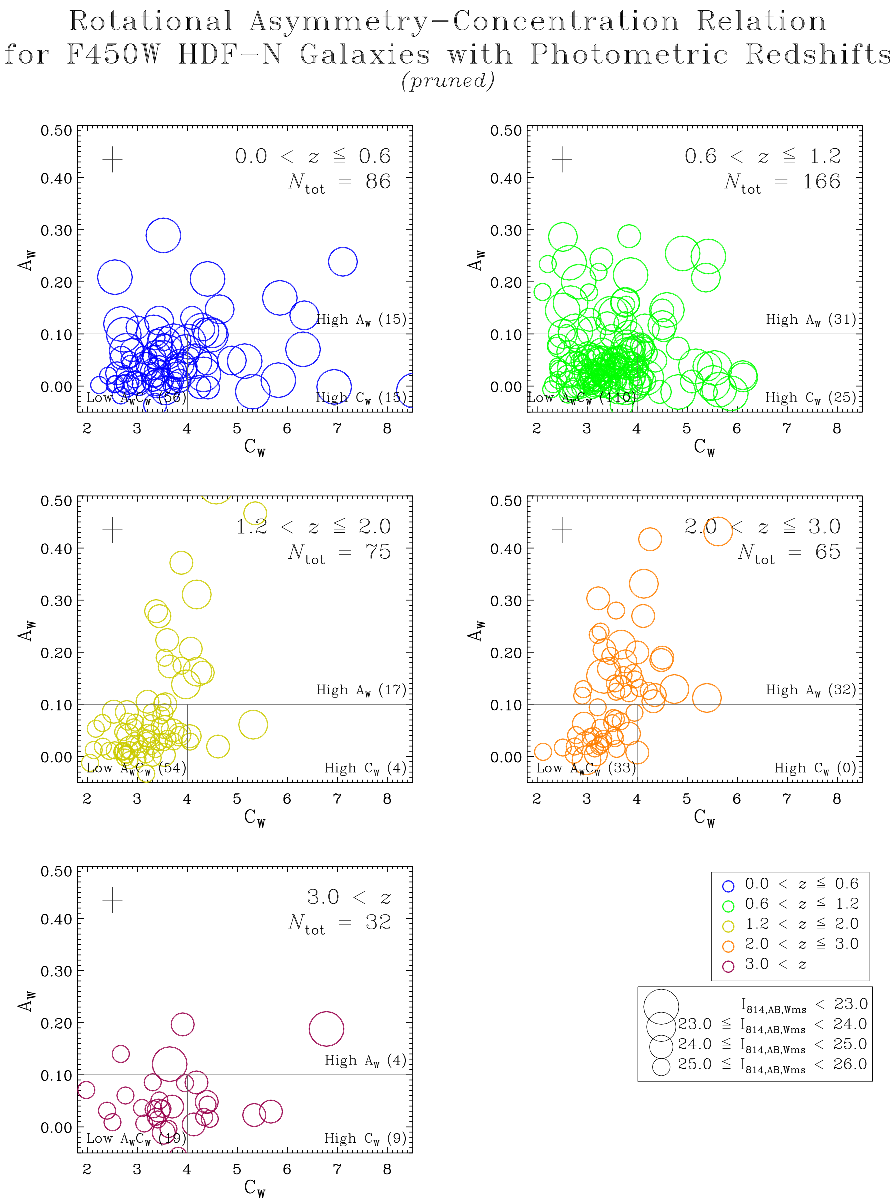

Fig. 6–12.— The A_W-C_W distribution for the pruned HDF galaxy sample observed through the F450W passband. As in Figure 6–8, symbol size scales with total apparent F814W magnitude. Comparison with Figure 6–8 shows that there is very little difference in the distribution of galaxies in the A_W-C_W plane when observed through the F814W versus the F450W passbands. The appearance of highly asymmetric objects around $z \sim 1.2$, therefore, is not simply due to observing the UV component of the galaxies.

Because of the drizzling of the HDF, the noise characteristics of the images are somewhat complicated; I, therefore, opted to follow the formulation presented in W96. Using the magnitudes, areas, and sky levels given in W96 and calculating the variance using Equation(6), the SNR for each object is computed.

Figure 6–13 shows the comparison of the SNR of $z \sim 0.8$ HDF objects in F814W versus F450W. On average, the SNR of objects observed through the F814W filter is at least twice that observed through the F450W filter. In order to make a meaningful comparison between data from the two filters, the F814W images were degraded to the SNR of the F450W images, and A_W and C_W were re-calculated on the noisier image. Figure 6–14 shows a comparison of A_W-C_W in the F814W before (open circles) and after (red dots) adding noise. The distributions are virtually unchanged. The most asymmetric and most highly concentrated objects become slightly less asymmetric and concentrated, respectively, but the magnitude of the change is small. A handful of border-line High-A_W objects cross over to the low-A_W side. This comparison indicates a tendency for observations in the F450W band to show slightly higher asymmetries that the F814W band at the same SNR levels, but the overall distributions are quite comparable. A one-to-one comparison of the individual indices (Figure 6–15) verifies this conclusion. Matching the SNR of the F450W images does not change the original conclusion that bandpass effects are negligible.

The same redshift bin ($0.6 < z < 1.2$) in F450W can also be used to test directly the bandpass shifting effects for galaxies at $z \sim$ 2-3. Observing objects at $z \sim 0.8$ through the F450W-band and at $2.0 < z < 3.0$ through the F814W-band is equivalent to observing these two sets of objects at the same rest-frame wavelength. A comparison of these two panels reveals two very different distributions: the fraction of highly asymmetric galaxies at $z \sim 0.8$ is clearly much smaller than at $z \sim 2 - 3$. As bandpass shifting, once again,

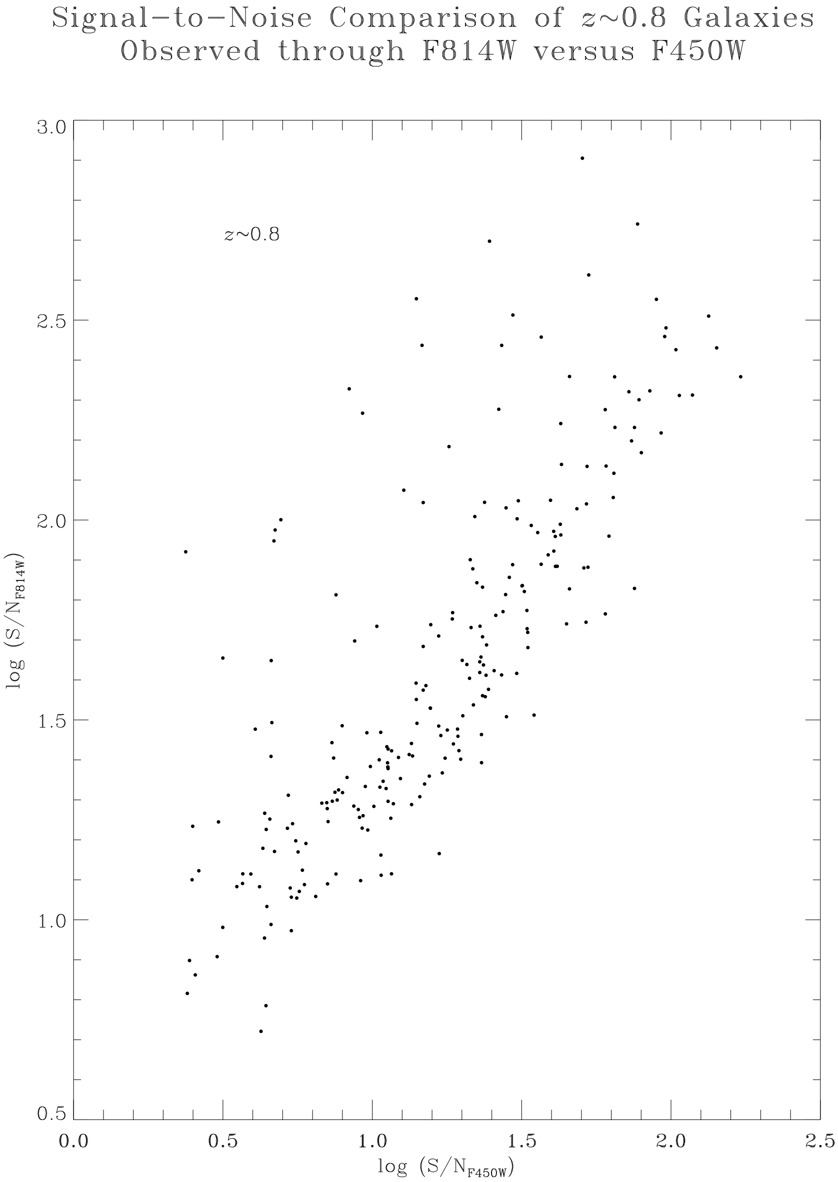

Fig. 6–13.— Comparison of the signal-to-noise ratio of objects observed through the F814W filter versus the F450W filter at $z \sim 0.8$, plotted in logarithmic units. The signal-to-noise in the F814W images is generally at least twice that of the F450W images. Some concern may arise that we are sampling different parts of the galaxies in the F814W band than in the F450W band, which may be the source of the differences (or similarities) in the two bands. Simulations have, therefore, been created to test the sensitivity of A_W and C_W of the objects observed in F814W to a change in SNR of a factor of two.

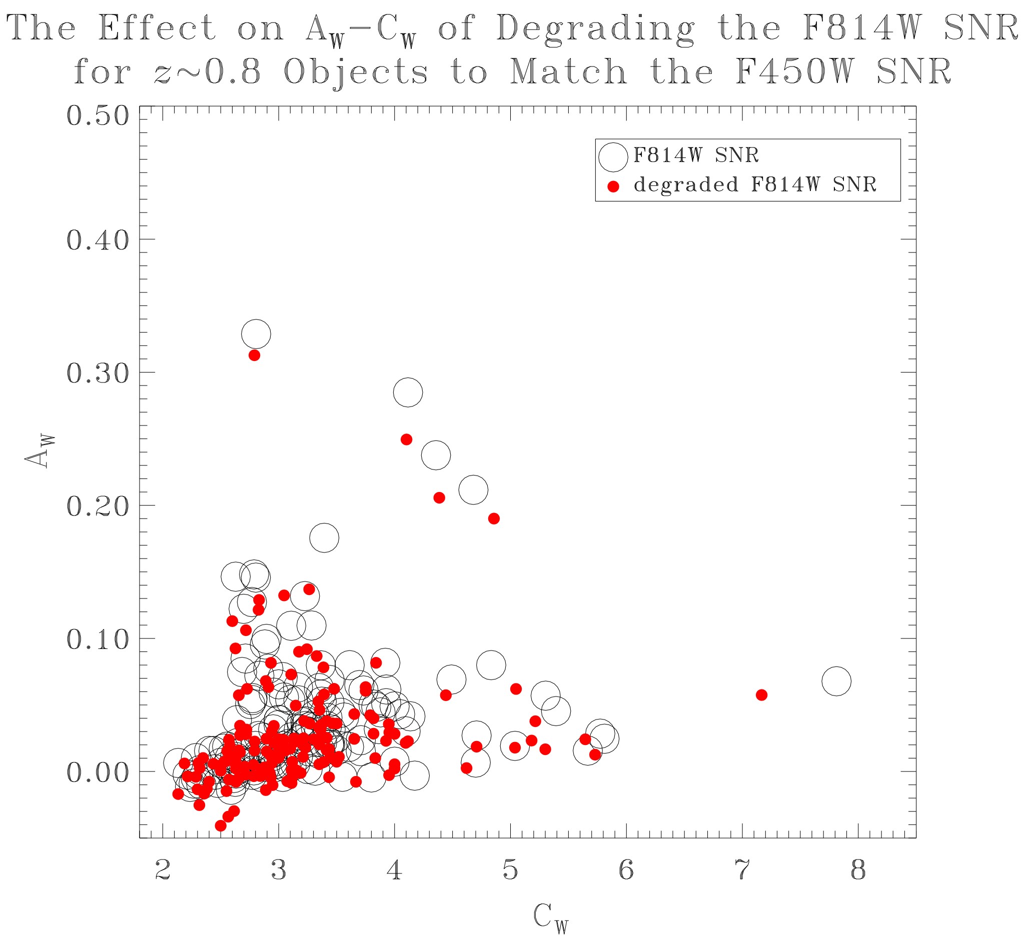

Fig. 6–14.— The A_W-C_W distribution of $z \sim 0.8$ HDF galaxies observed in F814W before *(black circles)* and after *(red dots)* adding noise to match the lower SNR of observations in F450W. There is a slight trend for many objects to become slightly less asymmetric, but the overall distribution in the A_W-C_W plane remains roughly constant. Comparison with the F450W distribution indicates that there are mildly higher asymmetries in the blue than in the F814W band. Nonetheless, the overall distributions are roughly comparable, implying that bandpass shifting effects are minimal.

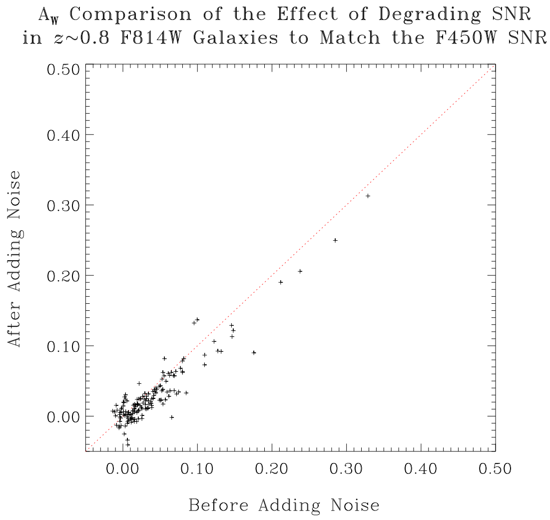

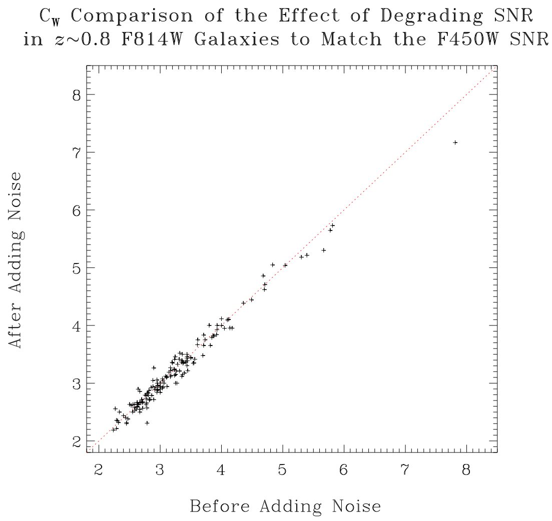

Fig. 6–15.— Comparison of A_W versus A_A and C_W versus C_A for $z \sim 0.8$ galaxies observed in F814W before and after degrading the SNR to match that observed in F450W. Adding noise to the F814W images does not significantly affect C_W, and only a slight decrease in A_W is seen. The similarity in the A_W-C_W diagrams for galaxies at $z \sim 0.8$ observed in F814W versus F450W, therefore, indicates that bandpass effects are minimal.

is fully accounted for in this comparison, it cannot be responsible for this difference. We conclude, therefore, that bandpass shifting is also not a significant effect on the A_W-C_W distribution of distant ($z \sim 2-3$) galaxies.

As for the previous comparison, the SNR of the two samples was calculated to determine whether the depth reached was comparable. Once again, the F814W images are found to have roughly twice the SNR of the F450W images (Figure 6–16). Simulations degrading the noise in the F814W images are created, and A_W and C_W are re-calculated and compared to the original data (Figure 6–17). Several border-line asymmetric objects cross over to the low-A_W side. Nonetheless, the distribution of galaxies in the A_W-C_W plane is still markedly different from that seen for the $z \sim 0.8$ objects in F450W. As the same rest-frame wavelength is represented at these two redshifts, bandpass effects cannot be responsible for the change in the distribution.

One final factor should be considered, which is suggested by the size-redshift plots of Figure 6–7. These plots indicate that, at $z \sim 0.8$, we are sampling the top 5-6 magnitudes of the luminosity function, while, at $z \sim 2.3$, we are sampling roughly only the brightest two magnitudes. At $z \sim 0.8$, High-A_W objects tend to preferentially populate the bright end of the luminosity function. Perhaps, therefore, the relatively larger fraction of High-A_W objects seen beyond $z \sim 1.2$ is simply a result of preferentially seeing, at those redshifts, just the tip of the luminosity function, where galaxies at all redshifts tend to be more asymmetric. Figure 6–18 shows the A_W-C_W distribution of objects between $0.6 < z < 1.2$ with radii larger than $\log(r_{1,Wms}) > 0.4$, i.e., $0''.4$, to better match the luminosity function of objects sampled at $z \sim 2-3$. Clearly, the relative percentage of High-A_W objects in this newly pruned bin is a much more comparable to that at $z \sim 2-3$: the High-A_W fraction in both samples now appears to be roughly 50%. It is viable, therefore, that the relative

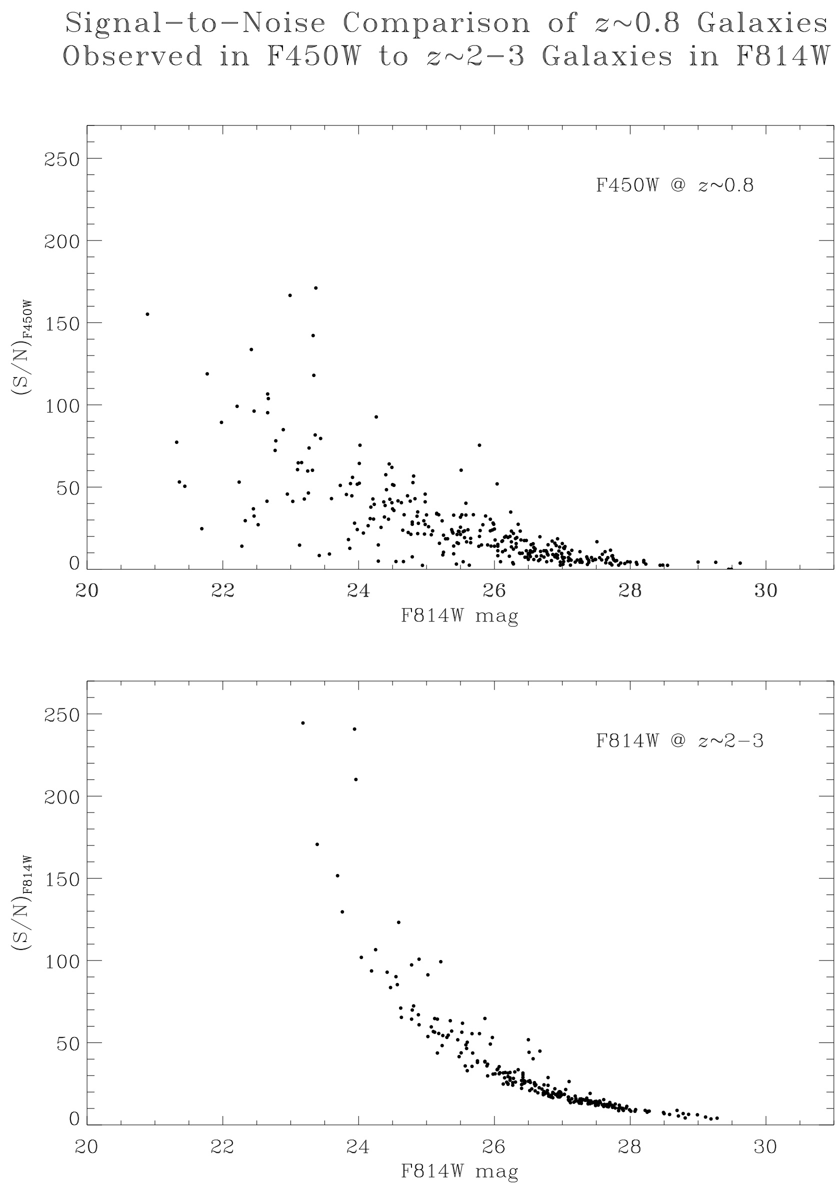

Fig. 6–16.— Comparison of signal-to-noise ratio of $z \sim 0.8$ objects observed through the F450W filter versus $2.0 < z < 3.0$ objects observed through the F814W filter, plotted against the F814W magnitude. At any given magnitude, the F814W images are again found to have roughly twice the SNR of the F450W images. Simulations, similar to those done for the $z \sim 0.8$ comparison, are also created and analyzed for this comparison.

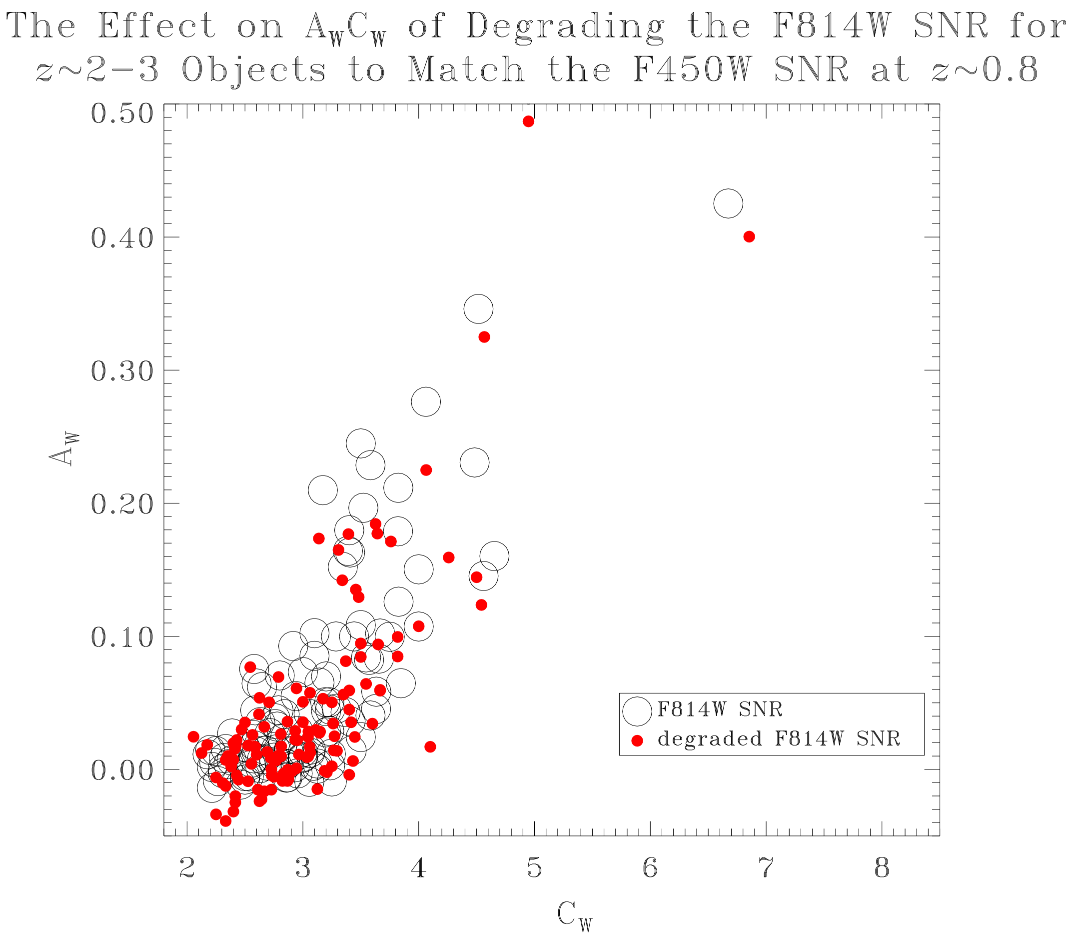

Fig. 6–17.— The A_W-C_W distribution of $2.0 < z < 3.0$ HDF galaxies observed in F814W before *(black circles)* and after *(red dots)* adding noise to match the lower SNR of observations in F450W. Though several border-line asymmetric objects cross over to the low-A_W side when noise is added, the overall distribution of the galaxies is still markedly different from that seen in F450W at $z \sim 0.8$. As the same rest-frame wavelength is represented at these two redshifts, bandpass effects cannot be responsible for the change in the distribution.

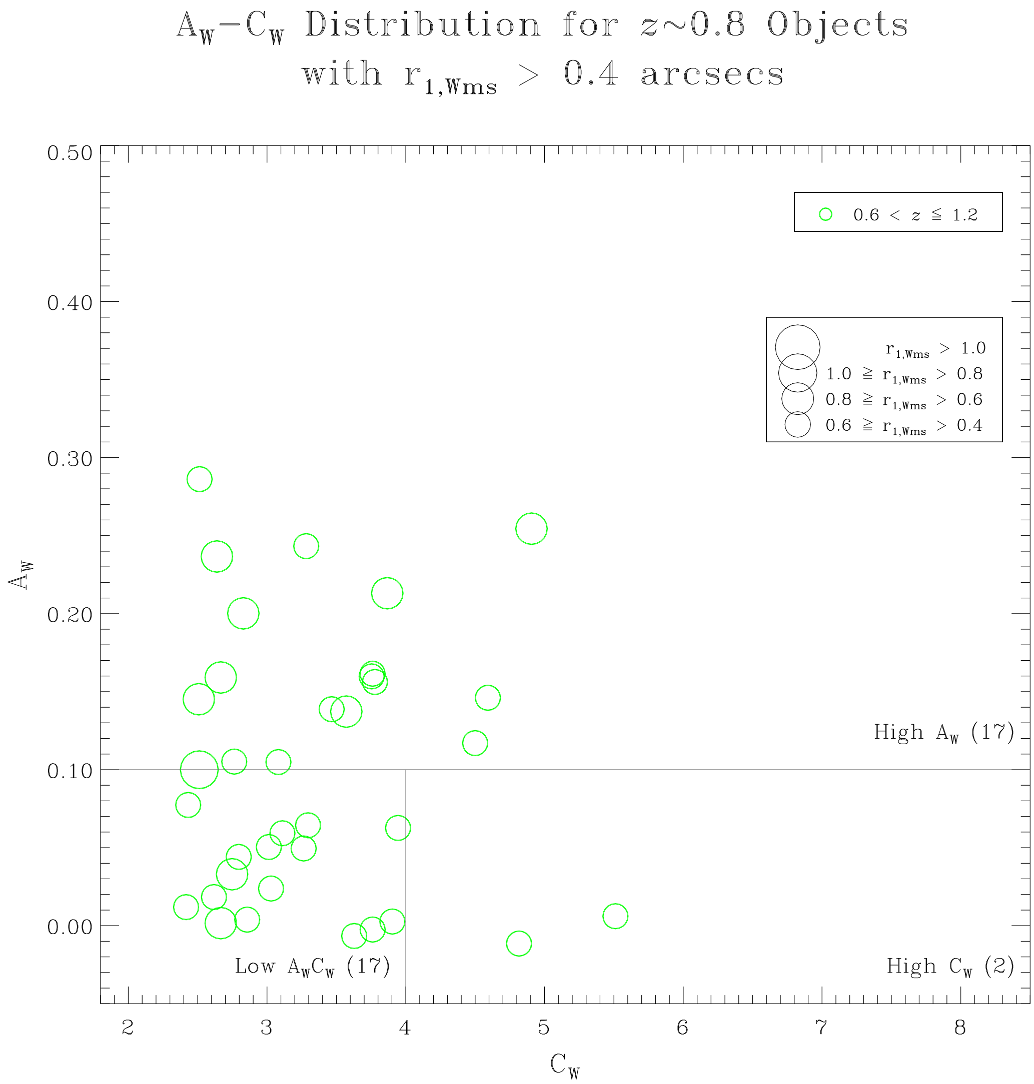

Fig. 6–18.— The A_W-C_W distribution of $z \sim 0.8$ objects with $r_{1,Wms} > 0''.4$. A test of whether the high percentage of asymmetric objects at high redshift may simply be a result of sampling only the bright end of the luminosity function where asymmetric objects tend to lie at all redshifts. Clearly, a comparison of this figure with the $z \sim 2-3$ panel of Figure 6–8 shows that both populations appear to have roughly 50% of their objects in High-A_W.

increase in the asymmetric population relative to the full population at low versus high redshift is, in part, a result of sampling deeper into the luminosity function at low redshift than at high redshift.

2.3. Summary of Results Thus Far

- The distribution of galaxies in the A_W-C_W plane between now and $z \sim 1.2$ has not changed significantly. A closer comparison to the local sample will be presented in the next section.
- The disappearance of high concentration, low asymmetry (High-C_W) objects from the A_W-C_W plane above $z \sim 1.2$ is almost certainly strongly influenced by selection effects. More precisely, if all objects at $z \sim 1.5$ or $z \sim 2.3$ have SEDs similar to those of objects around $z \sim 0.8$, they would be largely undetectable with the currently available telescopes and instruments. On the other hand, the mere fact that many objects are, indeed, seen beyond $z \sim 1.2$ indicates that the assumption of steady SEDs is too conservative. More precise conclusions will depend on the development and implementation of realistic evolutionary models.
- The appearance of high asymmetry (High-A_W) objects at $z \sim 1.2$ cannot be explained by the same selection effects as those operating on High-C_W objects, as those effects would act to decrease the measured asymmetry. High asymmetries probably also cannot be attributed merely to measuring A_W for the UV component of highly redshifted galaxies. On the other hand, the preponderance of high A_W objects beyond $z \sim 1.2$ may be consistent with a picture in which the most asymmetric objects (at all redshifts) are also generally the brightest objects. This explanation appears to be plausible for objects in the $0.6 < z < 1.2$ redshift bin. The relative

increase in the number of High-A_W objects beyond $z \sim 1.2$, therefore, would be primarily a result of sampling only the upper end of the luminosity function. This scenario would predict that a large population of smaller, less-asymmetric galaxies exists below the magnitude/radius cutoff of this sample. These galaxies, however, would be extremely difficult to detect given the HST flux and resolution sensitivities.

3. A Closer Look at Galaxies at $z \sim 0.8$

An alternate means of exploring bandpass shifting effects on the distribution of galaxies in the A_W-C_W plane is to simulate the appearance of local galaxies at various redshifts, carefully accounting for the effects of cosmology at those redshifts. If galaxies at high redshift have the same range of morphology as local galaxies, these simulations should reveal a similar A_W-C_W distribution for both samples.

In order to understand the effects of cosmology on the appearance of local galaxies at high redshift, galaxies in the local sample are cosmologically shifted and observed as if they were in the HDF. In the previous section, we noted the importance of using representative SEDs to estimate K-corrections for simulations of galaxies to high redshift. Given the available comparison high redshift data (i.e., the HDF in F300W, F450W, F606W, and F814W), we chose to create high redshift simulations at $z = 0.8$ from local $\sim B$ band images. As mentioned previously, the F814W band at $z = 0.8$ corresponds directly to rest-frame B. As a result, no K-corrections are necessary for these simulations, and uncertainties due to bandpass shifting are not an issue.

The simulations were created using the local B_J-band images for the Lowell sub-sample of the Frei catalog, Thuan-Gunn g images for the Palomar sub-sample of the Frei catalog, and B-band images for the HvG galaxies. Assuming a cosmology of $H_0 = 75$, $q_0 = 0.5$, the angular size change and surface brightness dimming of each galaxy were calculated and applied. The images were then rebinned and noise was added to simulate observing the "redshifted" galaxies through the F814W filter, as if they were in the HDF. Figure 6–19 shows the montage of the simulated local sample. The calculated values of A_W and C_W are given in the bottom left and right corners, respectively. The HvG galaxies are the last four in the montage (Figure 6–19c). Unfortunately, because of the non-standard size and shape of the images, these last four images are slightly distorted (especially, NGC 7252 and NGC 295). The pertinent features are, nonetheless, still evident.

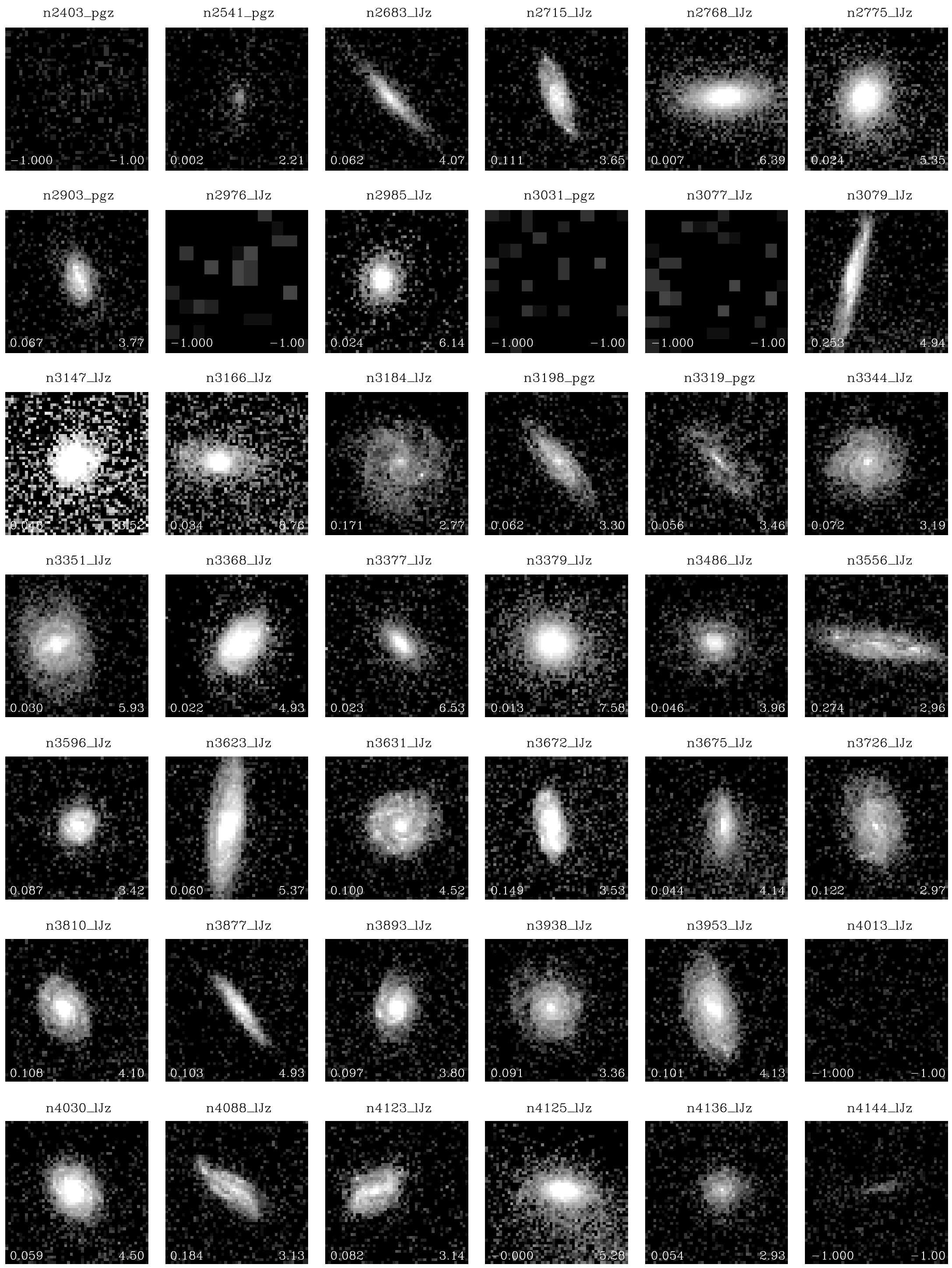

Fig. 6–19.— Montage of the local sample simulated at $z \sim 0.8$. A_W and C_W are given in the bottom left and right corners, respectively. The four merger candidates from Hibbard and van Gorkom (1996) are the last four objects in the montage (Figure 6–19c). Unfortunately, because of their non-standard shape, these images were slightly distorted when being placed in this montage. The pertinent features are, nonetheless, still evident.

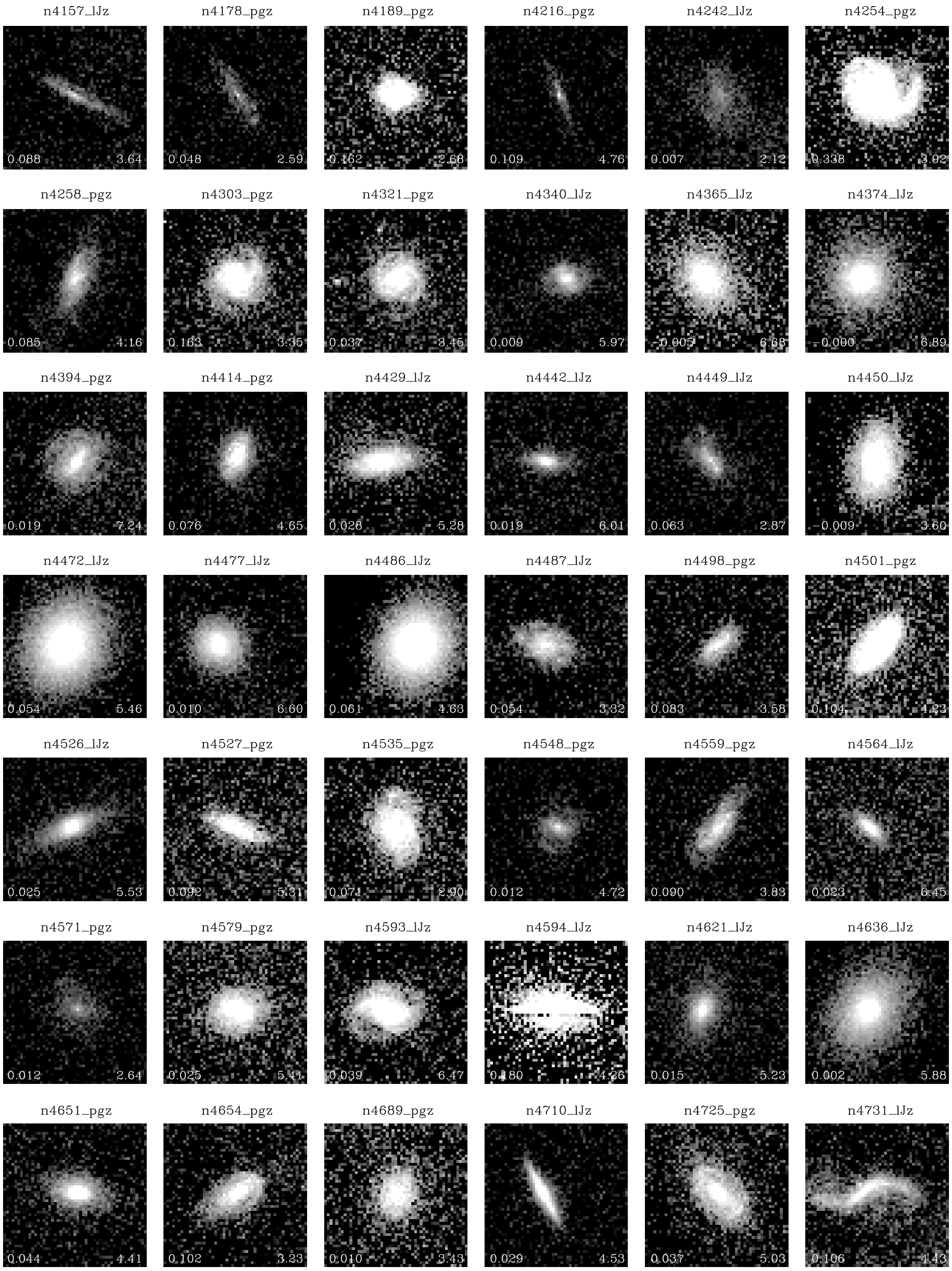

Fig. 6–19b. Montage of simulated $z \sim 0.8$ galaxies *(continued).*

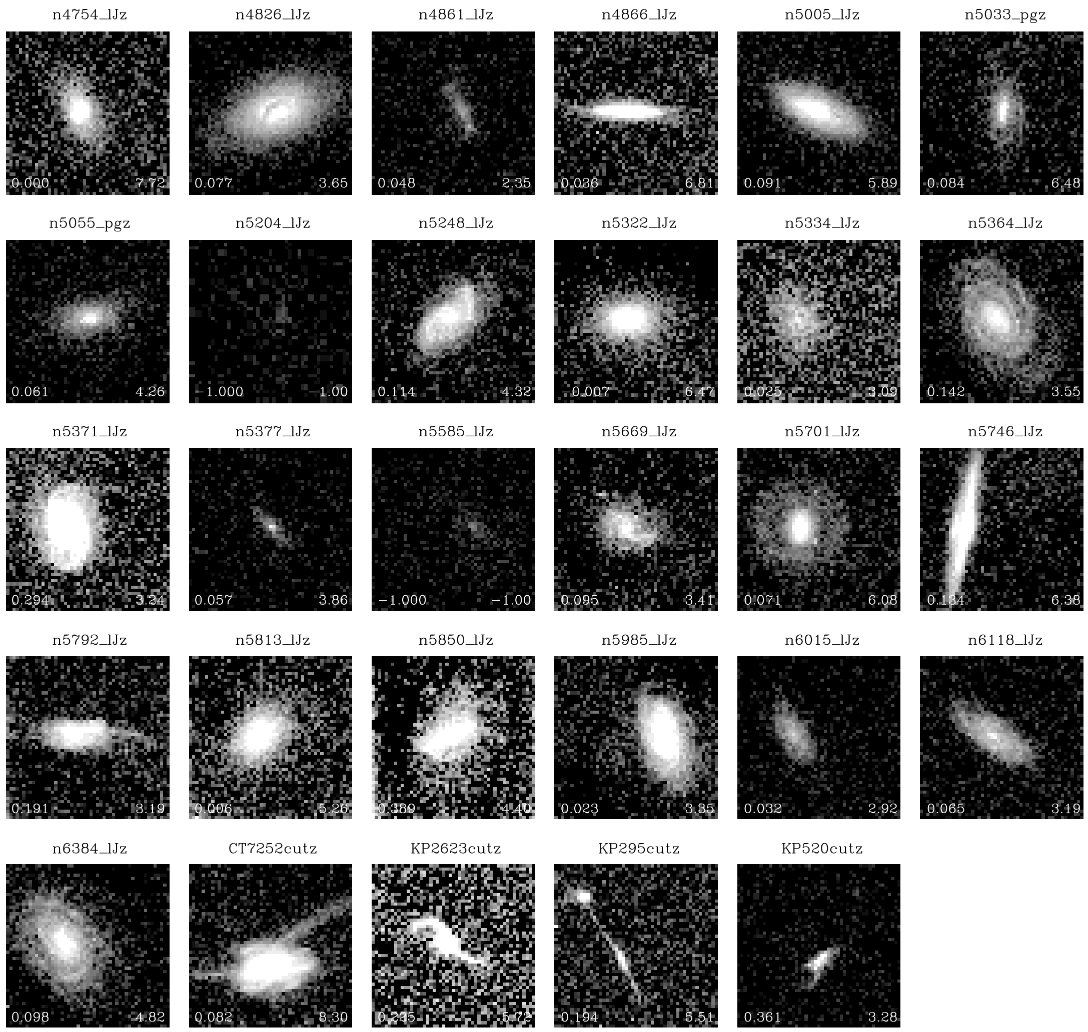

Fig. 6–19c. Montage of simulated $z \sim 0.8$ galaxies *(continued).*

Figure 6–20 shows the A_W-C_W distribution of the simulated $z = 0.8$ galaxies. Comparison of this figure with Figure 5–4 from the previous chapter shows that the overall distribution of the galaxies in the two samples is quite similar, though galaxies in the simulated sample generally have slightly smaller values of both A_W and C_W. E/S0s in both samples exhibit the same range of C_W, while a very slight drift towards slightly higher A_W is seen in the E/S0s of the simulated sample. This is likely simply a geometric effect and has also been noted in simulations created by both A96b and Conselice et al. (1999). Spirals in the simulated sample have moved to fill in, to some extent, the Low-$A_W C_W$ corner of the A_W-C_W diagram, though the overall range of spirals in both A_W and C_W is still roughly the same. The few irregulars that have survived the shrinking and dimming are now well-imbedded in the midst of the spirals in the Low-$A_W C_W$ corner. In contrast, the three HvG peculiars remain well-segregated from the rest of the population.

Figure 6–21 replots the $z = 0.8$ simulations and compares them to the A_W-C_W distribution for observed HDF galaxies with redshifts $0.75 \leq z \leq 1.14$. This comparison shows that the two samples populate roughly the same region of the A_W-C_W plane. This supports the earlier finding (from the comparison of the A_W-C_W distributions in Figure 6–8) that there is little evolution in the A_W-C_W distribution out to $z \sim 1.2$. Figure 6–21 adds a further strong comparison to the local sample at $z \sim 0$, which bolsters the view that the continuity of Hubble types extends from the present all the way to $z \sim 1.2$.

Though the simulated and observed $z \sim 0.8$ samples populate roughly the same range of A_W and C_W, their distributions are somewhat different. The simulated sample shows a fairly uniform A_W-C_W distribution in the High-C_W and Low-$A_W C_W$ classes with a tail into the High-A_W regime. There is, however, a dearth of very low A_W-C_W objects in the

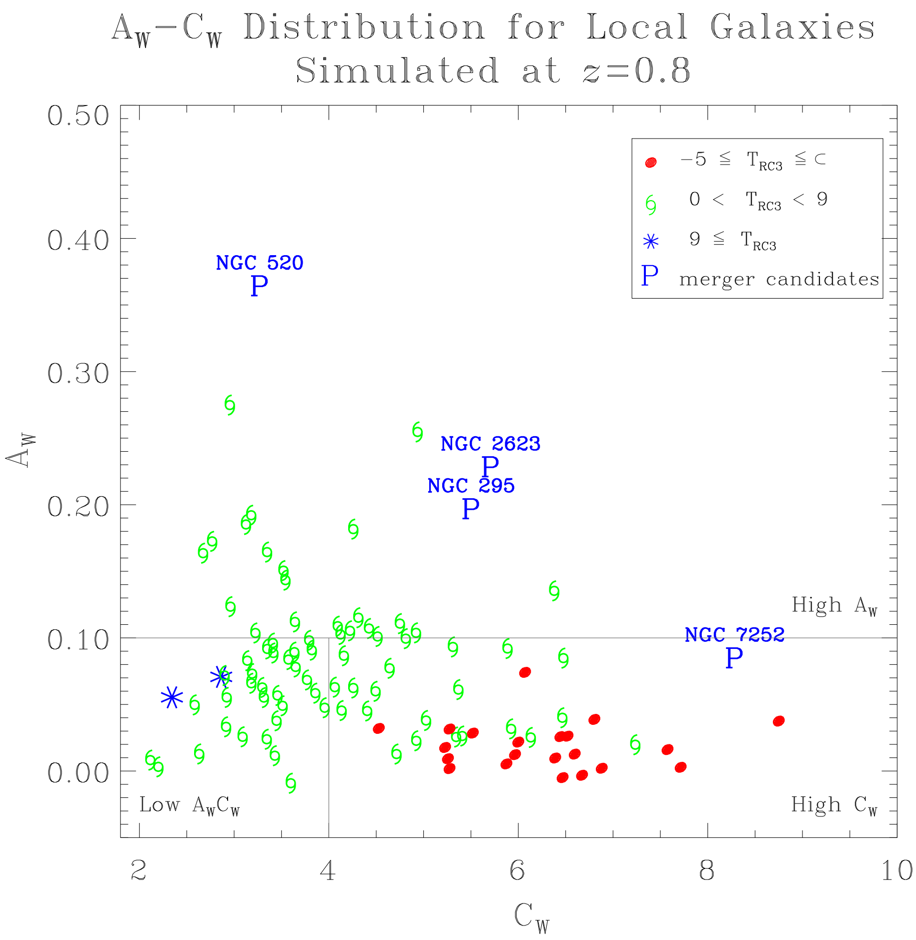

Fig. 6–20.— The A_W-C_W distribution for local galaxies simulated at $z = 0.8$. Comparison of this figure with Figure 5–4 from the previous chapter shows that the overall distribution of the galaxies in the two samples is quite similar, though galaxies in the simulated sample generally tend towards slightly smaller values of both A_W and C_W. E/S0s *(red ellipses)* in both samples cover the same range of C_W, while a very slight drift towards slightly higher A_W is seen in the E/S0s of the simulated sample. This is likely simply a geometric effect and has also been noted in simulations created by both A96b and Conselice et al. (1999). Spirals in the simulated sample have moved to fill in, to some extent, the Low-A_WC_W corner of the A_W-C_W diagram, though the overall range of spirals in both A_W and C_W is still roughly the same. The few irregulars that have survived the shrinking and dimming are now well imbedded in the midst of the spirals in the Low-A_WC_W corner. In contrast, the three HvG peculiars remain well segregated from the rest of the population.

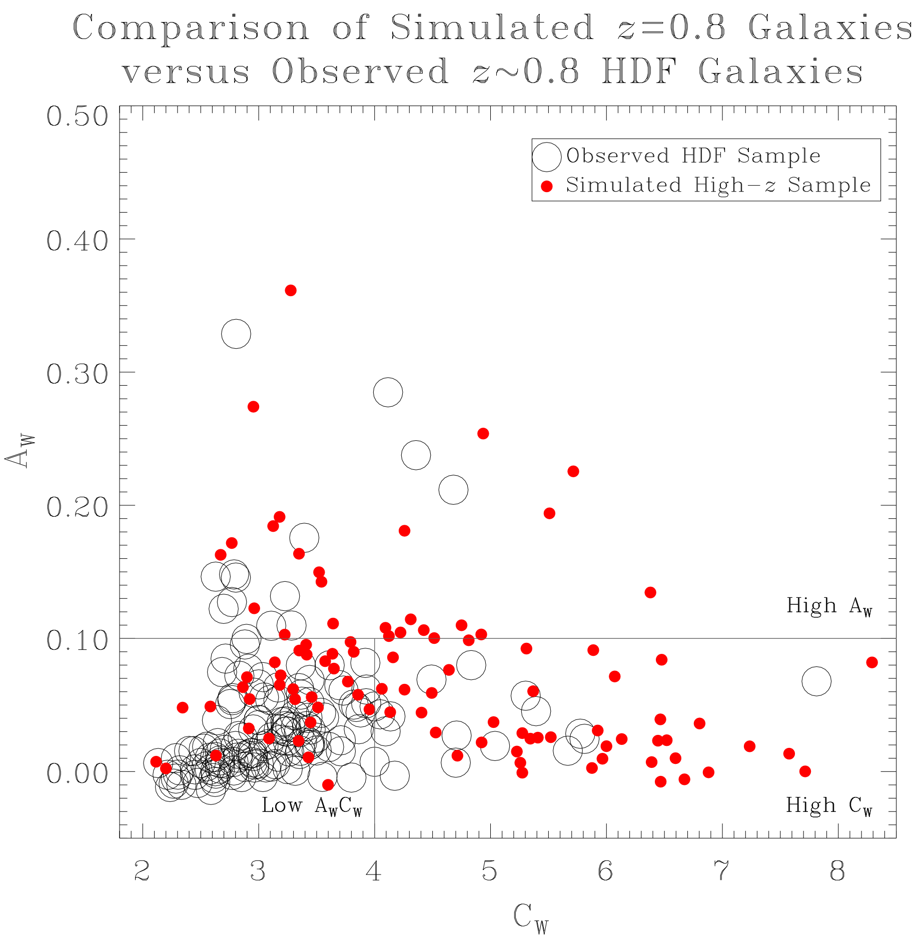

Fig. 6–21.— Comparison of the A_W-C_W distribution of local galaxies simulated at $z = 0.8$ galaxies *(red dots)* with observed HDF $z \sim 0.8$ galaxies *(open circles)*. The two populations occupy roughly the same region of the A_W-C_W plane, indicating that the range of A_W-C_W values populated by galaxies out to $z \sim 1.2$ remains roughly constant. This supports the view that Hubble-type galaxies persist out to $z \sim 1.2$.

simulated sample. The HDF sample, on the other hand, shows a high concentration of such low A_W-C_W objects, which tails off into the High-C_W and High-A_W regimes. This is likely a result of the local sample being basically a magnitude-limited sample (which weights the luminosity function towards bright galaxies), while the HDF is more likely a volume-limited sample (and, therefore, weighted towards faint galaxies). Ideally, a more representative simulated sample should be created, preferably by starting with an initial local sample more representative of the true galaxy luminosity function. In lieu of such a sample, however, it may be possible to synthesize a simulated sample, matched in absolute magnitude, using the local sample that is currently available. I have attempted to create such simulations, but they are not yet well-matched to the high redshift sample. The shift of objects in the A_W-C_W distribution, however, is primarily seen in C_W, which is more sensitive to Hubble type. Since this work focusses more closely on asymmetry, it is the A_W distribution that is more important. For this dimension, the local sample appears to be adequate.

Another concern arises from a possible mis-match in the overall size and magnitude between the local sample and the HDF sample. Since the local sample is more luminous than the high redshift sample, the shifted and dimmed simulations may result in systematically larger and/or higher surface brightness objects than the HDF galaxies they are meant to simulate. The size-magnitude relation of the simulated sample and the observed HDF sample are plotted in Figure 6–22. Though the galaxies in the local sample are generally larger and brighter than the HDF galaxies, the two samples follow roughly the same size-magnitude relation. In order to better sample the faint end of the HDF sample, however, an experiment was made to "pre-shrink and dim" the simulated galaxy sample to better match the HDF. The noise in these "pre-shrunk" images, however, was difficult klwu; Mon Oct 4 07:44:08 1999

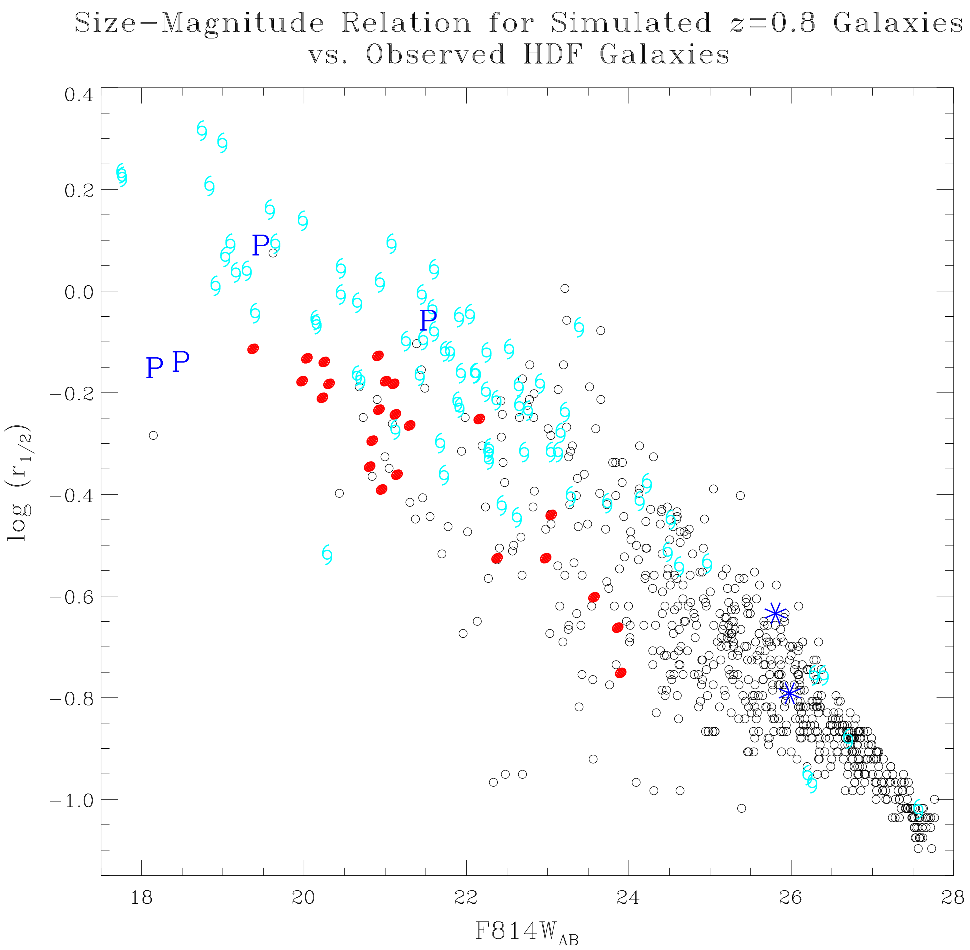

Fig. 6–22.— Comparison of the size-magnitude relation for the simulated $z = 0.8$ galaxies (marked by galaxy symbols) versus the observed HDF galaxies (open circles). The two samples clearly follow roughly the same size-magnitude relation, though the simulated local sample is generally larger and brighter than the HDF sample.

to characterize, and re-creating the HDF noise in these images was not possible in the time available. A_W and C_W were, therefore, calculated on the "pre-shrunk-and-dimmed" images without reproducing the proper HDF noise. Preliminary results indicate that the pre-shrunk-and-dimmed galaxies continue to tend toward smaller values of A_W and C_W, but further conclusions will await improved simulations.

The general indication from the simulations that have been presented in this section is that the A_W-C_W distribution of galaxies redshifted from the local sample to $z = 0.8$ is not very different from the local A_W-C_W distribution. A trend towards smaller values of both A_W and C_W is seen, but the range of values is not significantly different and the separation of the various types of galaxies remains comparable to the separation of these types in the local sample.

The A_W-C_W distribution of the simulated sample was used to guide the definition of the three A_W-C_W classes. In a separate set of simulations, the local sample was simulated at a wide range of redshifts between $z = 0.2$ and $z = 5$. These simulations showed very clearly that A_W and C_W both decrease as an object is moved to higher redshift. At redshifts of around $z = 2 - 3$, however, many objects have become so small and dim that useful morphological information is difficult to extract. It is desirable, therefore, to define the classes using a sample of galaxies that is reasonably representative of the galaxies for which meaningful values of A_W and C_W may be measured. Since there are very few low redshift or bright galaxies in the HDF, it may be misleading to define the A_W-C_W classes using the A_W-C_W distribution of the local sample. The simulated $z = 0.8$ sample, however, appears to match the observed $z \sim 0.8$ HDF galaxies quite well, and, therefore, defining the classes using this sample (where morphological types are also well-known) seems reasonable. One does note that there are several spirals in the simulated sample that fall in the high asymmetry class. As mentioned earlier, however, several of these objects show structure indicative of a possible recent interaction. A few appear to simply be spirals with bright, perhaps slightly asymmetric, arms. Only one object has a high A_W which is caused by the persistence of the peculiar brightening of the sky background, mentioned in Chapter 3, into the $z = 0.8$ simulations. As expected, application of the A_W-C_W classes to the local sample finds several more spirals in the high asymmetry (High-A_W) class. This is simply a consequence of the high resolution of the local images: spiral arms and dust lanes are well-defined and result in a higher measured asymmetry. The final boundaries chosen for the three A_W-C_W classes are as follows: High-C_W: $A_W < 0.10$, $C_W > 4.0$; Low-$A_W C_W$: $A_W < 0.10$, $C_W > 4.0$; and High-A_W: $A_W > 0.10$. Note that shifting these boundaries by ~ 0.02 in A_W or ~ 0.5 in C_W does not severely affect our conclusions.

4. A Comparison to Previous Work

As mentioned in Chapter 1, several groups have studied the morphologies of faint galaxies. Glazebrook et al. (1995) present visual classifications of galaxies in the Medium Deep Survey (MDS, Griffiths et al. 1994, Glazebrook et al. 1995), while Odewahn et al. (1996) present morphological classification of galaxies both visually and using artificial neural networks (ANNs) trained on visual classifications. Though both of these present similar results based on their classifications (i.e., ellipticals and spirals show number counts consistent with little or no evolution, while a significant excess of very late-type spirals, irregulars, and peculiars is found), it is difficult to compare to their works as the classification methods are quite different and the actual classifications are often unpublished.

The only comparable set of published data on high redshift galaxy morphology is from A96b and Abraham et al. (1996a, hereafter A96a), who present classifications using a very similar pair of indices to those presented in this dissertation: A_A and C_A. (In fact, A_W is a refined version of A_A. For a detailed comparison of these two pairs of indices, please see Chapter 3.) Based on the measurements of A_A and C_A in the HDF, several results were presented. Simulations of the Lowell sub-sample of the Frei catalog to redshifts of $z = 0.3, 0.5, 0.7$ indicate that cosmological effects on their indices are small. The Frei catalog and the HDF catalog should, thus, be directly comparable. Most HDF galaxies appear to populate the same region of their A_A-C_A diagram as the local sample, suggesting that the morphologies of these galaxies are similar to those of the Frei sample. Visual classifications of these objects by R. S. Ellis, presented in van den Bergh et al. (1996, hereafter vdB), support this claim. A rather well-defined separation between their E/S0, spiral, and "Irregular/Peculiar/Merger" galaxy classes is seen, which matches quite well the division of these galaxy types seen in the local sample. A significant new population of high-A_A, low-C_A objects is seen in the HDF. These objects are classified as "Irr/Pec/Merger" galaxies; no distinction is made, therefore, between the traditional irregular Hubble-type galaxies and "irregular-looking" (i.e., peculiar) galaxies. Recall, from Chapter 1, that one should be cautious of conclusions reached when these two types of galaxies are combined into one group. Though they note that the Frei catalog clearly does not represent the full range of morphologies seen locally, A96a, nevertheless, imply that these objects may represent the appearance of a significant morphologically disturbed population of galaxies at faint levels.

As was shown in Chapter 5, measurements of asymmetry and concentration for the local sample using the two pairs of morphological parameters, A_W-C_W and A_A-C_A, agree reasonably well. There are some differences, which were discussed in Chapter 5, but they are not fundamental. How well, then, do we compare at high redshift? A comparison of A_W-C_W and A_A-C_A for the A96a-vdB sample follows.

4.1. A Comparison of A_W-C_W versus A_A-C_A in the Hubble Deep Field

A96a and vdB present measurements of A_A and C_A for galaxies in the Hubble Deep Field with magnitudes $21 <$ F814W$_{VEGA} < 25$ ($21.44 <$ F814W$_{AB} < 25.44$). Recall that the limiting magnitude of the HDF sample presented earlier for which A_W and C_W are measured is F814W$_{AB} \sim 26$. A_W and C_W were, therefore, measured roughly $0.5 - 1$ magnitudes deeper than the A96a-vdB sample. On the bright end, the A96b-vdB sample loses roughly 10-15 bright ellipticals and spirals, a fact which will be revisited later.

The positions of the objects on the WF chips given in vdB were used to create postage stamps of the galaxies in their sample. A_W and C_W were then calculated on this set of objects. The results of the two pairs of morphological algorithms are shown in Figure 6–23. Note that the A96a-vdB A_A-C_A plot has been re-created using the data presented in vdB and is shown plotted on a linear (rather than logarithmic) scale. The symbols in both plots correspond to the visual classifications of these galaxies done by R. S. Ellis. The boundaries of the A_W-C_W classes are shown in the A_W-C_W diagram. An approximate curve corresponding to the division between the spiral and "Irr/Pec/M" (hereafter, IPM) classes is drawn on the A_A-C_A diagram.

Several differences in the two diagrams are evident:

- The mean value of A_A at all values of C_A is higher than the mean A_W value at corresponding values of C_W. In other words, A96a appears to find many more high

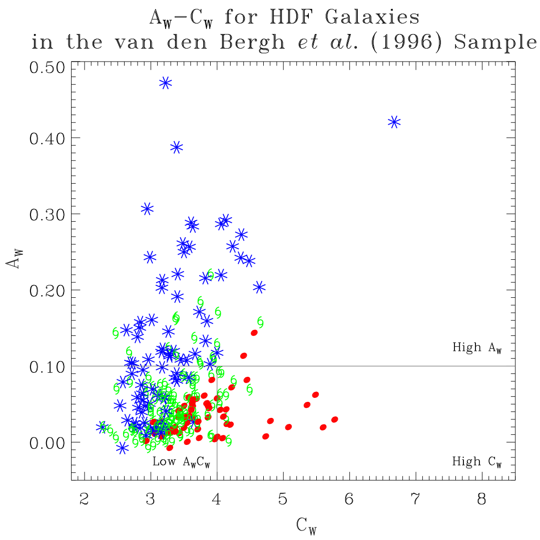

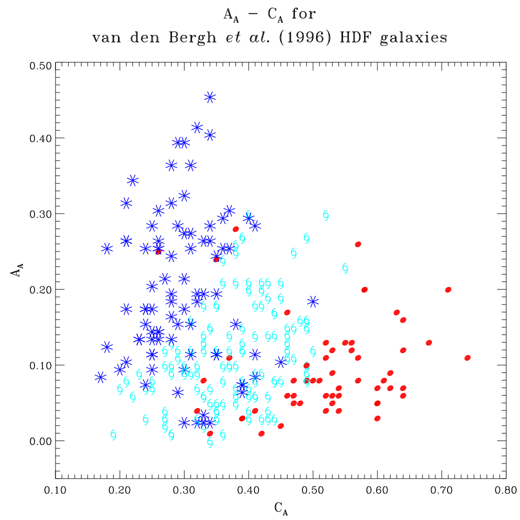

Fig. 6–23.— Comparison of A_W-C_W *(left panel)* and A_A-C_A *(right panel)* for the subset of HDF galaxies presented in A96a and vdB, whose magnitudes range between $21 < \mathrm{F814W}_{VEGA} < 25$. Symbols in both panels are the visual classifications of these galaxies done by Richard S. Ellis into three broad groups: E/S0, Spiral, and Irregular/Peculiar/Merger. The A_W-C_W class boundaries are drawn on the A_W-C_W diagram. The Abraham et al. boundaries (which would be curves in linear space) have not been drawn as they are well reflected in the separation of the three classes. This separation is not nearly so clear in A_W-C_W, possible explanations for which will become clear from the next few figures.

asymmetry galaxies than are found using A_W-C_W. If one uses the A96a dividing line between spiral and IPM galaxies, however, the number of IPM galaxies is only roughly half the total number of high-asymmetry objects. From the comparison of Frei versus HvG galaxies, however, there is no motivation for using a slanted curve, such as that of A96a, to identify asymmetric peculiar objects. If anything, this comparison would indicate that the dividing line for peculiar objects should slant in the opposite direction, i.e., down towards higher concentration, as early-type galaxies do not need to show A_W values as high as later-type galaxies in order to be considered peculiar.

- A96a-vdB also generally show a much larger spread in A_A at all values of C_A. In the IPM class, in particular, the spread in A_A is rather uniformly populated. In A_W, however, there is a concentration of IPM galaxies in the Low-$A_W C_W$ corner with a tail to higher A_W values.
- The E/S0 galaxies in A96a-vdB show high values of C_A. This is not seen in C_W. In fact, the majority of the E/S0 galaxies lie in the Low-$A_W C_W$ corner of the A_W-C_W diagram, where one would not expect to find E/S0s at all.
- The E/S0 galaxies in A96a-vdB also show high values of A_A. This is very likely a side effect of the A_A algorithm, which uses an integer pivot point, rather than a sub-pixel pivot point. As mentioned in Chapter 3, this can result in a significant over-estimate of A_W, especially at high redshift where the resolution is low.
- The various galaxy types are very clearly separated in A_A-C_A, but not in A_W-C_W. In particular, a much greater overlap between spirals and IPM galaxies is seen in A_W-C_W.

Each of these points will now be discussed in more detail and several factors which contribute to these differences will be presented.

4.2. A Comparison of Simulated High Redshift Galaxies

As described in Chapter 3, the A_W-C_W and A_A-C_A algorithms differ primarily just in the details. Could it be, however, that these detailed differences result in dramatically different results being calculated at high redshift, even when the galaxies have not changed? To test this notion, the simulated $z = 0.8$ sample created in this work is compared to a sample of galaxies simulated $z = 0.7$ by A96b.

Figure 6–24 shows the comparison of A_W-C_W measured for the simulated $z = 0.8$ galaxies to A_A-C_A measured for A96b's simulated $z = 0.7$ galaxies. The comparison here consists of only the Lowell sub-sample of the Frei catalog, as these are the only objects in the local sample for which A96b created simulations and measured $A_A\dot{T}$he details of the simulations are different; for example, the background counts of the simulated images in A96b are "calculated assuming that HST is pointed at 15° from the North Galactic Cap, and that the gain of the CCD controller is set to 7 electrons/ADU" (A96b), while, as mentioned earlier, the simulations created in this dissertation are created to simulate the noise characteristics typical of the HDF.

Comparison with Figure 5–3, which shows the corresponding pair of figures for the local sample (in logarithmic coordinates), reveals several differences between the local and simulated samples. The separation between E/S0s and spirals in the A96b simulations is less clear than in the local sample. The most asymmetric objects in the simulated sample also show significantly lower values of A_A ($A_A\sim 0.1$) than their counterparts in the local sample ($A_A\sim 0.25 - 0.3$). In fact, a general reduction in A_A is seen for all galaxies.

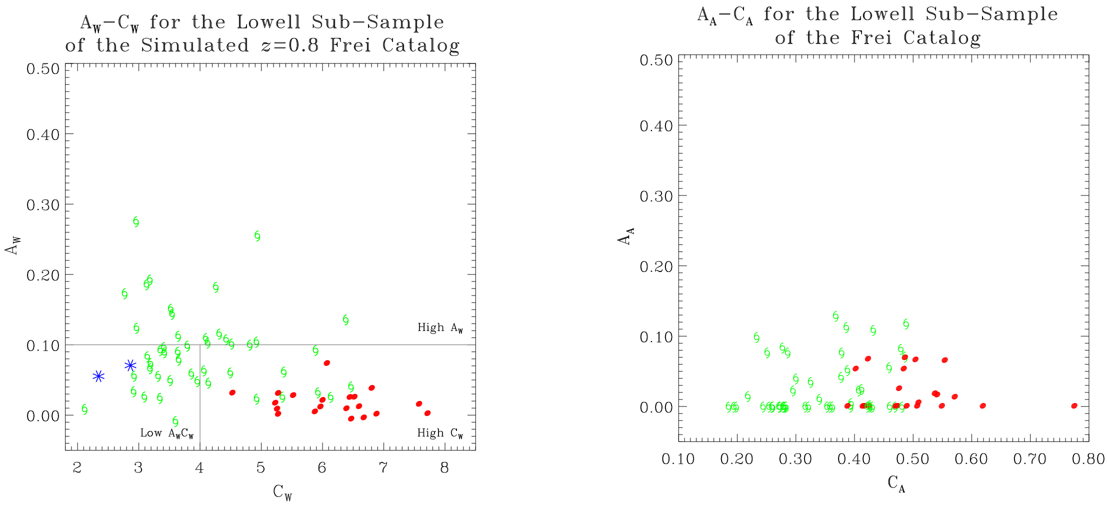

Fig. 6–24.— Comparison of A_W-C_W and A_A-C_A for the Lowell sub-sample of the Frei Catalog simulated at $z \sim 0.8$. The comparison is made with only the Lowell sample as Abraham et al. created simulations with only those galaxies. General trends for both pairs of indices are as follows: (1) a decrease in the asymmetry of all objects, (2) the disappearance of some objects into the noise, and (3) a decrease in the separation between E/S0s and spirals.

37 objects in the simulated sample were found with negative A_A i.e., the background correction for these galaxies was higher than their raw asymmetries, whereas only 17 such objects exist in their local sample. In contrast, only one and two galaxies in the local and simulated $z = 0.8$ samples, respectively, were found to have a negative value of A_W. This difference may be a result of the difference in the the noise characteristics used for the two simulated samples. A more thorough understanding of these differences would require a better understanding of exactly how the A96b simulations were created. This information has not yet been made available. Note that a value of A_A= 0.001 was assigned to these galaxies in order to still be able to plot them on the logarithmic plots of A96a,b. Galaxies with negative A_W were simply not plotted in the logarithmic plot.

Most of the trends seen in the A96b simulated vs. local comparison are also seen in the comparison of the simulated and local samples in A_W-C_W: a decrease in A_W of the most asymmetric objects, an overall decrease in the A_W, and the disappearance of some galaxies into the noise of the simulations. The magnitude of the trends in A_W-C_W, however, are much smaller. As was described earlier in this chapter, aside from a drift to somewhat smaller values of both A_W and C_W, the overall appearance of the A_W-C_W distribution of galaxies in the local and simulated samples is quite similar. It is important to note that, as mentioned earlier, irregular galaxies become well-mixed with the spiral population at high redshift. Unfortunately, all of the irregular galaxies in the A96b simulations are no longer detected and, therefore, cannot be directly compared. Recall, however, from Figure 5–3, that local irregulars were found to co-exist with spirals in A_A-C_A; it is expected that they would continue to do so in their simulations.

Though there are clearly some differences in the relative comparison of the simulated and local samples, the overall agreement between the two simulated samples, as well as the two local samples, is fairly reasonable. This can be more clearly seen by plotting A_W vs. A_A and C_W vs. C_A for both the local and simulated samples, as shown in Figures 6–25 and 6–26, respectively. Note that all plots are scaled to the range of values seen in the high redshift sample to facilitate a direct comparison later between the samples.

A general trend between A_A and A_W exists, though there is a slight tendency for A_W to be slightly larger than A_A. The advantage of including the minimization algorithm is visible primarily for the E/S0 galaxies, where A_W is consistently lower than A_A. Between C_A and C_W there is a definite relation, though it is non-linear. Both algorithms find E/S0s to be most highly concentrated, with spirals and irregulars becoming progressively less concentrated. It is interesting to note, however, that the E/S0s, as measured by C_A, are not significantly more concentrated than the highest concentration spirals in either the local or the simulated samples. In contrast, the distinction in C_W between E/S0s and spirals is much clearer, though an overlap region still exists. In addition, note that the limiting value of C_A for galaxies in both samples appears to be roughly 0.6, though there is one outlier in the simulated sample, which has not been explained. This apparent limiting value will become important in the upcoming comparison of C_W and C_A for the high redshift A96a-vdB HDF sample.

From comparison of A_A-C_A and A_W-C_W for the local and simulated $z \sim 0.8$ samples, the following conclusions may be drawn if the galaxy population is not changing significantly. A_W and A_A should both decrease at high redshift. This does not agree with what is seen by A96a for the HDF galaxies, suggesting that the increase in their A_A values cannot be explained simply as the expected response of their algorithm at high redshift. C_W and C_A are also both expected to decrease slightly for early-type galaxies, though they remain roughly constant for spirals. The distinction between E/S0s and spirals, therefore,

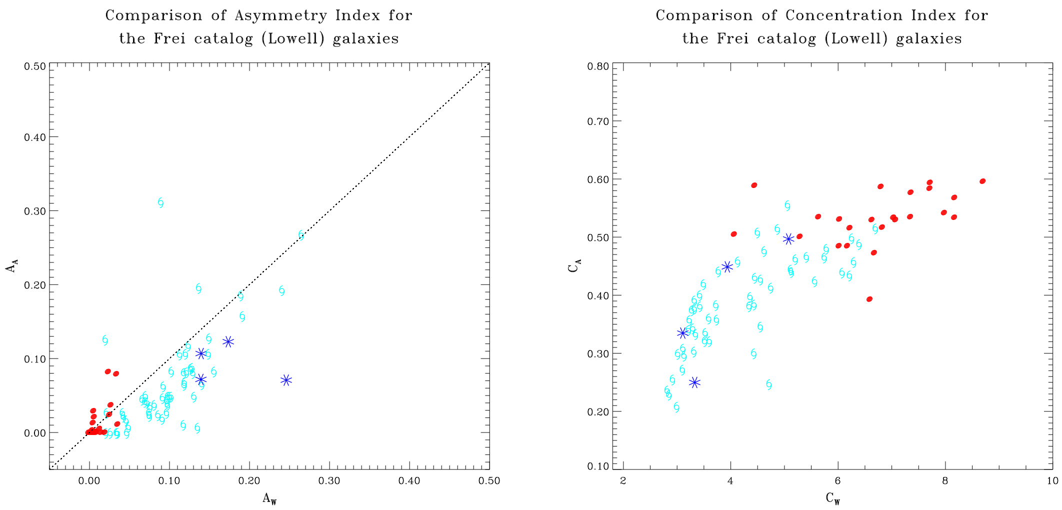

Fig. 6–25.— Comparison of A_W vs. A_A and C_W vs. C_A for the Lowell sub-sample of the Frei catalog. Symbol types are the same as in the previous two figures. Though the agreement is not perfect, the general trends in asymmetry and concentration for both algorithms are similar. Note that all plots are scaled to the range of values seen in the high redshift sample to facilitate a direct comparison later between the samples.

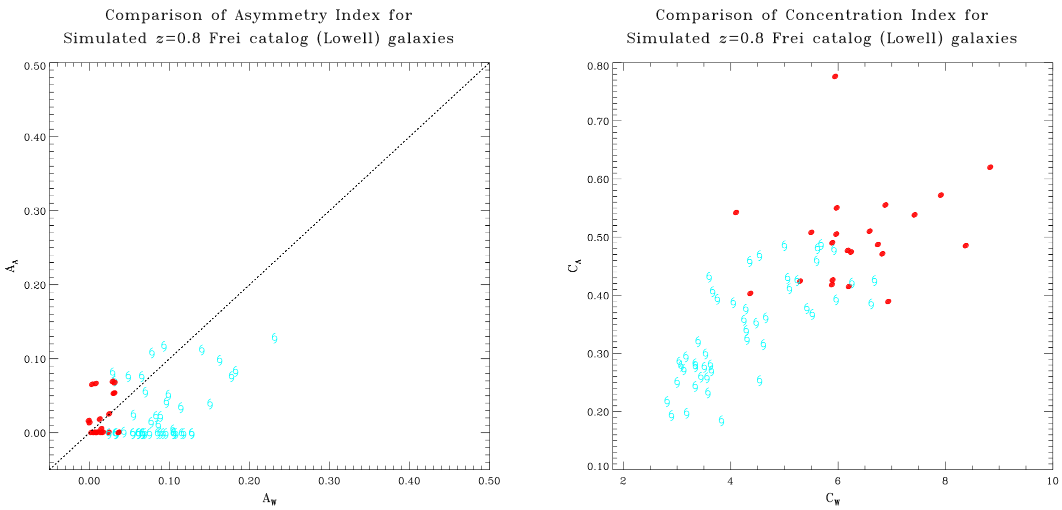

Fig. 6–26.— Comparison of A_W vs. A_A and C_W vs. C_A for the simulated $z = 0.8$ sample. Once again, the symbol types are the same as in previous figures and plots are scaled to the range of values seen in the high redshift sample for easier direct comparison. As was seen in Figure 6–25, a rough correspondence between A_W-C_W and A_A-C_A exists. The relation is consistent with what is seen for the local sample.

should become less clear. This also is not seen by A96a in their HDF data. The differences seen in the A_W-C_W versus A_A-C_A diagrams for the HDF galaxies, therefore, cannot be explained simply as a difference in the response of the two different algorithms at high redshift. One final note: irregular and spiral galaxies have been shown to have comparable values of asymmetry and concentration in both A_A-C_A and A_W-C_W. An intermixing of spirals and IPM galaxies is therefore also expected. The A_A-C_A diagram for the A96a-vdB sample, however, appears to show a very strong division between these two classes with only a few overlaps.

4.3. Possible Explanations for the Differences in A_W-C_W and A_A-C_A at High Redshift

In Figure 6–23, we noted the large number of high asymmetry objects seen by A96a in all three morphological classes. Figure 6–27 shows the comparison of the individual asymmetry and concentration parameters for the A96a-vdB sample: A_W vs. A_A *(left)* and C_W vs. C_A *(right)*. Consider first the A_W-A_A comparison. This plot looks nothing like the corresponding plots for the local and simulated sample presented above. A_A values are systematically higher than A_W values for all types of galaxies. Such high asymmetries are particularly surprising for E/S0s. Perhaps, however, these objects are merely "best" classified as E/S0s, but, in fact, show indications of peculiarity, such as faint tidal features similar to NGC 7252. A "by eye" inspection of these objects, however, suggests that this is not the case. An alternative explanation, therefore, is that the algorithm is yielding spurious asymmetry values for these objects. This is quite possible as the A_A algorithm does not determine its pivot point to better than an integer pixel. The advantage of including the minimization algorithm in A_W is clear.

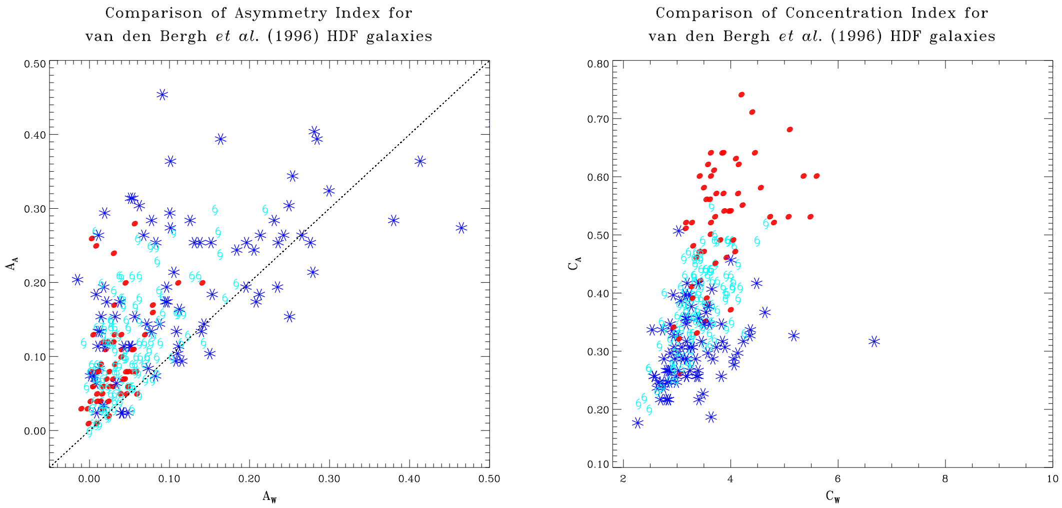

Fig. 6–27.— Comparison of A_W vs. A_A and C_W vs. C_A for the subset of HDF galaxies presented in A96a and vdB. Plot symbols are the same as in previous plots. This pair of plots looks nothing like the two pairs in the previous two comparisons. High values of A_A are seen for all types of galaxies, most surprisingly, even for E/S0s, whereas A_W values are high for some of the "irregular/peculiar/merger" class, but remain relatively low for E/S0s. This difference is likely a result of the inclusion of the minimization algorithm in A_W, since, at high redshifts, small errors in the choice of pivot point may result in significantly larger asymmetry values. In the concentration parameter, much larger values of C_A are seen at high redshift than locally. This is likely a consequence of the Abraham et al. detection algorithm, which uses a σ_{sky} isophote to determine the extent of the galaxy. At high redshift, this isophotal level reaches a magnitude fainter than locally. As the galaxy profile is probed to fainter levels, it is not surprising that higher concentrations may be found. C_W is designed to better match the galaxy area probed at various redshift (currently optimized for $z \sim 0.8$) and, therefore, finds smaller concentrations at higher redshifts, as would be expected for the fainter galaxies and poorer resolution that are being probed.

The large number of high asymmetry IPM galaxies is particularly important, as they contribute so strongly to the claimed increase in peculiar galaxies at high redshift. 87 (32%) out of the 270 objects in the A96a-vdB catalog are visually classified by R. S. Ellis as IPM galaxies. These 87 objects were examined individually and run through a simulation of the A_A algorithm. 23 of these objects are pairs or multiple components that have photometric redshift estimates that indicate that they are not likely related, but that were probably blended into one object by the A_A algorithm. Using the additional photometric redshift information, A_W was tuned to find these objects as separate objects, and, therefore, the asymmetry value returned for these objects was much smaller. Another 12 objects have a bright off-center knot that is clearly not the core of the galaxy, but that may have been chosen as the center of rotation by A_A (this does not include cases where the core itself is off-center). The use of the centroid of the light distribution as the pivot point (as is done by A_W) again results in a lower asymmetry. 12 other galaxies appear to be simple irregulars or LSB galaxies. As expected, most of these 12 galaxies have much lower A_W than the true peculiars; unfortunately, for a few of the LSB objects, this may be due in part to an object mask that does not include the whole galaxy (one of the limitations of the chosen object mask parameters, as described in Chapter 3). 35 out of the original 87 "Irr/Pec/M" objects, therefore, had artificially high asymmetries due to blending of objects or a poor choice of pivot point. The low values of both A_A and A_W found for the 12 irregular or LSB galaxies emphasizes, once again, the error in grouping these galaxies with peculiars. Once these 47 objects are taken out of the sample, the percentage of truly peculiar objects drops from $\sim$30% to $\sim$15%. This is more consistent with the results found using the A_W-C_W indices.

The comparison of C_A versus C_W (Figure 6–27b) also looks very different from its local and simulated counterparts. A96a find much higher concentrations for early type galaxies than even the most concentrated local ellipticals. This contradicts the results of the simulations (Figure 6–26b), which show that, if anything, the measured C_A should decrease at high redshift. To confirm our result that the most concentrated HDF objects in the A96a-vdB sample are less concentrated than local galaxies, a "by-eye" inspection using an independent aperture photometry algorithm was made. This inspection confirmed our results.

The question, then, is why A96a found such high concentrations for the HDF E/S0s. The answer is almost certainly that this is a consequence of defining the galaxy area using an isophotal cut that is based on the sky noise. As described in Chapter 3, the $1.5\sigma_{sky}$ cut used by A96b probes a full magnitude fainter in the HDF than in the local sample. Recall, from Figure 3–8, that changing μ_{det} by one magnitude can significantly change the calculated concentration for an object, in the sense that the concentration increases when a fainter μ_{det} is used. As was explained in Chapter 3, this is a result of probing deeper into the galaxy profile. Not surprisingly, this effect is especially pronounced for ellipticals, where one is probing the faint wings of the galaxy.

One final note about the A96a-vdB sample: When comparing the A_W-C_W distribution of these galaxies (Figure 6–23a) with that of the full HDF sample with photometric redshifts (Figure 6–8), a distinct lack of high concentration objects ($C_W \gtrsim 5.5$) is evident in the vdB sample. This apparent deficiency is simply a result of the magnitude range being studied by vdB. All of the objects in the HDF sample with $C_W \gtrsim 5.5$ are brighter than the upper magnitude limit of the vdB sample, F814W$_{AB} \sim 21.44$.

4.4. Summary of High Redshift Comparison

- Fewer highly asymmetric galaxies are found in the A96a-vdB sample using the A_W-C_W algorithms than are claimed by A96a. Roughly 15% of the A96a-vdB sample are found in High-A_W, while A96a claimed that roughly 25-30% of these galaxies are "Irr/Pec/Merger" galaxies.
- Roughly half of the IPM class (47 out of 87 objects) are not truly peculiar. Their high asymmetries are a side effect of the A_A algorithm.
- Most of the E/S0 galaxies are found to occupy the Low-$A_W C_W$ corner of the A_W-C_W diagram, which is identified locally with spiral galaxies.
- The strong distinction between the three morphological classes in the A_A-C_A plane is not seen in the A_W-C_W plane. This effect is apparently a result of the tendency for A96a to over-estimate A_A for late-type galaxies (and unphysical pairs) and to over-estimate C_A for early types.

Chapter 7

Summary and Conclusions

I have developed several algorithms to quantify peculiarities in galaxy morphology. I focus primarily on two of these "peculiarity indices" in this work: rotational asymmetry, A_W, and concentration, C_W. This pair of indices is compared primarily to a similar pair of indices, A_A and C_A, presented by Abraham et al. (1996a,b).

Though the rotational asymmetry index developed in this work is based on the Abraham asymmetry parameter, the refinements that have been incorporated in A_W are shown to overcome several of the limitations of A_A. The two primary improvements are (1) a definition of the total area of the galaxy that more consistently samples the same physical area of galaxies at various redshifts and (2) a minimization algorithm that finds the minimum rotational asymmetry by calculating A_W using a set of pivot points on a grid centered on the intensity-weighted galaxy centroid. The first refinement is designed to enable more consistent comparison of objects at various redshifts. The current algorithm is optimized for comparisons between local and $z \sim 0.8$ objects. The second refinement is designed to avoid finding artificially high asymmetry values due to a poor choice of pivot point. Using the intensity-weighted centroid of the galaxy for the initial pivot point (rather than, for example, the brightest point in the galaxy) avoids finding localized bright knots or companions as the pivot point. The minimization algorithm enables the minimum asymmetry to be determined even if the "best" pivot point is not found initially.

Comparison of A_W-C_W and A_A-C_A for a sample of local galaxies taken from the Frei et al. (1996) "Catalog of Nearby Galaxies" indicates that the two pairs of algorithms are qualitatively equivalent on images of normal local galaxies. This is also the case for simulations of these galaxies at redshift $z \sim 0.8$.

A_W-C_W are then applied to a sample of 1079 galaxies in the Hubble Deep Field for which photometric redshifts were kindly provided by Andrew Connolly. These objects reach a limiting magnitude of $\mathrm{F814W}_{AB} \lesssim 28.0$. The final catalog of objects, however, totals ~350 galaxies which are detected by the A_W-C_W algorithms and which have a first-moment radius, r_1, greater than $0''.2$, smaller than which no meaningful asymmetry information can be obtained. For reference, this radius corresponds roughly to a magnitude of $\mathrm{F814W}_{AB} \sim 26$. Several interesting features are seen in the A_W-C_W distribution as a function of redshift.

The range of A_W-C_W values seen for HDF galaxies out to $z \sim 1.2$ is comparable to that seen for the local sample, which consists of the Frei et al. (1996) catalog augmented by 4 merger candidates from Hibbard & van Gorkom (1996). The overall locus of the HDF sample is slightly lower, in both A_W and C_W, than that of the local sample, primarily as a result of the lower resolution and surface brightness of the high redshift objects. There is also a large concentration of HDF objects at very low A_W and C_W values that is not seen in the local sample. Recall, however, that the local sample consists almost exclusively of large bright galaxies. Inclusion of local dwarfs and low surface brightness objects would likely fill in this regime of the A_W-C_W distribution for the local sample. These exceptions aside, however, the overall impression is a sense of strong similarity in the regions of the A_W-C_W plane populated by the local sample and the HDF galaxies out to $z \lesssim 1.2$.

Beyond $z \sim 1.2$, the number of high concentration (High-C_W) objects decreases sharply. Using the colors given in Williams et al. (1996), coarse SEDs were created for a subset of objects at $z \sim 0.8$. Assuming the SEDs and luminosities of these objects do not change significantly out to $z \sim 2$, simulations of the appearance of these objects at $z = 1.5$ and $z = 2.3$ were created. At $z = 1.5$, 100 out of the original 150 objects are no longer detected. By $z = 2.3$, only 5 objects survive the detection limits. Though a true drop in the number density of these high concentration objects is not ruled out by these data, any such real change will be virtually impossible to detect in the presence of such strong selection effects.

Beyond $z \sim 1.2$, the number of high asymmetry objects increases. The magnitude of the calculated asymmetries also increases. Selection effects that applied for the High-C_W galaxies are not the cause of this increase as they would act in the opposite sense, i.e., they would tend to decrease, rather than increase, the asymmetry. The increase in the number and degree of asymmetry also cannot be attributed simply to observing the ultraviolet component of highly redshifted objects. Such bandpass shifting effects were address by comparing two pairs of data: (1) a single population of objects at $z \sim 0.8$ as observed through the F450W bandpass and the F814W bandpass, and (2) a set of galaxies observed at $z \sim 0.8$ in the F450W bandpass versus a set of galaxies observed at $2 < z < 3$ through the F814W bandpass. In the former comparison, the F814W data sample roughly the rest-frame B-band, while the F450W samples well into the ultraviolet part of the galaxy spectrum. The similarity in the two distributions indicates that the bandpass effects are quite small, though not completely negligible. In the latter comparison, the two samples are compared at the same rest-frame wavelength, though they reside at different redshifts. Since the same rest wavelength is observed, no bandpass effects should be present. The difference in the two distributions, then, must be real.

An important concern must be addressed, however, before we can truly believe the apparent increase in the number of asymmetric objects at redshifts beyond $z \sim 1.2$: the signal-to-noise characteristics in the two passbands are different. The signal-to-noise ratio (SNR) of the F814W objects (in both comparisons) is roughly twice that of the F450W objects. To understand how strongly this difference in SNR affects the galaxy distribution in A_W-C_W, the F814W images are degraded and re-analyzed. The effect of decreasing the SNR by a factor of two does generally decrease both the asymmetry and the concentration of these objects, but the overall result is unchanged. It appears, therefore, that the increase in the number of asymmetric galaxies beyond $z \sim 1.2$ is indeed a genuine phenomenon.

The large number of High-A_W objects beyond $z \sim 1.2$ may, however, also be consistent with a scenario in which the most asymmetric objects at any redshift are also the brightest objects. In this case, the relative increase in the number of High-A_W objects beyond $z \sim 1.2$ would be primarily a consequence of sampling only the bright end of the luminosity function at these redshifts. This scenario would also predict the existence of a large population of smaller, less asymmetric galaxies below the radial cut of this sample, but also perhaps below the detection limit of current telescopes and instruments.

A comparison between A_W-C_W and A_A-C_A was also conducted on a sample of 270 HDF galaxies between $21 < \mathrm{F814W}_{VEGA} < 25$, presented in van den Bergh et al. (1996). Abraham et al. (1996b) find that roughly 30% of these galaxies fall into their

"Irregular/Peculiar/Merger" (IPM) class, a region in the log(A_A)-log(C_A) diagram that is not populated by the local Frei et al. (1996) sample. This percentage is roughly twice that found in the High-A_W class. A few caveats for the Abraham et al. sample, however, must be considered. Irregular and peculiar/merger galaxies are combined into one group. Though these two types of galaxies share some similar characteristics (blue, star-forming), they are physically quite different and, therefore, should not be studied as one. Roughly half of the galaxies in the IPM class do not appear to be truly peculiar (both by eye and by A_W). Accounting for these objects brings the total number of truly peculiar objects in the Abraham et al. study into much closer agreement with that found using the A_W-C_W parameters.

Another feature of the A_A-C_A diagram for the same sample of HDF galaxies is a remarkably sharp distinction between the three A_A-C_A classes. This clear separation between classes not seen in A_W-C_W. A direct comparison of the individual parameters provides a possible explanation. Comparison of A_W versus A_A shows a strong tendency for A_A to be over-estimated for all galaxy types, likely a result of a poor choice of pivot point. In addition, comparison of C_W versus C_A suggests that C_A values in the HDF are systematically *higher* than those found in local galaxies, likely due to the fact that Abraham et al.'s σ_{sky}-based detection isophote probes a magnitude fainter at high redshift than locally. If the Abraham et al. results are adjusted for these limitations, the general trends seen by these two algorithms may become roughly consistent.

So what does this all mean in the context of galaxy evolution?

In the last several years, many groups have claimed that a large percentage (30%-45%) of faint galaxies have peculiar morphologies (Forbes et al. 1994, Cowie et al. 1995, Driver et al. 1995, Glazebrook et al. 1995, Schade et al. 1995). In some cases, completely new classes of galaxies have even been proposed, e.g., "chain" galaxies (Cowie et al, 1995). More recently, Abraham et al. (1996b) claimed that roughly 30% of 270 HDF galaxies with $21 < \mathrm{F814W} < 25$ are of the "Irregular/Peculiar/Merger" class. Brinchmann et al. (1998) also find an increase in the number of galaxies with "irregular" morphology at $z \lesssim 1$.

In the last couple of years, however, evidence has begun to emerge that suggests that very little evolution of "normal" (generally, elliptical and early-type spiral) galaxies has occurred out to $z \sim 1$ (Driver et al. 1998, Takamiya 1999, this work). Shortcomings in the algorithms and methods of earlier work have been discovered that result in over-estimating the percentage of peculiar galaxies. Both Abraham et al. (1996b) and Brinchmann et al. (1998) use the A_A and C_A algorithms presented in Abraham et al. (1996b), which, as described earlier, have a tendency to find spuriously high asymmetry values simply due to a poor choice of parameters. In addition, Abraham et al. have combined irregular and peculiar galaxies into a single group, which, not surprisingly, results in a deceptively high percentage of "peculiar" galaxies. In contrast, Takamiya (1999) presents a study of galaxy "flocculency" (power at high spatial frequencies) and metric radius. She finds little difference in the number of objects locally and at $z \lesssim 1$ with similar degrees of flocculency. She also finds that the metric radii of the objects in both samples are $\gtrsim$5-10 kpc. No obvious differences in either parameter are seen between the local and $z \lesssim 1$ sample.

Driver et al. (1998) find that the number of early-type objects (both ellipticals and early-type spirals) in the HDF remains roughly constant out to $z \sim 1.5$, consistent with what is found in this dissertation. Driver et al. also note a sharp decrease in the number of early-type galaxies beyond $z \sim 1.5$ and an increase in the number of objects with "late-type/irregular" morphology beyond $z \sim 1.5$-2. They interpret this combination of phenomena as evidence that the formation of “normal” early-type galaxies may have occurred at these redshifts. Though evolutionary effects may indeed be occurring at these redshifts, simulations presented in this dissertation of $z \sim 0.8$ galaxies at $z = 1.5$ and $z = 2.3$ indicate that selection effects are strong and will likely mask any true evolution.

Though refinements to the A_W-C_W algorithms still need to be made to better handle low surface brightness and elongated objects and to tune calculations to the actual redshifts of objects, the results of this dissertation indicate that this pair of parameters provides a useful means of exploring galaxy morphology over a wide redshift range. Of course, we still have much to learn about the interpretation of the current data and what insight it gives to the evolution of galaxies. With the large amounts of multi-wavelength data that are becoming available, more detailed spectral energy distributions and evolutionary models can now be created and more accurate photometric redshifts can be determined in order to better model the expected appearance of galaxies at various redshifts for comparison with observations. Application of the peculiarity indices to numerical simulations of galaxy interactions may enable mapping out the path through the A_W-C_W plane followed by galaxies in the course of a merger. Combined with observed trends in morphological peculiarity with redshift, a better understanding of the merger history of galaxies may be obtained. Clearly, there is much that we have yet to learn about galaxy evolution through the study of morphological peculiarities.

Appendix:

HDF Galaxy Properties

Table 2–1. HDF Galaxy Properties

	Williams et al. (1996)								
ID	ID	$F814W_{AB}$	r_1 ($''$.)	$V_{606} - I_{814}$	z_{ph}[a]	A_W	C_W	AC[b] Class	In pruned sample?
hdf2_1969_0123	2-35.0	24.79	0.29	0.10	2.58	0.013	2.60	L	Y
hdf2_1810_0129	2-37.0	27.47	0.13	0.07	3.18	−1.000	−1.00	-	N
hdf2_1507_0134	2-39.0	26.59	0.20	0.11	3.59	−0.025	2.71	L	Y
hdf2_1763_0137	2-40.0	28.13	0.13	−0.18	1.73	−1.000	−1.00	-	N
hdf2_1436_0139	2-41.0	27.09	0.18	−0.03	2.28	−1.000	−1.00	-	N
hdf2_0756_0151	2-43.0	27.37	0.24	−0.01	1.84	−1.000	−1.00	-	Y
hdf2_1510_0154	2-45.0	26.88	0.13	0.06	1.80	0.008	2.93	L	N
hdf2_0372_0151	2-46.0	26.72	0.23	−0.00	2.05	−1.000	−1.00	-	Y
hdf2_0708_0160	2-47.0	26.79	0.15	0.52	0.50	0.003	2.59	L	N
hdf2_1786_0186	2-59.0	27.09	0.14	−0.04	2.25	−1.000	−1.00	-	N
hdf2_1135_0187	2-60.2	27.94	0.15	0.35	1.26	−1.000	−1.00	-	N
hdf2_0997_0182	2-61.0	25.23	0.16	0.52	0.71	0.014	3.37	L	N
hdf2_1259_0178	2-62.0	25.23	0.23	0.20	0.39	0.038	3.31	L	Y
hdf2_0406_0193	2-63.0	26.62	0.21	0.76	1.11	−1.000	−1.00	-	Y
hdf2_0967_0194	2-65.1	26.23	0.24	0.63	0.92	−1.000	−1.00	-	Y
hdf2_1996_0195	2-67.0	26.35	0.15	0.24	1.16	0.014	2.71	L	N
hdf2_0553_0201	2-68.0	27.26	0.18	0.70	3.57	−1.000	−1.00	-	N
hdf2_0907_0204	2-69.0	28.19	0.12	0.28	1.27	−1.000	−1.00	-	N
hdf2_1696_0211	2-71.0	27.68	0.13	0.01	2.88	−1.000	−1.00	-	N
hdf2_1334_0182	2-76.0	24.98	0.42	0.14	3.09	0.154	2.78	A	Y
hdf2_1012_0217	2-77.0	27.09	0.13	0.96	0.93	−1.000	−1.00	-	N
hdf2_0856_0220	2-79.0	26.00	0.18	0.70	0.81	0.100	2.89	L	N
hdf2_1403_0223	2-80.0	25.46	0.18	0.13	2.07	0.029	2.96	L	N
hdf2_1926_0215	2-81.0	25.74	0.25	0.31	1.33	0.009	2.45	L	Y
hdf2_1954_0209	2-82.0	24.47	0.29	0.02	2.32	0.231	4.48	A	Y
hdf2_0418_0234	2-88.0	26.99	0.11	0.65	0.84	0.000	2.63	L	N
hdf2_1046_0227	2-90.0	26.79	0.18	−0.05	2.10	−1.000	−1.00	-	N
hdf2_0828_0238	2-91.0	27.78	0.12	0.51	2.18	−1.000	−1.00	-	N
hdf2_1468_0237	2-93.0	26.23	0.17	0.14	2.86	0.044	2.79	L	N
hdf2_0358_0245	2-96.0	26.47	0.22	0.46	1.15	−1.000	−1.00	-	Y
hdf2_0562_0253	2-98.0	28.29	0.16	0.47	1.29	−1.000	−1.00	-	N
hdf2_1247_0249	2-100.0	25.92	0.19	0.24	0.42	0.041	3.05	L	N
hdf2_0949_0254	2-104.0	26.53	0.15	0.86	0.88	0.017	2.53	L	N
hdf2_1749_0260	2-107.0	26.91	0.15	0.36	1.10	−1.000	−1.00	-	N
hdf2_0784_0252	2-108.0	24.84	0.58	0.35	0.41	−1.000	−1.00	-	Y
hdf2_1436_0270	2-110.0	26.70	0.16	0.14	2.73	0.014	2.25	L	N
hdf2_0996_0271	2-116.0	26.46	0.17	0.16	3.25	0.019	2.58	L	N
hdf2_1329_0288	2-118.0	27.68	0.14	0.15	2.04	−1.000	−1.00	-	N
hdf2_0270_0237	2-121.0	20.39	0.64	1.00	0.57	0.035	7.69	C	Y
hdf2_0521_0287	2-122.0	25.59	0.17	0.11	3.00	0.042	3.05	L	N
hdf2_1506_0303	2-124.0	28.55	0.11	1.47	1.22	−1.000	−1.00	-	N
hdf2_1557_0302	2-126.0	26.05	0.14	0.87	0.85	0.026	3.11	L	N
hdf2_1808_0299	2-127.0	24.63	0.28	0.39	1.95	0.073	3.39	L	Y
hdf2_0959_0313	2-128.0	26.84	0.19	0.63	0.89	−1.000	−1.00	-	N
hdf2_1377_0320	2-130.0	28.04	0.24	−0.14	1.90	−1.000	−1.00	-	Y
hdf2_0893_0318	2-133.0	25.37	0.29	0.68	0.93	0.021	3.09	L	Y
hdf2_0367_0315	2-139.0	24.07	0.37	1.16	1.09	0.053	3.17	L	Y
hdf2_1266_0340	2-140.0	27.48	0.12	0.32	2.66	−1.000	−1.00	-	N
hdf2_2013_0338	2-141.0	27.61	0.11	0.43	1.94	−1.000	−1.00	-	N

Table 2–1 — Continued

ID	Williams et al. (1996) ID	F814W$_{AB}$	r_1 (″.)	$V_{606} - I_{814}$	z_{ph}[a]	A_W	C_W	AC[b] Class	In pruned sample?
hdf2_0979_0348	2-143.0	28.77	0.12	0.60	1.45	−1.000	−1.00	-	N
hdf2_0667_0334	2-146.0	26.39	0.17	0.41	1.18	−0.003	2.83	L	N
hdf2_0278_0353	2-147.0	28.86	0.10	0.17	2.23	−1.000	−1.00	-	N
hdf2_0522_0347	2-150.0	26.35	0.29	0.49	0.51	−0.003	2.50	L	Y
hdf2_1784_0351	2-151.0	26.99	0.20	0.72	1.00	−1.000	−1.00	-	Y
hdf2_0796_0349	2-153.0	23.60	0.41	0.98	0.88	0.075	2.68	L	Y
hdf2_0270_0363	2-154.0	27.30	0.32	0.53	0.44	−1.000	−1.00	-	Y
hdf2_0865_0366	2-155.0	27.42	0.12	0.19	2.09	−1.000	−1.00	-	N
hdf2_0832_0370	2-156.0	27.39	0.10	1.71	4.27	−1.000	−1.00	-	N
hdf2_1687_0371	2-158.0	28.10	0.09	1.36	4.51	−1.000	−1.00	-	N
hdf2_1280_0368	2-159.0	27.73	0.12	0.27	2.80	−1.000	−1.00	-	N
hdf2_0361_0359	2-160.0	25.59	0.26	0.50	0.52	0.000	2.87	L	Y
hdf2_1801_0376	2-163.0	25.50	0.15	0.58	0.67	0.049	3.22	L	N
hdf2_0514_0391	2-168.0	26.96	0.13	0.28	2.82	0.015	2.76	L	N
hdf2_0417_0377	2-173.0	23.39	0.32	0.84	0.53	0.003	3.97	L	Y
hdf2_1504_0388	2-175.0	24.22	0.30	0.94	0.89	0.024	3.19	L	Y
hdf2_0216_0398	2-180.0	24.01	0.23	0.69	0.85	0.044	3.54	L	Y
hdf2_1742_0413	2-186.0	26.73	0.19	0.07	2.03	−1.000	−1.00	-	N
hdf2_1859_0433	2-190.0	26.37	0.23	0.45	1.15	−1.000	−1.00	-	Y
hdf2_1620_0437	2-191.0	27.10	0.20	−0.05	2.20	−1.000	−1.00	-	Y
hdf2_1959_0438	2-194.0	26.48	0.28	0.66	0.93	−1.000	−1.00	-	Y
hdf2_0803_0453	2-197.0	27.19	0.12	0.24	2.12	−1.000	−1.00	-	N
hdf2_0557_0444	2-200.0	24.80	0.21	0.44	1.08	0.063	3.35	L	Y
hdf2_1088_0424	2-201.0	23.71	0.24	0.47	1.26	0.081	4.50	C	Y
hdf2_0711_0467	2-203.0	27.76	0.10	−0.16	1.69	−1.000	−1.00	-	N
hdf2_0534_0476	2-208.0	27.98	0.12	0.09	1.34	−1.000	−1.00	-	N
hdf2_0434_0446	2-210.0	22.78	0.65	0.73	0.78	0.146	2.63	A	Y
hdf2_1406_0476	2-213.1	26.18	0.42	0.13	2.78	−1.000	−1.00	-	Y
hdf2_1109_0486	2-216.0	27.09	0.16	0.23	2.16	−1.000	−1.00	-	N
hdf2_1881_0486	2-218.0	27.16	0.12	0.39	3.82	−0.041	2.42	L	N
hdf2_1842_0496	2-225.0	26.05	0.27	0.72	0.82	−1.000	−1.00	-	Y
hdf2_0551_0507	2-226.0	27.56	0.10	0.29	1.35	−1.000	−1.00	-	N
hdf2_0607_0508	2-228.0	25.80	0.22	0.53	0.45	0.000	2.60	L	Y
hdf2_1359_0512	2-231.0	24.61	0.33	0.55	0.58	0.071	3.14	L	Y
hdf2_1985_0528	2-234.0	26.50	0.13	0.88	0.93	0.003	3.06	L	N
hdf2_0490_0523	2-236.1	24.63	0.26	1.61	0.55	0.025	2.87	L	Y
hdf2_0503_0509	2-236.2	24.37	0.14	0.33	1.26	0.049	3.57	L	N
hdf2_1875_0523	2-239.11	25.02	0.20	0.06	2.44	0.012	3.24	L	Y
hdf2_1843_0532	2-239.12	25.67	0.28	0.09	2.25	−1.000	−1.00	-	Y
hdf2_1901_0520	2-239.2	27.41	0.11	−0.01	2.96	−1.000	−1.00	-	N
hdf2_0393_0553	2-244.0	27.92	0.14	1.57	1.42	−1.000	−1.00	-	N
hdf2_1152_0549	2-245.0	25.45	0.29	0.73	0.92	0.019	2.56	L	Y
hdf2_0679_0513	2-246.0	22.77	0.74	0.89	0.89	0.238	4.36	A	Y
hdf2_1089_0556	2-247.0	27.03	0.21	0.44	1.18	−1.000	−1.00	-	Y
hdf2_1671_0521	2-251.0	21.32	0.46	1.17	0.90	0.068	7.81	C	Y
hdf2_0347_0533	2-256.0	23.25	0.49	0.73	1.17	0.113	3.95	A	Y
hdf2_1913_0582	2-260.0	26.78	0.27	0.61	1.03	−1.000	−1.00	-	Y
hdf2_1053_0575	2-263.0	24.38	0.49	0.62	0.78	0.085	2.71	L	Y
hdf2_0245_0547	2-264.1	21.46	0.73	0.78	0.47	0.093	3.99	L	Y

Table 2–1 — Continued

ID	Williams et al. (1996) ID	F814W$_{AB}$	r_1 (″.)	$V_{606}-I_{814}$	z_{ph}[a]	A_W	C_W	AC[b] Class	In pruned sample?
hdf2_0229_0467	2-264.2	22.07	0.26	0.57	0.50	0.023	4.15	C	Y
hdf2_1725_0583	2-270.0	23.72	0.36	0.33	0.50	0.020	3.65	L	Y
hdf2_0579_0609	2-271.0	29.45	0.19	1.12	1.17	−1.000	−1.00	-	N
hdf2_1270_0600	2-272.0	25.93	0.17	0.11	1.73	−0.007	2.91	L	N
hdf2_1115_0608	2-273.0	26.35	0.24	1.03	3.44	0.003	2.78	L	Y
hdf2_0485_0614	2-275.0	27.38	0.14	0.77	0.45	−1.000	−1.00	-	N
hdf2_0691_0621	2-282.0	25.98	0.21	1.20	4.33	0.107	3.33	A	Y
hdf2_1634_0625	2-285.0	26.56	0.16	0.69	0.82	−0.008	2.63	L	N
hdf2_1583_0629	2-288.0	26.16	0.31	0.75	0.92	−1.000	−1.00	-	Y
hdf2_0809_0643	2-289.1	25.58	0.45	0.21	1.18	−0.007	2.31	L	Y
hdf2_0775_0643	2-289.2	27.40	0.13	0.03	1.85	−1.000	−1.00	-	N
hdf2_0776_0670	2-299.0	27.74	0.14	0.35	0.67	−1.000	−1.00	-	N
hdf2_1660_0681	2-302.0	27.34	0.11	0.19	1.31	−1.000	−1.00	-	N
hdf2_1980_0668	2-303.0	24.97	0.33	0.71	0.80	0.014	2.67	L	Y
hdf2_0179_0684	2-309.0	26.37	0.16	0.23	3.05	0.021	2.94	L	N
hdf2_1892_0675	2-310.0	25.25	0.35	0.77	0.90	0.001	2.32	L	Y
hdf2_1596_0694	2-312.0	28.45	0.10	0.57	1.40	−1.000	−1.00	-	N
hdf2_0611_0691	2-313.0	25.54	0.17	0.33	3.05	0.020	3.32	L	N
hdf2_1620_0697	2-316.0	26.73	0.13	0.91	0.85	0.003	2.88	L	N
hdf2_0759_0695	2-317.0	27.42	0.14	0.36	0.47	−1.000	−1.00	-	N
hdf2_1564_0674	2-321.1	24.63	0.41	0.12	2.28	0.016	2.88	L	Y
hdf2_1552_0704	2-321.2	25.35	0.14	0.14	2.58	0.003	3.24	L	N
hdf2_0847_0712	2-322.0	26.67	0.23	0.22	1.34	−1.000	−1.00	-	Y
hdf2_1489_0717	2-325.0	27.76	0.13	0.49	1.09	−1.000	−1.00	-	N
hdf2_0608_0726	2-328.0	26.83	0.27	0.22	1.27	−1.000	−1.00	-	Y
hdf2_0265_0693	2-339.0	22.65	0.78	1.12	0.67	0.086	3.69	L	Y
hdf2_1605_0742	2-340.0	25.59	0.17	0.81	0.82	0.030	3.24	L	N
hdf2_0615_0743	2-343.0	27.71	0.12	0.18	1.43	−1.000	−1.00	-	N
hdf2_1831_0753	2-353.0	23.55	0.26	1.04	0.55	0.035	3.57	L	Y
hdf2_1874_0764	2-354.0	25.51	0.12	0.17	0.99	0.052	3.44	L	N
hdf2_1685_0788	2-363.0	25.77	0.16	0.15	1.49	0.067	3.37	L	N
hdf2_0589_0803	2-373.0	25.07	0.23	0.13	2.07	0.107	4.00	A	Y
hdf2_1836_0835	2-378.0	27.50	0.14	0.03	2.20	−1.000	−1.00	-	N
hdf2_1466_0841	2-382.0	27.28	0.20	−0.22	2.53	−1.000	−1.00	-	Y
hdf2_1697_0844	2-388.0	25.58	0.16	0.57	1.10	0.011	2.82	L	N
hdf2_0491_0851	2-389.0	27.88	0.17	0.66	4.46	−1.000	−1.00	-	N
hdf2_1567_0860	2-390.0	27.97	0.12	0.64	1.23	−1.000	−1.00	-	N
hdf2_0929_0859	2-392.0	26.40	0.23	−0.00	2.38	0.008	2.65	L	Y
hdf2_1510_0864	2-394.0	25.99	0.23	0.09	1.96	−0.007	2.43	L	Y
hdf2_0693_0892	2-400.0	27.39	0.11	0.86	0.97	−1.000	−1.00	-	N
hdf2_0327_0837	2-404.0	19.61	1.25	0.31	2.57	0.152	3.34	A	Y
hdf2_1771_0904	2-412.0	24.46	0.23	0.79	0.90	0.050	3.82	L	Y
hdf2_1586_0908	2-414.0	25.25	0.23	1.14	1.00	0.038	3.23	L	Y
hdf2_0874_0912	2-420.0	24.77	0.38	0.31	1.35	0.109	3.17	A	Y
hdf2_1975_0924	2-421.1	26.20	0.26	−0.08	2.11	−1.000	−1.00	-	Y
hdf2_1952_0925	2-421.2	26.04	0.19	0.18	2.11	0.009	2.32	L	N
hdf2_0510_0943	2-429.0	26.97	0.11	0.07	2.14	−0.005	2.53	L	N
hdf2_1711_0918	2-432.0	23.88	0.55	0.70	0.93	0.212	4.68	A	Y
hdf2_0980_0953	2-436.0	26.60	0.12	1.10	3.86	0.001	2.80	L	N

Table 2–1 — Continued

	Williams et al. (1996)								
ID	ID	F814W$_{\rm AB}$	r_1 ($''$)	$V_{606}-I_{814}$	z_{ph}[a]	A_W	C_W	AC[b] Class	In pruned sample?
hdf2_1208_0961	2-438.0	28.71	0.14	1.92	5.98	−1.000	−1.00	-	N
hdf2_1806_0962	2-449.0	23.39	0.27	0.29	2.21	0.160	4.65	A	Y
hdf2_1228_0973	2-453.0	26.32	0.13	0.79	0.91	0.007	2.95	L	N
hdf2_1852_0969	2-454.0	24.19	0.32	0.21	2.11	0.164	3.39	A	Y
hdf2_1044_0838	2-456.1111	18.13	0.63	0.61	0.00	0.016	6.41	C	Y
hdf2_1093_0969	2-456.211	24.02	0.30	0.77	1.15	0.051	2.75	L	Y
hdf2_0559_1014	2-475.0	26.44	0.15	0.15	2.40	0.004	2.85	L	N
hdf2_1424_1020	2-476.0	28.21	0.17	−0.15	1.73	−1.000	−1.00	-	N
hdf2_0249_1022	2-477.0	29.28	0.11	−0.35	2.04	−1.000	−1.00	-	N
hdf2_0744_1012	2-480.1	26.50	0.11	0.71	0.66	0.005	3.20	L	N
hdf2_0306_1042	2-486.0	26.53	0.14	0.04	0.34	0.017	2.61	L	N
hdf2_1016_1056	2-493.0	27.44	0.18	0.10	3.29	−1.000	−1.00	-	N
hdf2_1291_1063	2-494.0	28.95	0.15	−0.16	1.94	−1.000	−1.00	-	N
hdf2_1258_1058	2-496.0	26.42	0.12	0.25	2.83	0.044	3.20	L	N
hdf2_1635_1058	2-497.0	26.00	0.15	0.55	1.02	0.032	2.95	L	N
hdf2_0807_1065	2-499.0	28.38	0.11	0.15	7.79	−1.000	−1.00	-	N
hdf2_0575_1069	2-502.0	25.90	0.34	0.24	1.30	−1.000	−1.00	-	Y
hdf2_0356_1069	2-506.0	26.31	0.21	0.29	2.71	0.036	2.63	L	Y
hdf2_0909_1074	2-507.0	26.85	0.12	0.44	0.86	0.002	2.67	L	N
hdf2_1496_1051	2-514.0	21.77	0.41	0.98	0.68	0.069	4.22	C	Y
hdf2_0990_1100	2-524.0	26.30	0.25	0.14	3.13	0.010	2.50	L	Y
hdf2_1321_1091	2-525.0	24.62	0.29	0.18	2.33	0.179	3.82	A	Y
hdf2_1266_1098	2-526.0	24.72	0.20	0.41	1.28	0.041	3.63	L	Y
hdf2_0527_1096	2-531.0	23.11	0.30	0.99	0.89	0.016	2.71	L	Y
hdf2_1382_1111	2-535.0	26.65	0.23	1.03	0.83	−1.000	−1.00	-	Y
hdf2_0618_1115	2-539.0	26.15	0.19	0.33	1.39	0.010	2.68	L	N
hdf2_1283_1127	2-545.0	27.83	0.14	−0.06	2.08	−1.000	−1.00	-	N
hdf2_0857_1124	2-547.0	25.86	0.19	0.03	2.32	0.093	2.92	L	N
hdf2_0690_1140	2-551.0	27.84	0.12	0.70	2.67	−1.000	−1.00	-	N
hdf2_0399_1151	2-554.1	27.70	0.12	0.13	2.93	−1.000	−1.00	-	N
hdf2_0253_1152	2-557.0	27.28	0.13	0.43	2.81	−1.000	−1.00	-	N
hdf2_1523_1157	2-558.0	29.19	0.15	−0.71	2.27	−1.000	−1.00	-	N
hdf2_1762_1153	2-560.0	27.20	0.26	0.48	3.87	−1.000	−1.00	-	Y
hdf2_0964_1138	2-565.1	25.21	0.15	0.27	2.64	0.014	2.88	L	N
hdf2_1181_1177	2-568.0	26.28	0.14	0.52	0.91	0.072	2.83	L	N
hdf2_1243_1181	2-569.0	27.29	0.12	0.78	0.68	−1.000	−1.00	-	N
hdf2_1736_1183	2-571.0	28.62	0.11	−0.01	1.88	−1.000	−1.00	-	N
hdf2_0512_1181	2-572.0	27.26	0.21	0.64	2.77	−1.000	−1.00	-	Y
hdf2_1465_1173	2-575.0	25.65	0.25	0.39	0.62	0.020	3.14	L	Y
hdf2_1535_1189	2-577.0	26.80	0.13	−0.04	1.74	0.002	2.63	L	N
hdf2_0900_1196	2-578.0	25.40	0.10	0.92	0.68	0.045	3.15	L	N
hdf2_1497_1199	2-579.0	28.22	0.10	0.12	2.36	−1.000	−1.00	-	N
hdf2_1609_1210	2-582.0	28.55	0.14	0.48	0.92	−1.000	−1.00	-	N
hdf2_1942_1197	2-584.1	25.76	0.18	0.12	1.73	0.007	3.09	L	N
hdf2_1934_1214	2-584.2	28.69	0.08	0.09	2.16	−1.000	−1.00	-	N
hdf2_1668_1184	2-585.1111	24.05	0.26	0.40	1.37	0.236	2.99	A	Y
hdf2_1683_1178	2-585.1112	24.88	0.15	0.17	2.00	0.290	3.63	A	N
hdf2_1672_1141	2-585.2	24.37	0.38	0.75	0.93	0.032	3.17	L	Y
hdf2_0552_1216	2-586.0	28.55	0.10	0.09	1.50	−1.000	−1.00	-	N

Table 2–1 — Continued

ID	Williams et al. (1996) ID	F814W$_{AB}$	r_1 ($''$.)	$V_{606}-I_{814}$	z_{ph}[a]	A_W	C_W	AC[b] Class	In pruned sample?
hdf2_0698_1215	2-587.0	26.96	0.23	0.25	2.06	−1.000	−1.00	-	Y
hdf2_2013_1213	2-588.0	26.57	0.32	0.05	3.14	−1.000	−1.00	-	Y
hdf2_1826_1195	2-590.0	25.45	0.31	−0.02	3.36	0.065	3.06	L	Y
hdf2_0190_1193	2-591.1	24.32	0.30	0.12	1.95	0.105	3.74	A	Y
hdf2_0225_1194	2-591.2	24.78	0.18	0.13	2.73	0.102	3.67	A	N
hdf2_1330_1202	2-594.1	25.60	0.20	0.26	2.22	0.003	2.69	L	Y
hdf2_1344_1218	2-594.2	26.42	0.16	0.04	2.19	0.032	2.78	L	N
hdf2_1760_1223	2-600.0	25.55	0.16	0.18	1.90	0.062	3.15	L	N
hdf2_1729_1230	2-601.0	27.62	0.13	0.36	2.44	−1.000	−1.00	-	N
hdf2_0623_1230	2-604.0	24.87	0.42	0.38	3.27	0.078	3.35	L	Y
hdf2_0480_1243	2-608.0	27.45	0.17	0.51	0.59	−1.000	−1.00	-	N
hdf2_0421_1250	2-614.0	26.13	0.25	0.41	2.63	−1.000	−1.00	-	Y
hdf2_0490_1260	2-616.0	28.50	0.12	−0.10	2.78	−1.000	−1.00	-	N
hdf2_1504_1260	2-617.0	27.65	0.15	0.26	2.81	−1.000	−1.00	-	N
hdf2_0677_1265	2-620.0	28.50	0.12	−0.29	1.73	−1.000	−1.00	-	N
hdf2_1368_1275	2-627.0	27.83	0.18	−0.40	2.20	−1.000	−1.00	-	N
hdf2_0322_1278	2-628.0	26.47	0.21	0.22	3.18	0.036	3.00	L	Y
hdf2_1636_1274	2-632.0	24.73	0.36	0.80	0.80	0.056	3.05	L	Y
hdf2_0432_1279	2-635.0	25.51	0.16	0.53	3.63	0.021	3.41	L	N
hdf2_0630_1292	2-637.0	25.02	0.16	0.25	3.22	0.054	3.33	L	N
hdf2_0833_1304	2-640.0	26.50	0.13	0.63	0.64	−0.000	2.78	L	N
hdf2_1362_1305	2-641.0	27.34	0.14	0.16	2.12	−1.000	−1.00	-	N
hdf2_0363_1302	2-643.0	24.60	0.25	0.27	3.08	0.279	3.61	A	Y
hdf2_1804_1310	2-645.0	26.22	0.20	0.10	0.35	0.014	3.08	L	Y
hdf2_0874_1298	2-646.0	24.32	0.23	0.67	0.60	0.021	3.28	L	Y
hdf2_1415_1317	2-648.0	28.05	0.10	−0.15	3.25	−1.000	−1.00	-	N
hdf2_1036_1283	2-652.0	21.08	0.62	0.86	0.52	0.122	3.90	A	Y
hdf2_0243_1319	2-656.0	25.02	0.31	0.18	2.01	0.075	2.58	L	Y
hdf2_0840_1340	2-660.0	27.06	0.13	0.25	3.20	0.014	2.42	L	N
hdf2_1709_1307	2-661.0	23.16	0.55	0.78	0.82	0.110	3.28	A	Y
hdf2_1255_1349	2-664.0	27.04	0.13	0.44	1.19	0.003	2.29	L	N
hdf2_1993_1357	2-667.0	28.57	0.10	−0.17	3.28	−1.000	−1.00	-	N
hdf2_0222_1361	2-671.0	26.37	0.18	0.66	0.54	−0.007	2.47	L	N
hdf2_1393_1368	2-673.0	25.28	0.19	0.78	1.15	0.029	3.35	L	N
hdf2_1700_1371	2-675.0	26.17	0.18	0.19	1.40	0.027	3.00	L	N
hdf2_0862_1372	2-677.0	26.44	0.16	0.24	1.80	0.006	2.81	L	N
hdf2_0670_1381	2-679.0	27.94	0.13	0.18	2.03	−1.000	−1.00	-	N
hdf2_1956_1366	2-681.0	26.81	0.35	0.32	1.27	−1.000	−1.00	-	Y
hdf2_0654_1387	2-682.0	26.84	0.29	0.26	3.13	−1.000	−1.00	-	Y
hdf2_0446_1389	2-684.0	27.08	0.15	0.40	0.53	−1.000	−1.00	-	N
hdf2_0668_1396	2-687.0	27.76	0.12	0.24	1.36	−1.000	−1.00	-	N
hdf2_0728_1375	2-689.0	24.12	0.42	0.14	1.98	0.462	4.46	A	Y
hdf2_1464_1388	2-693.0	24.42	0.35	0.10	2.01	0.346	4.52	A	Y
hdf2_0335_1414	2-700.0	28.94	0.11	−0.37	1.38	−1.000	−1.00	-	N
hdf2_1351_1410	2-701.0	26.69	0.13	0.08	1.28	0.024	2.69	L	N
hdf2_1184_1394	2-702.0	23.02	0.48	0.67	0.54	0.125	4.00	A	Y
hdf2_1246_1415	2-706.0	26.58	0.15	0.54	0.78	−0.005	2.61	L	N
hdf2_0701_1407	2-712.0	25.65	0.36	0.55	0.65	0.026	2.29	L	Y
hdf2_1293_1425	2-713.0	27.18	0.15	0.11	1.55	−1.000	−1.00	-	N

Table 2–1 — Continued

ID	Williams et al. (1996) ID	F814W$_{AB}$	r_1 (″.)	$V_{606} - I_{814}$	z_{ph}[a]	A_W	C_W	AC[b] Class	In pruned sample?
hdf2_0865_1440	2-723.0	26.12	0.37	0.38	1.17	−1.000	−1.00	-	Y
hdf2_1654_1442	2-724.0	26.28	0.23	0.56	0.99	−1.000	−1.00	-	Y
hdf2_1921_1438	2-725.0	24.87	0.18	0.54	0.68	0.016	3.14	L	N
hdf2_0769_1423	2-726.1	25.88	0.25	0.18	3.25	0.140	3.75	A	Y
hdf2_0744_1444	2-726.2	26.90	0.29	0.22	2.19	−1.000	−1.00	-	Y
hdf2_1412_1464	2-733.0	27.82	0.11	0.55	0.59	−1.000	−1.00	-	N
hdf2_0982_1452	2-736.0	21.98	0.67	0.28	1.35	0.507	5.18	A	Y
hdf2_1286_1464	2-741.1	26.51	0.12	0.02	2.75	−0.014	2.21	L	N
hdf2_1355_1464	2-743.0	25.70	0.34	0.28	3.15	0.001	2.33	L	Y
hdf2_0687_1470	2-746.1	26.08	0.31	0.15	2.91	0.041	3.58	L	Y
hdf2_0958_1488	2-748.0	27.18	0.16	0.23	1.31	−1.000	−1.00	-	N
hdf2_1730_1492	2-749.1	28.74	0.08	0.16	1.28	−1.000	−1.00	-	N
hdf2_0453_1491	2-751.0	26.45	0.15	−0.06	2.31	0.013	3.00	L	N
hdf2_1281_1493	2-752.0	27.10	0.16	0.08	1.68	−1.000	−1.00	-	N
hdf2_1591_1502	2-755.1	26.42	0.17	0.21	2.05	0.011	2.18	L	N
hdf2_1607_1494	2-755.2	27.55	0.09	0.71	1.06	−1.000	−1.00	-	N
hdf2_1687_1495	2-762.0	23.34	0.44	0.39	0.45	0.083	3.50	L	Y
hdf2_1812_1521	2-763.0	29.78	0.08	−0.08	1.70	−1.000	−1.00	-	N
hdf2_0530_1510	2-764.1	27.05	0.10	−0.06	2.32	0.027	2.71	L	N
hdf2_1138_1526	2-766.0	27.65	0.11	0.83	0.92	−1.000	−1.00	-	N
hdf2_0418_1530	2-773.0	26.84	0.20	0.19	2.22	−1.000	−1.00	-	Y
hdf2_1650_1543	2-779.0	27.23	0.22	0.31	3.34	−1.000	−1.00	-	Y
hdf2_1439_1547	2-782.0	27.39	0.12	−0.00	2.13	−1.000	−1.00	-	N
hdf2_0375_1540	2-787.0	24.79	0.43	0.85	0.91	0.011	2.63	L	Y
hdf2_0402_1566	2-789.0	27.03	0.13	−0.02	2.79	0.007	2.38	L	N
hdf2_1415_1561	2-790.0	26.20	0.18	0.03	2.10	0.038	2.76	L	N
hdf2_1919_1569	2-791.0	26.25	0.33	0.43	0.76	−1.000	−1.00	-	Y
hdf2_1150_1566	2-793.0	25.48	0.24	0.30	2.60	0.001	2.63	L	Y
hdf2_2015_1581	2-798.0	26.21	0.24	0.04	1.38	0.029	2.61	L	Y
hdf2_1857_1594	2-805.0	27.96	0.15	0.70	1.11	−1.000	−1.00	-	N
hdf2_1783_1593	2-806.0	27.49	0.19	0.69	1.12	−1.000	−1.00	-	N
hdf2_1220_1574	2-809.0	23.26	0.46	0.79	0.67	0.092	3.12	L	Y
hdf2_0631_1604	2-816.0	26.40	0.16	0.18	2.43	0.073	3.00	L	N
hdf2_1804_1615	2-821.0	28.63	0.11	−0.22	1.49	−1.000	−1.00	-	N
hdf2_0830_1618	2-822.0	26.79	0.10	−0.09	2.36	0.009	3.00	L	N
hdf2_1770_1619	2-823.0	27.48	0.16	0.49	1.29	−1.000	−1.00	-	N
hdf2_0550_1615	2-824.0	25.24	0.23	−0.01	2.48	0.210	3.17	A	Y
hdf2_0447_1625	2-829.0	26.48	0.61	0.24	1.22	−1.000	−1.00	-	Y
hdf2_1462_1615	2-831.0	25.47	0.27	0.66	0.89	0.021	2.65	L	Y
hdf2_0231_1622	2-833.0	25.15	0.25	0.52	1.16	0.012	3.26	L	Y
hdf2_1295_1613	2-834.1	26.35	0.13	0.02	2.25	0.015	2.94	L	N
hdf2_1288_1626	2-834.2	26.96	0.13	0.09	3.59	0.007	2.29	L	N
hdf2_1927_1631	2-835.0	26.15	0.15	0.41	0.59	0.013	2.84	L	N
hdf2_1115_1639	2-836.0	27.11	0.16	0.14	1.42	−1.000	−1.00	-	N
hdf2_1687_1639	2-837.0	26.86	0.25	−0.07	2.13	−1.000	−1.00	-	Y
hdf2_0351_1643	2-843.0	24.98	0.39	0.23	1.44	0.015	2.39	L	Y
hdf2_1774_1646	2-844.0	26.26	0.21	0.30	0.42	−1.000	−1.00	-	Y
hdf2_0208_1659	2-846.0	27.11	0.14	0.63	0.68	−1.000	−1.00	-	N
hdf2_1331_1664	2-847.0	29.20	0.08	0.05	1.40	−1.000	−1.00	-	N

Table 2–1 — Continued

ID	Williams et al. (1996) ID	F814W$_{AB}$	r_1 ($''$)	$V_{606}-I_{814}$	z_{ph}[a]	A_W	C_W	AC[b] Class	In pruned sample?
hdf2_1618_1657	2-849.0	25.45	0.19	0.15	1.82	0.061	3.14	L	N
hdf2_1517_1670	2-853.0	29.49	0.11	1.33	0.63	−1.000	−1.00	-	N
hdf2_0384_1673	2-854.0	26.52	0.18	0.43	0.61	0.002	2.13	L	N
hdf2_1370_1678	2-855.0	29.55	0.10	0.08	1.54	−1.000	−1.00	-	N
hdf2_1170_1672	2-856.0	25.54	0.21	0.69	0.92	0.033	3.27	L	Y
hdf2_0886_1662	2-860.0	22.46	0.46	0.91	0.82	0.071	3.04	L	Y
hdf2_0450_1693	2-865.0	27.37	0.12	0.18	2.02	−1.000	−1.00	-	N
hdf2_1212_1708	2-871.0	26.64	0.17	0.32	3.47	−1.000	−1.00	-	N
hdf2_1663_1714	2-873.0	27.54	0.15	0.55	2.44	−1.000	−1.00	-	N
hdf2_1872_1721	2-876.0	28.02	0.14	0.38	0.33	−1.000	−1.00	-	N
hdf2_0826_1733	2-882.0	27.35	0.15	1.64	4.63	−1.000	−1.00	-	N
hdf2_0443_1729	2-884.1	26.79	0.15	0.06	2.64	0.071	2.80	L	N
hdf2_0432_1732	2-884.2	26.58	0.12	0.09	1.32	0.017	2.67	L	N
hdf2_1985_1737	2-885.0	27.56	0.13	0.41	0.22	−1.000	−1.00	-	N
hdf2_1585_1738	2-886.0	27.59	0.15	0.50	0.90	−1.000	−1.00	-	N
hdf2_1904_1723	2-887.0	25.46	0.38	0.36	1.30	−1.000	−1.00	-	Y
hdf2_0539_1743	2-888.0	27.72	0.14	0.13	1.85	−1.000	−1.00	-	N
hdf2_1849_1729	2-889.0	25.67	0.42	0.16	2.88	0.065	3.85	L	Y
hdf2_1937_1736	2-890.0	25.75	0.19	0.14	2.33	−0.003	2.95	L	N
hdf2_0806_1745	2-892.0	27.01	0.28	1.71	4.72	−1.000	−1.00	-	Y
hdf2_0755_1734	2-898.0	24.23	0.27	0.89	0.84	0.039	3.00	L	Y
hdf2_1285_1741	2-901.0	24.54	0.27	0.33	3.23	0.073	3.63	L	Y
hdf2_0648_1744	2-903.0	24.55	0.23	0.05	2.40	0.163	3.41	A	Y
hdf2_1907_1756	2-905.0	25.94	0.15	0.30	0.41	0.021	3.16	L	N
hdf2_0177_1738	2-906.0	23.44	0.44	0.56	1.07	0.077	2.91	L	Y
hdf2_1637_1758	2-907.0	25.10	0.22	−0.04	2.13	0.084	3.55	L	Y
hdf2_0789_1764	2-910.0	27.94	0.11	1.17	3.35	−1.000	−1.00	-	N
hdf2_0665_1772	2-916.0	25.32	0.25	0.16	2.49	0.082	3.57	L	Y
hdf2_1704_1785	2-918.0	27.75	0.15	0.49	0.80	−1.000	−1.00	-	N
hdf2_1932_1794	2-924.0	28.25	0.11	−0.37	2.79	−1.000	−1.00	-	N
hdf2_0315_1797	2-928.0	24.88	0.27	0.70	0.82	0.021	3.44	L	Y
hdf2_1137_1807	2-934.0	26.45	0.15	0.11	2.72	0.062	2.65	L	N
hdf2_0378_1816	2-936.0	29.06	0.14	−0.14	3.19	−1.000	−1.00	-	N
hdf2_0663_1815	2-940.0	27.22	0.19	0.15	1.76	−1.000	−1.00	-	N
hdf2_0783_1827	2-942.0	27.43	0.13	0.66	0.65	−1.000	−1.00	-	N
hdf2_1102_1834	2-945.0	27.17	0.12	0.17	3.04	−1.000	−1.00	-	N
hdf2_1065_1836	2-949.0	25.51	0.23	0.09	2.51	0.046	3.29	L	Y
hdf2_1451_1826	2-950.0	23.46	0.41	0.57	0.52	0.036	3.83	L	Y
hdf2_0414_1854	2-956.0	27.76	0.17	0.19	1.48	−1.000	−1.00	-	N
hdf2_0641_1845	2-958.0	26.18	0.23	0.14	1.85	0.028	2.44	L	Y
hdf2_1727_1866	2-961.0	27.79	0.11	0.44	1.24	−1.000	−1.00	-	N
hdf2_1452_1863	2-963.0	25.54	0.24	0.26	3.40	0.076	3.35	L	Y
hdf2_0321_1876	2-965.0	27.89	0.16	0.24	2.75	−1.000	−1.00	-	N
hdf2_0640_1873	2-966.0	24.96	0.17	0.85	0.90	0.020	3.43	L	N
hdf2_0255_1878	2-968.0	26.44	0.18	0.34	1.18	0.000	2.75	L	N
hdf2_0407_1880	2-970.0	28.81	0.15	−0.24	2.22	−1.000	−1.00	-	N
hdf2_1487_1890	2-972.0	28.71	0.12	−0.56	2.77	−1.000	−1.00	-	N
hdf2_1160_1876	2-973.1	24.89	0.24	−0.01	2.18	0.100	3.29	L	Y
hdf2_1175_1866	2-973.2	25.86	0.12	−0.10	2.14	0.003	3.09	L	N

Table 2–1 — Continued

ID	Williams et al. (1996) ID	F814W$_{AB}$	r_1 (″.)	$V_{606}-I_{814}$	z_{ph}[a]	A_W	C_W	AC[b] Class	In pruned sample?
hdf2_0385_1898	2-976.0	26.42	0.16	0.39	3.20	0.038	2.89	L	N
hdf2_0689_1895	2-977.0	26.14	0.17	0.46	3.93	0.043	3.22	L	N
hdf2_1193_1905	2-979.0	26.54	0.20	0.03	3.06	−1.000	−1.00	-	Y
hdf2_0765_1882	2-982.0	22.66	0.68	0.57	1.11	0.132	3.23	A	Y
hdf2_1912_1917	2-991.0	27.22	0.22	0.76	1.15	−1.000	−1.00	-	Y
hdf2_1136_1921	2-995.0	25.02	0.21	0.20	1.78	0.030	3.38	L	Y
hdf2_0885_1935	2-998.0	26.63	0.13	−0.05	1.34	0.019	3.00	L	N
hdf2_0372_1921	2-999.0	25.21	0.30	0.54	1.84	0.040	2.81	L	Y
hdf2_0834_1935	2-1001.0	25.71	0.27	0.29	1.40	0.027	2.76	L	Y
hdf2_0310_1955	2-1003.0	27.71	0.11	0.79	0.89	−1.000	−1.00	-	N
hdf2_0731_1957	2-1004.0	27.50	0.11	−0.02	2.23	−1.000	−1.00	-	N
hdf2_1959_1950	2-1006.0	24.40	0.33	0.22	0.40	0.028	3.19	L	Y
hdf2_1559_1964	2-1008.0	28.26	0.13	0.87	2.68	−1.000	−1.00	-	N
hdf2_0616_1971	2-1012.1	27.24	0.12	0.18	3.21	−1.000	−1.00	-	N
hdf2_1624_1966	2-1014.0	26.76	0.21	0.67	0.90	−1.000	−1.00	-	Y
hdf2_0907_1959	2-1018.0	23.82	0.45	0.56	0.61	0.085	4.20	C	Y
hdf2_0381_1991	2-1020.0	28.24	0.09	2.17	4.18	−1.000	−1.00	-	N
hdf2_0547_1979	2-1022.0	25.53	0.29	0.45	0.57	0.005	3.41	L	Y
hdf2_0979_1971	2-1023.0	23.03	0.58	0.85	0.62	0.017	3.92	L	Y
hdf2_0843_2002	2-1024.0	28.44	0.12	0.81	0.99	−1.000	−1.00	-	N
hdf2_0948_1997	2-1025.0	26.50	0.16	0.32	2.05	0.008	2.58	L	N
hdf2_0475_2015	2-1031.0	25.40	0.19	0.57	0.93	0.065	3.00	L	N
hdf3_0946_0163	3-24.0	25.90	0.19	0.21	1.79	0.003	3.20	L	N
hdf3_1627_0171	3-27.0	29.12	0.11	0.06	1.51	−1.000	−1.00	-	N
hdf3_0267_0180	3-33.0	26.62	0.20	0.56	0.60	−1.000	−1.00	-	Y
hdf3_1798_0190	3-36.0	25.69	0.14	0.43	1.13	0.013	3.35	L	N
hdf3_0496_0175	3-37.0	24.21	0.34	0.69	0.92	0.052	3.37	L	Y
hdf3_1231_0204	3-41.0	26.07	0.13	−0.03	2.58	−0.009	3.25	L	N
hdf3_0156_0205	3-43.0	26.20	0.21	0.54	1.08	−0.002	2.45	L	Y
hdf3_1354_0215	3-44.0	27.64	0.23	1.67	4.40	−1.000	−1.00	-	Y
hdf3_0368_0203	3-45.0	27.92	0.27	−0.13	1.66	−1.000	−1.00	-	Y
hdf3_1712_0215	3-48.0	25.25	0.19	1.66	1.30	0.022	3.71	L	N
hdf3_0409_0222	3-50.0	27.92	0.14	0.35	1.47	−1.000	−1.00	-	N
hdf3_0291_0219	3-51.0	25.45	0.16	0.52	0.48	−0.009	3.29	L	N
hdf3_1069_0231	3-56.0	26.25	0.18	0.39	1.15	−0.003	2.77	L	N
hdf3_1950_0258	3-66.0	27.95	0.10	0.59	2.59	−1.000	−1.00	-	N
hdf3_0564_0275	3-72.0	29.42	0.12	1.29	3.08	−1.000	−1.00	-	N
hdf3_0938_0275	3-75.0	27.28	0.15	0.67	0.43	−1.000	−1.00	-	N
hdf3_0445_0283	3-76.0	28.55	0.10	0.07	1.50	−1.000	−1.00	-	N
hdf3_1587_0269	3-77.0	25.90	0.27	0.36	2.67	0.005	2.24	L	Y
hdf3_1307_0280	3-79.0	24.40	0.25	0.50	1.16	0.067	3.06	L	Y
hdf3_1469_0285	3-82.0	25.25	0.22	1.43	0.36	−0.002	3.22	L	Y
hdf3_1807_0285	3-83.1	25.78	0.20	0.07	2.44	0.197	3.52	A	Y
hdf3_1831_0278	3-83.2	27.09	0.14	0.22	1.94	−1.000	−1.00	-	N
hdf3_0227_0317	3-90.0	26.95	0.12	0.02	2.82	0.027	2.60	L	N
hdf3_1120_0326	3-92.0	28.23	0.13	1.14	0.81	−1.000	−1.00	-	N
hdf3_0277_0336	3-98.0	26.33	0.16	0.56	0.96	0.054	2.77	L	N
hdf3_1309_0345	3-107.0	25.14	0.29	0.07	1.41	0.213	3.32	A	Y
hdf3_1380_0356	3-118.0	24.25	0.19	0.13	2.16	0.045	3.63	L	N

Table 2–1 — Continued

	Williams et al. (1996)								
ID	ID	$F814W_{AB}$	r_1 (″.)	$V_{606} - I_{814}$	z_{ph}[a]	A_W	C_W	AC[b] Class	In pruned sample?
hdf3_1070_0367	3-119.0	27.74	0.11	0.21	1.72	−1.000	−1.00	-	N
hdf3_1905_0372	3-122.0	28.58	0.11	−0.37	2.15	−1.000	−1.00	-	N
hdf3_0337_0376	3-124.0	27.12	0.19	0.47	1.49	−1.000	−1.00	-	N
hdf3_1275_0377	3-125.0	26.68	0.18	0.12	3.05	−1.000	−1.00	-	N
hdf3_1025_0370	3-126.1	26.50	0.10	0.02	2.48	0.018	2.58	L	N
hdf3_1013_0367	3-126.2	26.67	0.10	−0.06	2.35	0.004	2.36	L	N
hdf3_1182_0368	3-127.0	25.84	0.23	0.17	1.36	0.032	2.81	L	Y
hdf3_1426_0375	3-132.0	23.83	0.30	0.50	0.55	0.058	3.27	L	Y
hdf3_0527_0395	3-136.0	28.30	0.11	1.43	4.12	−1.000	−1.00	-	N
hdf3_1612_0393	3-138.0	26.83	0.23	0.08	2.06	−1.000	−1.00	-	Y
hdf3_0308_0403	3-140.0	27.78	0.13	−0.01	2.22	−1.000	−1.00	-	N
hdf3_0389_0399	3-143.0	21.98	0.40	0.73	0.46	0.086	3.64	L	Y
hdf3_1614_0427	3-145.0	28.01	0.19	0.25	2.39	−1.000	−1.00	-	N
hdf3_0335_0438	3-153.0	26.62	0.31	1.03	4.56	−1.000	−1.00	-	Y
hdf3_0257_0455	3-159.0	27.97	0.17	0.26	1.63	−1.000	−1.00	-	N
hdf3_0884_0463	3-164.0	25.80	0.22	0.20	3.06	0.065	2.91	L	Y
hdf3_1643_0475	3-167.0	27.67	0.17	0.98	0.93	−1.000	−1.00	-	N
hdf3_1323_0479	3-170.0	26.37	0.18	0.60	0.52	0.037	2.63	L	N
hdf3_0698_0456	3-174.0	22.80	1.08	0.19	0.08	0.098	2.63	L	Y
hdf3_1656_0510	3-179.0	27.45	0.12	1.29	4.51	−0.002	2.29	L	N
hdf3_1463_0489	3-180.1	22.28	0.40	1.74	0.90	0.027	4.71	C	Y
hdf3_1414_0464	3-180.2	23.68	0.30	0.25	0.22	0.050	3.13	L	Y
hdf3_1688_0511	3-181.0	28.48	0.14	1.03	1.03	−1.000	−1.00	-	N
hdf3_1851_0501	3-184.0	25.19	0.29	0.35	0.42	0.004	2.78	L	Y
hdf3_1393_0522	3-193.0	25.60	0.31	0.80	1.33	−0.013	2.56	L	Y
hdf3_0128_0530	3-195.0	25.86	0.23	0.41	2.82	0.003	2.83	L	Y
hdf3_1737_0537	3-199.0	27.53	0.21	0.36	1.81	−1.000	−1.00	-	Y
hdf3_0453_0536	3-201.0	27.26	0.14	0.49	2.21	−1.000	−1.00	-	N
hdf3_0329_0545	3-202.0	27.66	0.13	0.14	2.43	−1.000	−1.00	-	N
hdf3_0564_0517	3-203.0	22.54	0.37	0.24	0.29	0.048	4.00	L	Y
hdf3_0585_0559	3-208.0	26.07	0.15	0.35	0.51	−0.004	3.00	L	N
hdf3_0301_0566	3-213.0	26.97	0.21	0.98	0.99	−1.000	−1.00	-	Y
hdf3_1676_0579	3-218.0	26.93	0.16	1.01	0.90	0.010	2.29	L	N
hdf3_1859_0548	3-221.0	22.89	0.68	0.74	0.78	0.285	4.12	A	Y
hdf3_0910_0584	3-223.0	26.73	0.13	0.64	2.86	0.055	2.94	L	N
hdf3_1148_0585	3-224.0	25.79	0.17	0.63	0.90	0.059	2.96	L	N
hdf3_0199_0585	3-225.0	27.37	0.17	0.88	0.70	−1.000	−1.00	-	N
hdf3_1013_0586	3-227.0	26.10	0.17	0.41	0.54	0.026	2.88	L	N
hdf3_0966_0595	3-228.0	27.56	0.13	2.30	4.70	−1.000	−1.00	-	N
hdf3_0275_0588	3-229.0	23.98	0.24	0.95	0.71	0.012	3.30	L	Y
hdf3_0737_0598	3-231.1	26.46	0.26	0.93	3.16	−1.000	−1.00	-	Y
hdf3_0610_0600	3-233.0	26.17	0.18	0.54	1.07	0.039	2.64	L	N
hdf3_1328_0604	3-234.0	26.97	0.16	1.50	0.68	−1.000	−1.00	-	N
hdf3_1955_0604	3-238.0	25.54	0.22	1.50	1.15	0.003	2.96	L	Y
hdf3_0672_0593	3-239.0	25.99	0.32	0.20	1.17	−0.008	2.84	L	Y
hdf3_1689_0620	3-242.0	27.65	0.13	1.61	0.45	−1.000	−1.00	-	N
hdf3_0330_0610	3-243.0	25.29	0.19	0.31	3.10	0.039	3.61	L	N
hdf3_0411_0625	3-246.0	26.21	0.25	0.57	1.55	0.005	2.75	L	Y
hdf3_1643_0630	3-250.0	26.74	0.18	0.07	2.33	−1.000	−1.00	-	N

Table 2–1 — Continued

ID	Williams et al. (1996) ID	F814W$_{AB}$	r_1 ($''$)	$V_{606}-I_{814}$	z_{ph} [a]	A_W	C_W	AC[b] Class	In pruned sample?
hdf3_1588_0638	3-254.0	26.64	0.22	−0.04	2.95	−1.000	−1.00	-	Y
hdf3_0328_0642	3-255.0	27.54	0.13	2.16	3.97	−1.000	−1.00	-	N
hdf3_0726_0642	3-256.0	27.31	0.15	0.17	1.90	−1.000	−1.00	-	N
hdf3_1158_0633	3-257.0	24.98	0.26	0.64	1.22	0.016	2.86	L	Y
hdf3_0169_0617	3-258.0	23.59	0.46	0.49	0.50	0.043	3.45	L	Y
hdf3_1339_0643	3-266.0	23.57	0.21	1.65	0.79	0.030	4.10	C	Y
hdf3_0941_0654	3-271.1	25.34	0.30	0.35	0.50	−0.001	2.77	L	Y
hdf3_0918_0648	3-271.21	25.50	0.13	0.64	0.81	0.022	3.38	L	N
hdf3_0908_0666	3-271.22	26.10	0.15	0.07	3.02	0.052	3.33	L	N
hdf3_0256_0691	3-286.0	26.27	0.22	0.03	2.33	0.015	2.20	L	Y
hdf3_1711_0695	3-289.0	24.66	0.20	1.77	1.06	0.023	3.71	L	Y
hdf3_1460_0703	3-290.0	26.97	0.17	0.22	2.80	−1.000	−1.00	-	N
hdf3_1509_0708	3-292.0	28.57	0.11	0.45	1.47	−1.000	−1.00	-	N
hdf3_0756_0704	3-296.1	25.97	0.14	0.15	2.42	−0.006	2.86	L	N
hdf3_0750_0717	3-296.2	27.00	0.09	0.79	0.87	−0.002	2.63	L	N
hdf3_1364_0727	3-302.0	25.47	0.16	0.95	0.87	0.037	3.20	L	N
hdf3_1620_0727	3-303.0	28.10	0.18	0.56	1.00	−1.000	−1.00	-	N
hdf3_0133_0733	3-306.0	27.64	0.13	1.06	0.84	−1.000	−1.00	-	N
hdf3_0951_0738	3-308.0	27.02	0.10	0.73	1.16	0.033	2.71	L	N
hdf3_0844_0739	3-309.0	27.51	0.18	−0.00	2.46	−1.000	−1.00	-	N
hdf3_0801_0740	3-310.0	27.03	0.15	0.80	0.83	−1.000	−1.00	-	N
hdf3_1695_0738	3-311.0	27.38	0.17	0.04	2.55	−1.000	−1.00	-	N
hdf3_1226_0746	3-318.0	24.39	0.43	0.74	0.89	0.127	2.77	A	Y
hdf3_0299_0741	3-320.0	25.53	0.28	0.11	1.89	0.039	2.48	L	Y
hdf3_0373_0712	3-321.1	21.44	0.35	1.47	0.75	0.025	5.81	C	Y
hdf3_1782_0761	3-329.0	27.26	0.25	0.25	1.10	−1.000	−1.00	-	Y
hdf3_0729_0767	3-330.0	25.56	0.16	0.72	0.88	0.002	3.25	L	N
hdf3_0277_0767	3-331.0	24.58	0.40	0.55	0.83	0.080	3.36	L	Y
hdf3_0935_0777	3-335.0	25.75	0.28	0.36	2.52	0.058	3.63	L	Y
hdf3_1699_0791	3-339.0	29.00	0.10	0.58	0.75	−1.000	−1.00	-	N
hdf3_1856_0786	3-342.0	24.46	0.45	0.43	0.53	0.126	3.50	A	Y
hdf3_1479_0802	3-349.11	26.70	0.12	0.21	3.06	−1.000	−1.00	-	N
hdf3_1495_0806	3-349.12	26.89	0.14	0.55	0.73	−1.000	−1.00	-	N
hdf3_1041_0775	3-350.0	20.89	0.66	0.99	0.64	0.101	3.49	A	Y
hdf3_1602_0813	3-355.0	23.20	0.33	1.16	1.13	0.007	4.70	C	Y
hdf3_1906_0838	3-363.1	25.94	0.12	0.09	2.10	0.024	3.50	L	N
hdf3_1285_0841	3-367.0	25.44	0.26	1.48	0.83	−0.004	2.85	L	Y
hdf3_1540_0837	3-368.0	26.15	0.29	0.55	1.04	−1.000	−1.00	-	Y
hdf3_0651_0851	3-369.0	26.69	0.16	1.00	0.90	0.013	2.82	L	N
hdf3_0860_0832	3-370.0	26.49	0.54	0.18	1.69	−1.000	−1.00	-	Y
hdf3_1960_0861	3-372.0	28.02	0.24	0.11	1.56	−1.000	−1.00	-	Y
hdf3_0438_0875	3-377.0	27.27	0.13	0.67	0.67	−1.000	−1.00	-	N
hdf3_1505_0887	3-378.0	25.63	0.14	1.74	1.16	0.014	3.22	L	N
hdf3_0648_0887	3-380.0	27.61	0.20	−0.03	2.10	−1.000	−1.00	-	Y
hdf3_1858_0890	3-382.0	26.41	0.17	0.15	2.90	0.003	2.55	L	N
hdf3_0310_0850	3-386.111	20.67	0.71	0.55	0.49	0.270	3.48	A	Y
hdf3_1206_0895	3-387.0	26.28	0.17	1.32	0.70	−0.002	2.81	L	N
hdf3_0163_0888	3-389.0	24.58	0.30	0.25	1.98	0.057	3.60	L	Y
hdf3_1875_0916	3-392.0	27.56	0.15	0.59	1.72	−1.000	−1.00	-	N

Table 2–1 — Continued

ID	Williams et al. (1996) ID	F814W$_{AB}$	r_1 ($''$)	$V_{606}-I_{814}$	z_{ph}[a]	A_W	C_W	AC[b] Class	In pruned sample?
hdf3_0553_0919	3-397.0	27.17	0.20	0.10	2.93	−1.000	−1.00	-	Y
hdf3_1243_0905	3-398.0	24.18	0.55	0.52	0.67	0.010	3.09	L	Y
hdf3_0835_0931	3-399.0	27.14	0.16	0.06	2.79	−1.000	−1.00	-	N
hdf3_1648_0886	3-400.1	21.37	0.82	0.42	0.50	0.180	4.00	A	Y
hdf3_1481_0943	3-402.0	26.85	0.18	0.45	1.25	−1.000	−1.00	-	N
hdf3_1563_0938	3-404.1	24.59	0.55	0.55	0.55	0.044	3.00	L	Y
hdf3_1570_0892	3-404.2	23.60	0.30	0.76	0.53	0.003	3.44	L	Y
hdf3_1775_0921	3-405.1	22.32	0.41	0.23	0.30	0.063	4.14	C	Y
hdf3_1735_0955	3-405.2	26.86	0.20	0.08	2.94	−1.000	−1.00	-	Y
hdf3_1618_0967	3-412.0	25.60	0.21	0.50	0.51	−0.006	2.96	L	Y
hdf3_0824_0976	3-413.0	27.28	0.19	0.61	2.65	−1.000	−1.00	-	N
hdf3_0186_0967	3-414.0	26.79	0.21	0.58	0.78	−1.000	−1.00	-	Y
hdf3_1102_0979	3-416.0	26.05	0.14	1.03	0.89	0.006	3.00	L	N
hdf3_0980_0981	3-419.0	22.71	0.14	1.57	4.17	0.086	3.86	L	N
hdf3_1057_1000	3-422.0	26.61	0.14	0.17	2.85	0.009	2.75	L	N
hdf3_0716_1007	3-424.0	27.25	0.13	0.49	0.57	−1.000	−1.00	-	N
hdf3_1352_1017	3-429.0	27.53	0.14	0.12	2.19	−1.000	−1.00	-	N
hdf3_1462_0995	3-430.1	24.04	0.29	0.34	1.22	0.094	3.07	L	Y
hdf3_1481_1009	3-430.2	24.14	0.18	1.51	1.13	0.062	3.93	L	N
hdf3_0443_1014	3-431.0	27.07	0.31	0.29	1.26	−1.000	−1.00	-	Y
hdf3_1683_1022	3-433.0	26.96	0.15	0.44	1.14	−1.000	−1.00	-	N
hdf3_1186_1030	3-439.0	27.63	0.12	−0.10	2.22	−1.000	−1.00	-	N
hdf3_1271_1012	3-443.0	23.10	0.82	0.79	0.90	0.095	2.88	L	Y
hdf3_1977_1052	3-449.0	26.59	0.19	0.15	1.81	0.022	2.46	L	N
hdf3_0820_1056	3-451.0	26.67	0.16	0.46	0.56	0.012	2.42	L	N
hdf3_1606_1065	3-453.0	29.53	0.10	0.56	1.56	−1.000	−1.00	-	N
hdf3_1782_1030	3-454.11	24.50	0.27	0.48	0.54	0.040	3.19	L	Y
hdf3_1766_1054	3-454.12	26.03	0.15	0.29	0.43	−0.004	2.86	L	N
hdf3_1760_1027	3-454.2	27.03	0.14	0.07	2.33	−1.000	−1.00	-	N
hdf3_0998_1063	3-457.0	27.48	0.10	2.90	5.42	−0.011	2.31	L	N
hdf3_0621_1074	3-463.0	27.31	0.12	0.05	2.41	0.015	2.33	L	N
hdf3_0416_1060	3-464.0	25.12	0.24	0.10	2.01	0.100	3.75	L	Y
hdf3_0499_1077	3-466.0	27.02	0.14	0.51	1.29	−1.000	−1.00	-	N
hdf3_0225_1079	3-467.0	27.61	0.12	0.05	2.27	−1.000	−1.00	-	N
hdf3_1735_1102	3-479.0	28.83	0.08	0.28	1.63	−1.000	−1.00	-	N
hdf3_0628_1104	3-480.0	27.59	0.13	−0.13	2.94	−1.000	−1.00	-	N
hdf3_0678_1112	3-483.0	26.55	0.20	0.09	1.82	0.008	2.29	L	Y
hdf3_0534_1111	3-484.0	26.76	0.13	0.38	1.29	−0.006	2.71	L	N
hdf3_1225_1091	3-486.0	21.98	0.56	1.00	0.77	0.069	4.49	C	Y
hdf3_1541_1121	3-489.0	27.47	0.12	1.90	4.68	0.023	2.43	L	N
hdf3_1928_1113	3-491.0	22.48	0.14	1.94	4.27	0.095	3.86	L	N
hdf3_0439_1128	3-494.0	28.00	0.14	0.94	3.95	−1.000	−1.00	-	N
hdf3_0938_1139	3-501.0	26.16	0.16	0.40	2.74	0.014	2.68	L	N
hdf3_1591_1147	3-504.0	26.05	0.19	0.07	2.34	0.050	3.23	L	N
hdf3_0253_1150	3-505.0	26.82	0.18	0.08	2.21	−1.000	−1.00	-	N
hdf3_0622_1152	3-509.0	26.09	0.21	0.98	0.80	0.006	2.50	L	Y
hdf3_0501_1159	3-510.1	26.57	0.12	0.04	2.85	−0.011	2.46	L	N
hdf3_0509_1150	3-510.2	27.10	0.12	0.13	2.29	−1.000	−1.00	-	N
hdf3_1304_1146	3-512.0	25.49	0.25	0.36	3.98	0.034	3.37	L	Y

Table 2–1 — Continued

ID	Williams et al. (1996) ID	F814W$_{AB}$	r_1 ($''$.)	$V_{606}-I_{814}$	z_{ph}[a]	A_W	C_W	AC[b] Class	In pruned sample?
hdf3_0137_1143	3-515.11	24.59	0.24	0.27	2.03	0.083	3.66	L	Y
hdf3_0119_1158	3-515.12	24.26	0.16	0.58	1.14	−0.004	3.80	L	N
hdf3_0127_1119	3-515.2	26.61	0.15	0.17	1.88	−0.009	2.19	L	N
hdf3_0187_1170	3-516.0	27.43	0.12	2.22	4.64	0.006	2.31	L	N
hdf3_0515_1172	3-518.0	29.26	0.08	0.80	1.11	−1.000	−1.00	-	N
hdf3_0283_1178	3-528.1	24.33	0.36	0.83	0.74	0.017	2.76	L	Y
hdf3_1806_1154	3-534.11	21.24	0.90	0.42	0.43	0.081	3.51	L	Y
hdf3_1725_1150	3-534.12	24.21	0.44	0.25	0.26	0.021	3.04	L	Y
hdf3_0417_1197	3-535.0	27.44	0.13	−0.06	3.19	−1.000	−1.00	-	N
hdf3_0386_1208	3-538.0	28.99	0.09	0.67	2.11	−1.000	−1.00	-	N
hdf3_1936_1210	3-542.0	28.03	0.12	0.02	1.61	−1.000	−1.00	-	N
hdf3_1572_1211	3-544.0	26.73	0.15	0.67	1.07	0.006	2.67	L	N
hdf3_0641_1215	3-546.0	28.36	0.15	−0.14	1.73	−1.000	−1.00	-	N
hdf3_0362_1207	3-550.0	24.78	0.34	0.02	2.24	0.276	4.06	A	Y
hdf3_0772_1193	3-551.0	22.81	0.44	0.69	0.58	0.087	3.91	L	Y
hdf3_0865_1225	3-554.0	26.45	0.32	0.11	1.52	−1.000	−1.00	-	Y
hdf3_0552_1223	3-556.2	27.73	0.14	0.95	1.06	−1.000	−1.00	-	N
hdf3_1426_1238	3-557.0	27.47	0.13	−0.08	3.76	−1.000	−1.00	-	N
hdf3_1734_1242	3-558.0	27.62	0.23	0.36	1.26	−1.000	−1.00	-	Y
hdf3_0160_1243	3-561.0	25.77	0.24	0.67	0.68	−0.003	3.05	L	Y
hdf3_1638_1242	3-563.1	25.52	0.16	0.53	1.03	0.006	3.14	L	N
hdf3_0285_1246	3-564.0	26.12	0.20	0.51	0.44	0.004	2.43	L	Y
hdf3_0753_1262	3-568.0	26.45	0.15	0.92	1.10	0.012	2.89	L	N
hdf3_0630_1265	3-571.0	24.79	0.32	1.13	0.81	0.012	2.95	L	Y
hdf3_1972_1270	3-572.0	26.93	0.14	0.69	1.19	−1.000	−1.00	-	N
hdf3_1672_1283	3-581.0	24.87	0.21	0.85	0.78	0.033	3.32	L	Y
hdf3_0737_1296	3-584.0	27.17	0.29	0.09	1.60	−1.000	−1.00	-	Y
hdf3_0473_1288	3-586.0	24.29	0.24	1.74	0.98	0.007	4.00	L	Y
hdf3_0665_1298	3-588.0	27.50	0.16	0.49	1.30	−1.000	−1.00	-	N
hdf3_0374_1303	3-590.0	27.54	0.12	0.12	2.00	−1.000	−1.00	-	N
hdf3_0428_1287	3-593.0	25.56	0.33	0.33	1.83	0.001	2.75	L	Y
hdf3_0238_1313	3-594.0	28.16	0.09	1.67	4.59	−1.000	−1.00	-	N
hdf3_1998_1307	3-597.0	24.44	0.20	0.47	1.23	0.034	3.38	L	Y
hdf3_0213_1310	3-599.0	24.67	0.19	0.49	0.61	0.017	3.13	L	N
hdf3_0757_1315	3-600.0	26.77	0.19	0.13	2.31	−0.003	2.31	L	N
hdf3_1026_1312	3-601.0	24.29	0.26	1.43	1.08	0.015	3.71	L	Y
hdf3_1664_1320	3-602.0	27.80	0.11	0.27	1.42	−1.000	−1.00	-	N
hdf3_0423_1322	3-605.0	28.09	0.12	−0.18	1.78	−1.000	−1.00	-	N
hdf3_1161_1320	3-607.0	26.78	0.18	0.28	3.20	−1.000	−1.00	-	N
hdf3_1693_1331	3-608.0	28.80	0.07	1.99	4.79	−1.000	−1.00	-	N
hdf3_1834_1338	3-616.0	27.55	0.13	0.57	0.60	−1.000	−1.00	-	N
hdf3_0183_1349	3-622.0	27.36	0.19	0.44	0.76	−1.000	−1.00	-	N
hdf3_0524_1352	3-625.0	25.37	0.20	−0.03	2.19	0.126	3.83	A	Y
hdf3_1130_1363	3-628.0	28.55	0.10	−0.03	1.58	−1.000	−1.00	-	N
hdf3_0355_1342	3-633.1	25.57	0.44	0.14	2.15	−1.000	−1.00	-	Y
hdf3_0384_1318	3-633.2	26.77	0.16	0.81	0.80	−1.000	−1.00	-	N
hdf3_1875_1374	3-635.0	28.08	0.11	0.01	2.33	−1.000	−1.00	-	N
hdf3_0900_1387	3-639.0	26.90	0.13	0.25	1.37	−0.008	2.53	L	N
hdf3_1288_1389	3-640.0	27.39	0.12	0.01	2.30	−1.000	−1.00	-	N

Table 2–1 — Continued

	Williams et al. (1996)								
ID	ID	F814W$_{\rm AB}$	r_1 ($''$)	$V_{606} - I_{814}$	z_{ph}[a]	A_W	C_W	AC[b] Class	In pruned sample?
hdf3_0836_1400	3-648.0	27.69	0.14	0.41	2.73	−1.000	−1.00	-	N
hdf3_1908_1409	3-655.0	26.52	0.21	0.22	1.30	−1.000	−1.00	-	Y
hdf3_0351_1403	3-659.1	21.55	0.41	0.69	0.45	0.054	3.67	L	Y
hdf3_0311_1371	3-659.2	24.98	0.15	0.63	0.80	0.020	3.44	L	N
hdf3_1534_1434	3-660.0	28.78	0.15	0.61	2.66	−1.000	−1.00	-	N
hdf3_1680_1432	3-661.0	26.34	0.20	0.77	0.58	−0.001	2.25	L	Y
hdf3_1073_1441	3-662.0	28.77	0.08	0.35	5.84	−1.000	−1.00	-	N
hdf3_1325_1442	3-663.0	28.28	0.11	0.21	1.58	−1.000	−1.00	-	N
hdf3_1183_1441	3-668.1	27.61	0.11	0.36	2.10	−1.000	−1.00	-	N
hdf3_1828_1444	3-669.0	27.25	0.33	0.33	2.66	−1.000	−1.00	-	Y
hdf3_0625_1452	3-670.1	25.00	0.15	0.66	0.71	0.016	3.28	L	N
hdf3_1907_1458	3-671.0	27.71	0.17	0.08	1.68	−1.000	−1.00	-	N
hdf3_1546_1462	3-672.0	28.31	0.13	−0.01	3.04	−1.000	−1.00	-	N
hdf3_0748_1457	3-674.0	25.63	0.24	0.39	1.52	0.001	3.17	L	Y
hdf3_1370_1459	3-675.0	25.62	0.25	0.46	3.36	0.010	2.66	L	Y
hdf3_1658_1467	3-676.0	28.20	0.12	0.60	0.92	−1.000	−1.00	-	N
hdf3_0306_1462	3-677.0	25.08	0.22	0.41	1.94	0.066	3.19	L	Y
hdf3_1105_1470	3-678.0	26.89	0.12	0.09	2.30	0.065	2.60	L	N
hdf3_1683_1472	3-681.0	27.19	0.13	0.78	1.00	−1.000	−1.00	-	N
hdf3_1078_1474	3-683.0	27.64	0.13	0.44	1.37	−1.000	−1.00	-	N
hdf3_0388_1463	3-684.1	26.69	0.12	0.01	1.35	0.003	2.65	L	N
hdf3_0382_1472	3-684.2	27.03	0.10	0.39	0.56	0.002	2.29	L	N
hdf3_0698_1455	3-687.1	25.28	0.28	−0.01	1.84	0.048	3.29	L	Y
hdf3_1547_1481	3-688.0	26.85	0.17	0.08	1.67	−0.006	2.23	L	N
hdf3_1769_1486	3-692.0	28.20	0.10	0.42	1.07	−1.000	−1.00	-	N
hdf3_1029_1488	3-695.0	26.23	0.24	0.05	2.14	−0.009	2.27	L	Y
hdf3_0502_1481	3-696.0	23.17	0.23	0.46	0.47	0.033	3.58	L	Y
hdf3_0422_1495	3-697.0	27.63	0.11	0.77	0.91	−1.000	−1.00	-	N
hdf3_1515_1489	3-698.0	26.14	0.20	0.26	0.41	0.001	2.48	L	Y
hdf3_0640_1492	3-704.11	24.14	0.22	0.02	1.82	0.206	3.90	A	Y
hdf3_0295_1518	3-705.0	26.50	0.17	0.31	0.39	−0.008	2.38	L	N
hdf3_0906_1517	3-706.0	26.37	0.26	0.43	0.59	−1.000	−1.00	-	Y
hdf3_0432_1528	3-707.0	28.28	0.10	−0.19	2.89	−1.000	−1.00	-	N
hdf3_0639_1517	3-708.1	25.95	0.18	0.19	0.45	0.003	2.78	L	N
hdf3_1768_1530	3-712.0	25.24	0.26	1.03	0.75	0.014	2.93	L	Y
hdf3_1841_1544	3-714.0	26.70	0.15	0.48	0.45	−0.004	2.45	L	N
hdf3_0353_1558	3-719.0	26.51	0.15	0.45	0.47	0.017	2.67	L	N
hdf3_0211_1569	3-720.0	28.10	0.10	0.30	1.98	−1.000	−1.00	-	N
hdf3_1273_1559	3-722.0	25.33	0.44	0.08	1.85	0.061	2.43	L	Y
hdf3_0516_1573	3-724.0	27.37	0.16	0.74	1.19	−1.000	−1.00	-	N
hdf3_1581_1570	3-726.0	25.45	0.16	0.73	0.68	0.003	3.00	L	N
hdf3_1549_1577	3-728.0	27.92	0.16	0.29	1.80	−1.000	−1.00	-	N
hdf3_1638_1579	3-729.0	27.89	0.12	0.11	2.07	−1.000	−1.00	-	N
hdf3_1248_1585	3-730.0	27.20	0.17	0.75	3.57	−1.000	−1.00	-	N
hdf3_1784_1585	3-731.0	27.01	0.19	0.21	0.23	−1.000	−1.00	-	N
hdf3_0697_1586	3-735.0	26.47	0.21	0.31	1.61	0.018	2.40	L	Y
hdf3_1016_1597	3-736.0	26.30	0.12	0.02	2.25	0.028	3.20	L	N
hdf3_0884_1600	3-743.0	25.39	0.21	0.07	1.94	0.096	3.46	L	Y
hdf3_1838_1617	3-748.0	26.07	0.17	0.09	2.49	0.045	3.24	L	N

Table 2–1 — Continued

ID	Williams et al. (1996) ID	F814W$_{AB}$	r_1 ($''$)	$V_{606} - I_{814}$	z_{ph}[a]	A_W	C_W	AC[b] Class	In pruned sample?
hdf3_0939_1631	3-751.0	27.13	0.19	0.44	0.16	−1.000	−1.00	-	N
hdf3_1835_1638	3-752.0	27.99	0.13	0.19	2.20	−1.000	−1.00	-	N
hdf3_0886_1641	3-754.0	26.51	0.15	0.03	1.73	0.003	2.56	L	N
hdf3_0405_1642	3-755.0	26.43	0.14	0.06	2.79	0.009	3.00	L	N
hdf3_0974_1639	3-757.0	26.08	0.24	−0.00	1.87	0.014	2.40	L	Y
hdf3_1504_1637	3-761.0	24.98	0.33	0.60	0.73	0.036	3.17	L	Y
hdf3_0509_1652	3-762.0	29.11	0.11	−0.08	2.22	−1.000	−1.00	-	N
hdf3_1365_1656	3-765.0	25.18	0.25	0.50	1.17	0.052	2.87	L	Y
hdf3_1577_1679	3-771.0	28.18	0.13	0.72	1.37	−1.000	−1.00	-	N
hdf3_1292_1657	3-773.1	22.44	0.56	0.58	0.60	0.157	3.01	A	Y
hdf3_0712_1683	3-775.0	26.54	0.14	0.99	0.26	0.011	2.75	L	N
hdf3_0294_1667	3-777.1	22.92	0.45	0.49	0.51	0.074	4.56	C	Y
hdf3_0324_1630	3-777.2	27.55	0.12	0.04	2.06	−1.000	−1.00	-	N
hdf3_0220_1690	3-779.0	27.69	0.13	0.33	1.34	−1.000	−1.00	-	N
hdf3_0256_1694	3-780.0	25.44	0.23	0.19	1.81	0.020	2.85	L	Y
hdf3_1604_1705	3-783.0	26.20	0.15	0.84	3.26	0.057	2.86	L	N
hdf3_1436_1710	3-787.0	25.61	0.30	0.62	0.88	0.055	2.77	L	Y
hdf3_1919_1689	3-790.0	21.36	0.46	1.14	0.67	0.018	5.18	C	Y
hdf3_0127_1719	3-792.0	25.43	0.28	0.25	3.12	−0.009	3.00	L	Y
hdf3_0990_1729	3-794.0	27.41	0.16	0.00	2.22	−1.000	−1.00	-	N
hdf3_0234_1741	3-798.0	27.92	0.11	1.03	0.90	−1.000	−1.00	-	N
hdf3_0543_1738	3-801.0	26.80	0.20	0.22	2.49	−1.000	−1.00	-	Y
hdf3_0761_1746	3-802.0	27.51	0.12	0.46	1.32	−1.000	−1.00	-	N
hdf3_0727_1751	3-806.0	26.72	0.16	−0.03	2.11	0.044	2.59	L	N
hdf3_1356_1754	3-810.0	27.12	0.25	0.22	1.74	−1.000	−1.00	-	Y
hdf3_1517_1759	3-812.0	26.85	0.19	0.09	1.89	0.020	2.33	L	N
hdf3_1633_1765	3-813.0	25.72	0.19	0.08	3.14	0.031	3.23	L	N
hdf3_1144_1749	3-815.0	22.52	0.45	1.50	0.83	0.057	5.30	C	Y
hdf3_1975_1776	3-818.0	25.64	0.34	0.37	1.55	0.005	2.53	L	Y
hdf3_1383_1789	3-821.0	28.80	0.11	0.08	1.50	−1.000	−1.00	-	N
hdf3_0236_1802	3-828.0	26.91	0.21	0.46	0.36	−1.000	−1.00	-	Y
hdf3_1227_1812	3-832.0	27.01	0.21	0.99	1.05	−1.000	−1.00	-	Y
hdf3_1868_1813	3-835.0	26.22	0.18	0.78	1.13	0.006	2.71	L	N
hdf3_0684_1817	3-838.0	27.11	0.18	−0.08	2.60	−1.000	−1.00	-	N
hdf3_0872_1816	3-839.0	24.66	0.12	2.16	4.38	0.041	3.36	L	N
hdf3_0988_1827	3-843.0	24.94	0.29	0.31	1.32	0.064	2.92	L	Y
hdf3_0364_1830	3-844.0	26.27	0.18	0.99	0.79	0.007	2.78	L	N
hdf3_0462_1839	3-845.0	28.72	0.09	0.25	1.56	−1.000	−1.00	-	N
hdf3_0961_1840	3-847.0	27.29	0.19	0.61	1.27	−1.000	−1.00	-	N
hdf3_0607_1847	3-851.0	27.12	0.17	1.05	0.76	−1.000	−1.00	-	N
hdf3_1576_1837	3-853.1	25.31	0.34	0.67	0.52	0.096	2.73	L	Y
hdf3_1550_1835	3-853.2	25.65	0.37	0.16	2.00	0.099	2.58	L	Y
hdf3_1107_1847	3-856.0	27.86	0.17	−0.04	1.70	−1.000	−1.00	-	N
hdf3_1482_1852	3-863.0	23.36	0.24	0.65	0.70	0.029	3.16	L	Y
hdf3_1068_1866	3-865.0	28.04	0.14	0.17	1.57	−1.000	−1.00	-	N
hdf3_0487_1865	3-866.0	27.70	0.14	1.07	0.77	−1.000	−1.00	-	N
hdf3_0225_1867	3-869.0	27.21	0.23	0.95	1.58	−1.000	−1.00	-	Y
hdf3_1890_1873	3-872.0	26.79	0.19	0.16	1.45	−1.000	−1.00	-	N
hdf3_1755_1875	3-875.0	23.76	0.45	0.16	2.17	0.212	3.82	A	Y

Table 2–1 — Continued

ID	Williams et al. (1996) ID	F814W$_{AB}$	r_1 ($''$.)	$V_{606} - I_{814}$	z_{ph}[a]	A_W	C_W	AC[b] Class	In pruned sample?
hdf3_0373_1880	3-886.0	24.49	0.21	0.45	1.03	0.040	3.42	L	Y
hdf3_1464_1905	3-887.0	26.84	0.15	0.78	0.66	−0.012	2.31	L	N
hdf3_1825_1889	3-888.0	24.52	0.32	0.56	0.93	0.049	4.00	L	Y
hdf3_0301_1888	3-890.1	23.47	0.21	0.56	0.51	0.112	4.40	A	Y
hdf3_0324_1875	3-890.2	26.60	0.17	0.09	2.02	0.005	2.56	L	N
hdf3_0478_1913	3-891.0	29.87	0.08	0.04	5.83	−1.000	−1.00	-	N
hdf3_0138_1923	3-902.1	26.20	0.16	−0.13	2.52	−0.009	3.06	L	N
hdf3_0938_1917	3-904.0	24.59	0.17	0.52	1.33	0.023	3.70	L	N
hdf3_1601_1903	3-908.1	24.16	0.32	0.38	0.51	0.070	2.85	L	Y
hdf3_1619_1926	3-908.2	24.50	0.21	0.64	0.71	0.015	3.06	L	Y
hdf3_1681_1944	3-911.0	26.87	0.15	0.07	2.40	−1.000	−1.00	-	N
hdf3_0380_1948	3-915.0	24.88	0.26	0.11	2.07	0.245	3.50	A	Y
hdf3_1374_1946	3-916.0	25.35	0.19	0.24	1.93	−0.003	3.32	L	N
hdf3_1890_1925	3-920.1	25.91	0.33	0.13	3.02	−1.000	−1.00	-	Y
hdf3_1446_1960	3-923.0	24.65	0.35	0.51	0.45	0.030	3.67	L	Y
hdf3_0845_1954	3-925.0	25.03	0.49	0.81	0.90	0.080	4.83	C	Y
hdf3_1315_1984	3-939.0	26.79	0.22	0.18	1.48	−1.000	−1.00	-	Y
hdf3_0341_1991	3-942.0	26.44	0.21	−0.06	2.10	0.027	2.39	L	Y
hdf3_1001_1983	3-943.0	23.27	0.42	0.32	0.41	0.030	3.46	L	Y
hdf3_0465_1995	3-945.0	26.48	0.15	0.23	3.16	−0.006	2.50	L	N
hdf3_0785_1994	3-946.0	25.83	0.16	0.50	0.93	0.015	3.26	L	N
hdf3_1765_2000	3-947.0	28.13	0.14	0.98	6.88	−1.000	−1.00	-	N
hdf3_1273_2001	3-948.0	26.87	0.14	0.59	0.49	0.008	2.36	L	N
hdf3_0604_1996	3-950.1	24.74	0.26	0.75	1.22	0.013	3.43	L	Y
hdf3_1636_2001	3-951.1	26.24	0.17	2.48	4.83	0.030	2.55	L	N
hdf3_1651_1999	3-951.2	27.00	0.12	1.92	4.50	0.020	2.67	L	N
hdf3_1811_1995	3-952.0	26.05	0.26	0.74	1.19	0.004	2.47	L	Y
hdf3_0669_2004	3-955.0	25.98	0.39	0.08	2.64	−1.000	−1.00	-	Y
hdf3_0143_1991	3-956.1	23.69	0.43	0.44	2.77	0.050	3.19	L	Y
hdf3_0168_2000	3-956.2	26.49	0.12	−0.03	3.01	−0.007	2.78	L	N
hdf3_1352_2002	3-957.0	23.34	0.23	0.58	1.03	0.032	3.45	L	Y
hdf3_1720_2017	3-958.0	25.90	0.13	0.87	0.99	0.001	3.32	L	N
hdf4_0986_0166	4-20.0	27.80	0.14	0.61	0.92	−1.000	−1.00	-	N
hdf4_0569_0181	4-30.0	27.35	0.11	1.36	3.97	−1.000	−1.00	-	N
hdf4_1154_0179	4-31.0	27.17	0.20	0.03	1.93	−1.000	−1.00	-	Y
hdf4_1363_0172	4-33.0	22.46	0.48	1.55	0.73	0.060	3.54	L	Y
hdf4_1065_0180	4-34.0	27.86	0.20	0.38	0.69	−1.000	−1.00	-	Y
hdf4_1845_0199	4-51.0	26.72	0.20	0.16	3.19	−1.000	−1.00	-	Y
hdf4_1547_0204	4-54.0	26.93	0.15	0.18	2.12	0.017	2.50	L	N
hdf4_1003_0228	4-69.0	27.29	0.11	1.01	0.85	−0.014	2.59	L	N
hdf4_1426_0218	4-70.0	27.19	0.29	0.08	1.57	−1.000	−1.00	-	Y
hdf4_1779_0221	4-71.0	25.88	0.25	0.38	0.52	0.001	2.74	L	Y
hdf4_0452_0236	4-73.0	27.73	0.13	0.09	1.49	−1.000	−1.00	-	N
hdf4_1193_0235	4-74.0	27.12	0.30	0.09	2.54	−1.000	−1.00	-	Y
hdf4_1483_0240	4-75.0	26.98	0.22	−0.11	2.93	−1.000	−1.00	-	Y
hdf4_0290_0247	4-77.0	27.55	0.20	0.27	2.00	−1.000	−1.00	-	Y
hdf4_1887_0252	4-81.0	26.91	0.16	0.61	0.64	−1.000	−1.00	-	N
hdf4_1653_0252	4-83.0	26.01	0.24	0.14	2.82	0.034	2.76	L	Y
hdf4_1246_0245	4-85.1	24.41	0.26	0.76	0.92	0.058	3.36	L	Y

Table 2–1 — Continued

ID	Williams et al. (1996) ID	F814W$_{AB}$	r_1 ($''$.)	$V_{606}-I_{814}$	z_{ph}[a]	A_W	C_W	AC[b] Class	In pruned sample?
hdf4_1268_0223	4-85.2	25.16	0.21	0.09	2.59	0.002	2.93	L	Y
hdf4_0359_0245	4-89.0	23.90	0.39	0.68	0.72	0.053	3.61	L	Y
hdf4_0188_0274	4-93.0	27.58	0.19	0.49	1.13	−1.000	−1.00	-	N
hdf4_0995_0275	4-94.0	27.49	0.14	−0.11	1.89	−1.000	−1.00	-	N
hdf4_1364_0279	4-95.0	28.34	0.11	0.03	1.93	−1.000	−1.00	-	N
hdf4_0604_0280	4-96.0	26.60	0.20	−0.02	2.48	−1.000	−1.00	-	Y
hdf4_1606_0292	4-104.0	27.49	0.17	0.09	2.33	−1.000	−1.00	-	N
hdf4_0704_0291	4-107.0	25.90	0.37	0.67	0.24	−1.000	−1.00	-	Y
hdf4_1423_0305	4-109.0	25.12	0.17	0.07	2.18	0.029	3.23	L	N
hdf4_1824_0315	4-110.0	28.26	0.11	−0.10	1.93	−1.000	−1.00	-	N
hdf4_1474_0319	4-118.0	26.99	0.18	0.17	2.32	−1.000	−1.00	-	N
hdf4_1432_0325	4-119.0	27.71	0.11	0.23	1.13	−1.000	−1.00	-	N
hdf4_1194_0319	4-120.0	22.42	0.61	0.77	0.89	0.122	2.70	A	Y
hdf4_1014_0327	4-122.0	27.01	0.30	0.14	1.37	−1.000	−1.00	-	Y
hdf4_1615_0335	4-123.0	27.38	0.19	0.07	2.52	−1.000	−1.00	-	N
hdf4_1362_0323	4-131.0	24.86	0.36	0.68	0.88	0.069	3.44	L	Y
hdf4_0334_0350	4-132.0	28.53	0.12	0.93	1.28	−1.000	−1.00	-	N
hdf4_1013_0354	4-135.0	27.66	0.12	0.38	2.12	−1.000	−1.00	-	N
hdf4_0643_0353	4-136.0	26.13	0.17	−0.01	2.19	0.085	3.10	L	N
hdf4_1520_0362	4-140.0	27.27	0.11	0.17	1.50	−0.001	2.54	L	N
hdf4_1286_0374	4-148.0	28.34	0.12	1.70	4.27	−1.000	−1.00	-	N
hdf4_2014_0372	4-149.0	26.67	0.19	0.48	0.93	−1.000	−1.00	-	N
hdf4_1217_0378	4-154.0	25.83	0.26	0.53	0.43	−0.001	2.81	L	Y
hdf4_1688_0386	4-155.0	27.58	0.16	0.18	1.66	−1.000	−1.00	-	N
hdf4_0721_0387	4-160.0	25.16	0.24	0.55	0.46	0.018	3.04	L	Y
hdf4_0230_0386	4-161.0	24.79	0.26	0.85	0.90	0.034	3.23	L	Y
hdf4_1802_0398	4-163.0	27.27	0.17	0.59	1.20	−1.000	−1.00	-	N
hdf4_0392_0402	4-166.1	26.98	0.17	0.03	2.21	−1.000	−1.00	-	N
hdf4_1271_0408	4-169.0	27.15	0.16	3.01	5.92	0.007	2.88	L	N
hdf4_1104_0413	4-170.0	27.95	0.14	0.94	3.77	−1.000	−1.00	-	N
hdf4_1528_0405	4-171.0	24.77	0.24	1.07	0.93	0.063	3.17	L	Y
hdf4_0831_0400	4-173.0	23.32	0.31	0.91	0.93	0.034	3.42	L	Y
hdf4_0917_0417	4-174.0	27.56	0.11	0.26	2.13	−1.000	−1.00	-	N
hdf4_0541_0419	4-175.0	25.78	0.20	0.54	0.68	0.015	3.13	L	Y
hdf4_1560_0421	4-180.0	27.54	0.23	−0.02	1.57	−1.000	−1.00	-	Y
hdf4_1971_0434	4-185.0	29.03	0.11	1.64	1.28	−1.000	−1.00	-	N
hdf4_1284_0432	4-186.0	24.68	0.19	0.77	1.82	0.105	2.96	A	N
hdf4_1664_0434	4-193.0	26.40	0.18	0.06	2.36	0.004	2.75	L	N
hdf4_1836_0441	4-194.0	25.73	0.20	0.19	3.03	0.007	3.20	L	Y
hdf4_1232_0461	4-200.0	27.04	0.21	1.68	4.33	−1.000	−1.00	-	Y
hdf4_0316_0462	4-201.0	26.71	0.16	0.25	1.77	−0.009	2.39	L	N
hdf4_1485_0461	4-203.11	25.70	0.17	0.59	0.56	0.016	3.13	L	N
hdf4_1488_0444	4-203.12	27.70	0.12	0.02	2.11	−1.000	−1.00	-	N
hdf4_0472_0471	4-210.0	26.41	0.25	0.68	3.66	0.002	2.13	L	Y
hdf4_1037_0481	4-212.0	26.38	0.21	0.26	1.14	0.002	2.45	L	Y
hdf4_1622_0494	4-217.0	27.08	0.17	0.12	1.69	−1.000	−1.00	-	N
hdf4_0491_0497	4-219.0	27.44	0.15	−0.08	2.05	−1.000	−1.00	-	N
hdf4_1469_0510	4-229.0	25.97	0.17	0.46	1.10	0.011	3.17	L	N
hdf4_1588_0522	4-230.0	27.07	0.12	−0.03	1.95	0.015	2.36	L	N

Table 2–1 — Continued

ID	Williams et al. (1996) ID	F814W$_{AB}$	r_1 ($''$.)	$V_{606} - I_{814}$	z_{ph}[a]	A_W	C_W	AC[b] Class	In pruned sample?
hdf4_0846_0503	4-232.12	22.86	0.25	0.37	0.46	0.097	4.04	C	Y
hdf4_0304_0521	4-233.0	24.30	0.11	0.70	0.53	0.078	3.36	L	N
hdf4_0215_0528	4-234.0	27.23	0.15	0.21	1.36	−1.000	−1.00	-	N
hdf4_1813_0518	4-235.0	23.37	0.17	0.43	0.99	0.049	3.84	L	N
hdf4_0689_0481	4-241.1	20.98	0.46	0.42	0.44	0.052	5.06	C	Y
hdf4_0666_0524	4-241.3	22.24	0.11	1.45	4.27	0.084	3.86	L	N
hdf4_1980_0520	4-242.0	25.61	0.41	0.41	1.22	−1.000	−1.00	-	Y
hdf4_0223_0539	4-243.0	27.50	0.12	−0.11	2.34	−1.000	−1.00	-	N
hdf4_1612_0539	4-244.0	26.08	0.15	1.22	0.31	0.014	3.16	L	N
hdf4_1694_0533	4-245.0	25.60	0.40	0.48	2.77	−1.000	−1.00	-	Y
hdf4_0178_0542	4-252.0	26.27	0.24	0.04	2.20	0.000	2.31	L	Y
hdf4_0404_0535	4-254.0	22.33	0.37	1.52	0.78	0.016	5.67	C	Y
hdf4_1555_0555	4-257.0	25.48	0.15	0.81	0.86	0.023	3.25	L	N
hdf4_1307_0514	4-260.111	22.67	0.71	0.85	0.88	0.148	2.79	A	Y
hdf4_1271_0521	4-260.112	24.34	0.18	0.49	0.57	0.008	4.17	C	N
hdf4_1324_0441	4-260.2	24.50	0.39	0.60	0.82	0.030	3.24	L	Y
hdf4_0578_0569	4-263.0	26.89	0.23	0.12	3.08	−1.000	−1.00	-	Y
hdf4_1916_0564	4-264.1	24.45	0.27	0.65	0.93	0.109	3.11	A	Y
hdf4_0154_0600	4-273.0	26.79	0.18	0.38	0.46	−1.000	−1.00	-	N
hdf4_1902_0599	4-274.0	25.44	0.20	0.39	1.67	0.018	3.45	L	Y
hdf4_1837_0604	4-277.0	26.10	0.14	1.07	3.89	0.021	3.27	L	N
hdf4_0279_0604	4-278.0	27.12	0.21	0.17	1.42	−1.000	−1.00	-	Y
hdf4_0456_0607	4-279.0	28.00	0.12	0.70	0.86	−1.000	−1.00	-	N
hdf4_0820_0607	4-280.0	26.83	0.15	0.29	3.87	−1.000	−1.00	-	N
hdf4_1961_0599	4-284.0	22.95	0.38	1.17	0.92	0.061	3.73	L	Y
hdf4_0160_0626	4-287.0	27.39	0.20	0.82	0.69	−1.000	−1.00	-	Y
hdf4_0932_0602	4-289.0	25.18	0.23	−0.01	2.72	0.229	3.58	A	Y
hdf4_1248_0629	4-291.0	28.09	0.09	1.19	1.00	−1.000	−1.00	-	N
hdf4_0433_0634	4-292.0	26.87	0.24	0.59	1.29	−1.000	−1.00	-	Y
hdf4_1002_0634	4-295.0	26.60	0.27	0.76	0.94	−1.000	−1.00	-	Y
hdf4_0715_0640	4-300.0	25.09	0.21	0.88	0.85	−0.004	3.04	L	Y
hdf4_0287_0652	4-302.0	27.20	0.17	0.26	2.13	−1.000	−1.00	-	N
hdf4_1472_0657	4-304.0	27.00	0.12	0.90	0.98	0.001	2.79	L	N
hdf4_0580_0642	4-305.0	25.81	0.25	0.84	0.90	0.019	2.80	L	Y
hdf4_0478_0657	4-307.0	25.77	0.21	1.04	1.85	0.086	3.35	L	Y
hdf4_1394_0660	4-308.0	27.74	0.14	−0.26	2.31	−1.000	−1.00	-	N
hdf4_1589_0680	4-314.0	27.27	0.13	1.77	3.57	−1.000	−1.00	-	N
hdf4_1313_0662	4-315.0	25.18	0.40	0.12	1.52	0.095	3.42	L	Y
hdf4_0233_0661	4-316.0	24.09	0.62	0.16	1.75	0.369	3.39	A	Y
hdf4_1944_0686	4-317.0	26.23	0.13	−0.07	2.80	0.004	3.13	L	N
hdf4_1375_0694	4-319.0	26.47	0.20	0.58	0.96	−0.005	2.29	L	Y
hdf4_0240_0699	4-320.0	27.49	0.14	−0.05	2.09	−1.000	−1.00	-	N
hdf4_0814_0685	4-322.1	25.03	0.23	0.18	1.68	0.067	3.21	L	Y
hdf4_0827_0699	4-322.2	25.06	0.12	0.33	1.49	0.029	3.43	L	N
hdf4_0334_0703	4-325.0	26.38	0.18	0.70	0.72	−0.007	2.60	L	N
hdf4_0738_0710	4-326.0	27.55	0.13	−0.04	1.82	−1.000	−1.00	-	N
hdf4_0923_0710	4-327.0	26.55	0.19	0.18	2.12	0.002	2.21	L	N
hdf4_0387_0709	4-329.0	26.66	0.14	0.09	2.71	−0.006	2.87	L	N
hdf4_1254_0714	4-332.1	24.76	0.22	0.48	0.72	0.101	3.50	A	Y

Table 2–1 — Continued

	Williams et al. (1996)								
ID	ID	$F814W_{AB}$	r_1 ($''$)	$V_{606} - I_{814}$	z_{ph}[a]	A_W	C_W	AC[b] Class	In pruned sample?
hdf4_1264_0687	4-332.2	25.87	0.14	0.35	0.72	0.051	3.05	L	N
hdf4_1114_0720	4-334.0	26.67	0.15	0.82	0.72	0.022	2.75	L	N
hdf4_1355_0730	4-335.0	27.14	0.14	0.39	0.82	−1.000	−1.00	-	N
hdf4_1147_0734	4-336.0	27.19	0.20	0.30	2.36	−1.000	−1.00	-	Y
hdf4_0638_0751	4-344.0	26.79	0.19	0.29	1.19	−0.013	2.46	L	N
hdf4_0665_0752	4-345.0	27.09	0.12	0.16	1.80	−0.007	2.46	L	N
hdf4_1514_0740	4-346.0	24.47	0.34	0.89	0.11	0.110	2.81	A	Y
hdf4_1948_0753	4-349.0	25.31	0.18	0.94	1.03	0.019	3.04	L	N
hdf4_1151_0763	4-350.0	27.60	0.11	0.56	1.32	−1.000	−1.00	-	N
hdf4_1929_0766	4-352.0	26.89	0.16	0.68	1.12	−1.000	−1.00	-	N
hdf4_0922_0770	4-353.0	27.49	0.13	−0.02	2.52	−1.000	−1.00	-	N
hdf4_1766_0771	4-354.0	26.93	0.14	0.03	2.90	−0.005	2.50	L	N
hdf4_1552_0775	4-356.0	27.68	0.12	0.24	1.32	−1.000	−1.00	-	N
hdf4_1825_0771	4-357.0	25.52	0.21	0.29	1.52	0.047	3.13	L	Y
hdf4_1309_0785	4-360.0	28.24	0.10	0.08	1.29	−1.000	−1.00	-	N
hdf4_1955_0776	4-363.0	24.89	0.31	0.16	3.00	0.015	3.07	L	Y
hdf4_0647_0785	4-368.0	25.95	0.19	0.23	1.86	0.019	2.86	L	N
hdf4_1858_0796	4-369.0	29.28	0.09	−0.07	7.81	−1.000	−1.00	-	N
hdf4_1131_0792	4-372.0	26.41	0.21	0.60	0.61	0.008	2.27	L	Y
hdf4_0487_0772	4-378.0	23.98	0.80	0.49	1.20	0.021	2.35	L	Y
hdf4_1412_0804	4-382.1	24.04	0.31	0.35	2.61	0.014	3.42	L	Y
hdf4_1579_0821	4-385.0	25.88	0.20	0.25	2.00	−0.003	2.56	L	Y
hdf4_1736_0823	4-386.0	26.11	0.24	0.63	0.90	−0.010	2.33	L	Y
hdf4_0934_0820	4-387.0	26.86	0.22	0.68	0.90	−1.000	−1.00	-	Y
hdf4_0869_0827	4-389.0	26.15	0.20	0.04	2.77	0.041	2.84	L	Y
hdf4_0350_0824	4-393.0	23.92	0.55	0.12	1.92	0.258	4.38	A	Y
hdf4_0805_0852	4-395.0	25.94	0.20	0.47	0.91	0.027	2.83	L	Y
hdf4_0305_0877	4-403.0	25.05	0.25	1.64	1.68	0.085	3.27	L	Y
hdf4_1779_0866	4-406.0	24.01	0.24	0.86	0.89	0.042	3.31	L	Y
hdf4_0829_0876	4-407.0	25.39	0.27	0.53	0.68	0.102	2.62	A	Y
hdf4_1957_0879	4-408.0	26.93	0.16	0.09	1.87	−1.000	−1.00	-	N
hdf4_1623_0883	4-415.0	25.56	0.30	0.51	0.67	0.011	2.77	L	Y
hdf4_1437_0890	4-416.0	24.33	0.22	0.42	0.50	0.042	3.64	L	Y
hdf4_1403_0901	4-418.0	24.72	0.57	0.32	1.06	0.025	2.86	L	Y
hdf4_1138_0911	4-419.0	27.87	0.14	0.58	1.47	−1.000	−1.00	-	N
hdf4_0783_0923	4-423.0	26.82	0.22	0.38	1.66	−1.000	−1.00	-	Y
hdf4_0173_0921	4-427.0	26.49	0.26	0.29	1.23	−1.000	−1.00	-	Y
hdf4_0412_0909	4-430.0	23.27	0.50	0.75	0.89	0.146	2.80	A	Y
hdf4_1673_0944	4-432.0	27.27	0.21	0.44	2.66	−1.000	−1.00	-	Y
hdf4_1576_0944	4-434.0	25.58	0.18	0.19	0.38	0.023	2.96	L	N
hdf4_0662_0955	4-438.0	26.96	0.27	0.23	1.48	−1.000	−1.00	-	Y
hdf4_0361_0952	4-439.0	24.88	0.22	1.09	4.40	0.085	3.48	L	Y
hdf4_1655_0963	4-442.0	25.60	0.22	0.75	0.60	0.026	3.23	L	Y
hdf4_0744_0962	4-445.0	23.71	0.29	0.37	1.49	0.112	3.93	A	Y
hdf4_1494_0970	4-448.0	24.52	0.41	0.53	0.51	0.022	2.93	L	Y
hdf4_0838_0999	4-453.0	28.89	0.11	0.50	1.53	−1.000	−1.00	-	N
hdf4_0948_0999	4-455.0	27.27	0.11	0.00	1.86	0.014	2.46	L	N
hdf4_1432_1002	4-460.0	23.73	0.35	0.72	0.74	0.040	3.35	L	Y
hdf4_0367_1033	4-469.0	26.53	0.15	0.04	2.72	−0.008	2.50	L	N

Table 2–1 — Continued

ID	Williams et al. (1996) ID	F814W$_{AB}$	r_1 ($''$)	$V_{606} - I_{814}$	z_{ph}[a]	A_W	C_W	AC[b] Class	In pruned sample?
hdf4_1706_1012	4-471.0	21.91	0.29	1.04	0.59	0.021	4.28	C	Y
hdf4_0902_1034	4-472.0	27.07	0.27	0.18	1.94	−1.000	−1.00	-	Y
hdf4_1505_1043	4-473.0	28.10	0.10	2.31	4.42	−1.000	−1.00	-	N
hdf4_1832_1038	4-475.0	26.41	0.20	0.51	0.48	0.005	2.44	L	Y
hdf4_0168_1048	4-476.0	27.86	0.13	0.40	2.51	−1.000	−1.00	-	N
hdf4_0577_1054	4-479.0	26.24	0.13	0.13	1.14	0.035	3.00	L	N
hdf4_1388_1071	4-487.0	27.75	0.10	−0.19	2.04	−1.000	−1.00	-	N
hdf4_1840_1066	4-488.0	25.90	0.17	0.05	2.42	0.070	3.20	L	N
hdf4_0384_1074	4-491.0	24.81	0.28	0.03	2.53	0.180	3.40	A	Y
hdf4_0300_1057	4-493.0	21.69	0.38	1.65	0.76	0.028	5.77	C	Y
hdf4_1514_1080	4-497.0	25.68	0.16	0.08	2.74	0.043	3.37	L	N
hdf4_1342_1086	4-498.0	26.78	0.16	0.03	2.16	−1.000	−1.00	-	N
hdf4_0807_1089	4-500.0	27.23	0.18	0.06	2.15	−1.000	−1.00	-	N
hdf4_1293_1091	4-502.0	25.23	0.44	0.00	2.09	0.100	3.44	L	Y
hdf4_1011_1099	4-505.0	25.42	0.50	0.97	1.78	0.002	2.36	L	Y
hdf4_1214_1122	4-509.0	28.30	0.10	1.27	1.28	−1.000	−1.00	-	N
hdf4_0733_1126	4-513.0	28.48	0.13	0.18	5.84	−1.000	−1.00	-	N
hdf4_1707_1120	4-514.0	26.17	0.18	0.15	1.28	0.069	2.95	L	N
hdf4_1586_1125	4-516.0	24.52	0.19	0.77	1.11	0.043	4.05	C	N
hdf4_1366_1142	4-519.0	29.62	0.09	−0.12	1.20	−1.000	−1.00	-	N
hdf4_0298_0187	4-52.11	24.41	0.39	0.30	3.10	0.103	3.89	A	Y
hdf4_0322_0161	4-52.12	25.53	0.24	0.37	2.68	0.026	2.57	L	Y
hdf4_1675_1137	4-520.0	25.83	0.14	0.14	1.76	0.024	3.11	L	N
hdf4_0187_1138	4-521.0	25.94	0.13	0.42	1.02	0.014	2.95	L	N
hdf4_1829_1132	4-522.0	25.50	0.25	0.58	1.01	0.005	2.96	L	Y
hdf4_0802_1144	4-525.0	26.93	0.13	0.12	0.68	−0.018	2.56	L	N
hdf4_1151_1146	4-527.0	26.87	0.15	0.52	0.59	−0.001	2.25	L	N
hdf4_1420_1149	4-530.0	27.51	0.15	1.19	4.36	−1.000	−1.00	-	N
hdf4_0506_1151	4-531.0	26.31	0.18	0.53	1.04	0.001	2.58	L	N
hdf4_1450_1180	4-543.0	25.70	0.26	0.07	1.82	0.029	2.71	L	Y
hdf4_0222_1190	4-544.0	28.99	0.11	0.53	1.60	−1.000	−1.00	-	N
hdf4_0624_1199	4-554.0	24.63	0.23	0.69	0.91	0.065	3.70	L	Y
hdf4_1605_1205	4-555.11	23.96	0.33	0.16	2.92	0.511	4.95	A	Y
hdf4_1588_1172	4-555.12	23.94	0.18	0.27	2.89	0.425	6.67	A	N
hdf4_1551_1172	4-555.2	23.13	0.24	1.67	0.93	0.019	5.04	C	Y
hdf4_1686_1213	4-557.0	25.93	0.19	0.24	1.88	0.023	3.12	L	N
hdf4_1385_1199	4-558.0	23.00	0.54	0.48	0.49	0.052	3.30	L	Y
hdf4_1837_1233	4-563.0	27.83	0.11	1.57	1.02	−1.000	−1.00	-	N
hdf4_0886_1215	4-565.0	22.66	0.31	0.82	0.78	0.044	3.88	L	Y
hdf4_1977_1232	4-567.0	26.25	0.17	0.59	0.82	0.004	2.55	L	N
hdf4_1540_1220	4-571.0	24.27	0.39	0.78	0.09	0.039	2.93	L	Y
hdf4_0955_1231	4-572.0	25.07	0.34	0.57	0.67	0.024	2.28	L	Y
hdf4_1635_1244	4-573.0	28.28	0.10	0.17	3.05	−1.000	−1.00	-	N
hdf4_1113_1235	4-576.1	25.47	0.20	0.18	3.06	0.129	3.45	A	Y
hdf4_1126_1232	4-576.2	27.05	0.12	0.13	1.50	−0.002	2.38	L	N
hdf4_1452_1243	4-579.0	25.04	0.13	0.41	0.56	0.011	3.17	L	N
hdf4_1281_1247	4-580.0	28.62	0.11	0.36	1.40	−1.000	−1.00	-	N
hdf4_0612_1244	4-581.1	25.58	0.16	0.03	2.12	0.036	3.41	L	N
hdf4_0648_1241	4-581.2	26.26	0.20	0.06	1.93	0.003	2.63	L	Y

Table 2–1 — Continued

ID	Williams et al. (1996) ID	F814W$_{AB}$	r_1 ($''$)	$V_{606}-I_{814}$	z_{ph}[a]	A_W	C_W	AC[b] Class	In pruned sample?
hdf4_0179_1249	4-588.0	25.16	0.41	0.12	2.07	−1.000	−1.00	-	Y
hdf4_0864_1266	4-590.0	25.78	0.19	0.21	1.94	0.064	3.30	L	N
hdf4_1758_1270	4-593.0	26.32	0.18	0.35	0.34	−0.005	2.45	L	N
hdf4_1651_1272	4-596.0	26.57	0.18	0.42	0.81	0.015	2.44	L	N
hdf4_1060_1273	4-598.0	27.26	0.18	0.69	0.92	−1.000	−1.00	-	N
hdf4_0835_1276	4-599.0	26.28	0.15	−0.01	2.76	0.000	3.13	L	N
hdf4_0474_1272	4-602.0	25.07	0.17	0.23	1.96	0.051	3.63	L	N
hdf4_1512_1267	4-603.0	26.52	0.24	−0.08	2.52	−1.000	−1.00	-	Y
hdf4_1785_1298	4-613.0	27.73	0.13	0.44	0.69	−1.000	−1.00	-	N
hdf4_1814_1287	4-618.0	23.91	0.37	0.51	0.66	0.218	4.64	A	Y
hdf4_1604_1322	4-625.1	25.40	0.23	1.43	4.42	0.057	2.87	L	Y
hdf4_1582_1316	4-625.2	27.49	0.12	1.78	4.65	−1.000	−1.00	-	N
hdf4_1522_1323	4-627.0	26.48	0.19	0.25	0.34	−1.000	−1.00	-	N
hdf4_1732_1330	4-628.0	26.91	0.20	0.72	0.93	−1.000	−1.00	-	Y
hdf4_1921_1332	4-631.0	25.30	0.21	0.03	2.21	0.108	3.50	A	Y
hdf4_0577_1337	4-635.0	25.95	0.24	0.55	0.78	−0.012	2.24	L	Y
hdf4_0759_1347	4-636.0	26.34	0.13	0.50	0.53	0.003	2.88	L	N
hdf4_1712_1347	4-637.0	26.64	0.21	0.33	1.24	−1.000	−1.00	-	Y
hdf4_0178_1342	4-638.0	25.19	0.28	0.65	0.61	0.012	3.21	L	Y
hdf4_0281_1324	4-639.1	24.57	0.25	0.17	2.44	0.150	4.00	A	Y
hdf4_0266_1351	4-639.2	25.22	0.19	0.96	4.24	0.052	3.30	L	N
hdf4_0485_1366	4-646.0	27.02	0.14	0.06	1.73	−1.000	−1.00	-	N
hdf4_0164_1375	4-651.0	26.36	0.18	0.13	1.56	−0.019	2.57	L	N
hdf4_1499_1380	4-653.0	27.90	0.19	−0.38	2.63	−1.000	−1.00	-	N
hdf4_0883_1350	4-656.1	20.71	0.56	0.56	0.47	0.086	2.82	L	Y
hdf4_1759_1373	4-658.1	24.83	0.19	0.45	0.64	0.019	3.32	L	N
hdf4_0995_1390	4-660.0	25.89	0.21	−0.02	2.42	0.102	3.10	A	Y
hdf4_0346_1369	4-661.1	24.44	0.18	0.68	0.62	0.022	3.67	L	N
hdf4_1105_1405	4-664.0	28.27	0.11	−0.06	1.73	−1.000	−1.00	-	N
hdf4_0676_1404	4-665.0	26.41	0.15	0.15	1.50	0.003	2.75	L	N
hdf4_0782_1413	4-671.0	26.59	0.17	0.75	1.03	0.015	2.40	L	N
hdf4_0574_1399	4-672.0	25.46	0.47	−0.07	1.96	−1.000	−1.00	-	Y
hdf4_0459_1400	4-676.1	25.52	0.18	0.06	2.36	0.065	3.14	L	N
hdf4_1270_1421	4-677.0	28.04	0.16	−0.25	1.76	−1.000	−1.00	-	N
hdf4_1322_1435	4-679.0	28.78	0.13	0.41	5.55	−1.000	−1.00	-	N
hdf4_1850_1437	4-681.0	26.52	0.12	−0.07	2.49	0.004	2.87	L	N
hdf4_1645_1440	4-682.0	28.07	0.13	−0.13	2.14	−1.000	−1.00	-	N
hdf4_0973_1452	4-687.0	26.93	0.17	0.36	2.38	−1.000	−1.00	-	N
hdf4_0172_1457	4-689.0	27.36	0.12	0.44	2.56	−1.000	−1.00	-	N
hdf4_0902_1460	4-690.0	27.52	0.12	0.78	1.26	−1.000	−1.00	-	N
hdf4_1179_1477	4-697.0	26.59	0.13	0.07	2.41	0.012	3.06	L	N
hdf4_0521_1478	4-700.0	26.77	0.17	0.55	1.15	−0.002	2.21	L	N
hdf4_1846_1472	4-701.0	25.98	0.21	0.26	1.09	0.004	3.11	L	Y
hdf4_0335_1504	4-713.0	24.10	0.12	1.29	4.07	0.085	3.64	L	N
hdf4_1104_1512	4-715.0	28.57	0.12	0.53	1.30	−1.000	−1.00	-	N
hdf4_1390_1513	4-717.0	28.40	0.10	0.64	1.29	−1.000	−1.00	-	N
hdf4_0429_1513	4-724.0	24.67	0.39	0.33	1.53	0.082	2.97	L	Y
hdf4_1146_1510	4-725.0	25.99	0.38	0.23	1.53	−1.000	−1.00	-	Y
hdf4_0176_1528	4-726.0	28.18	0.11	0.31	1.77	−1.000	−1.00	-	N

Table 2–1 — Continued

ID	Williams et al. (1996) ID	F814W$_{AB}$	r_1 ($''$)	$V_{606}-I_{814}$	z_{ph}[a]	A_W	C_W	AC[b] Class	In pruned sample?
hdf4_1488_1511	4-727.0	22.99	0.25	0.38	1.16	0.029	3.59	L	Y
hdf4_0261_1539	4-730.0	27.45	0.22	0.34	0.75	−1.000	−1.00	-	Y
hdf4_1632_1545	4-733.0	26.32	0.18	0.69	1.14	−0.009	2.47	L	N
hdf4_1499_1553	4-737.0	27.30	0.15	1.30	4.10	−1.000	−1.00	-	N
hdf4_0443_1557	4-742.0	26.58	0.24	0.83	0.71	−1.000	−1.00	-	Y
hdf4_1201_1568	4-743.0	27.78	0.15	0.60	0.70	−1.000	−1.00	-	N
hdf4_1716_1532	4-744.0	20.82	0.53	1.58	0.33	0.030	6.25	C	Y
hdf4_0481_1567	4-745.0	25.56	0.37	0.17	1.92	0.005	2.65	L	Y
hdf4_1452_1566	4-747.0	27.10	0.14	0.20	1.61	−0.000	2.38	L	N
hdf4_1997_1472	4-752.2	24.55	0.23	1.57	0.80	−0.003	4.17	C	Y
hdf4_0221_1575	4-753.0	27.51	0.11	0.22	0.84	−1.000	−1.00	-	N
hdf4_1411_1580	4-756.0	27.22	0.11	0.29	3.46	0.001	2.33	L	N
hdf4_0584_1586	4-759.0	27.13	0.19	0.80	1.12	−1.000	−1.00	-	N
hdf4_0815_1593	4-767.0	23.42	0.20	1.67	0.94	0.032	3.86	L	Y
hdf4_1184_1595	4-769.0	26.01	0.24	0.61	0.95	0.006	2.13	L	Y
hdf4_0386_1601	4-770.0	25.66	0.22	0.30	1.30	0.036	2.96	L	Y
hdf4_1370_1597	4-774.2	26.04	0.12	0.25	0.79	0.054	3.10	L	N
hdf4_1382_1587	4-774.3	25.78	0.11	0.07	0.77	0.025	3.50	L	N
hdf4_1554_1582	4-775.0	22.45	0.51	1.42	0.94	0.051	3.93	L	Y
hdf4_1922_1604	4-776.0	24.94	0.16	1.70	1.08	−0.004	3.55	L	N
hdf4_0492_1619	4-786.0	26.33	0.18	−0.01	1.87	0.021	2.80	L	N
hdf4_1927_1644	4-792.0	27.51	0.14	1.07	1.52	−1.000	−1.00	-	N
hdf4_0981_1650	4-794.0	26.54	0.20	0.39	1.06	−1.000	−1.00	-	Y
hdf4_1068_1612	4-795.111	20.90	0.51	0.64	0.47	0.037	3.50	L	Y
hdf4_0281_1652	4-801.0	24.49	0.23	0.75	0.98	0.082	3.92	L	Y
hdf4_1464_1668	4-804.0	24.98	0.20	0.52	0.93	0.016	3.36	L	Y
hdf4_0448_1677	4-809.0	26.95	0.12	0.63	1.14	0.008	2.67	L	N
hdf4_1007_1665	4-813.1	26.18	0.15	0.27	3.16	−0.006	2.68	L	N
hdf4_1000_1683	4-813.2	27.51	0.14	0.52	3.05	−1.000	−1.00	-	N
hdf4_0533_1675	4-814.0	26.00	0.18	0.26	1.52	0.001	3.00	L	N
hdf4_0751_1685	4-816.0	27.09	0.15	0.54	1.15	−1.000	−1.00	-	N
hdf4_1852_1691	4-820.0	26.12	0.22	0.88	0.92	−0.002	2.30	L	Y
hdf4_0894_1691	4-822.0	25.00	0.25	0.61	0.49	0.007	3.10	L	Y
hdf4_0321_1692	4-823.0	24.17	0.24	0.81	0.76	0.018	3.61	L	Y
hdf4_1442_1698	4-825.0	26.20	0.28	0.07	2.15	−1.000	−1.00	-	Y
hdf4_0878_1718	4-830.0	27.33	0.16	0.51	2.53	−1.000	−1.00	-	N
hdf4_1209_1726	4-832.0	27.12	0.16	1.55	3.71	−1.000	−1.00	-	N
hdf4_1558_1702	4-833.0	25.38	0.34	0.64	0.90	0.039	3.00	L	Y
hdf4_1030_1729	4-834.0	27.01	0.24	0.70	1.20	−1.000	−1.00	-	Y
hdf4_0600_1730	4-837.0	26.53	0.16	0.84	0.91	0.010	2.58	L	N
hdf4_1490_1735	4-838.0	26.95	0.37	0.15	1.64	−1.000	−1.00	-	Y
hdf4_1158_1714	4-839.0	24.79	0.43	0.41	0.44	0.002	2.47	L	Y
hdf4_1785_1730	4-845.0	24.81	0.19	0.41	1.17	0.029	3.30	L	N
hdf4_1185_1743	4-846.0	27.48	0.12	0.71	0.98	−1.000	−1.00	-	N
hdf4_1684_1737	4-848.0	26.60	0.24	0.41	1.47	−1.000	−1.00	-	Y
hdf4_1243_1754	4-850.0	28.49	0.12	0.30	2.09	−1.000	−1.00	-	N
hdf4_0894_1755	4-851.1	28.04	0.16	−0.07	1.61	−1.000	−1.00	-	N
hdf4_0386_1737	4-852.1111	23.53	0.28	0.23	0.09	0.259	4.23	A	Y
hdf4_0360_1735	4-852.1112	25.15	0.21	0.83	0.87	0.329	2.81	A	Y

Table 2–1 — Continued

ID	Williams et al. (1996) ID	F814W$_{AB}$	r_1 ($''$.)	$V_{606}-I_{814}$	z_{ph}[a]	A_W	C_W	AC[b] Class	In pruned sample?
hdf4_0326_1752	4-852.12	25.49	0.16	0.62	3.06	0.021	3.45	L	N
hdf4_1398_1761	4-854.0	27.43	0.20	0.08	1.79	−1.000	−1.00	-	Y
hdf4_1073_1764	4-858.11	25.55	0.13	0.34	0.41	0.101	3.74	A	N
hdf4_1074_1748	4-858.13	24.82	0.12	0.22	3.14	0.023	3.65	L	N
hdf4_0568_1765	4-860.11	25.00	0.26	0.37	0.46	0.018	2.78	L	Y
hdf4_0245_1790	4-864.0	26.77	0.16	1.22	4.16	−0.004	2.40	L	N
hdf4_0439_1790	4-866.0	26.18	0.17	0.03	1.86	0.037	2.77	L	N
hdf4_1557_1779	4-868.0	24.48	0.35	0.09	1.75	0.135	3.26	A	Y
hdf4_0619_1804	4-869.0	26.95	0.12	0.01	3.13	−0.007	2.86	L	N
hdf4_1237_1802	4-870.0	26.94	0.21	0.19	2.19	−1.000	−1.00	-	Y
hdf4_1442_1810	4-875.0	27.46	0.18	0.74	2.74	−1.000	−1.00	-	N
hdf4_0883_1816	4-877.0	27.09	0.15	0.94	1.05	−1.000	−1.00	-	N
hdf4_1003_1772	4-878.1	23.18	0.25	0.30	2.20	0.145	4.56	A	Y
hdf4_0996_1811	4-878.2	24.65	0.18	1.18	0.92	0.016	3.50	L	N
hdf4_1328_1817	4-879.0	27.11	0.16	0.65	0.97	−1.000	−1.00	-	N
hdf4_0605_1824	4-881.0	27.22	0.14	0.04	3.16	−1.000	−1.00	-	N
hdf4_0361_1827	4-884.0	27.80	0.12	1.77	4.19	−1.000	−1.00	-	N
hdf4_1047_1821	4-888.11	23.33	0.41	0.64	0.99	0.176	3.39	A	Y
hdf4_1446_1852	4-893.0	27.03	0.40	0.72	0.54	−1.000	−1.00	-	Y
hdf4_0999_1855	4-894.0	27.50	0.15	1.01	3.83	−1.000	−1.00	-	N
hdf4_1555_1852	4-895.0	26.53	0.24	0.70	0.81	−1.000	−1.00	-	Y
hdf4_1302_1865	4-902.0	28.41	0.12	−0.28	1.98	−1.000	−1.00	-	N
hdf4_0290_1868	4-906.0	27.61	0.17	0.48	2.11	−1.000	−1.00	-	N
hdf4_1278_1875	4-908.0	26.80	0.13	0.16	1.80	−0.015	2.69	L	N
hdf4_1799_1854	4-910.0	23.94	0.37	0.93	0.76	0.041	3.56	L	Y
hdf4_1373_1881	4-912.0	26.06	0.26	0.79	0.55	0.005	2.53	L	Y
hdf4_1138_1893	4-914.0	29.33	0.08	0.64	5.84	−1.000	−1.00	-	N
hdf4_0182_1874	4-916.0	23.98	0.37	0.37	0.43	0.015	3.55	L	Y
hdf4_1438_1907	4-924.0	27.02	0.32	0.42	1.09	−1.000	−1.00	-	Y
hdf4_0713_1884	4-926.1	23.87	0.56	1.36	0.91	0.080	3.61	L	Y
hdf4_0710_1915	4-926.2	25.31	0.16	0.16	0.34	0.079	3.21	L	N
hdf4_0890_1906	4-928.1	22.24	0.32	1.32	0.87	0.045	5.39	C	Y
hdf4_0377_1919	4-930.0	25.40	0.26	0.59	0.62	0.016	2.79	L	Y
hdf4_0640_1928	4-931.0	26.63	0.14	0.12	3.64	−0.015	2.65	L	N
hdf4_1332_1942	4-936.0	26.59	0.12	0.00	2.43	0.023	2.82	L	N
hdf4_1998_1941	4-937.0	25.04	0.15	0.55	0.60	0.027	3.52	L	N
hdf4_1278_1941	4-938.0	24.84	0.22	0.25	0.18	0.031	3.46	L	Y
hdf4_1039_1949	4-940.0	26.72	0.16	1.27	3.87	0.027	2.94	L	N
hdf4_0749_1956	4-942.0	23.85	0.21	1.43	0.88	0.041	4.14	C	Y
hdf4_0610_1962	4-944.1	27.00	0.14	0.54	0.43	−1.000	−1.00	-	N
hdf4_0228_1925	4-946.0	22.68	0.61	1.04	0.50	0.050	3.62	L	Y
hdf4_1553_1916	4-948.11	23.12	0.59	0.73	1.44	0.374	3.49	A	Y
hdf4_1592_1954	4-948.12	22.59	0.32	1.20	0.56	0.034	4.05	C	Y
hdf4_0537_1950	4-950.0	22.21	0.53	0.70	0.63	0.138	3.66	A	Y
hdf4_1307_1990	4-956.0	26.68	0.18	0.68	0.90	−0.009	2.27	L	N
hdf4_1384_1990	4-957.0	27.34	0.14	0.16	1.30	−1.000	−1.00	-	N
hdf4_0733_1998	4-960.0	26.54	0.20	0.04	1.92	0.027	2.40	L	Y
hdf4_1679_2003	4-963.0	25.99	0.21	0.51	0.48	0.015	2.88	L	Y
hdf4_0947_2020	4-967.0	26.97	0.13	0.37	1.47	−0.003	2.62	L	N

Table 2–1 — Continued

	Williams et al. (1996)								
ID	ID	$F814W_{AB}$	r_1 ($''$)	$V_{606} - I_{814}$	z_{ph}[a]	A_W	C_W	AC[b] Class	In pruned sample?
hdf4_1887_1945	4-976.2	24.04	0.58	0.18	0.26	0.025	3.02	L	Y

[a]Connolly (1999)

[b]A = High A_W, C = High C_W, L = Low $A_W C_W$

REFERENCES

Abraham, R. G. 1998, *private communication*

Abraham, R. G., Tanvir, N. R., Santiago, B. X., Ellis, R. S., Glazebrook, K., & van den Bergh, S. 1996a, MNRAS, 279, L47 (A96a)

Abraham, R. G., Valdes, F., Yee, H. K. C., & van den Bergh, S. 1994, ApJ, 432, 75

Abraham, R. G., van den Bergh, S., Glazebrook, K., Ellis, R. S., Santiago, B. X., Surma, P., & Griffiths, R. E. 1996b, ApJS, 107, 1 (A96b)

Arp, H. 1966, Atlas of Peculiar Galaxies (Pasadena: California Institute of Technology); also ApJS, 14, 1

Baum, W. A. 1962, IAU Symposium 15, 390

Benítez, N. 1998, astro-ph/9811189

Bertin, E. & Arnouts, S. 1996, A&AS, 117, 393

Brinchmann, J., Abraham, R. G., Schade, D., Tresse, L., Ellis, R. S., Lilly, S. J., Le Fèvre, O., Glazebrook, K., Hammer, F., Colless, M., Crampton, D., & Broadhurst, T. 1998, ApJ, 499, 112

Brunner, R. J., Connolly, A. J., Szalay, A. S., & Bershady, M. A. 1997, ApJ, 482, L21

Bruzual, A. G. & Charlot, S. 1993, ApJ, 405, 538

Cohen, J. G., Cowie, L. L., Hogg, D. W., Songaila, A., Blandford, R., Hu, E. M., & Shopbell, P. 1996, ApJ, 471, L5

Coleman, G. D., Wu, C.-C., & Weedman, D. W. 1980, ApJS, 43, 393

Connolly, A. J. 1998, *private communication* (C98)

Connolly, A. J. 1999a, *private communication* (C99)

Connolly, A. J. 1999b, Proceedings of the Workshop on Photometric Redshifts and High Redshift Galaxies, ASP Conference Series, eds. R. Weymann, L. Storrie-Lombardi, M. Sawicki, & R. Brunner, *in press*

Connolly, A. J., Csabai, I., Szalay, A. S., Koo, D. C., Kron, R. G, & Munn, J. A. 1995, AJ, 110, 2655

Conselice, C. J. 1999, *private communication*

Conselice, C. J., Bershady, M. A., & Jangren, A. 1999, ApJ, *in press*; also astro-ph/9907399

Cowie, L. L., Hu, E. M., & Songaila, A. 1995, AJ, 110, 1576

de Vaucouleurs, G. 1959, Handbuch der Physik, 53, 275

de Vaucouleurs, G. 1963, ApJS, 8, 31

de Vaucouleurs, G., de Vaucouleurs, A., Corwin, H. G., Jr., Buta, R. J., Paturel, G., & Fouqué, P. 1991, Third Reference Catalogue of Bright Galaxies (New York: Springer-Verlag)

Dickinson, M. 1999 in *After the Dark Ages: When Galaxies were Young (the Universe at* $2 < z < 5$*).* 9th Annual October Astrophysics Conference, College Park, MD, eds. S. Holt & E. Smith. (New York: American Institute of Physics Press), 122

Driver, S. P., Windhorst, R. A., Ostrander, E. J., Keel, W. C., Griffiths, R. E., & Ratnatunga, K. U. 1995, ApJ, 449, L23

Driver, S. P., Fernández-Soto, A., Couch, W. J., Odewahn, S. C., Windhorst, R. A., Phillipps, S., Lanzetta, K., & Yahil, A. 1998, ApJ, 496, L93

Ellis, R. S., Colless, M., Broadhurst, T., Heyl, J., & Glazebrook, K. 1996, MNRAS, 280, 235

Fernández-Soto, A., Lanzetta, K. M., & Yahil, A. 1999, ApJ, 513, 34 (FLY99)

Forbes, D. A., Elson, R. A. W., Phillips, A. C., Koo, D. C., & Illingworth, G. D. 1994, ApJ, 380, L47

Frei, Z. 1996, PASP, 108, 624

Frei, Z., Guhathakurta, P., Gunn, J. E., & Tyson, J. A. 1996, AJ, 111, 174

Gallagher, J. S., Hunter, D. A., & Tutukov, A. V. 1984, ApJ, 284, 544

Glazebrook, K., Ellis, R. S., Santiago, B., & Griffiths, R. E. 1995, MNRAS, 275, L19

Griffiths, R. E., Casertano, S., Ratnatunga, K. U., Neuschaefer, L. W., Ellis, R. S., Gilmore, G. F., Glazebrook, K., Santiago, B., Huchra, J. P., Windhorst, R. A., Pascarelle, S. M., Green, R. F., Illingworth, G. D., Koo, D. C., & Tyson, A. J. 1994, ApJ, 435, L19

Gullixson, C. A., Boeshaar, P. C., Tyson, J. A., & Seitzer, P. 1995, ApJS, 99, 281

Gwyn, S. D. J. & Hartwick, F. D. A. 1996, ApJ, 468, L77

Hibbard, J. E. & van Gorkom, J. H. 1996, AJ, 111, 655

Hubble, E. 1936, The Realm of Nebulae (New Haven: Yale University Press)

Kent, S. M. 1985, ApJS, 59, 115

Kohonen, T. 1989, Self-Organization and Associative Memory (3rd ed.; Berlin: Springer)

Koo, D. C. 1985, AJ, 90, 418

Koo, D. C. 1986, ApJ, 311, 651

Koo, D. C. 1999, Proceedings of the Workshop on Photometric Redshifts and High Redshift Galaxies, ASP Conference Series, eds. R. Weymann, L. Storrie-Lombardi, M. Sawicki, & R. Brunner, *in press*

Kron, R. G. 1995, in The Deep Universe, eds. B. Binggeli & R. Buser (Berlin: Springer)

Landsman, W. 1987, IDL Astronomy Library, header documentation for procedure FIND.pro

Lanzetta, K. M. & Yahata, N. 1999, *private communication*

Lanzetta, K. M., Yahil, A., & Fernández-Soto, A. 1996, Nature, 381, 759

Larson, R. B. & Tinsley, B. M. 1978, ApJ, 219, 46

Lilly, S. J., Tresse, L., Hammer, F., Crampton, D., & Le Fèvre, O. 1995, ApJ, 455, 108

Lowenthal, J. D., Koo, D. C., Guzmán, R., Gallego, J., Phillips, A. C., Vogt, N. P., Faber, S. M., Illingworth, G. D., & Gronwall, C. 1997, ApJ, 481, 673

Mähönen, P. H. & Hakala, P. J. 1995, ApJ, 452, L77

Mihos, J. C. 1995, ApJ, 438, L75

Mihos, J. C. & Hernquist, L. 1994, ApJ, 431, L9

Mihos, J. C. & Hernquist, L. 1996, ApJ, 464, 641

Mobasher, B. & Mazzei, P. 1999, Proceedings of the Workshop on Photometric Redshifts and High Redshift Galaxies, ASP Conference Series, eds. R. Weymann, L. Storrie-Lombardi, M. Sawicki, & R. Brunner, *in press*

Naim, A & Lahav, O. 1997, MNRAS, 286, 969

Naim, A., Ratnatunga, K. U., & Griffiths, R. E. 1997a, ApJ, 476, 510

Naim, A., Ratnatunga, K. U., & Griffiths, R. E. 1997b, ApJS, 111, 357

O'Connell, R. W. 1997, in The Ultraviolet Universe at Low and High Redshift: Probing the Progress of Galaxy Evolution (College Park, MD). ed. W. H. Waller [et al.], (New York: American Institute of Physics Press); also, AIP Conference Proceedings, 408, 11

Odewahn, S. C., Windhorst, R. A., Driver, S. P., & Keel, W. C. 1996, ApJ, 472, L13

Partridge, R. B. 1974, ApJ, 192, 241

Petrosian, V. 1976, ApJ, 209, L1

Pozzetti, L., Bruzual, A. G., & Zamorani, G. 1996, MNRAS, 281, 953

Rix, H.-W. & Zaritsky, D. 1995, ApJ, 447, 82

Sandage, A. R. 1961, The Hubble Atlas of Galaxies (Washington: Carnegie Institute of Washington)

Sawicki, M. J. 1997, http://www.its.caltech.edu/ sawicki/HDFstuff/HDFcatalog.out

Sawicki, M. J., Lin, H., & Yee, H. K. C. 1997, AJ, 113, 1 (SLY97)

Schade, D., Lilly, S. J., Crampton, D., Hammer, F., LeFèvre, O., & Tresse, L. 1995, ApJ, 451, L1

Schweizer, F. & Seitzer, P. 1992, AJ, 104, 1039

Simard, L., Koo, D. C., Faber, S. M., Sarajedini, V. L., Vogt, N. P., Phillips, A. C., Gebhardt, K., Illingworth, G. D., & Wu, K. L. 1999, ApJ, 519, 563

Steidel, C. C. & Hamilton, D. 1993, AJ, 105, 2017

Steidel, C. C., Giavalisco, M., Dickinson, M., & Adelberger, K. L. 1996, AJ, 112, 352

Takamiya, M. 1999, ApJS, 122, 109

Thuan, T. X. & Gunn, J. E. 1976, PASP, 88, 543

Toomre, A. & Toomre, J. 1972, ApJ, 178, 623

van den Bergh, S., Abraham, R. G., Ellis, R. S., Tanvir, N. R., Santiago, B. X., and Glazebrook, K. G. 1996, AJ, 112, 359

Vogt, N. P., Forbes, D. A., Phillips, A. C., Gronwall, C., Faber, S. M., Illingworth, G. D., & Koo, D. C. 1996, ApJ, 465, L15

Vorontsov-Velyaminov, B. A. 1959, Atlas and Catalog of Interacting Galaxies (Moscow: Sternberg State Astronomical Institute)

Williams, R. E., Blacker, B., Dickinson, M., Dixon, W. V., Ferguson, H. C., Fruchter, A. S., Giavalisco, M., Gilliland, R., Heyer, I., Katsanis, R., Levay, Z., Lucas, R. A., McElroy, D. B., Petro, L., Postman, M., Adorf, H.-M., & Hook, R. N. 1996, AJ, 112, 1335

Yee, H. K. C. 1991, PASP, 103, 396

Zwicky, F. 1953, Physics Today, 6, 7

Zwicky, F. 1956, Ergebnisse der Exakten Naturwissenschaften, 29, 344

Zwicky, F. 1959, Handbuch der Physik, 53, 373